Charge Transport Phenomena in Fe-Based High Surface Area Materials

by

Jacob McKenzie

A dissertation accepted and approved in partial fulfillment of the

requirements for the degree of

Doctor of Philosophy

in Chemistry

Dissertation Committee:

Ramesh Jasti, Chair

Carl K. Brozek, Advisor

Kenneth Doxsee, Core Member

James Watkins, Institutional Representative

University of Oregon

Spring 2024

DISSERTATION ABSTRACT:

Jacob McKenzie
Doctor of Philosophy in Chemistry

Title: Charge Transport Phenomena in Fe-Based High Surface Area Materials

While conductive metal-organic frameworks (MOFs) and open-framework metal chalcogenides (OFMCs) have received considerable attention in recent years, there are still fundamental questions that remain unanswered. With literature abound describing ion and solvent-dependent conductivity in mesoporous media and nonporous conductive polymers we expect such phenomena to be heightened and unique at the interfacial extremes that microporous materials and 2D Van Der Waals (vdw) materials possess. We utilize the unique properties of Fe-based materials to design model systems in TMA2FeGe4S10 (TMA: tetramethyl ammonium) and Fe(SCN)2(pyz)2 to explore the impact of solvent and electrochemically inert ions on charge transfer and transport. Taken together, this dissertation describes for the first time, critical solvent and ion interactions at interfacial extremes, which must be considered in the design of advanced energy storage technologies where solvent and ion presence is ubiquitous. These advanced energy storage technologies will prove critical in supporting renewable energy generation, to reduce and eventually eliminate CO2 emission.

This dissertation contains previously published and unpublished co-authored material.

ACKNOWLEDGMENTS

Throughout my graduate education I owe a tremendous amount to so many people in my life, that loved me even when I was truly undeserving. I'm so incredibly proud of the body of work I can lay in front of them as a testament to my absence.

For starters, my mother and father, I love you both more then I know I say. You have been tremendously supportive and gave me the freedom to fail, which has been critical in my growth, not only as a human but a scientist. To my brand-new sisters, welcome to the family, and I appreciate having more board game opponents around the holidays. To my brothers, Ryan, Travis, and Josh. Ryan, your commitment to keeping the family group chat alive is admirable, and our shared interest in Slipknot, who I'm looking forward to seeing absolutely decimate this upcoming Fall. Travis, for being the older brother who I got to watch play Halo as you never shared, and for always wanting to discuss potential business opportunities, I look forward to helping you develop the next billion-dollar idea. Josh, for giving me a home away from home in Portland when growing up, you taught me so much about how to be a rational and ethical human being, I look forward to visiting you in my new home away home in France one day.

I'm blessed in having not only a tremendous supportive family, but also a tremendous friend group. Kennedy, Kyle, Brandon, Bria, and Joseph, I've known some of you since I was just a wee child, trading cheese and crackers on the playground. As long as there are videogames to play, no matter where we all are, we will always have something to share in. I owe you all for providing important escapes back to Washington to party, and for a moment forget I have a billion experiments to run and papers to write.

I also could not have done this without the tremendous lab that Carl K. Brozek has cultivated. Obviously, I first must thank Carl for believing in me and giving me the freedom to

fall down horrifying esoteric electrochemical impedance rabbit holes, and extending at times, friendship. You went above and beyond what is expected of a PI, and your passion for chemistry is inspiring. Under your guidance, I have become a scientist I never would have imagined I could be, when I first sat down in my undergraduate General Chemistry course in 2014, with only an English Literature major on my mind. To my fellow lab members past and present: Checkers Marshall, Kevin Fabrizio, LeRoy, Ashley Mapile, Audrey Davenport, Quinn Valentine, Faiqa Khaliq, Golnaz Navidi, Erik Grape, Jiawei Huang, Kentaro Kadota, Stacey Andreeca, Jeffrey Gombart, Jeremy Love, and others, thank you for dealing with my at times neurotic, disorganized, and messy self, and providing a safe space to ask stupid questions and offer simple solutions to what at times seems like impossible tasks. And to LeRoy, for always being down to get a PBR and talk trash, and at times mosh among fellow degenerates of Eugene at John Henrys. We've likely taken years off our life, but it's not like graduate school wasn't already.

Lastly, I want to thank my partner Victoria Dow, who besides showing me there is a town in Oregon called Cresswell, has been an integral part of my formative years in graduate school. She taught me that you don't have to be pursuing a PhD in STEM to be brilliant. I will never stop laughing at literally everything you say. I didn't think I'd come out of Eugene with anything but a PhD, debt, and a bad attitude, but I somehow managed to stumble out of it with a PhD, debt, a bad attitude, and a life partner.

This dissertation is dedicated to Johnathan Henrys,
music you can smell.

TABLE OF CONTENTS

LIST OF FIGURES

Figure Page

Figure Page

Figure Page

Figure Page

Figure Page

Figure Page

Figure Page

LIST OF TABLES

LIST OF SCHEMES

Scheme Page

CHAPTER I

INTRODUCTION

Chapter **I** is written by myself.

Chapter **II** is based on published work in *Chemistry of Materials*, with coauthors: Le, K. N.; Bardgett, D. J.; Collins, K. A.; Ericson, T.; Wojnar, M. K.; Chouinard, J.; Golledge, S.; Cozzolino, A. F.; Johnson, D. C.; Hendon, C. H.; Brozek, C. K.

Chapter **III** is based on published work in *Chemical Science* with coauthors: Brozek, C. K.; Kempler, P. A

Chapter **IV** is based on currently unpublished work with coauthors: Pennington, L. P.; Kadota, K.; Ericson, T.; Cope, E.; Cozzolino, A. F.; Hendon, C. H.; Brozek, C. K.

Chapter **V** is written by myself.

1.1 Energy Storage is Critical for Decarbonization.

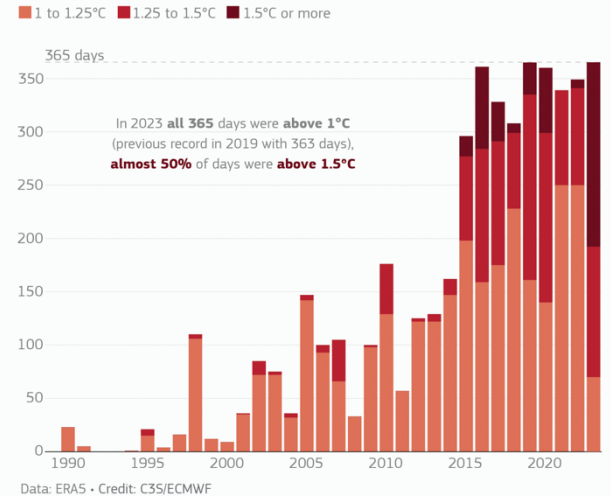

Figure 1.1 Copernicus Climate Change Service/European Centre for Medium-Range Weather Forecasts Data showing by the year the number of days with temperature increases between 1-1.25 °C, 1.25-1.5°C, and above 1.5°C vs. average pre-industrial temperature (1850-1900).

Recently, 2023 was the hottest year on record, with every day of the year ≥1°C warmer than preindustrial temperatures (Figure 1.1).[1] Of these days, nearly half of these days were 1.5°C warmer than preindustrial temperatures. This warming is especially concerning as 1.5°C warming is the often-cited limit to avoid catastrophic climate collapse.[2] As is, a continued upward trend is predicted as CO_2 concentrations in the atmosphere continue to grow, with worldwide atmospheric CO_2 levels in February 2024 a record-breaking 425ppm.[3] Continued global temperature changes will dramatically impact human and animal well-being as the world faces increasing strife from droughts, storms, and flooding.[4]

The Global Carbon Project has reported that in 2023, 90% of global CO_2 emissions were the result of fossil fuel combustion for energy.[5] For this reason, transitioning from fossil fuels to clean renewable technologies is the primary strategy for reducing CO_2 emissions. While renewable technologies have seen price drops competitive with fossil fuel technologies, they still have underlying flaws that limit their application in total replacement of fossil fuels.[6] For example, renewable technologies such as solar and wind are inherently intermittent, and fossil fuels are burned in the interim. The solution commonly proposed is the joint deployment of sustainable energy generation with energy storage technologies.[7] Any energy not immediately consumed can be stored and used when energy generation isn't possible. Such energy storage is often accomplished with pumped storage hydropower, which comprises a sizable ~99% of all deployed energy storage.[8] However, this technology has distinct disadvantages. For example, the effective deployment of this technology requires a tremendous upfront economic and environmental cost. In addition, leading experts suggest due to stringent land requirements, we've reached the limit on constructable pumped hydropower plants.[8] Furthermore, lakes which comprise 87% of Earth's freshwater and are critical to pumped hydropower's function are seeing

a dramatic increase in evaporation rates due to climate change.[9] Climate change also manifests in frequent flooding and droughts, affecting water reservoirs critical to functioning hydropower plants.[10]

1.2 Better Energy Storage with Intercalation Pseudocapacitors.

In selecting energy storage replacements for pumped hydropower, many would argue for lithium-ion batteries, which were paramount in decarbonizing the automotive sector. However, the energy to power a small vehicle is far smaller than the energy needed to power massive industrial processes or entire electrical grids. Even in battery arrays containing 25,600 lithium-ion batteries, the energy density is still far less than pumped hydropower, only generating 5 MWh, 2700 times less than a typical pumped hydropower plant.[11] Moreover, lithium-ion

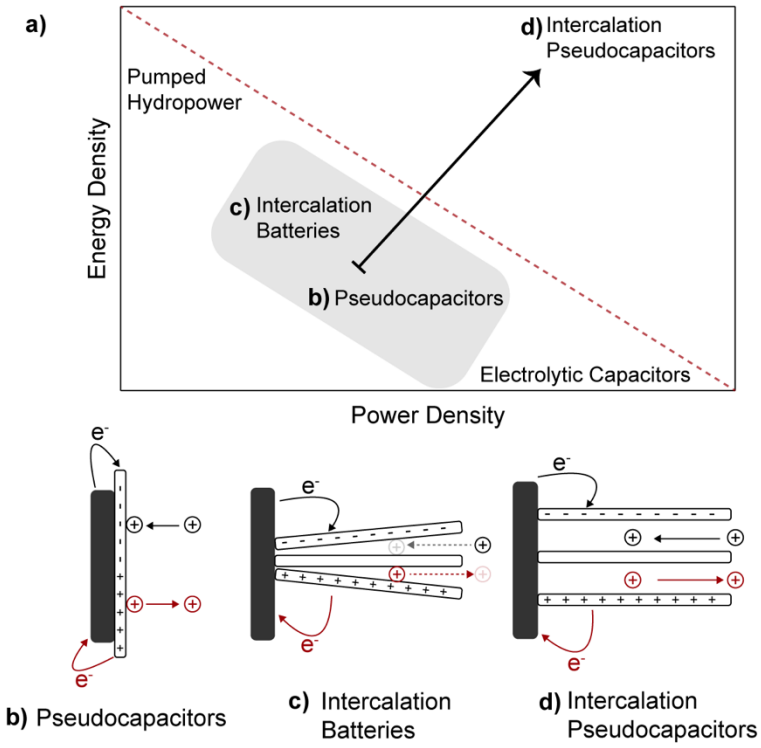

Figure 1.2 a) Relative energy vs. power densities for selected energy storage technologies. Depiction of the mechanism of charge storage for b) pseudocapacitors, c) intercalation batteries, and d) intercalation pseudocapacitors.

batteries often have inherent device stability due to sluggish intercalation and phase change-induced volumetric expansions.

Unlike lithium-ion batteries, supercapacitors or pseudocapacitors are energy storage technologies hailed for their near-infinite cyclability. However, they have minimal energy density, with charge only stored at the material surface. Herein lies the fundamental tradeoff. Visualized in Figure 1.2, energy storage can have either massive power or energy densities, but never both. Ideally, when selecting energy storage to support renewable energy generation one wants a technology with high energy density, power density, and long device lifetimes. Recent research has described a new elusive energy storage mechanism that could realize such a device, intercalation pseudocapacitance.

Pseudocapacitors, like batteries, store charge through reversible redox couples. However, while batteries store charge throughout the entire material, pseudocapacitors only utilize surface redox sites. For this reason, the redox in pseudocapacitors is ultra-fast as it doesn't rely on the massive kinetic barriers ion intercalation requires. Similarly, intercalation pseudocapacitors intercalate without massive kinetic barriers at time scales comparable to surface adsorption in pseudocapacitors. Furthermore, there is no kinetically limiting phase change as often seen in traditional intercalating technologies, which further hinders device performance. As is, not many materials currently display this charge storage mechanism as intercalation is almost always a kinetically limiting and diffusion-controlled process. The classic intercalation pseudocapacitors in the literature are Nb_2O_5 and bronze phase TiO_2. These materials reversibly store charge through Nb^{5+} and Ti^{4+} reduction throughout the entire material, with ion diffusion time scales comparable to ion adsorption. Researchers hypothesize that this behavior manifests from these materials' open-pore structure. Visualized in Figure 1.3 are the crystal structures of both Nb_2O_5

and TiO_2 where the 2D tunnels of 3.5 and 4.6 Å respectively are hypothesized to provide low-energy Li^+ diffusion pathways.[12,13] These relatively small micropores with sizes similar to Li^+ (0.74 Å) are most effective in minimizing energy barriers for Li^+ conduction.[14] These low-energy pathways for Li^+ transport allow for rapid transport without substantial material deformation, suppressing undesirable phase changes. In the case of Nb_2O_5 composite technologies, the cycle stability has been reported as high as 120,000 cycles.[15] However, these materials still have not seen widespread industrial application due to expensive titanium and niobium metals, and poor electronic conductivity requiring composite engineering to achieve device viability.[13] To realize the industrial application of this superior energy storage mechanism, broadening the material landscape is critical, and identifying tunable model systems to understand scarcely understood structure-property relationships.

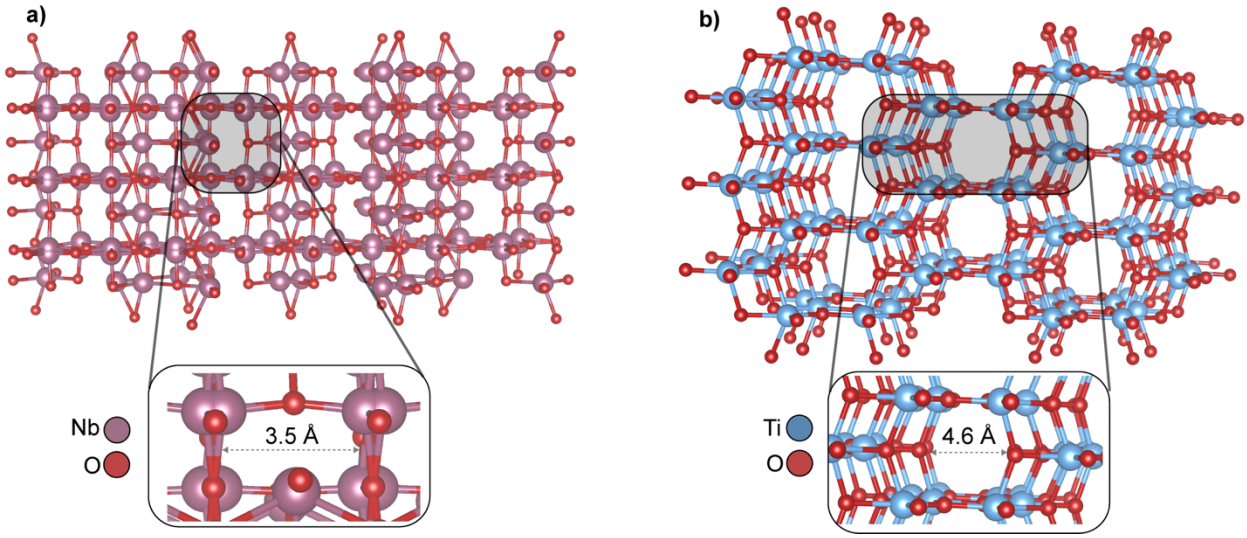

Figure 1.3 Crystal Structure of a) Nb_2O_5 and b) B-TiO_2. The insets showcase the 2D channels responsible for low energy Li^+ diffusion pathways.

1.3 Open-Framework Materials Offer Ideal Platforms for Studying Energy Storage.

Open-framework materials are renowned for their synthetic diversity due to the bottom-up modular approach to material design and synthesis. Classic examples of these materials are metal-organic frameworks (MOFs), open-framework metal chalcogenides (OFMCs), and polyoxometallic frameworks (POMs). Judicial selection of linking metals/clusters and organic linkers/inorganic clusters can lead to a broad range of materials. For example, MOFs have over 90,000 structures synthesized with over 500,000 currently predicted.[16] Another important property of these materials is their high surface area, with the large size of the ligand/inorganic cluster relative to linking metal leading to periodic void spaces with surface areas that have reached a record-breaking 7,100 m^2/g in the MOF NU-110.[17]

Their high surface area and near-infinite tunability make them promising candidates for next-generation energy storage. In fact, MOF and POM materials have found use in supercapacitor and battery applications with similar performance to commercial batteries.[18–20] However, technologies with the theoretical promise of high energy and power density are still unrealized, and material costs are not yet competitive with current energy storage materials. Furthermore, until recently, most MOFs and POMs are electronically insulative due to the inherent ionic nature of metal-ligand coordination bonds.[21,22] However, design strategies have improved, and with proper linker and metal selections, electrical conductivities can vary across 17 magnitudes when comparing MOFs.[21] Even still, metal-like conductivities have only been realized in some 2D MOF materials, with minimal compositional diversity.[23,24] In contrast to band-type, metal-like conduction, which conducts charge through delocalized orbitals, most MOFs conduct charge through redox hopping, where electrons tunnel from one localized state to another. In addition, OFMCs while often hailed as porous semiconductors have had no explicit

studies on their electrical conductivity.[25] These systems are merely 3D porous analogs of the traditional 2D metal chalcogenides which are semiconductive and have seen wide appeal in energy storage and harvesting applications.[26,27]

When designing electrically conductive systems both the metal and linker can be modulated to achieve conduction pathways. For metals, redox-active metals are the most promising candidates for conductive materials. In particular, Fe is one of the most promising metals, in part because of the highly accessible $Fe^{2+/3+}$ redox couple, with Fe oxidation promoting charge transport in either conduction pathway.[28] For redox hopping, $Fe^{2+/3+}$ mixed valency gives well-resolved donor and acceptor states. For band-type conduction, high energy valence electrons in Fe^{2+} dominate valence band edges, so p-type charge carriers can be generated with Fe oxidation.[28] In addition, Fe is one of the most abundant elements on earth and is substantially cheaper than typical Co or Ni based Li-ion batteries. In fact, all Fe-based batteries are ten times cheaper than these traditional lithium-ion batteries.[29]

The facile redox activity of Fe can also improve charge hopping between ligands through intraframework electron transfer from Fe^{2+} to ligands. Such phenomena explain the unusually high conductivity in several MOF structures composed entirely of Fe^{3+}.[30,31] However, to better promote band-type conduction ligand selection is paramount, as electronegativity matching between the metal and ligand is important in generating covalent bonds.

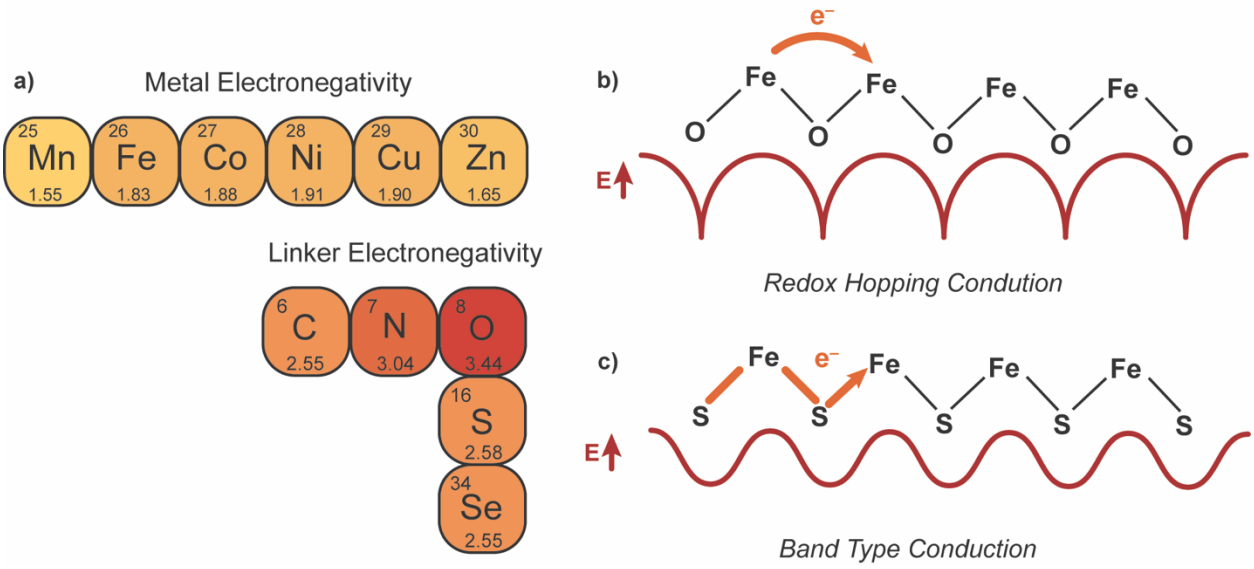

Figure 1.4 a) electronegativities of common metals and coordinating linker atoms in design of framework materials. b) Potential energy wells associated with ionic Fe-O bond redox hopping conduction. c) Potential energy wells associated with covalent Fe-S bond band type conduction

Improved electronegativity matching between the metal and linker leads to covalent bonds and shallower potential energy wells along the conduction pathway (Figure 1.4). For example, replacing oxygen-based linkers with sulfur or nitrogen-based linkers has improved conductivity in MOF systems.[28] This improved electronegativity matching has led to some of the highest conductivities reported in Fe-containing MOFs such as in Fe(1,2,3-triazolate)$_2$ (0.3 S cm^{-1}) and Fe$_2$(5,5′-(1,4-phenylene)bis(1H-tetrazole))$_3$ (1.2 S cm^{-1}).[32,33] In addition, some of the highest conductivities were recently seen in an analogous open-framework chalcogenide material composed of [Fe$_4$S$_4$] linked by carbon-based linkers.[34] The high conductivity is hypothesized to be due to strong electronegativity matching between carbon and Fe. Even still, in conductive Fe-containing frameworks, the origin of the conductivity mechanism is still hotly debated. Is it redox hopping through $Fe^{2+/3+}$ mixed valency or band-type transport promoted by strong metal-ligand covalency?

1.4 Charge Conduction in High Surface Area Materials.

The design of conductive MOFs is seeing a major surge as many studies on new conductive MOFs and conductive MOF design are released. In 2016, only ~30 studies were published concerning conductive MOFs in contrast to 2020, where nearly 130 studies were published.[21] Even still, only 0.2% of all MOFs synthesized are reported as electrically conductive. This is in part because there are still many fundamental questions that remain unanswered. For example, the high surface area in these materials challenges notions of typical charge transport. Fundamentally, how do charges move in a material that is mostly empty space? Studies have found that such massive surface areas can lead to guest-dependent conductivity through absorption.[35] However, in these situations, the guests are electroactive and serve as donor or acceptor states in promoting electron transfer via redox hopping. The question remains, how do non-electroactive components like Li^+ in a lithium-ion battery or solvent in an electrolyte solution impact charge transport? In mesoporous TiO_2, solvent and electrolyte pore infiltration dramatically affects electronic transport and performance in battery electrodes and solar cells.[36–38] The most extreme effects have been observed for nonporous conductive polymers where both the electronic conductivity and the charge transport mechanism depend on ion and solvent presence. Poly(benzimidazobenzophenanthroline), which is often hailed as a through-bond conductor when dry, when instead immersed in an electrolyte solution, has substantially lower electronic conductivity and instead conducts charge through redox hopping.[39] In addition, after the experiment and the sample is allowed to dry, it again becomes a through-bond conductor but electrolyte ions entangled within the polymer chains lower the electronic conductivity 1000-fold.

Such effects observed in nonporous and mesoporous materials indicate clear influences from ions and solvents. However, what about in microporous media? Framework materials are

often microporous with pores and void spaces on the order of Angstroms to ~1nm scales. We expect that any solvent and ion effects seen previously will be enhanced in microporous materials, due to increased interfacial interactions, and nanoconfinement of solvent and ions. Nanoconfinement has led to emergent phenomena such as drastically smaller dielectric constants in nanoconfined water or increased ionic conduction for nanoconfined Li^+ vs larger pore Li^+ conduction.[14,40,41] The nanoconfinement of ions within the micropores of an electrically conductive framework should affect charge transport, and in some extreme cases control it. This is analogous to the molecular phenomenon of proton-coupled charge transport, which enables important biological process and is characterized by the concerted ambipolar-like diffusion of protons and electrons.[42–44] Such mechanisms are only recently beginning to be realized in MOFs.[45,46] However, only in well-controlled ideal redox hopping systems, with little insight into the exact nature of the ion-electron coupling, and what variables control it.

This dissertation utilizes the unique properties of Fe to design model systems to study fundamental questions on charge transport in microporous and high surface area conductors, where ion-charge interactions on the Ångstrom scale, lead to emergent interfacial phenomena. In Chapter II, we synthesize a diverse and forgotten class of materials known as open-framework metal chalcogenides (OFMCs) and explore the structure-property relationships of charge conduction in inorganic microporous materials. We found the materials are semiconductive with metal, chalcogenide, and defect concentrations playing large roles in promoting electronic conductivity. Like MOFs, owing to its facile redox activity, $TMA_2FeGe_4S_{10}$ (Fe-S) led to the highest electrical conductivity and defect tolerance. In contrast, the other metal systems (M-S; M: Mn, Co, Ni, and Zn) were mixed conductors of both electrons and the tetramethylammonium (TMA^+) cations contained within the micropores. Unlike most conductive MOFs, experimental

results suggest the Fe materials are band-type conductors with small amounts of Fe^{3+} producing p-type charge carriers. In Chapter III, we leveraged the unique nanoconfined TMA^+ and the modulation of charge transport mechanism from band-type with Fe-S to classical redox hopping with Zn-S, to study the impact of solvent and nanoconfined ions on both mechanisms of charge transport. We found that solvent aids in electrical conductivity, with conductivity scaling with the dielectric strength of the solvent for both Fe and Zn-S. For Zn-S, high dielectric strength solvents improved the diffusion of TMA^+, facilitating charge hopping processes. For Fe-S, the solvent functions as a dielectric screen between the electron and TMA^+, improving charge carrier mobility. These conclusions were supported by pressed pellet impedance measurements which with a novel model developed, described the microscopic signatures of ion-coupled charge transport in microporous mixed conductors. From impedance fits, Zn-S was defined as an ion-coupled conductor and Fe-S as an ion-limited conductor, with evidence of concerted ion-electron movement in Zn-S. Finally, in Chapter IV, Fe's unique redox activity in the 2D MOF $Fe(SCN)_2(pyz)_2$ was leveraged to produce the largest reported interlayer coupling energies in Van Der Waal (vdw) materials. Such massive coupling energies manifested in a through-space, interlayer charge transfer seen as an intense visible light absorption in solution. The axial NCS^- endowed the material with high interactive surface area and Fe oxidation promoted interlayer coupling and charge transfer through a mixed charge state. The charge transfer bore substantial dependence on solvent dielectric and dissolved electrolyte and could be effectively turned on and off with variance of either. This dissertation builds off the already established work on Fe-based framework design by further showcasing its role in similarly classed OFMCs and indirectly promoting interlayer charge transfer in a 2D vdw MOF. Furthermore, this dissertation explores unique charge transport phenomena in microporous and high surface area materials, where

solvent and electrolyte interactions are greatly enhanced. Leveraged, these results will aid in the design of framework electrode materials where solvent and electrolyte will invariably be present, and in intercalation pseudocapacitors technologies where ion nanoconfinement is critical.

CHAPTER II

CONDUCTIVITY IN OPEN FRAMEWORK CHALCOGENIDES TUNED *VIA* BAND ENGINEERING AND REDOX CHEMISTRY

This section includes an excerpt from previously published and co-authored material from McKenzie, J.; Le, K. N.; Bardgett, D. J.; Collins, K. A.; Ericson, T.; Wojnar, M. K.; Chouinard, J.; Golledge, S.; Cozzolino, A. F.; Johnson, D. C.; Hendon, C. H.; Brozek, C. K. Conductivity in Open-Framework Chalcogenides Tuned via Band Engineering and Redox Chemistry. *Chem. Mater.* **2022**, 34 (4), 1905–1920.

In this chapter, the project idea was conceptualized by Jacob McKenzie and Carl. K. Brozek. The article was co-written by Jacob McKenzie, David C. Johnson, Anthony F. Cozzolino, Carl K. Brozek, and Christopher H. Hendon. Experiments and analysis were performed by Jacob McKenzie. Computations were performed by Khoa N. Le. Le Bail fits were performed by Dylan J. Bardgett. SQUID magnetometry and analysis was performed by Kelsey A. Collins and Michael K. Wojnar. XPS data collection and analysis was performed by Julie Chouinard and Stephen Golledge. Mössbauer spectra was collected and analyzed by Thomas Ericson.

Introduction.

Semiconductor technologies often rely on materials with accessible porosity and high surface areas. These structural features facilitate molecular diffusion of reagents to the active sites of photo- and electrochemical catalysts[47–51] and improve the activity of materials such as batteries and capacitors by increasing the exposed working areas.[19,52–56] In addition to device performance, high surface-to-volume ratios present unique opportunities in interfacial chemistry. For instance, the optical, electronic, and magnetic behaviors of semiconductors can vary with the

properties of the external media,[57–59] while high-energy surface defects can dominate the reactivity of semiconductor catalysts.[60,61] Studying these structure–function relationships benefits from well-defined architectures that can be tuned through precise molecular synthesis. The porosity of conventional semiconductors, such as porous metal oxides, is often irregular and difficult to modify, however.[62,63]

Crystalline materials with well-defined and regular porosity, such as metal–organic frameworks (MOFs), offer a powerful platform for studying the fundamental impact of high internal surface areas on wide-ranging material properties. Assembled from the combination of multitopic organic linkers and high-symmetry inorganic clusters or metal ions, MOFs have been generated into more than 90 000 structures from bottom-up synthetic routes that can be modified with molecular specificity.[64] Despite this plethora of materials, few MOFs exhibit electrically conductive behavior due to the highly ionic bonding between metal ions and the typical carboxylate linkages.[21] Attempts to improve covalency by employing chalcogenide and azolate ligands have afforded conductive MOFs, but the examples remain compositionally limited and most extend in only two dimensions.[65–67] "Open-framework chalcogenides" offer an alternative family of nanoporous materials, featuring main-group-chalcogenide clusters linked by transition-metal ions through covalent bonds. Like MOFs, these materials are available with a variety of metal ions, chalcogenides, and clusters, furnishing a diverse collection of networks with varying pore sizes and shapes. Although these materials have been widely studied for decades and frequently termed semiconductors,[24,67–79] few, if any, studies have examined their basic conductivity properties.[72,75,79] As three-dimensional (3-D) frameworks, these materials serve as low-density analogues to conventional metal chalcogenides, opening fundamental studies into the relationship of semiconductor form and function. These materials also benefit from well-

defined porosity, unlike two-dimensional (2-D) metal chalcogenides whose surface areas can become inaccessible through intersheet aggregation.[81,82] While new examples of conductive MOFs remain hotly pursued, many open-framework chalcogenides have already been reported and simply await studies into the relationship between their nanoporosity and semiconductor behavior.

Here, we report a combined experimental–computational investigation into the iconic family of materials $TMA_2MGe_4Q_{10}$ (M = Mn, Fe, Co, Ni, Zn; Q = S, Se, TMA = tetramethyl ammonium), as shown in Figure 2.1, first reported by Yaghi et al. prior to the advent of modern MOF chemistry.[68] A reexamination of these frameworks presents new insights into their optical, magnetic, and electronic behaviors, revealing the sensitivity of these properties to subtle differences in composition and their tunability through molecular redox chemistry. The charge transport of the frameworks is especially sensitive to these variables, with conductivities differing across several orders of magnitude and in the basic mechanism of transport. A key insight from the anomalously high conductivity of the Fe analogue is that charge mobilities and charge carrier densities—the essential parameters governing conductivity—can be tuned through molecular chemistry in the form of metal–ligand bond covalency and redox chemistry. These results provide direct confirmation of open-framework chalcogenides as porous semiconductors, while opening myriad investigations into their tunable charge transport behavior.

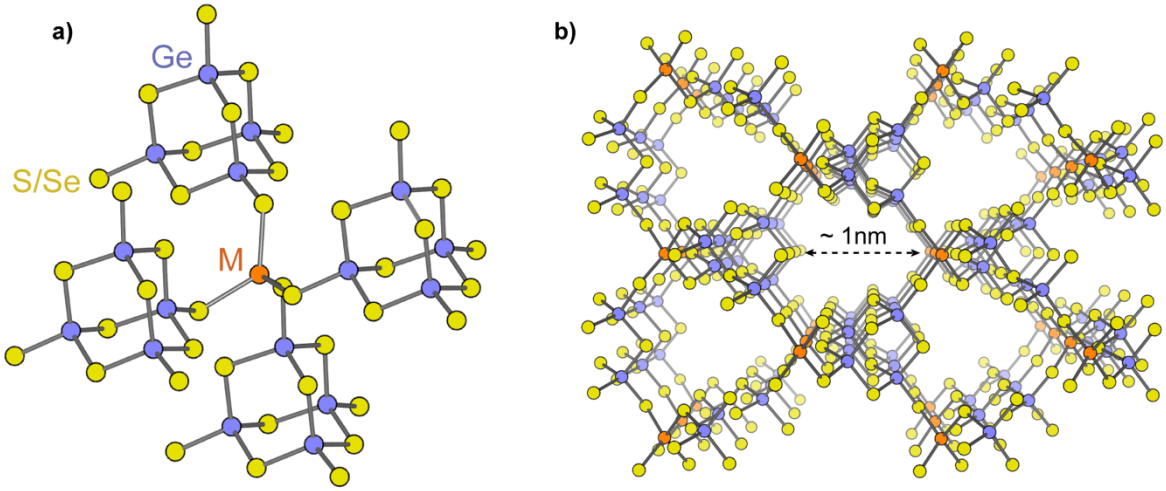

Figure 2.1 Crystal structure of open framework chalcogenides $TMA_2MGe_4Q_{10}$, TMA = tetramethylammonium, M = Mn, Fe, Co, Ni, Zn, Q = S or Se ($TMA_2MnGe_4S_{10}$ depicted). a) Local coordination and b) extended network representations with TMA cations omitted for clarity.

Results and Analysis.

Following synthetic procedures previously reported by Yaghi et al.,[68] the open-framework chalcogenides TMA_2MGe_4S10 (M = Zn; Zn–S, Co; Co–S, Fe; Fe–S, and Mn; Mn–S) and $TMA_2FeGe_4Se_{10}$ (Fe–Se) were prepared, affording crystalline powders as evidenced by

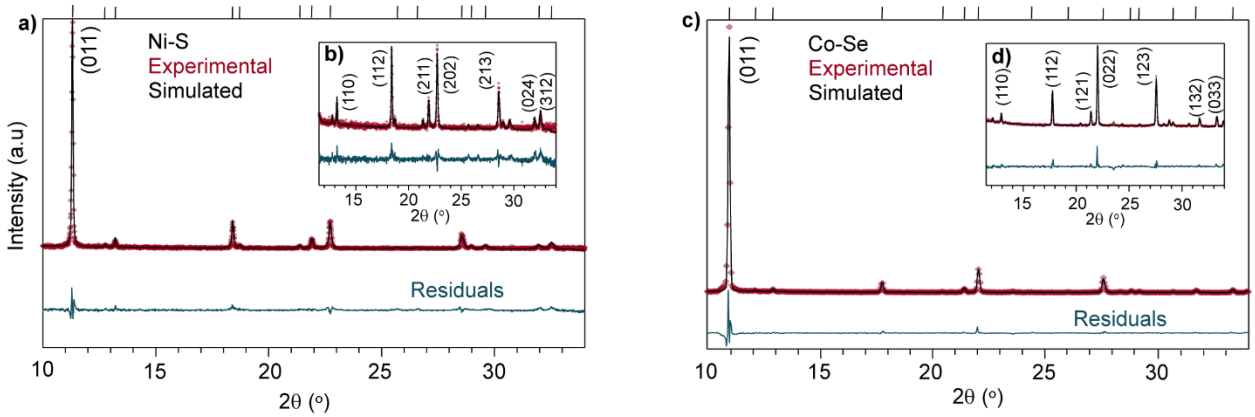

Figure 2.2 Experimental powder X-ray diffraction patterns (red) for Ni–S (a) and Co–Se (c) fitted with simulated patterns (black) and residuals (blue) after cell indexing with Le Bail fits. Insets showcase lower-intensity reflections (b, d), and tick marks on top of the plot denote expected reflections.

powder X-ray diffraction (PXRD) (Figures A3 and A4). Le Bail fits of the PXRD patterns indexed to single-crystal diffraction data of Mn–S or Fe–Se confirmed the materials to be isostructural and phase pure. In addition to the known structures, we prepared two new isostructural members, $TMA_2NiGe_4S_{10}$ (Ni–S) and $TMA_2CoGe_4Se_{10}$ (Co–Se). Figure 2.2 shows the resulting experimental PXRD patterns compared to the patterns simulated from indexing, along with the fit residuals.

Table A.1 summarizes the refined lattice parameters of all framework materials. The Ni–S tetragonal lattice parameters *a* and *c* index to 9.483(1) and 13.871(1) Å, respectively, indicating a unit cell contraction resulting from the reduced ionic size of Ni^{2+} as compared to that of Mn^{2+}. On the other hand, the refinement of the Co–Se cell parameters provides *a* and *c* values of 9.639(2) and 14.605(4) Å, respectively, a relative expansion of the unit cell due to the larger size of Se^{2-} as compared to that of S^{2-} in Co–S (Table A.1). This expanded family of isostructural frameworks provides a platform for studying the impact of systematic changes to bonding and electronic structure on charge transport through porous materials.

To understand the relationship of the tunable compositions and the electronic properties of the $TMA_2MGe_4Q_{10}$ frameworks, we computed the band diagrams for a variety of chalcogenides and first-row transition-metal ions in divalent and trivalent oxidation states, as summarized in Figures A.20 and A.21. Figure 2.3 plots the conduction band and valence band electron densities and corresponding density-of-state (DOS) diagrams of Fe–S, Ni–S, and Zn–S as representative examples. Although these materials differ only in metal ions, the atomic character of the band-edge orbitals diverges considerably. For example, whereas Fe and Ni d-orbitals contribute to both band edges in Fe–S and Ni–S, respectively, S p-orbitals dominate both band edges in Zn–S. These differences are due to high-energy unpaired d electrons in Fe–S and

Ni–S, which contribute substantially to the band edge(s), whereas Zn–S has no such electrons in its closed d shell. The partial atomic orbital character can be quantified for each material, as summarized in Table A.3, revealing considerable differences in bond covalency, as well. For

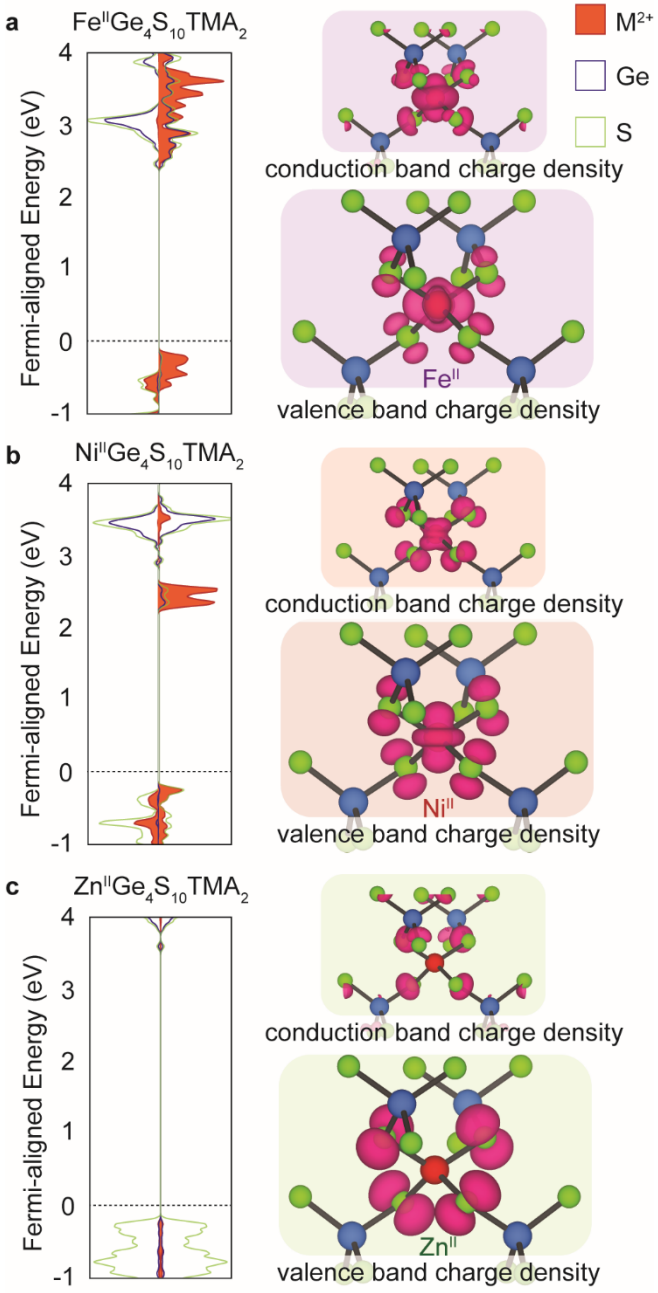

Figure 2.3 Calculated electronic structures of Fe–S (a), Ni–S (b), and Zn-S (c), with density-of-state diagrams and electron densities of valence and conduction bands, computed using the PBEsol structure, at the HSEsol06 level of theory.

example, d-orbitals comprise 84% of the valence band in Fe–S, whereas Ni and Zn d-orbitals make up 54% in Ni–S and just 4% in Zn–S. Bond covalency also depends strongly on the metal ion oxidation state and chalcogenide identity. For example, upon oxidation, the Fe d-orbital valence band contribution drops from 84 to 72% in Fe^{3+}–S and from 71% in Fe–Se to 39% in Fe^{3+}–Se. These significant differences in the electronic structures of these materials on the basis of oxidation state and chalcogenide provide a basis for understanding their diverse magnetic, optical, and charge transport behaviors.

The frameworks we expected to be paramagnetic (i.e., those containing Mn^{2+}, Fe^{2+}, Co^{2+}, and Ni^{2+}) were evaluated by SQUID magnetometry. Variable-temperature direct current (DC) magnetic susceptibility measurements of Mn–S, Co–S, and Ni–S reveal 300 K magnetic moments of 4.27, 2.32, and 1.93 cm^3 K mol^{-1}. For the Mn derivative, the value of the magnetic moment is slightly below the values expected for a g = 2 isolated Mn^{2+} (S = 5/2, χMT = 4.375 cm^3 K mol^{-1}) site. This suppression of the magnetic moment could be due to a small amount of defects at the Mn^{2+} site, resulting in slightly less than statistically one Mn^{2+} per site or radical containing S-based defects in the $[Ge4S10]^{4-}$ cluster. For the Co derivative, the value of the magnetic moment is consistent with that expected for a g = 2.2 Co^{2+} (S = 3/2, χMT = 2.269 cm^3 K mol^{-1}) site. For the Ni derivative, the magnetic moment is significantly higher than expected for a g = 2 Ni^{2+} site (S = 1, χMT = 1.0 cm^3 K mol^{-1}). However, a d^8 Ni^{2+} ion in a tetrahedral coordination environment is expected to be highly anisotropic with g > 2. For these three materials, the variable-temperature DC magnetic susceptibility measurements confirm the overall paramagnetic nature of the frameworks with negligible magnetic coupling between neighboring metal sites (Figures A.9, A.11, and A.13). The paramagnetic nature of these materials is further

reflected by their Curie–Weiss-type magnetic susceptibility and the lack of ordering as observed by alternating current (AC) magnetic susceptibility (see Appendix A).

Variable-temperature, DC magnetic susceptibility measurements of the Fe–S analogue reveal a more complex magnetic ground state than that observed in the previous materials. At 300 K, the magnetic moment of Fe–S is 3.13 cm^3 K mol^{-1}, consistent with an isolated high-spin S = 2 Fe^{2+} site. Upon cooling, the magnetic susceptibility decreases, signifying weak antiferromagnetic coupling between adjacent Fe^{2+} sites. The magnetic moment increases sharply at 3 K, consistent with either a ferromagnetic or a canted antiferromagnetic ordering event (Figure 2.4). To precisely determine the ordering temperature and the nature of the ordering, we collected variable-temperature AC susceptibility measurements at selected frequencies under zero applied DC field. The data show a frequency-independent peak in the in-phase (χM′) and out-of-phase (χM″) susceptibilities at 2.75 K, indicative of a magnetic ordering event. The

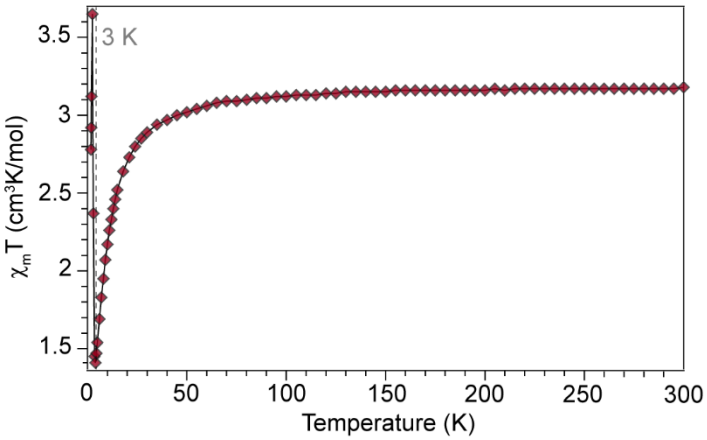

Figure 2.4 DC magnetic susceptibility for Fe–S at a 0.1 T external magnetic field strength.

frequency independence of the ordering suggests a true magnetic ordering event, not a spin freezing event (Figure A.5). Furthermore, variable-field magnetization measurements at 1.8 K show an open hysteresis loop with a coercive field of 50 Oe (Figure A.6), indicating that the Fe–S framework is a soft permanent magnet.

In contrast, the 300 K magnetic moment of Fe–Se is 2.76 cm^3 K mol^{-1}, which is slightly less than the spin-only magnetic moment of 3 cm^3 K mol^{-1} expected for an S = 2 Fe^{2+} ion and much lower than the spin-only magnetic moment of 4.375 cm^3 K mol^{-1} expected for an S = 5/2 Fe^{3+} ion. To investigate the oxidation state of iron in Fe–Se, we turned to Mössbauer spectroscopy, which probes the oxidation state, coordination environment, and spin state of the iron center. At 300 K, the Mössbauer spectrum of Fe–Se (Figure 2.5) has a single doublet with an isomer shift of 0.393 mm/s and a quadrupole splitting of 0.568 mm/s, which we assign as high-spin Fe^{3+}, indicating the material is isovalent Fe^{3+}.[83]

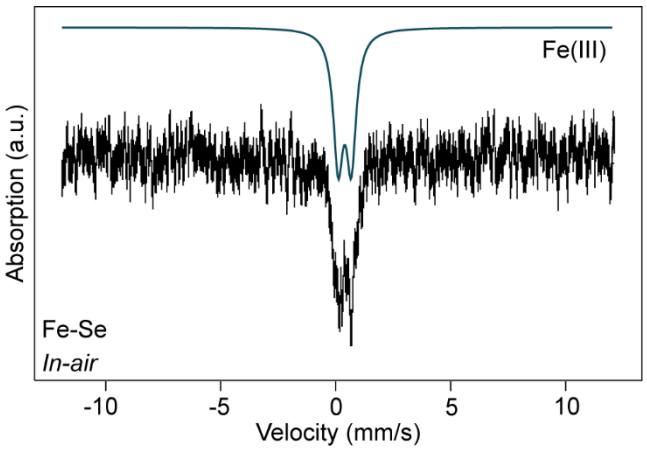

Figure 2.5 Room-temperature Mössbauer spectrum of Fe–Se prepared in-air.

As Mossbauer spectroscopy directly probes the oxidation and spin state of the iron site, the discrepancy with the DC magnetic susceptibility could be due to previously unresolved organic radicals in the [Ge_4Se_{10}] clusters. We hypothesize that the Fe^{2+} starting material used in the synthesis of the Fe–Se framework facilitates spontaneous electron transfer to the cluster, generating an Fe^{3+} site and a cluster-based radical. This in situ oxidation is supported by the fact that tetrahedral Fe^{2+} coordination complexes have been shown to oxidize at milder potentials when coordinated by selenium vs sulfur donors.[84] The Fe^{3+} spin and the radical would be

strongly antiferromagnetically coupled via direct coupling, as reflected in the low magnetic moment of the Fe–Se framework. Below 300 K, the magnetic moment of Fe–Se continuously decreases, which is indicative of both the very strong antiferromagnetic coupling between Fe^{3+} and the S = 1/2 [Ge_4Se_{10}] radical and the relatively weak antiferromagnetic coupling between neighboring $Fe3^{+}$–radical pairs. Both the DC and AC magnetic susceptibility measurements of Fe–Se reveal no ordering event in contrast to the Fe–S system (Figures A.7 and A.8). We attribute this magnetic difference to the dissimilar oxidation states of iron between the two materials and the increased distance between iron centers with the expansion of the unit cell by the larger selenide anion (Table A.1). The differences in electronic configurations and subtle alterations to bonding environments in this family of materials manifest in distinct magnetic interactions ranging from long-range ordering to localized paramagnetism.

To experimentally explore the electronic structures of the framework materials, their optical absorption spectra were measured by diffuse reflectance UV–vis–NIR spectroscopy. Figure 2.6 plots the Kubelka–Munk transforms of Mn–S, Fe–S, Fe–Se, Co–S, Co–Se, Ni–S, Zn–S, and the parent S- and Se-based cluster compounds. In general, we assign the highest-energy absorption bands between 20 000 and 30 000 cm^{-1} to the optical gap transitions and the lower-lying transitions to ligand field transitions of the M^{2+} d-orbitals subject to tetrahedrally symmetric ligand fields (Figure A.15). For the frameworks lacking allowed d–d transitions (Mn–S and Zn–S), the optical gaps arise from charge-transfer events from chalcogenide p-orbital to germanium empty sp^3 orbitals, with varying degrees of contributions from the metal d-orbital to the valence bands depending on the degree of metal–ligand covalency. For open-shell frameworks, the DOS diagrams in Figures 2.3, A.20, and A.21 suggest that the band-gap transitions involve a combination of both S-to-Ge and ligand field transitions. The spectra in

Figure 2.6 indicate a substantial narrowing of band-gap transitions for the open-shell systems, which agrees with density functional theory (DFT) calculations that the conduction band involves both low-lying d-orbitals and Ge-based orbitals stabilized by approximately 1 eV relative to the wider optical gap Zn–S. Indeed, the Mn–S and Zn–S frameworks display optical gaps similar to the parent $TMA_4Ge_4S_{10}$ cluster, whereas the open-shell frameworks exhibit narrowed gaps, suggesting that optical properties depend on the availability of d–d transitions, bond covalency, and electrostatic stabilization of atomic orbitals induced by the linking metal ions.

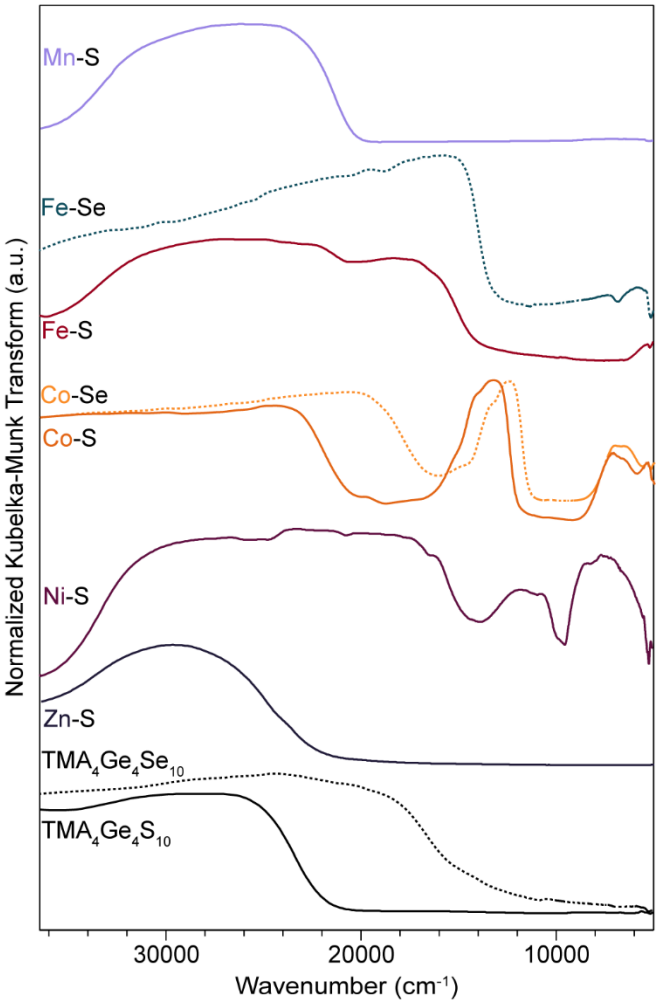

Figure 2.6 Diffuse reflectance UV–vis–NIR spectra of TMA2MGe4Q10 collected at 300 K.

The optical gap transitions of most materials could be assigned using Gaussian fits (Figure A.17), which produced the best agreement with optical gaps determined by DFT when the band-edge orbitals were dominated by linking metal d-orbitals (Fe–S, Fe–Se, Co–S, and Ni–S) or sulfur p-orbitals (Zn–S). In contrast, Tauc plot analysis (Figure A.16), traditionally reserved for defective and amorphous semiconductors, provided the best fits for Mn–S and Co–Se, which calculations suggest bear nearly equal contributions of chalcogenide and linking metal orbitals in the band-edge orbitals (Figure A.20 and Table A2). Table 2.1 summarizes the experimentally derived optical gaps with values determined from simulated band structures.

Material	Experimental E_g (eV)	Simulated E_g (eV)
Zn-S	3.6	3.8
Mn-S	3.4	3.2
Ni-S	2.7	2.6
Co-S	3.0	3.0
Fe-S	2.7	2.7
Fe-Se	2.0	2.2/1.9(Fe^{3+})
Co-Se	2.2	2.3

Table 2.1 Optical Gap Energies (E_g) as Determined Experimentally from Tauc and Gaussian Plots Compared against Those from Simulated Band Diagrams

Together, these data demonstrate the wide tunability of the framework optical properties, with selenium increasing valence band edges relative to sulfur and M^{2+} d-orbitals dominating both band edges to produce optical gaps spanning 2.0–3.6 eV.

Ligand field analysis of the spectra in Figure 2.6 provides insight into how tunable compositions impact the chemical bonding and electronics of the framework materials. The high intensities of the ligand field transitions between 5000 and 15 000 cm^{-1} for Fe–S, Ni–S, Co–S, and Co–Se reflect their Laporté allowed nature, as expected for tetrahedral ligand fields. Assigning these bands to the appropriate transitions and solving the corresponding Tanabe–Sugano matrices (see Appendix A) yields crystal field splitting energies (D_q) spanning 392–524 cm^{-1} for Fe–S, Ni–S, Co–S, and Co–Se systems (Table A.2).

These comparably small D_q values are consistent with tetrahedrally symmetric chalcogenide ligand fields.[85] Furthermore, the smaller D_q of Co–Se (392 cm^{-1}) compared to that of Co–S (402 cm^{-1}) reflects the more diffuse nature of Se^{2-} p-orbitals. Ligand field analysis also reveals differences in the metal–ligand bond covalency in the form of the interelectronic repulsion parameter (B). The percent reduction in B (B′) compared to the free ion values of $B_{free\ ion}$ (Ni^{2+} = 1080 cm^{-1} and Co^{2+} = 1117 cm^{-1})[86] for each material indicates shifting of metal-centered electron density onto ligands, i.e., covalency. We calculate B′ of 46% for Co–S and 31% for Ni–S, suggesting far more covalency in the Co–S system compared to that in the Ni–S. Furthermore, the reduction is even greater for Co–Se (51%), consistent with the better matching of electronegativities between Se^{2-} and Co^{2+}, leading to greater covalency. This quantification of bond covalency complements the computational results in Table A.3, showing nearly equal contributions of Co and S orbitals to the valence band in Co–S and a more polarized atomic character in Ni–S, while the valence band of Co–Se has a greater electron density contribution from Se. Differences in bond covalency and atomic character provide a basis for predicting other electronic aspects as well, such as charge transport, with greater covalency expected to engender higher charge mobilities.

Figure 2.7a summarizes the results of DC conductivity measurements of all frameworks using room-temperature two-electrode pressed pellet configurations. Most of the materials (Mn–S, Co–S, Co–Se, Ni–S, and Zn–S) exhibit low conductivities: 10^{-8}–10^{-9} S/cm, whereas Fe–S and Fe–Se displayed values typical of semiconductors: 10^{-7} S/cm. To understand the origin of this large difference in conductivity, we employed electrochemical impedance spectroscopy (EIS) to probe fundamental aspects of the charge transport mechanisms. AC measurements were performed on the Fe–S and Zn–S systems because they represent the high and low conductivity

extremes in this family of materials. Additionally, Fe and Zn typically exhibit markedly different redox chemistry, which we expect governs the observed conductivity. Figure 2.7b plots the EIS spectrum of Fe–S fitted to a parallel combination of the bulk resistance and bulk dielectric capacitance of the pellet, yielding a conductivity of 0.11 μS cm^{-1}, which is in good agreement with the 0.23 μS cm^{-1} found by DC measurements. Given the ion-blocking and electron transmissive nature of the two electrodes, this conductivity arises purely from electron transport.[87] In contrast, the Zn–S system (Figure 2.7c) displays a semicircle at high frequencies (low Re(Z)) and a linear feature at low frequencies. The linear feature is modeled as a constant phase element with n = 0.46 (high Re(Z)), which is characteristic of a distorted Warburg process that we attribute to the diffusion of TMA^+ ions. Fitting these data to the equivalent circuit shown in Figure 2.7c, often employed for mixed ion–electron conductors, produces an excellent fit, yielding a bulk conductivity far higher (0.15 μS cm^{-1}) than observed by DC measurements (0.024 μS cm^{-1}), which lack the contribution of ionic conductivity. These results imply that TMA^+ ions are the dominant charge carriers in Zn–S.[87] The influence of ions on the charge transport mechanism of Zn–S, as well as the other low-DC conductivity materials Co–S, Mn–S, and Ni–S, is evident in DC I–V curves, which appear nonlinear (non-Ohmic) (Figure A.39), likely due to the simultaneous movement of both ions and charges. The I–V curves eventually become linear (Ohmic) at later time points in the experiment due to the ion-blocking nature of the electrodes. DC conductivities were determined, therefore, from the linear portions of the I–V curves. On the other hand, both Fe–S and Fe–Se exhibited linear (Ohmic) I–V curves, suggesting that higher conductivities of the Fe systems result from a mechanism fundamentally different from the ion-coupled charge transport operative in the other frameworks.

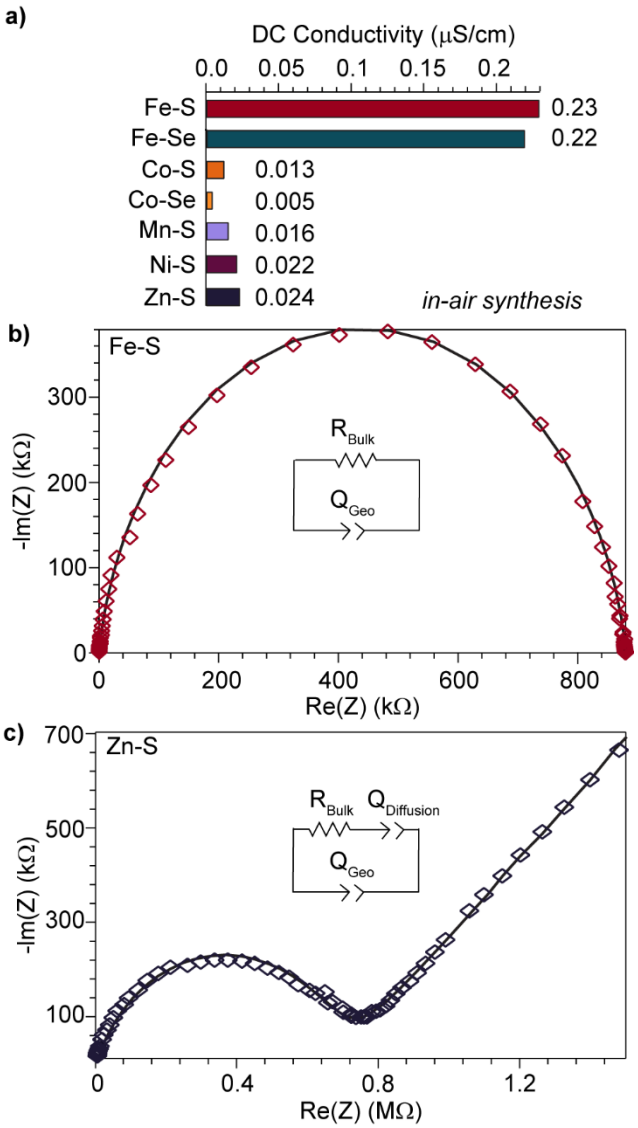

Figure 2.7 Conductivity of frameworks prepared in-air. (a) DC conductivity values of TMA2MGe4Q10 prepared in-air and measured with two-contact pressed pellet configurations at room temperature. EIS spectra of (b) Fe–S and (c) Zn–S collected at room temperature between 2 MHz and 0.1 Hz without an applied DC field and a 100 mV applied AC bias. Data are fitted to the equivalent circuits shown as insets, with fits shown as solid lines.

Suspecting that the generally high redox activity of Fe contributes to the greater DC conductivities of Fe–S and Fe–Se, we investigated the effect of the Fe oxidation states on the measured conductivity by modifying the preparation of the Fe-Q frameworks. The *in-air* preparation of all frameworks as reported in the data above was modified to be *air-free*.

Specifically, whereas *in-air* involves preparing, isolating, washing, and drying the materials in air (see Chapter 2 Experimental section), the synthesis, isolation, and washing steps of *air-free* are conducted under N_2. Furthermore, to avoid defect formation, the washing procedure was modified (see Chapter 2 Experimental section) to allow for drying without exposure to high heat or vacuum. Figure 2.8a summarizes the impact of synthetic preparation on the Fe framework conductivities. When made *air-free*, the Fe-Q systems showed lower DC conductivities (Fe–Se gives 0.011 μS cm^{-1} and Fe–S gives 0.13 μS cm^{-1}).

To further probe the Fe oxidation states resulting from these methods, room-temperature Mössbauer spectra were collected. Figure 2.8b plots the spectra of Fe–S prepared *in-air*, showing two species with isomer shifts of $\delta = 0.31$ (Fe^{3+}) and 0.68 (Fe^{2+}) mm/s with associated quadrupole splittings of $\Delta EQ = 0.55$ and 3.6 mm/s, respectively. The relative areas of the isomer shifts reveal mixed valency with 25% Fe^{3+}. In contrast to *in-air* Fe–S, the Mössbauer spectrum of the materials handled *air-free* (Figure 2.8c) shows two species with isomer shifts of 0.20 (Fe^{3+}) and 0.68 (Fe^{2+}) mm/s with associated quadrupole splittings of $\Delta EQ = 0.40$ and 3.6 mm/s, respectively. The relative areas of the isomer shifts reveal that the system is still mixed valent with 13% Fe^{3+}. Similarly, when Fe–Se was prepared *air-free* (Figure 2.8d), the Mössbauer spectrum shows two species with isomer shifts of 0.27 (Fe^{3+}) and 0.64 (Fe^{2+}) mm/s with associated quadrupole splittings of $\Delta EQ = 0.45$ and 3.6 mm/s, respectively. The relative areas of the isomer shifts indicate predominantly Fe^{2+} with 23% Fe^{3+}, whereas Fe–Se handled *in-air* shows only Fe^{3+}. The oxidation of these species even under *air-free* conditions is likely due to *in situ* oxidation of the Fe^{2+} sites by the oxidized cluster, as explained by the anomalous magnetism results for the *in-air* synthesis of Fe–Se. The presence of oxidized sulfur species is

supported by XPS, which shows that even under *air-free* procedures Fe–S contains sulfate species with binding energies of ~168 eV (Figure A34).

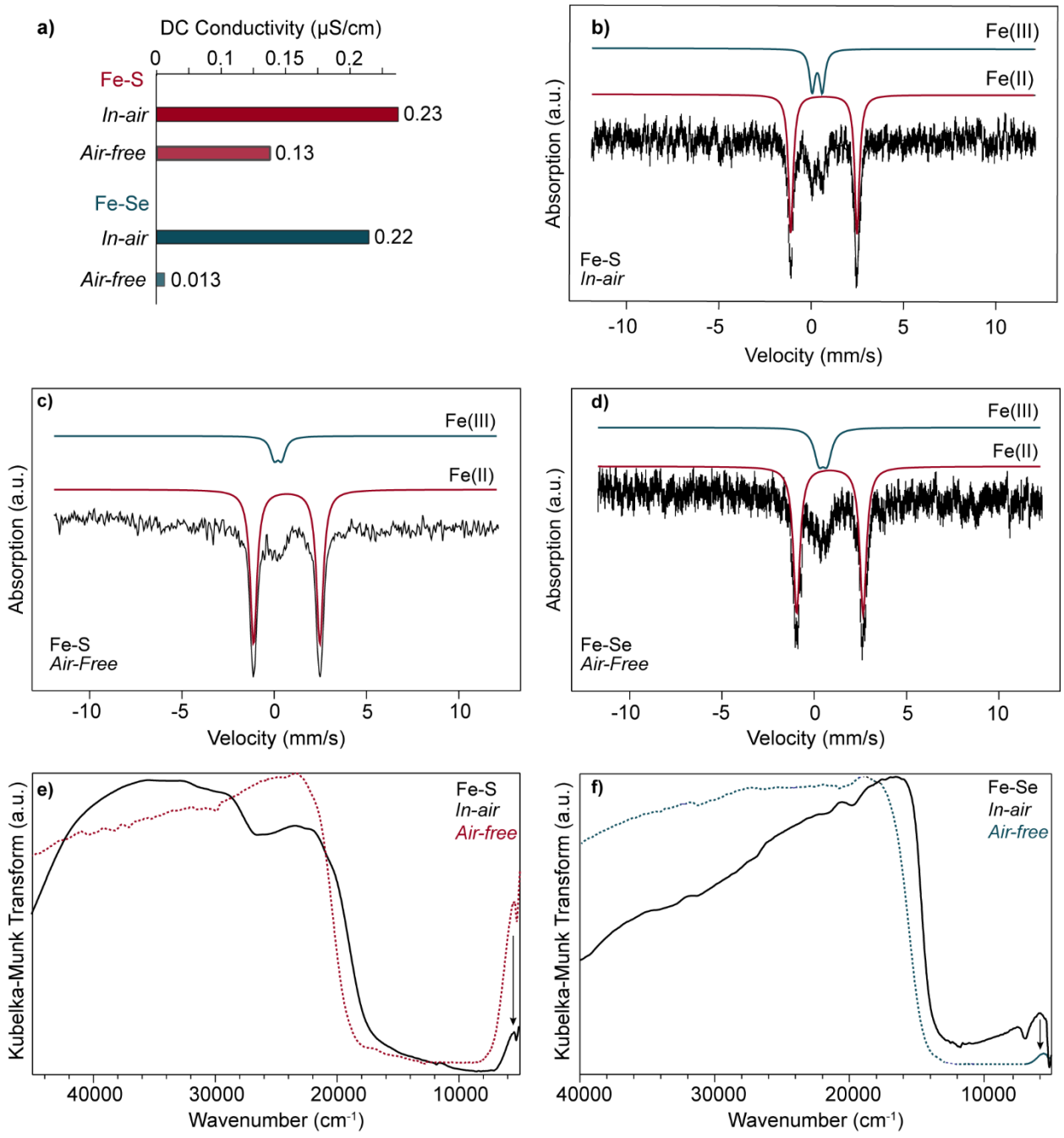

Figure 2.8 Effect of synthetic preparation on the physical properties of Fe frameworks. (a) Summary of DC conductivities, (b) Mössbauer spectrum of Fe–S prepared in-air, (c) Mössbauer spectrum of Fe–S prepared air-free, (d) Mössbauer spectrum of Fe–Se prepared air-free, (e) diffuse reflectance UV–vis–NIR spectra of Fe–S, and (f) Fe–Se frameworks.

Diffuse reflectance UV–vis–NIR spectroscopy provided additional insight into the effect of sample preparation on redox state and electronic structure. Figure 2.8e shows a decrease in the optical gap for Fe^{2+}–S prepared *air-free*. Gaussian analysis indicates that the gap decreases from 2.7 to 2.5 eV (Figure A.18). Because this transition likely involves a charge transfer from hybridized S(p)/Fe(d) to Ge(s) orbitals, the wider gap of Fe–S prepared *in-air* is consistent with the lowering of the Fermi level into the valence band caused by partial Fe oxidation. Similarly, Fe–Se prepared *in-air* shows a markedly decreased optical gap (Figure 2.8f), which Gaussian analysis fits to 2.2 eV from 2 eV, agreeing with the expected value from the simulated band structure for a Fe^{2+}–Se system (Figure A.19). Furthermore, the low-energy weak transition at around 6000 cm^{-1} for Fe–Se becomes weaker in the *air-free* synthesis. The decreased intensity with greater Fe^{2+} content suggests that this band arises from either the spin-forbidden high-spin Fe^{3+} ligand field transition $^6A_1 \rightarrow {}^4T_1$ or from an intervalence charge transfer between Fe^{3+} and Fe^{2+} centers. Typically, the Fe^{3+} ligand field transition occurs closer to 8000 cm^{-1} for tetrahedral metal sulfur systems, but the increased covalency and thus relatively small interelectronic repulsion of Fe–Se lower its energy.

With evidence that the Fe framework conductivities depend on the oxidation state of Fe, we sought to further control Fe–S conductivity through deliberate chemical oxidation with ferrocenium tetrafluoroborate ($FcBF_4$). To oxidize Fe–S, the *air-free* synthesis material was suspended in THF solutions of $FcBF_4$ under a N_2 atmosphere, followed by THF and hexane washes and drying. The washed and dried product had a marked color change from bright orange to brown. To quantify the extent of oxidation, room-temperature Mössbauer spectra were collected on the oxidized product. Figure 2.9a,b plots the spectra of the oxidized products of Fe–S after treatment with $FcBF_4$ in 0.5 and 1.5 eq. respectively. The sample treated with 0.5 eq. of

$FcBF_4$ shows two species with isomer shifts of 0.26 (Fe^{3+}) and 0.68 (Fe^{2+}) mm/s and associated quadrupole splittings of $\Delta EQ = 0.29$ and 3.6 mm/s, respectively. The relative areas of the isomer shifts reveal that the sample is 19% Fe^{3+}, a 6% increase from the as-synthesized *air-free* Fe–S material. The Fe–S treated with 1.5 equiv of $FcBF_4$ shows two species with isomer shifts of 0.21 and 0.68 mm/s with associated quadrupole splittings of $\Delta EQ = 0.40$ and 3.6 mm/s, respectively. The relative areas of the isomer shifts reveal that the sample is 26% Fe^{3+}, a 13% increase from the as-synthesized *air-free* Fe–S material. Figure 2.9c compares the DC conductivity of all Fe–S samples. The results show that the DC conductivity is strongly dependent on the redox state of Fe, with higher amounts of Fe^{3+} leading to increased conductivity.

To understand how redox chemistry impacts charge transport, we collected diffuse reflectance UV–vis–NIR spectra for insight into changes to the electronic structure of the Fe–S materials, specifically the increasing or lowering of the Fermi level, i.e., redox state and number of charge carriers. Figure 2.9d plots the normalized spectra, with a notable difference in the intensities of a band centered around 6000 cm^{-1}. Based on assigning this feature to the spin-allowed $^5E \rightarrow {}^5T_2$ d–d transition of T_d Fe^{2+}, the difference in intensities corroborates *air-free* Fe–S containing the most Fe^{2+} centers and the oxidized 1.5 eq. $FcBF_4$-treated Fe–S containing the most Fe^{3+}. Furthermore, the optical gap energy shifts from 2.5 to 2.7 eV post $FcBF_4$ treatment (Figure A.26). This is the same energy shift seen when comparing the optical gap energies for *air-free* and *in-air* Fe–S syntheses. Low-energy absorption is also observed post oxidation, which is attributed to the generation of mixed-valent mid-gap states. This assignment is corroborated by the simulated band structure of Fe^{3+}–S, which showcases stabilized conduction band mid-gap states with Fe oxidation (Figure A.21). PXRD confirms that materials maintain crystallinity, suggesting that these changes to conductivity and optical absorption arise from

alternations to the electronics of the Fe–S framework, rather than from the formation of new crystalline phases (Figure A.27).

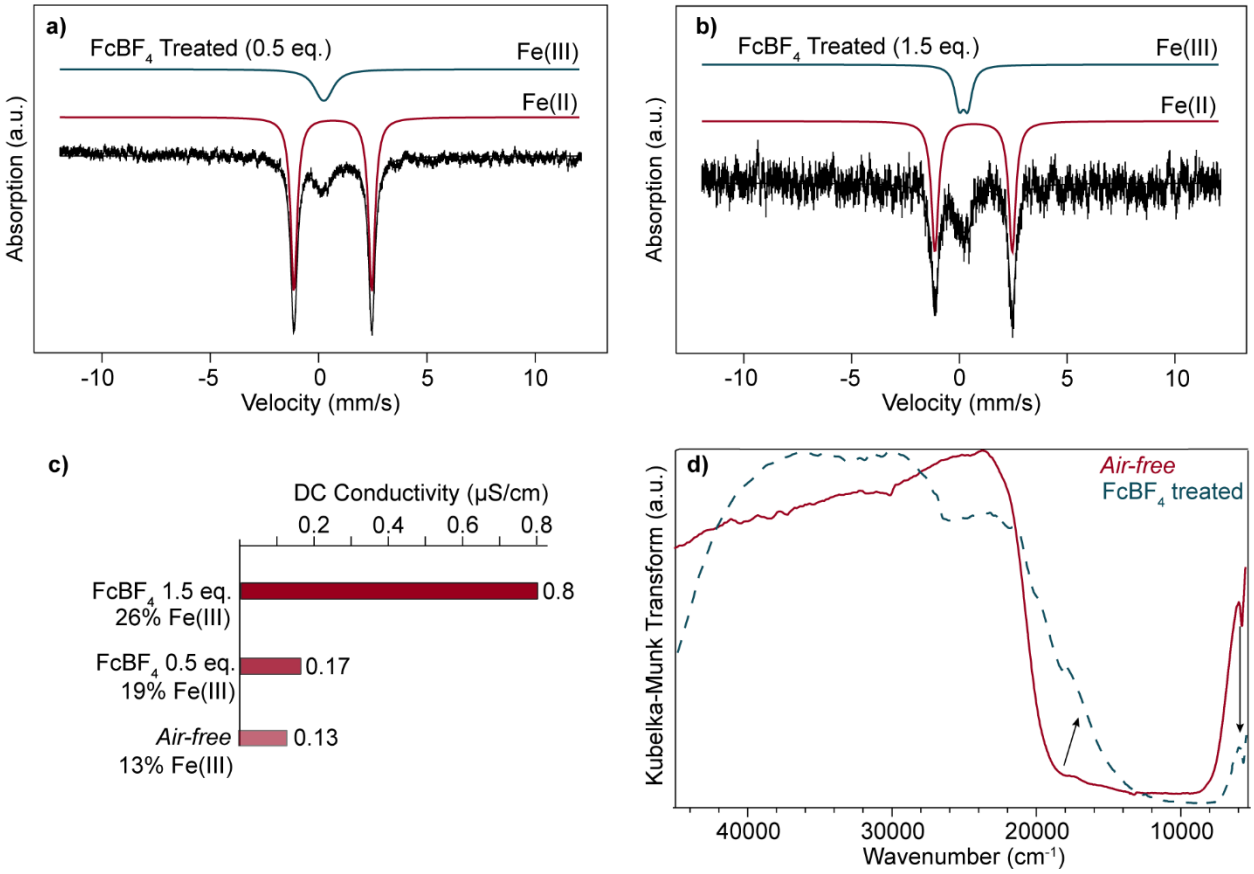

Figure 2.9 Comparison of Fe–S produced air-free and in-air versus postsynthetic treatment by redox reagents. (a) Room-temperature Mössbauer spectrum of Fe–S treated with 0.5 equiv of FcBF4, (b) room-temperature Mössbauer spectrum of Fe–S treated with 1.5 equiv of FcBF4, (c) summary of DC conductivity, and (d) diffuse reflectance UV–vis–NIR spectra of Fe–S in different redox states.

To further probe the impact of Fe redox state on the charge transport in the Fe–S/Se systems, potential-dependent conductivity was performed on the Fe–S air-free system using a three-electrode setup with $TBAPF_6$ as the supporting electrolyte (more details on this experiment can be found in Chapter 2 Experimental section). The EIS responses were monitored at different applied DC voltages relative to a $Ag/AgNO_3$ reference electrode, and the responses were well

fitted to an equivalent circuit to extract the electronic conductivity. Figure 2.10 plots the electronic conductivity as a function of applied DC potential relative to the open-circuit potential (OCP). These results show that at oxidizing potentials the conductivity increases with applied potential and plateaus at higher oxidizing potentials with a large conductivity value (90 μS/cm). By contrast, the electronic conductivity is potentially independent at reducing potentials, highlighting the need for p-type carriers from Fe^{2+} to Fe^{3+} oxidation.

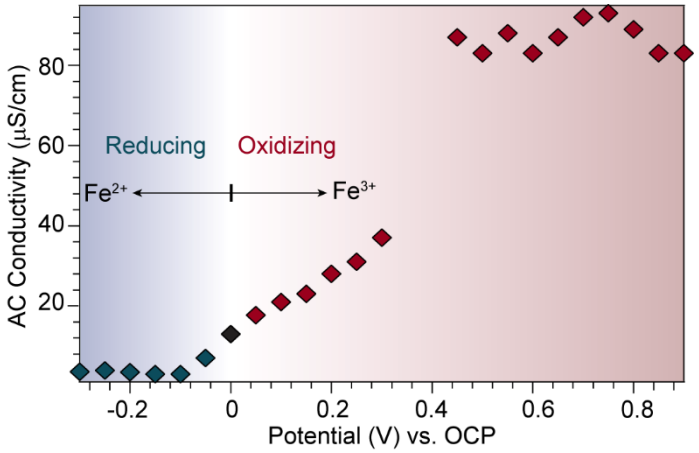

Figure 2.10 Summary of AC conductivity of air-free Fe–S as a function of applied potential with 0.1 M TBAPF6 in acetonitrile.

Given the importance of Fe^{3+} to the conductivity of the Fe frameworks, chemical oxidation was further explored to control the conductivity of the Mn, Co, and Ni materials. Figure 2.11a summarizes the effect of $FcPF_6$ treatment on the framework DC conductivities, indicating an increased conductivity for Mn–S but decreased for Co–S and Ni–S. Despite such significant changes to their charge transport, all frameworks retain crystallinity, as confirmed by PXRD analysis (Figure 2.11b). However, impurity phases forming can be detected as new unindexed peaks occurring (marked with asterisks). Unlike Co–S and Ni–S, which retained their original color, Mn–S changed from white to yellow-orange upon $FcPF_6$ treatment. Indeed,

diffuse reflectance UV–vis–NIR spectra of Mn–S display a substantial shift of the absorption peak maximum upon oxidation, with Tauc analysis indicating a reduction in the optical gap energy from 3.4 to 3.3 eV (Figure A.30), accompanied by increased absorption at lower energies (Figure 2.11c). This tailing is predicted by the simulated band structure calculations of $TMAMn^{3+}Ge_4S_{10}$, which predicts stabilized conduction band mid-gap states with Mn oxidation (Figure A.23). X-ray photoelectron spectroscopy (XPS) of Mn–S before and after treatment with $FcPF_6$ shows a shift toward higher binding energies for both the Mn 2p, from ~640 to ~642 eV, and S 2p, from ~161 to ~163 eV (Figure 2.11d, e), suggesting the oxidation of both species that comprise the valence band. Furthermore, no Fe was detected in the XPS, confirming the absence of ferrocene or ferrocenium contamination. However, fluorine was observed in the survey scan, indicating that some number of anions had accumulated in response to the oxidation.

In contrast, no color change was observed for Ni–S and Co–S upon treatment with $FcPF_6$, though the $FcPF_6$ solutions changed from dark blue to orange, indicating at least partial conversion to ferrocene. The diffuse reflectance UV–vis–NIR spectra of Co–S exhibited no change in the ligand field transitions but a marked increase in the optical gap energy from 3.0 to 3.2 eV (Figure A.28). Similarly, the ligand field transitions of Ni–S remained unchanged, yet, unlike Co–S, Gaussian analysis did not show any change to the optical gap energy. XPS results indicate that while Co and Ni 2p orbital binding energies do not shift after $FcPF_6$ treatment (Figures A.31 and A.32), the S 2p orbitals move to 164 eV (Figure 2.11f, g), indicative of disulfide bond formation. Taken together, these results suggest that sulfur bears the oxidation from $FcPF_6$ treatment of Co–S and Ni–S and that the frameworks are likely p-type conductors.

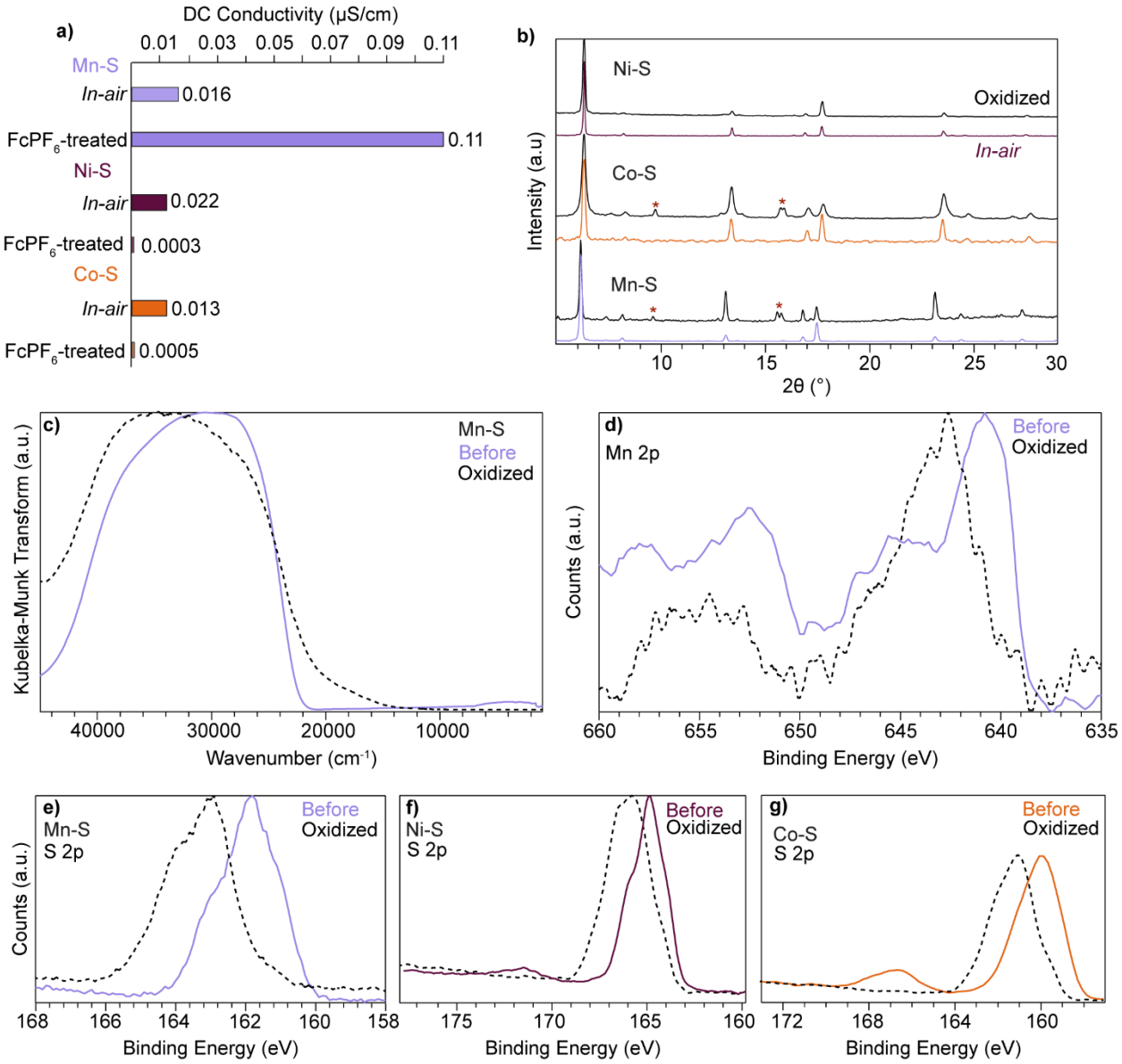

Figure 2.11 Summary of the effect of chemical oxidation on Mn–S, Co–S, and Ni–S frameworks. (a) Comparison of DC conductivities, (b) PXRD patterns, (c) Mn–S diffuse reflectance UV–vis–NIR spectra, (d) Mn 2p XPS of Mn–S, (e) S 2p XPS spectra of Mn–S, and (f) S 2p XPS spectra of Ni–S and (g) S 2p XPS spectra of Co–S before and after FcPF6 treatment.

To confirm the charge carrier sign, the thermoelectric effect was exploited. A pressed pellet of Fe–S was heated on one end to induce a temperature gradient across the pellet and the open-circuit potential of the system was measured. The open-circuit potential was negative,

indicating that the voltage gradient ran against the temperature gradient. This behavior is indicative of a positive Seebeck coefficient, with holes as the majority charge carrier in the Fe–S system.

To understand the role of redox chemistry in the charge transport mechanism, specifically a "charge hopping" versus band-type model, we compared the band diagrams of the framework materials bearing different metal ions, chalcogenides, and redox states. Specifically, we examined the dispersions of the valence bands because holes act as the dominant charge carriers. Figure 2.12 summarizes the widths of the valence bands, indicating that the Fe^{2+}–Q frameworks exhibit the greatest band dispersion. This result is expected as these bonds are the most covalent, while Zn–S shows the least covalency due to the low metal ion character. Interestingly, calculations of the Fe^{3+}-based frameworks show lower bandwidths compared to those of the Fe^{2+} analogues. Inspection of the geometry-optimized structures reveals a contraction of the unit cell upon oxidation to form Fe^{3+} (Figure A.22). Calculations also predict that this physical distortion causes a change in the optical gap, which helps explain the agreement between Fe and Se prepared *in-air* with an optical gap of 2.0 eV compared with the simulated band structure of Fe^{3+}–Se (1.9 eV). These results also imply that the superior conductivity of Fe frameworks, specifically those containing Fe^{2+}, arises from the greater mobility of holes in the dispersive valence bands.

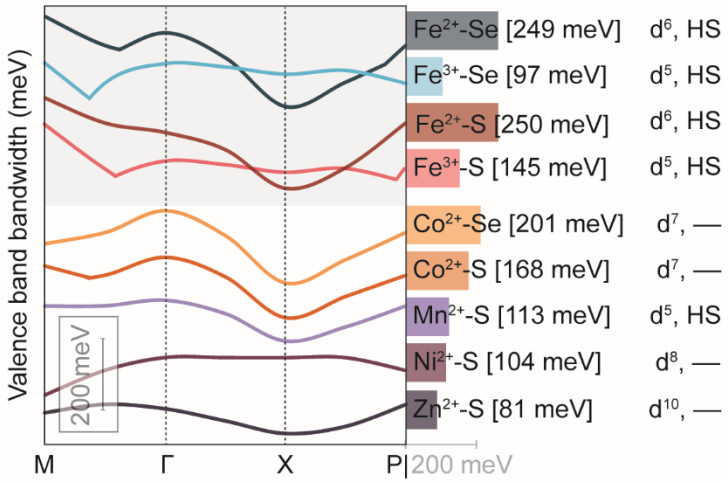

Figure 2.12 Comparison of valence band dispersions of frameworks with different metal ions, chalcogenides, and oxidation states. Diagrams of valence bands with arbitrary energy offsets for clarity. Frameworks with divalent and trivalent metal ions were simulated with two and one TMA+ cations, respectively.

For evidence that mid-gap orbitals and Fe redox chemistry affect the different energetics of charge transport between the Fe frameworks, we measured the variable-temperature DC conductivity of Fe–S prepared under *air-free* and *in-air* synthetic conditions and Fe–Se prepared under air-free conditions. Figure 2.13 shows the Arrhenius plots of these materials. The *in-air* synthesis of Fe–S boasts the lowest activation energy (0.36 eV) and results in the highest conductivity seen of materials explored by temperature dependence. Interestingly, while having substantially different conductivities the *air-free* syntheses of Fe–Se and Fe–S have nearly identical activation energies, within error of each other (0.53 and 0.56 eV, respectively). These results suggest that the presence of Fe^{3+} lowers the activation barrier by introducing charge carriers while decreasing charge mobility as a result of less dispersive bands. This effect is most pronounced for the Fe–Se system, which shows a larger decrease in conductivity compared to that for Fe–S while having a similar activation energy. Furthermore, this Arrhenius analysis

explains why the *in-air* synthesis of Fe–Se conductivity is lower than *in-air* synthesis of Fe–S while being entirely Fe^{3+} and having a far larger charge carrier density.

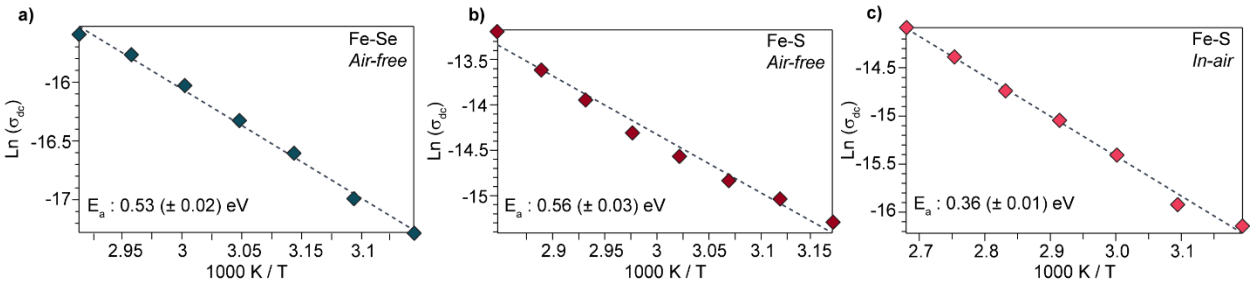

Figure 2.13 Arrhenius plots of variable DC conductivity of (a) Fe–Se prepared air-free and Fe–S prepared air-free (b) and in-air (c).

Furthermore, in the Fe-S system it was found that S defect formation had a measurable impact on charge transport. Inspired by the decomposition pathway of $H_4Ge_4S_{10}$ to $H_2Ge_4S_9$ it was expected that in the presence of water at high heat and vacuum to remove volatile generated H_2S, sulfur defects would be generated.[88] To Fe-S that was synthesized in *air-free* conditions a small amount of N_2 sparged deionized water was added and a paste was created. This paste was then heated at 160 ^oC under high vacuum, and the water collected to test for H_2S generation with the methylene blue assay (Scheme 2.1).[89] H_2S is the expected byproduct of desulfurization and is indicated by the methylene blue assay reactant solution going from orange to dark blue (Scheme 2.1).

Scheme 2.1 Conditions necessary to generate sulfur defects in $FeGe_4S_{10}$ and Methylene Blue Assay reaction for confirming presence of H_2S as the primary decomposition production in desulfurization.

The desulfurization was further confirmed by XPS results seen in Figure 2.14b which show a large reduction in atomic sulfur content. Even still, PXRD results indicate the retained crystallinity even after substantial desulfurization (Figure A.35). Upon desulfurization, the bright orange solid of *air-free* Fe-S turns dark brown. This color change is seen with UV–vis–NIR spectra seen in Figure 2.14d, which shows increased low energy absorption as a result of excitations from the valence band into mid-gap states generated by sulfur vacancy defects. Like Fe oxidation, this high density of mid-gap states could improve electronic conductivity. Figure 2.14a summarizes pressed pellet DC conductivities for Fe-S prepared under *in-air* and *air-free* conditions pre and post desulfurization (water-treatment). After desulfurization, the conductivity increases ×320 from 0.13 μS cm^{-1} to 42 μS cm^{-1}. Temperature dependent pressed pellet DC conductivities of Fe-S post desulfurization show the smallest activation barrier observed so far, 0.305 eV compared to 0.36 eV for *in-air* Fe-S. Pressed pellet Chronoamperometry and EIS results indicate that the charge transport is purely electronic, indicating mobile S^{2-} aren't responsible for the improved conductivity (Figure A.37). These results suggest that

desulfurization is generating sulfur vacancy defects which manifest in mid-gap states which improve electrical conductivity through a reduction in the conduction activation barrier.

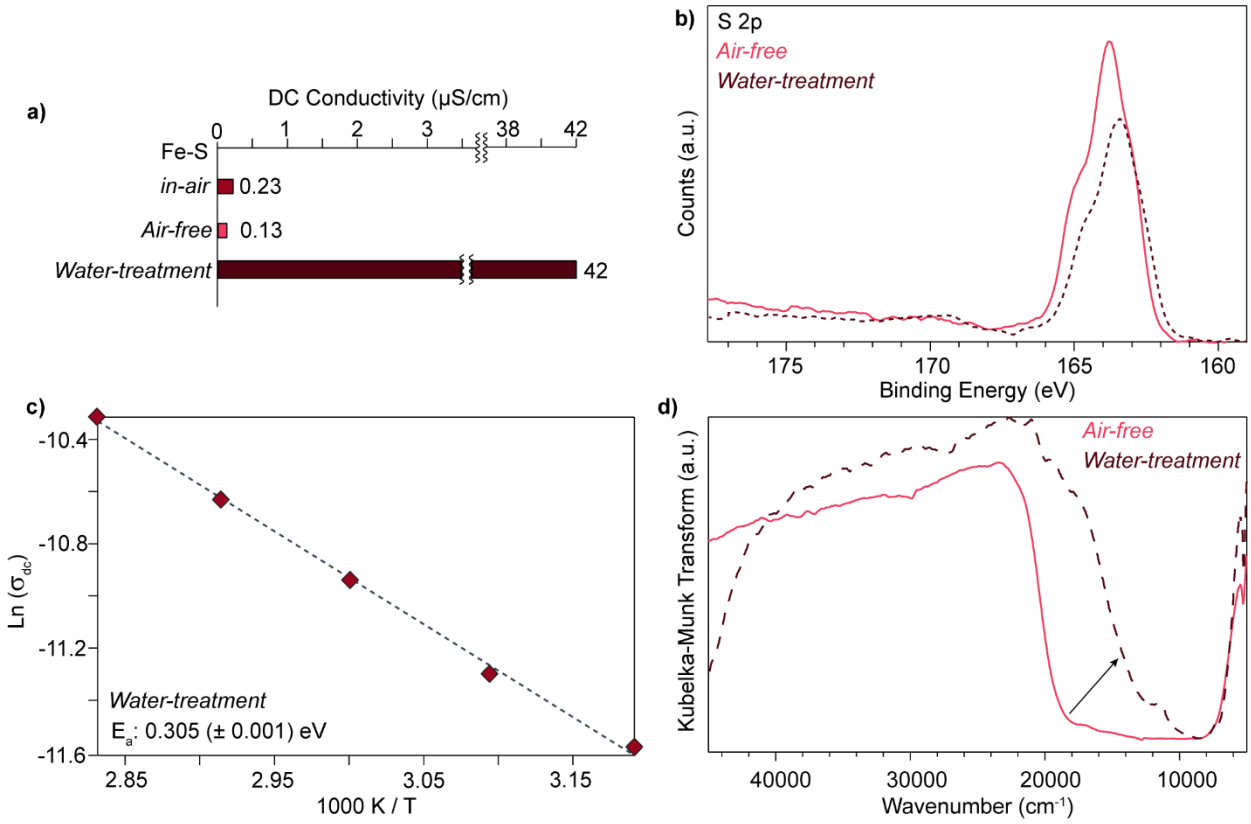

Figure 2.14 Summary of the effect of sulfur defects on Fe-S framework. a) Comparison of DC conductivities. b) XPS of Fe-S pre and post water treatment. c) Arrhenius plot of variable DC conductivity in water-treated Fe-S. d) Fe–S diffuse reflectance UV–vis–NIR spectra pre and post water treatment.

Discussion.

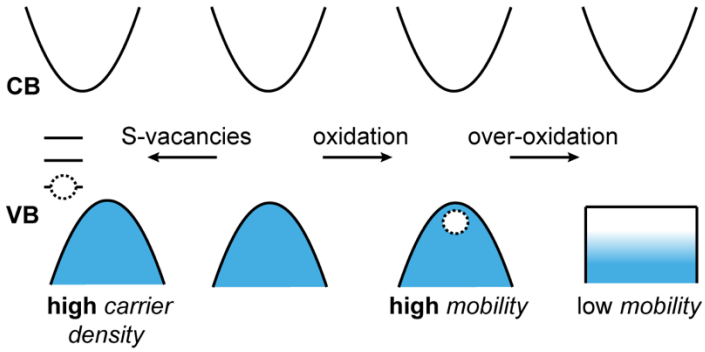

Scheme 2.2 Band diagrams summarizing the impact of redox chemistry, defect states, and framework composition on band curvature, carrier concentrations, and mid-gap states.

These results suggest a band-type charge transport mechanism for the Fe-containing frameworks and a redox-hopping-type mechanism for the Mn, Co, Ni, and Zn materials. Generally, band-type transport leads to higher conductivities in materials with greater bond covalency and, hence, high charge mobilities, while redox hopping depends on chemical factors that promote outer-sphere electron transfer, as outlined by Marcus theory.[90] Specifically, redox hopping benefits from materials with redox sites in close proximity by improving the likelihood of charge transfer and with mixed valency to provide both donor charges and acceptor orbitals.[91] Our measurements indicate that holes act as the dominant charge carriers, implying that the curvatures of valence bands should dictate charge mobilities, while our calculations predict that Fe^{2+} frameworks possess greater valence bandwidths. The EIS data in Figure 2.7 corroborate this assignment by showing that Fe–S charge transport involves pure electronic movement, whereas Zn–S conductivity involves the transfer of both electrons and ions, as expected for outer-sphere electron transfer to be accompanied by charge-balancing ions. While band dispersions for pristine Fe^{2+}–Se and Fe^{2+}–S are comparable, the dispersion drop is far more significant for Fe^{3+}–

Se than for Fe^{3+}–S, with bands comparable to the flat valence band of Zn–S. The conductivity for oxidized Fe-S was further improved by post-synthetic sulfur defect formation. As seen in Figure 2.14 sulfur defects increased charge carrier density and dramatically improved conductivity from 0.13 μS cm^{-1} to 42 μS cm^{-1}. Scheme 2.2 summarizes the key insight from these studies, namely, that high conductivity in these frameworks requires both higher charge carrier densities (from Fe oxidation and S defect formation) and dispersive band curvatures (high carrier mobility) but that a critical amount of oxidation causes the frameworks to distort into materials with lower charge mobilities.

The redox-dependent conductivity supports the assignment of a band-type mechanism for the Fe frameworks, as well, and explains the superior conductivity of the Fe frameworks. If the mechanism involved redox hopping, then conductivity would maximize with $Fe^{2+/3+}$ in a 50:50 mixture, with conductivity decreasing beyond this mixture, as has been observed for redox polymers.[39,92] Instead, the DC conductivity of Fe–S from potential-dependent conductivity (Figure 2.10) does not peak but rather continues to increase with greater oxidizing potentials before leveling off. Furthermore, the observation that the *in-air* synthesis of Fe^{3+}–Se produces a far more conductive material than the mixed-valent *air-free* synthesis of Fe–Se disputes a redox-hopping mechanism. For band-type materials, conductivity generally improves in materials with greater charge carrier concentrations. However, "overoxidation" of the Fe–S and Fe–Se frameworks to form the Fe^{3+} variants causes significant distortions to the lattices that flatten the valence bands and reduce hole mobility (Scheme 2.2). The general tendency of Fe^{2+} to engage in facile redox chemistry, therefore, implies that the higher conductivity of the Fe frameworks arises from their ability to form dilute charge carrier concentrations. Accordingly, the partial oxidation of Mn–S led to greater DC conductivity by forming an oxidized Mn species. If

oxidation had led to dilute concentrations of Ni^{3+} and Co^{3+}, rather than oxidized sulfides, we predict that Ni–S and Co–S also would have demonstrated improved conductivity. Instead, we propose that the Mn, Co, and Ni frameworks show similar charge transport to Zn–S when prepared *in air* despite their more dispersive valence bands because, like Zn–S, their charge transport involves intra- and intercluster hopping, rather than through bonds. Similarly, among MOF families that can be prepared with a variety of metal ions, the Fe derivatives often exhibit conductivities several orders of magnitude higher and smaller activation energies. Further investigations suggest that Fe promotes charge transport with its high-energy Fe d-orbitals susceptible to oxidation and, hence, $Fe^{2+/3+}$ mixed valency,[28] akin to the Fe frameworks studied here.

The conductivity of the Fe–S and Fe–Se frameworks represents rare examples of the three-dimensional band-type transport in porous frameworks. High conductivity in MOFs often arises from charge delocalization along infinite one-dimensional (1-D) chains of inorganic ligands, such as chalcogenides,[32,93,94] and metal ions within otherwise 3-D frameworks. In this "through-bond" transport mechanism, orbitals are conjugated along the chains but not across the organic cores of the linkers. In rare cases, the chains are 2-D or 3-D,[33,67] but orbital overlap does not involve the entire material in an "extended conjugation" fashion. Extended conjugation has been observed in MOFs that employ "redox noninnocent"[31] or "fully conjugated" linkers,[23,65,95,96] although the examples with the highest conductivities are typically 2-D sheets. For frameworks based on polyoxometalate clusters,[97] the exceptional conductivity of the Fe variants likely arises from redox-type hopping, rather than from band-type transport, due to the ionic nature of Fe^{2+}–O^{2-} bonds. The computed electron density in Figures 2.3 and A.21 and Table A.3 shows that the valence bands of most of the frameworks involve the metal d-orbitals and chalcogenide p-

orbitals but not the Ge atoms, whereas the conduction bands involve all elements. Hole transport, therefore, does not proceed strictly by "extended conjugation", whereas n-type doping would lead to such a mechanism. Although open-framework chalcogenides comprise a large and important family of materials, few reports have investigated their charge transport properties. The DC conductivities of the $MSn_4Se_{10}^{2-}$ (M = Fe, Mn) frameworks were ascribed primarily to ion transport and reported to be as low as 10^{-10} S cm^{-1},[72] compared to the ~10^{-6} S cm^{-1} reported here for $FeGe_4S_{10}$, which is dominated by electron transport. Such low electronic conductivity is surprising given the covalency of the Fe–S bonds, but it may be explained by low charge carrier densities afforded by the *air-free* synthetic conditions. However, charge carrier density could be improved with sulfur defect formation, to afford the highest conductivities seen for Fe-S with pressed pellet conductivity measurements.

Finally, these results reveal mixed-conducting and magnetic ordering behavior previously unknown for open-framework chalcogenides. The ferromagnetic ordering of $TMA_2FeGe_4S_{10}$ observed at ~2.75 K provides the first validation of an earlier computational study on this family of material, which predicted ferromagnetism in the Fe variant but not the other analogues.[98] This study also predicted half-metallicity, which has yet to be reported. The absence of ferromagnetic ordering in Fe–Se likely reflects the increased distance between Fe sites and/or the Fe sites being predominantly Fe^{3+} centers. This may explain the absence of magnetic ordering in the previously studied $TMA_2FeSn_4Se_{10}$.[77] Although open-framework chalcogenides have been widely studied as ionic conductors, the EIS data in Figure 2.7c demonstrate hallmark evidence of mixed ion–electron conductivity. Given the ability of these materials to be prepared with other cations, such as Cs,[78] K,[72] and Li,[79] their propensity for cation exchange,[68] and the variable pore sizes and environments, coupled with the tunable electronic conductivity reported here, these results reveal

that open-framework chalcogenides comprise an attractive new class of mixed conductors for studying energy storage and other electrochemical technologies.

Conclusions.

In conclusion, we report the preparation of two new open-framework chalcogenides, $TMA_2NiGe_4S_{10}$ and $TMA_2CoGe_4Se_{10}$, and investigate the electronic, magnetic, and charge transport properties of these new members and previously reported isostructural analogues. Comparison of these materials through conductivity measurements and DFT methods shows that the identity of the metal ions and chalcogenides controls charge transport by dictating the composition and curvature of the valence and conduction bands and hence the charge carrier mobilities. The Fe-containing variants exhibit the highest conductivities, whereas all other variants display similar DC conductivity magnitudes. Impedance spectroscopy reveals that charge transport in the former involves mostly electrons, whereas the latter depends on both ions and electrons. This insight and the strong dependence on the amount of oxidized metal ion dopants suggest that charge transport in the frameworks proceeds by a band-type mechanism that improves with dilute concentrations of holes but which diminishes at high concentrations due to structural distortions that flatten band curvatures. Although open-framework chalcogenides are well established, these results provide some of the only insights into their tunable physical properties, proving that they remain a powerful platform for studying fundamental aspects of porous materials.

CHAPTER III

SOLVENT-CONTROLLED ION-COUPLED CHARGE TRANSPORT IN MICROPOROUS METAL CHALCOGENIDES

This section includes an excerpt from previously published and co-authored material from McKenzie, J.; Kempler, P. A.; Brozek, C. K. Solvent-Controlled Ion-Coupled Charge Transport in Microporous Metal Chalcogenides. *Chem. Sci.* **2022**, 13 (43), 12747–12759.

In this chapter, the project idea was conceptualized by Jacob McKenzie and Carl. K. Brozek. The article was co-written by Jacob McKenzie, Carl K. Brozek, and Paul A. Kempler. Experiments and analysis were performed by Jacob McKenzie.

Introduction.

Semiconductors with permanent microporosity radically diverge from the performance and basic principles of conventional electrochemical materials.[56,56,99] With pores on the scale of Ångstroms or nanometers, these materials fundamentally challenge notions of electrochemical double layers and charge storage,[19,53,100] while offering diverse compositional diversity.[64] Such extreme surface-to-volume ratios, and architectures composed entirely of monolayers wrapped into a wide range of topologies, offer a powerful platform for investigating next-generation electrochemical technologies such as supercapacitors, electrocatalysts, and gas-diffusion electrodes. Metal–organic frameworks, open-framework metal chalcogenides, and microporous metal oxides comprise important classes of materials with opportunities in membranes, energy storage, and catalysis.[101–103] While studies into these systems continue to attract attention of wide-ranging communities, their basic conductivity behavior remains largely unexplored.

The mechanisms of charge transport and redox chemistry of molecular materials become dictated by ion–charge interactions when the distance between ions and charges approach

Ångstrom length scales.[104–106] For example, the movement of protons governs charge transfer in molecules[42,107] and biological systems[43] such that the concerted motion of protons and electrons (PCET) is thermodynamically favored over stepwise proton and electron transfer. The redox chemistry of molecules, conductive polymers, and colloidal nanocrystals[108–114] also becomes facilitated by ion pairing with redox-inactive metal ions, such as Sc^{3+} and Ca^{2+}.[115–117] Beyond microporous semiconductors, electrodes with high surface-to-volume ratios, such as 2D layered materials, exhibit redox chemistry and delocalized charge transport sensitive to the presence of electrolyte.[118,119] Ion-coupled charge transfer (ICCT) has been recently demonstrated to influence the electron mobility of MOFs as well.[45,46] We propose that ICCT must be considered in materials where external ions, such as electrolytes, exist within Ångstroms of itinerant charges. Conceived classically, the influence of each charge should scale as $\frac{1}{r\varepsilon_r\varepsilon_0}$ where r denotes the average inter-charge distance, ε_r the operative dielectric constant, and ε_0 the permittivity of vacuum. Therefore, the design of electrochemical capacitors, batteries, and electrocatalysts based on microporous conductors must consider these potentially strong interactions because they all involve the mixed conductivity of both ions and electrons.[120]

Open-framework metal chalcogenides (OFMCs) offer an ideal platform for studying the coupling of ions and electrons in nanoconfined spaces. Like MOFs, these materials afford a wide range of tunable structures through variable cluster sizes, the identity of the cluster elements and linking transition metal, and the identity of the cations that balance the anionic structures.[25,68–79,121,122] Previously, we explored the electronic, magnetic, and conductivity properties of the prototypical family of OFMCs, first reported by Yaghi et al.,[68] $TMA_2MGe_4Q_{10}$ (Q: S and Se; M: Fe^{2+}, Mn^{2+}, Co^{2+}, Zn^{2+}, and Ni^{2+}).[123] Scheme 3.1a displays a portion of a prototypical microporous metal chalcogenide framework and Scheme 3.1b highlights the close proximity of

the delocalized electron pathway (green) and the direction of cation movement (pink). Importantly, these studies established that whereas the Zn, Mn, Co, and Ni variants exhibit redox hopping-type, mixed conductivity, the Fe analogue exhibits band-type electronic transport. In particular, band structure calculations indicated non-dispersive valence bands localized on sulfur sites, corroborating the assignment of redox hopping between sulfurs as the likely conduction mechanism. In contrast, the partial density of states analysis of the Fe analogue revealed dispersive valence bands delocalized across both the sulfur and Fe atoms. Therefore, the contrast of Fe and Zn materials is convenient for understanding the chemical parameters, such as solvent, that govern ICCT and their impact on the two key forms of charge transport.

Here, we report solid-state conductivity data showing that this class of materials displays mixed ionic-electronic conductivity controlled by solvent. We hypothesize that solvent untethers the motion of charges from ions by facilitating the motion of ions and by screening strong ion–charge interactions. This effect enhances ambipolar diffusion and thus dramatically improves electronic conductivity. These results, therefore, present guidelines for rationalizing previous observations of conductivity in microporous materials sensitive to environmental conditions and establish design rules for controlling basic charge transport mechanisms.

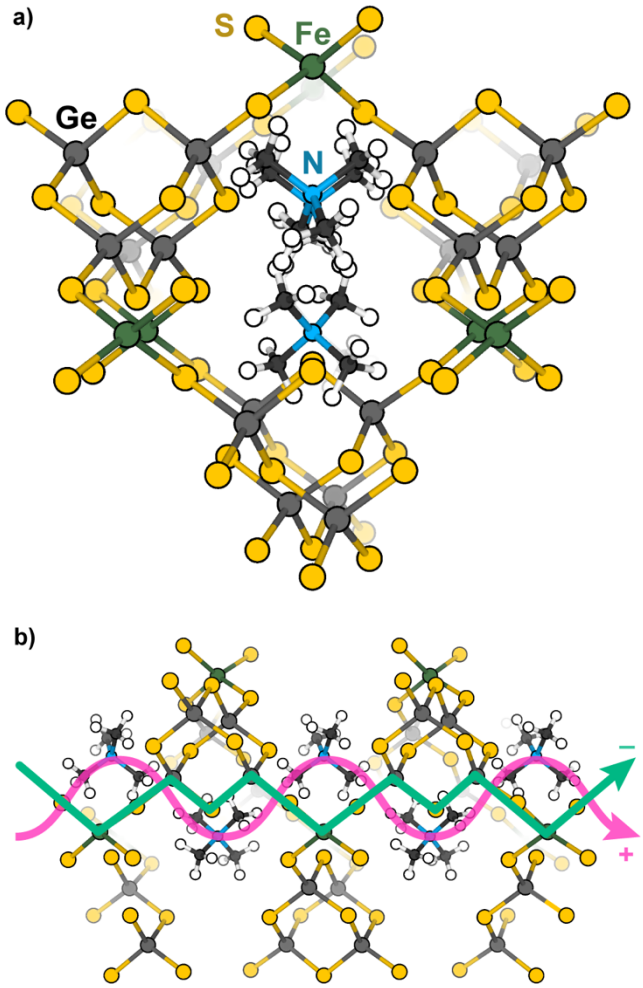

Scheme 3.1 Representations of $TMA_2FeGe_4S_{10}$ viewed along the a) [100] and b) [101] directions. Proposed conduction pathways of delocalized electrons and extra-framework cations are highlighted in green and pink, respectively.

Results and Analysis.

Microcrystalline powders of open-framework chalcogenides $TMA_2MGe_4S_{10}$ (M = Zn and Fe) were prepared following modified synthetic procedures previously reported by Yaghi et al.,[68] with phase purity verified by powder X-ray diffraction (PXRD) (Figures B.1 and B.2). To compare the distinct mechanisms of mixed conductivity in the Zn and Fe variants, pressed pellets were analyzed by chronoamperometry using stainless steel ion-blocking electrodes while stepping the applied voltages between −0.2 V and 0.1 V. Figure 3.1 shows the current transients

for both materials when dry and after treatment with deionized water. When dry, the Fe system exhibits steady current transients (Figure 3.1a) consistent with the Fe system being a purely electronic band-type conductor. Indeed, when considering the current transient at −0.2 V, an electronic transference number t_e of 0.97 and a minimal ionic contribution of $t_i = 0.03$ is found. By contrast, the dry Zn analogue (Figure 3.1c) displays a non-ohmic current response, indicative of ionic contributions ($t_i = 0.15$) and, therefore, mixed conductivity. Furthermore, plotting the steady-state current values versus applied voltage reveals a pronounced hysteresis in the Zn system, but no hysteresis in the Fe system (Figure. B.5). Hysteresis in current–voltage (I–V) curves on forward and reverse scans is commonly observed in other classes of mixed conductors, such as conductive organic polymers and perovskites, when analyzed with similar ion-blocking electrodes, and has been attributed to low ion mobilities.[124–127] Indeed, fits of the initial current transient at −0.2 V to the Cottrell relation yields an effective diffusion coefficient of 1.3×10^{-20} $cm^2\ s^{-1}$ for the Zn system (Figure. B.3). This low diffusivity could be explained by poor mobility of bulky TMA^+ in solid state, with transport limited by nearest neighbor hopping through the lattice. Thus, these current–voltage data corroborate our previous report that the Fe system conducts by pure electronic transport, whereas the Zn system conducts both cations and electrons.[123] Given that the Fe and Zn systems are isostructural, the substantial difference in conductivity likely arises from the materials possessing distinct transport mechanisms. For the Zn system, redox hopping between clusters necessitates ion movement to maintain charge neutrality,[46,91,128–131] whereas charge carrier delocalization in the Fe system maintains charge neutrality through motion of both electrons and holes.

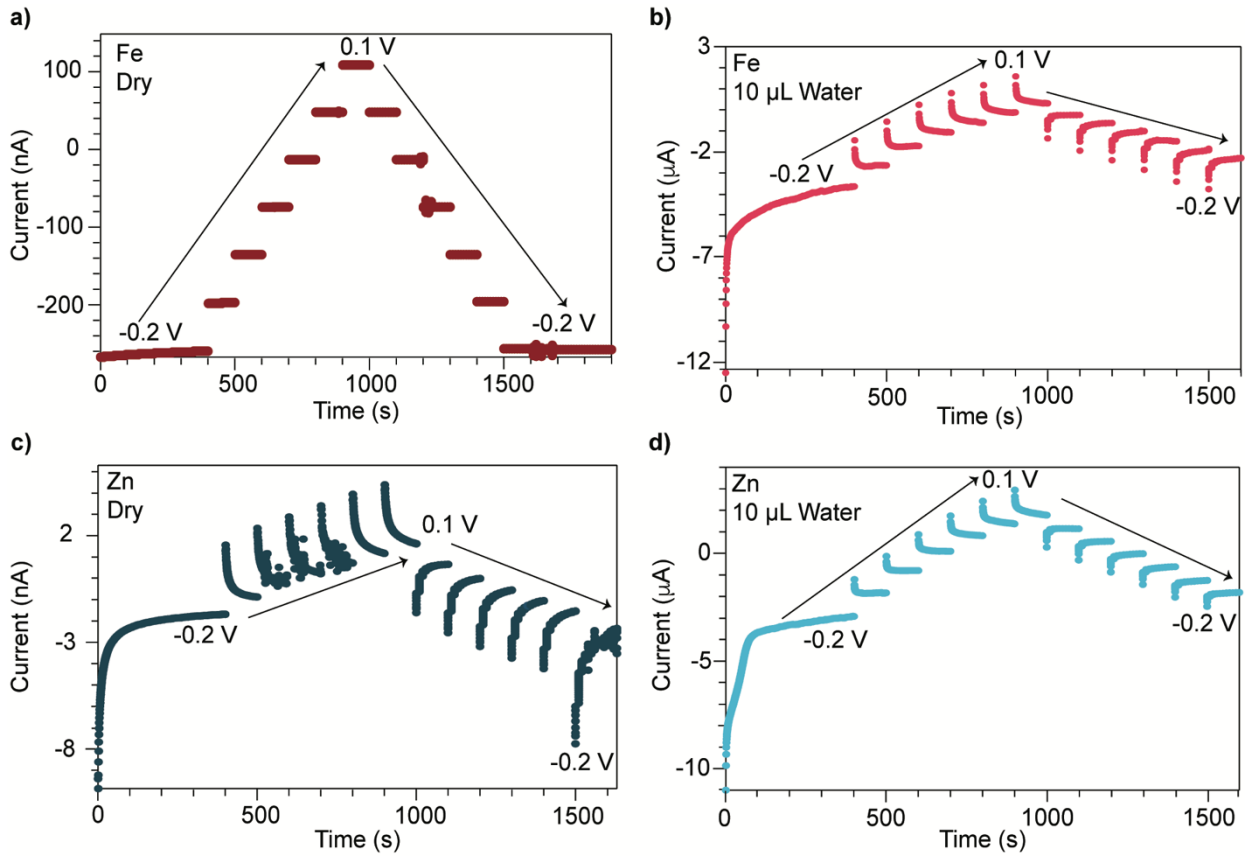

Figure 3.1 Chronoamperometry traces of $TMA_2FeGe_4S_{10}$ and $TMA_2ZnGe_4S_{10}$ pressed-pellets under applied voltages spanning −0.2 V to 0.1 V when dry (a and c), and after treatment with 10 µL of deionized water (b and d), respectively.

Given the proximity of TMA^+ cations to itinerant electrons in both the Zn and Fe systems, we expected solvent addition to facilitate TMA^+ movement and screen coulombic interactions between the TMA^+ and electrons. We therefore varied the solvent size and dielectric strength to explore these effects. The influence of solvent was quantified via chronoamperometry experiments, which were repeated following the treatment of pressed pellets with deionized water. Unlike the dry Fe system, the hydrated Fe system displayed a non-ohmic current response (Figure 3.1b). The corresponding ionic transference number increases to 0.77. Fits to the Cottrell relationship for this material yield an effective diffusion coefficient of 2.3×10^{-14} cm^2 s^{-1} (Figure

B.4). For the hydrated Zn system, ionic conductivity is enhanced (Figure 3.1d), with the Cottrell relationship producing an effective diffusion coefficient of 1.6×10^{-13} cm^2 s^{-1}—a ten-million-fold improvement compared to the dry Zn system (Figure B.3). These diffusion coefficients are comparable to diffusion coefficients found for PF_6 anions in metallocene-modified $(Zr_6O_{16}H_{16})(TBAPy)_2$ MOF systems (10^{-11}–10^{-13} cm^2 s^{-1}).[132]

The steady-state currents obtained from chronoamperometry across the hydrated Fe and Zn systems were compared as a function of the applied voltage to determine their DC (purely electronic) conductivities. Compared to DC conductivities when dry, the hydrated Fe system increases from 0.11 to 0.93 μS cm^{-1}, whereas the hydrated Zn system increases from 0.0011 to 1.2 μS cm^{-1}. Although the I–V hysteresis of the hydrated Zn system persists, it decreases in magnitude (Figure B.5). The hydrated Fe system exhibits an I–V curve hysteresis not previously observed for the dry Fe system. The larger hysteresis between steady-state current values observed at −0.2 V on the forward and reverse scan for the Fe system (1.4 μA) versus the Zn system (1.1 μA) reflects the smaller diffusion coefficient determined for the Fe system.

With the observation that water treatment improved the electronic conductivity of both the Fe and Zn systems, we explored the effect of solvents with a wide range of bulk dielectric constants. Figure 3.2 summarizes the pressed pellet DC conductivities after addition of solvent. Values were obtained from linear fits to the plateaued time points of I–V profiles collected at 2 mV s^{-1} (Figures B.6 and B.7). For a greater range of bulk dielectric values, water/EtOH mixtures were employed in precise ratios.[133] In general, the DC conductivities of both the Zn and Fe systems dramatically increases with increased solvent dielectric strength. For example, these data indicate a ten-thousand-fold improvement to the electronic conductivity of the Zn system in the presence of formamide compared to the dry pellet. The I–V curves resulting from these solvent-

dependent DC conductivities always exhibited non-linearity for the Zn framework, typical of a diffusion-limited process, (Figure B.7), whereas for the Fe system, the I–V curves appear linear for solvents with low dielectric constants, such as DCM and n-butanol, (Figure B.6) but non-linear for solvents with high dielectric constants, such as MeOH, acetone, or water (Figure B.6). Solvent size also correlates with changes to DC conductivity (Figure B.8). Specifically, smaller solvents generally correspond to higher conductivity values, helping to explain discrepancies in the relationship between dielectric and conductivity. For example, although t-butanol bears a larger bulk dielectric than CH_2Cl_2, the former leads to lower DC conductivities. This discrepancy could be attributed to its larger size (0.55 nm) compared to DCM (0.46 nm),[134] thereby impeding it from more effectively entering the framework ~1 nm micropores, to properly solvate TMA^+. However, conductivity generally improves when employing larger solvents unlikely to fit in the pores. This improvement likely results from solvent interactions with TMA^+ in the macropores that exist between particles in the pressed pellet. In the case of the Fe system, DC conductivity scales roughly linearly with solvent dielectric strength (Figure 3.2b), especially when excluding

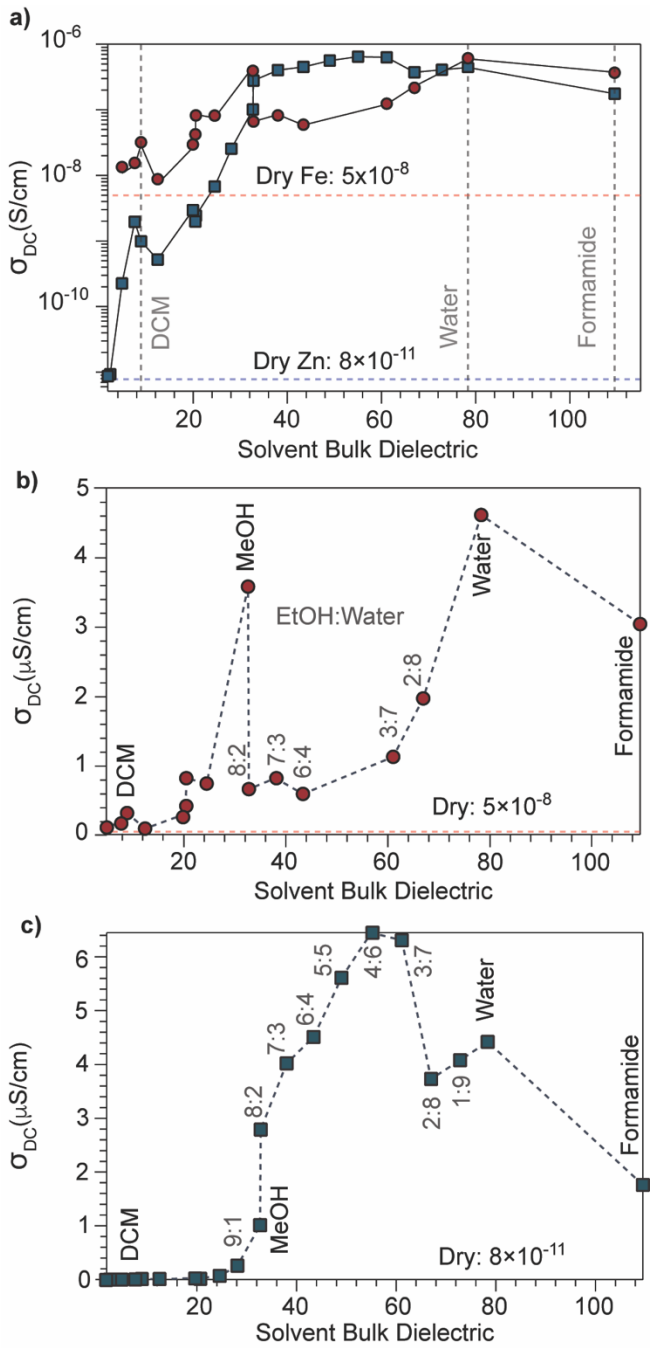

Figure 3.2 a) Solvent-dependent DC conductivity values of $TMA_2FeGe_4S_{10}$ and $TMA_2ZnGe_4S_{10}$ pressed-pellets obtained from linear fits to I–V curves swept voltammetrically between −0.2 V and 0.2 V at 2 mV s^{-1}. In increasing order of bulk dielectric constants, the solvents included hexanes, toluene, chloroform, DCM, THF, IPA, t-butanol, n-propanol, acetone, ethanol, methanol, (EtOH : water mixtures spanning 9 : 1 to 1 : 9), water, and formamide. Dotted lines correspond to dry-pellet DC conductivity values. Panels (b and c) represent the same data plotted on a linear scale.

outliers MeOH and water, likely due to their comparatively smaller size that facilitate improved packing in the micropores. The Zn system, however, shows a strongly non-linear dependence for solvents having a bulk dielectric constant >40 (Figure 3.1c). Collectively, these results suggest that for the Fe system, solvent serves to screen the attractions between itinerant electrons and less mobile TMA^+ cations, in accordance with a semi-classical coulombic interaction. For the Zn system, however, the non-linear relationship could be ascribed to solvent facilitating the ambipolar diffusion of hopping-type transport by improving ion transport, as has been observed for the solvent dependent conductivity of mixed conducting polymers.[135]

To further deconvolute the charge transport mechanism in the Fe and Zn systems, electrochemical impedance spectroscopy (EIS) was performed on dry and solvent-treated pressed-pellets. Figure 3.3 displays Nyquist plots for the Fe system with data fitted to models based on the corresponding equivalent circuit diagrams. The impedance response for the Fe system when dry (Figure 3.3a) produces a single semicircle as expected of a pure electronic conductor.[87] The right-most *x*-intercept (1.13 MΩ) gives the electronic resistance of the system, yielding an electronic conductivity of 0.09 μS cm^{-1}, comparable to DC methods (0.05 μS cm^{-1}) (Figure 3.2). Close inspection of the low frequency (right side) of the spectrum reveals a slight distortion of the semicircle that precludes fitting the impedance response to a parallel combination of an electronic resistance and idealized dielectric capacitance. We ascribe this distortion to an additional parallel constant phase element (CPE). Attempts to model this distortion to grain-boundary contributions—commonly modeled as a parallel resistor and capacitor—proved unsuccessful.[87,136–138] Constant phase elements are defined primarily by their phase, n, with their total impedance (Z) described by $Z = \frac{1}{(j\omega)^n Q_0}$. When n = 1, the CPE describes an ideal capacitor, whereas n = 0 corresponds to a pure resistor, and n = 0.5 denotes a

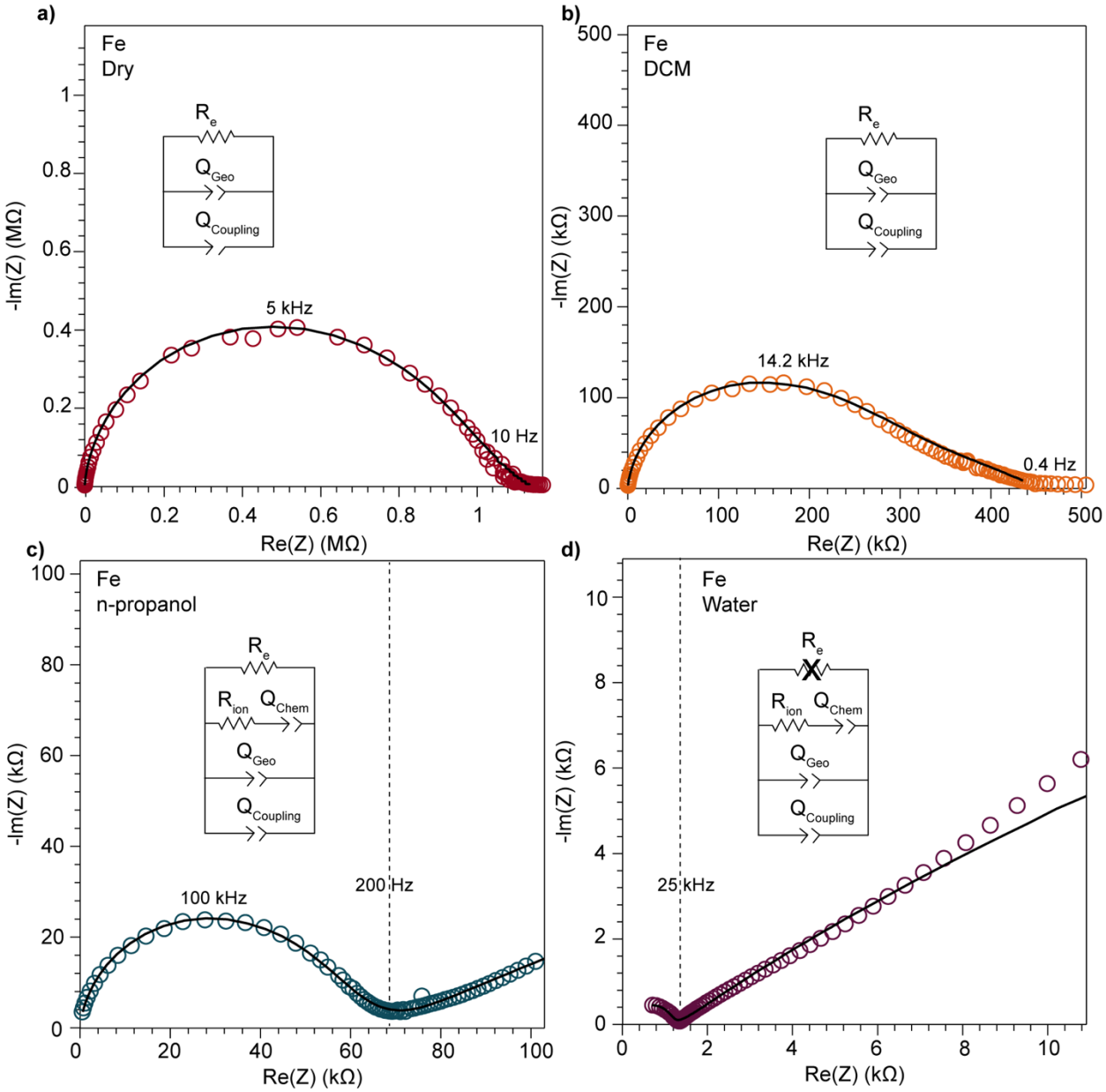

Figure 3.3 Nyquist plots of $TMA_2FeGe_4S_{10}$ pressed-pellets when dry a) and after addition of DCM b), n-propanol c), and deionized water d). Black traces represent fits to the equivalent circuit diagrams shown in the figure. Crossed-out circuit elements denote elements that are too large to adequately fit to the impedance response.

semi-infinite diffusion-related process, termed a Warburg element.[139,140] The phase that describes the distortion for the Fe system is 0.37, suggesting ion–electron interactions influence electronic conduction even when dry. This CPE could be attributed to a distribution of contact

resistances,[141] a distribution of conduction pathways through the pellet,[142,143] or a coupling constant between charge transfer pathways.[137,144] While dispersion of contact resistances and conduction pathways are expected to affect the EIS response at high frequencies, the dispersion observed in our systems appears in the low-frequency region (right-side) of the Nyquist plot. This dispersion likely reflects local ionic motion in the impedance response of the bulk material and the inhomogeneous pore resistances.[145] Therefore, we ascribe this circuit element to a CPE we term $Q_{coupling}$, which describes the electrostatic coupling between ions and charges. Previous reports theorized that this effect impacts the bulk impedance response of mixed conductors, but it is often neglected in circuit fitting because dielectric responses are typically far larger than any electrostatic coupling.[138,144]

By contrast, the Zn system displays an incomplete semicircle even when dry (Figure 3.4a). The *x*-intercept fit produces a high bulk resistance of 48 MΩ which corresponds to a conductivity of 0.002 μS cm^{-1}. We ascribe this resistance to be predominantly ionic in character. Fits to these data also suggest a significant distortion to the low frequency (right side) of the first semicircle. In contrast to the Fe system, the CPE associated with this distortion has n = 0.45. While the phase for the Fe system is too distorted to definitively define its origin, for the Zn system this phase can be ascribed to a diffusion process. Furthermore, in contrast to the Fe system, a CPE with n = 0.41 controls the impedance response below 0.4 Hz. Microscopically, we attribute this process to a "chemical capacitance" (Q_{chem}) arising from the hopping of electrons under the influence of TMA^+ concentration gradients induced by the ion-blocking interfaces.[87,138,146] The distorted impedance responses described by $Q_{coupling}$ observed for the dry Fe and Zn materials suggest distinct manifestations of ICCT. Although typical analysis of mixed

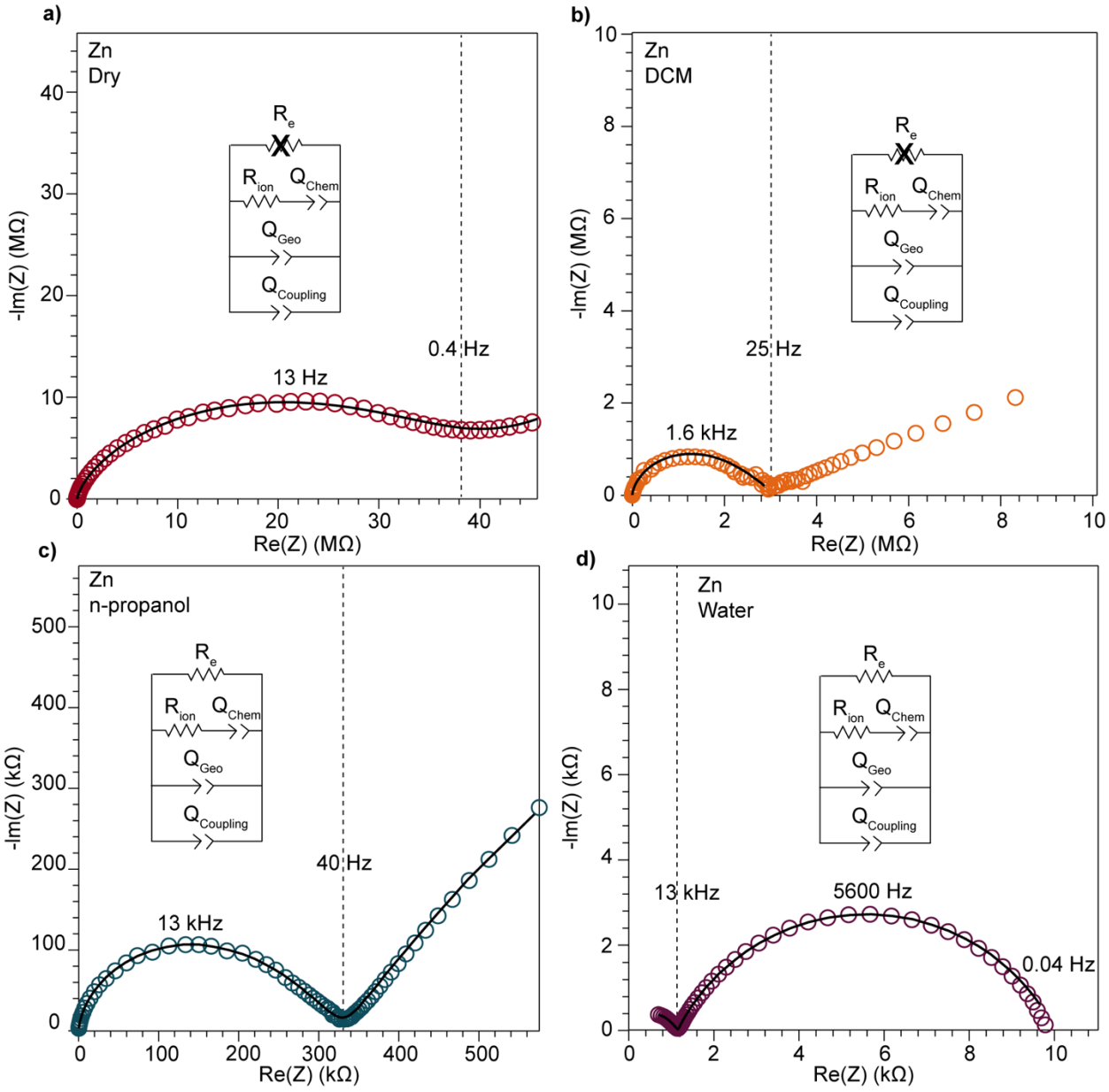

Figure 3.4 Nyquist plots of $TMA_2ZnGe_4S_{10}$ pressed-pellets when dry a) and after addition of DCM b), n-propanol c), and deionized water d). Black traces represent fits to the equivalent circuit diagrams shown in the figure. Crossed-out circuit elements denote elements that are too large to adequately fit to the impedance response.

conductors treats ions and electrons as separate charges with independent resistances and, hence, parallel resistors, these data suggest a partial convolution of the ionic and electronic rails, which manifests in the CPE we label as Qcoupling.[87,138,146] Furthermore, because $Q_{coupling}$ for the dry Zn

system fits to n = 0.45, these electrochemical process can be physically understood as a diffusion process. In fact, the CPE can be readily exchanged for a Warburg element with little change to the fit (Figure B.10). This result implies cation–electron ambipolar diffusion. Such Warburg-type responses have been observed for porous electrodes where the movement of ions and electrons are coupled.[147] In contrast, the Fe system shows n = 0.37, with this dispersion in the diffusive response potentially due to mean-field attraction from TMA^+ cations impeding the movement of delocalized electronic carriers.

To better understand the mechanistic role of solvent in a redox hopping-type system, EIS responses were recorded for the Zn system after treatment with solvents spanning a range of bulk dielectric values (DCM, n-propanol, and water; Figure 3.4). In general, with increased solvent dielectric strength, the Zn system displayed decreased impedance across all frequencies and a diffusion-related process dominates at low frequencies. As with the dry Zn system, these data were fit best to a circuit with a $Q_{coupling}$ element attributable to cation-coupled electron transport. With all solvents, the CPE bears an average phase of n = 0.48 equivalent to a Warburg diffusion element, suggesting charge transport proceeds by an ambipolar diffusion mechanism, i.e., by redox hopping compensated by diffusing TMA^+ cations. Furthermore, the ionic resistances decrease with solvents of greater bulk dielectrics, as observed by the position of the intermediate *x* intercepts in the Nyquist plots. In addition, the electronic resistances also decrease with solvents of greater bulk dielectrics, as calculated from circuit fits which provide the second low frequency *x* intercept (Figure 3.5). This result implies solvent improves ambipolar diffusion and manifests in decreases in Warburg coefficients for the $Q_{coupling}$ (Figure 3.5) and improved diffusion coefficients. Furthermore, fits for hydrated Zn system included a contact resistance (R_c) to ensure valid interpretation of the impedance results. The R_c found is 150 Ω, in close

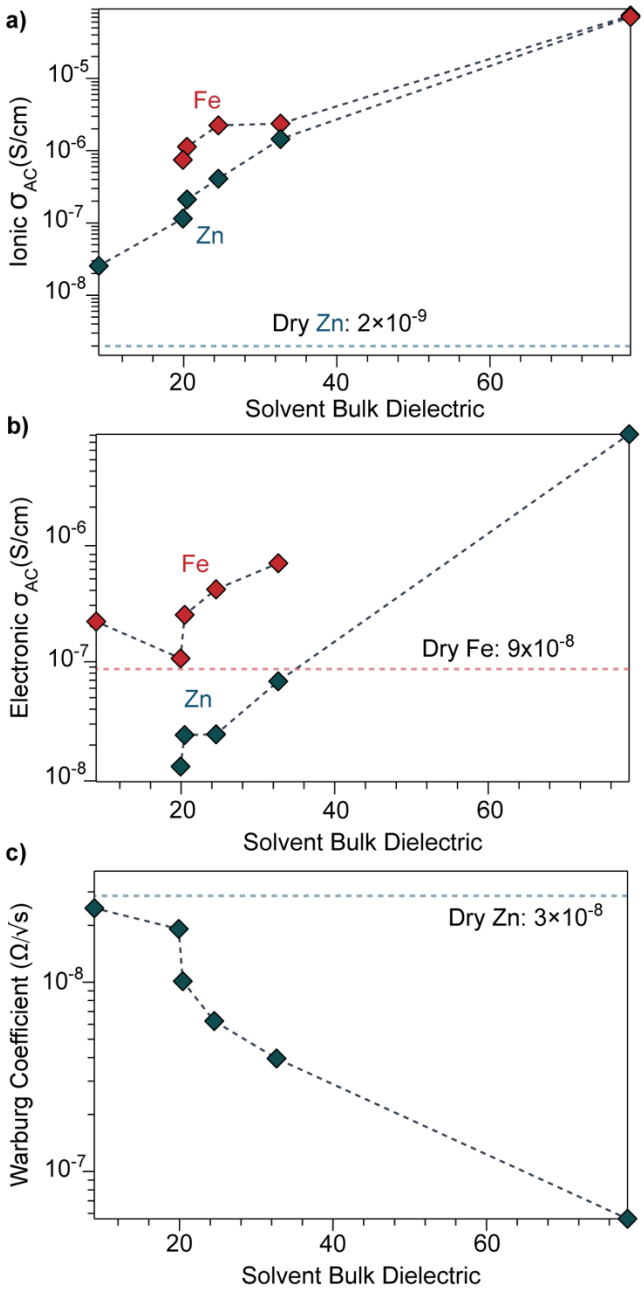

Figure 3.5 Solvent-dependent parameters fitted from EIS spectra modelled by equivalent circuits shown in Figures 3.3 and 3.4. (a) AC ionic conductivity as a function of solvent bulk dielectric for the Fe and Zn materials. (b) AC electronic conductivity as a function of solvent bulk dielectric for the Fe and Zn materials. (c) High frequency Warburg coefficients derived for $TMA_2ZnGe_4S_{10}$ from the $Q_{coupling}$.

agreement with the contact resistance found when considering the impedance of the dry Zn system, 106 Ω. This result implies that solvent treatment does not dramatically affect the ohmic

contact between the electrode and pellet. The low-frequency EIS response of the solvent-treated Zn analogues can be modeled by the CPE Q_{chem}, which corresponds to electron diffusion under the influence of a TMA^+ gradient. For all solvent treatments, $n > 0.5$ for Q_{chem}, with an average phase of 0.56. Like $Q_{coupling}$, this phase can be physically understood as a diffusion process and in the context of the mixed conducting literature corresponds to equal charge carrier concentrations of both electrons and ions.[87] This fact provides further evidence for concerted ambipolar motion, where electrons can only conduct with associated ion diffusion.

Based on the hypothesis that electronic conduction improves because of improved ambipolar diffusion promoted by increased ionic conductivity, the Zn system was treated with an aqueous solution of TMABr. After treatment, the electronic resistance further decreased to 8000 Ω (Figure B.12). This result suggests the increased availability of TMA^+ leads to greater cation concentration gradients and stronger electric fields to promote electron conduction.[136] Furthermore, the ionic resistance also decreases from 1300 Ω to 30 Ω, when considering the 150 Ω $R_{contact}$. Furthermore, when modeling $Q_{coupling}$ as a Warburg element, we find a Warburg coefficient of 2.4×10^6 Ω $s^{-1/2}$, in comparison to 6.7×10^6 Ω $s^{-1/2}$, with just deionized water. This result reflects the increased density of positive point charges that can stabilize hopping electrons leading to improved hopping.

Similarly, to better understand ICCT and the mechanistic role of solvent in a band-type system, the EIS response of the Fe system was recorded after solvent treatment (DCM, n-propanol, and water depicted in Figure 3.3). As with the Zn system, increased solvent dielectrics leads to an overall decrease in impedance, but due to a different mechanism. With nonpolar solvents such as DCM, the asymmetry at frequencies below 10 kHz became more pronounced and the low-frequency *x*-intercept reduced from 1.13 MΩ to 0.45 MΩ. We interpret these

changes to mean an increase in charge coupling concomitant with a decrease in DC conductivity. For more polar and higher dielectric materials, such as n-propanol and water, a low frequency impedance "tail" emerges, reminiscent of the chemical diffusion seen in the Zn system (Q_{chem}). These solvents cause a reduction in the ionic and electronic resistances of the Fe material. Whereas ionic resistance can be found directly from the first *x* intercepts, the electronic resistances were determined by fitting the spectra to the circuit diagrams shown in Figure 3.4. Like the Zn system, fits to the hydrated response included $R_{contact}$, producing values of 200 Ω that agree with $R_{contact}$ of the dry Fe system (114 Ω). Close inspection reveals that the phase of $Q_{coupling}$, the process describing coupled electron–cation motion, becomes highly distorted. Across all solvents, we observed an average n value of 0.33, with water treatment leading to the smallest phase of n = 0.15. Furthermore, when utilizing high dielectric solvents, the low frequency CPE Q_{chem} also exhibits a highly distorted phase that averaged to n = 0.31. These highly distorted CPE values indicate that unlike the ambipolar diffusion of the Zn system, electronic conduction dominates charge transport in the Fe system,[87] but under the influence of cation–electron interactions that become frequency dependent with solvent and cation motion. While solvent screens the interactions between iterant charges, leading to a net decrease in electronic DC resistance and AC resistance, the increase in ionic motion creates non-uniform electric fields and electronic resistances, leading to highly dispersive n values.[145] While electronic resistances were fitted for the Fe system from circuit fits for most solvents, the hydrated system was unable to be fitted to an electronic resistance due to the far lower ionic resistance. This result contrasts with the hydrated Zn system, where improvements to ionic conductivity led directly to a measurable improvement in electronic conductivity, further

supporting the claim that the charge transport mechanism for the Zn material proceeds by mixed, hopping-type transport.

Because concerted ion–charge motion improves the thermodynamic driving forces of charge transfer in related systems,[112] we investigated the impact of solvent on charge transport thermodynamics for the Fe and Zn systems. Temperature-dependent DC conductivity values of the Fe system after treatment with either o-dichlorobenzene or formamide reveals virtually no change in the activation barrier for electron conduction (Figures B.14 and B.15). In contrast, the temperature-dependent EIS response of the Zn system after formamide treatment exhibits a lower activation barrier when fitting both the first and second *x* intercept resistance (0.25/0.30 eV vs. 0.44/0.37 eV), suggesting increased carrier density for the Zn system (Figure B.13). Taken together, these results further support the assignment of the Fe system as a band-type conductor: the activation barrier remains unchanged because solvent simply screens the coulombic attraction between electrons and cations, leading to an improvement in the mobility of the electronic charges, but without increasing charge carrier density. For the Zn system, on the other hand, redox hopping becomes more facile with improved ion diffusion, increasing carrier density, and manifesting in a far lower activation barrier then the Fe system.

Discussion.

These results provide some of the first evidence that solvent controls both ion and electron transport in a microporous material. To summarize, the overall impedances of both the Zn and Fe materials decrease as the dielectric strength of the solvent increases, causing the purely electronic resistances to decrease as well, yet for different microscopic reasons. Solvent plays two roles mechanistically for both materials: decreasing electronic resistance and improving ion diffusion, yet these results suggest the relative importance of each role to the Fe

versus Zn materials depends on the charge transport mechanism. For the band-type Fe material, the dominant role of solvent is to screen resistive cation–electron interactions, while for the hopping-type Zn material, solvent improves ambipolar diffusion (at high frequencies) and generates large electric fields (at low frequencies) leading to improved chemical diffusion of electrons. The "screening" role of solvent for the Fe material is evidenced by the roughly linear dependence of DC conductivity versus dielectric strength, as expected for semi-classical Coulomb interactions. Furthermore, fitting the EIS data to the electron–cation coupling element $Q_{coupling}$ led to highly distorted phases more consistent with a resistive-based process, rather than classical diffusion expected from a redox hopping process. Lastly, the insensitivity of the charge transport activation barrier to solvent suggests electronic conductivity increases with solvent addition due to improved electron mobility brought about by charge screening, rather than improved ion diffusion aiding in a redox hopping process. In contrast, the Zn system exhibits a decreased activation barrier with solvent addition, which is consistent with a redox hopping process, as solvent decreases the activation barrier for ionic conduction.[135,148,149] The nonlinear dependence of DC conductivity with solvent dielectric also corroborates a hopping-type ICCT in the Zn material, as do the $n \sim 0.5$ phase angles for both $Q_{coupling}$ and Q_{chem} from EIS fittings. Finally, the nature of the ICCT process in the high frequency regime for the Zn material likely involves concerted cation–electron motion. Scheme 2 summarizes these conclusions. The TMA^+ provide shallow electrostatic traps in the case of the Fe system, creating increased resistance to the band-type conduction, whereas for Zn, they function as deep traps necessitating concerted motion of both hopping charges and mobile cations.

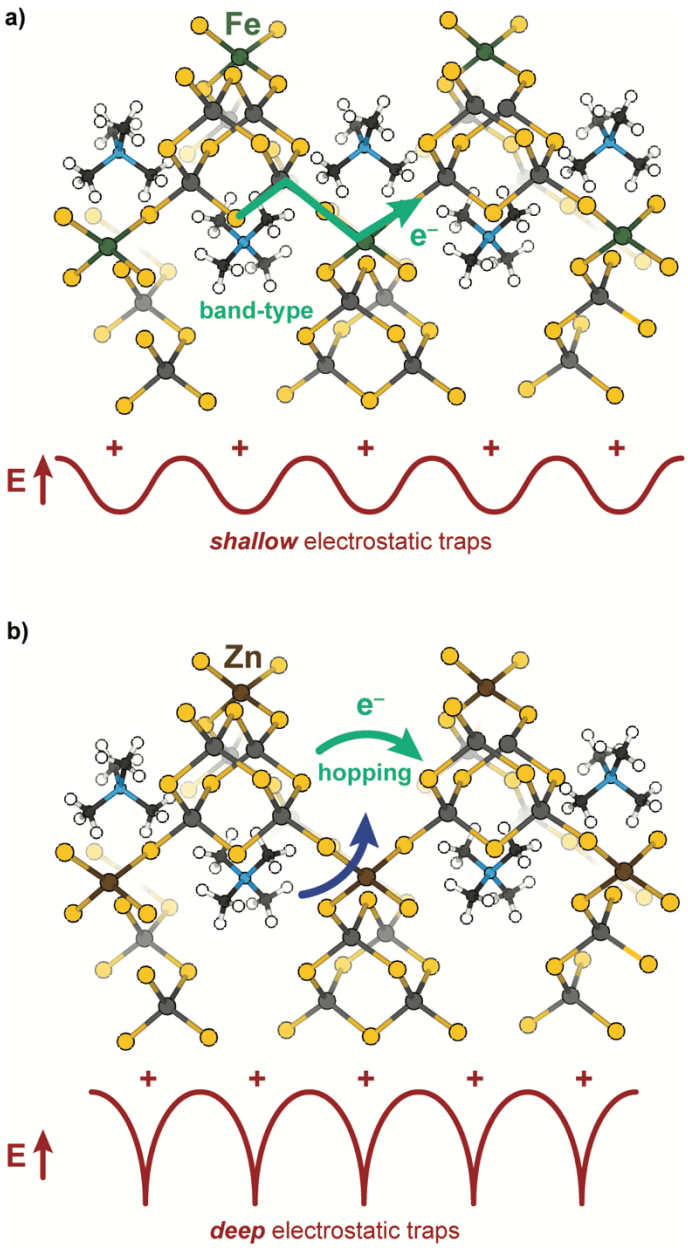

Scheme 3.2 Conduction pathways for the band-type Fe a) versus hopping-type Zn b) analogues.

Although solvent interactions have been reported to impact the conductivity of diverse classes of inorganic materials, this study provides unprecedented insight the mechanistic role of solvent on charge transport in microporous systems. Because ion diffusion dictates redox hopping mechanisms, as demonstrated in MOFs, metal oxides,[150] and redox polymers,[39,128] solvent-dependent ion diffusion has been explored. For example, conductivity studies of the

MOF Zr(3-hydroxy-2-[7-(4-carboxy-2-hydroxyphenyl)-1,3,6,8-tetraoxo-3,6,7,8-tetrahydro-1H-benzo[lmn][3,8]phenanthrolin-2-yl]benzoate) revealed that diffusion coefficients derived from chronoamperometry decreased with higher dielectric solvents.[46] However, the scope of the study was limited to few solvents and focused on just this hopping-type material. However, anecdotal evidence abounds for the solvent- and electrolyte-dependence of charge transport in large-pore MOFs and COFs.[46,129,132,151–153] We contend that this solvent dependence likely results from the pervasiveness of hopping-type charge transport in MOFs. Furthermore, we expect these effects to be magnified by nanoconfined ions. For example, as the pore sizes of isostructural MOFs decrease, reports have noted that diffusion coefficients of hexafluorophosphate and tetrakis(pentafluorophenyl)borate anions also decrease.[45] In the extreme limit (chemical bonding) of ion–charge confinement where ions are close or equal in size to the pore, such interactions could resemble PCET.[42] Elsewhere in the literature, the conductivity of the semiconductor material $Pb_3Na_{1.5}(OH)_{0.5}$(2,3,6,7,10,11-hexakis(butyrylthio)triphenylene) was reported to increase by 10 000-fold upon introduction of water and when measured at high humidity, but without explanation or comparison to other solvent treatments.[154] Similarly, the conductivity of mesoporous $NaSbS_2$ was shown to increase 1000-fold in humid air as opposed to vacuum, although the exact mechanism remains unknown.[39,128,148,155]

These results resemble evidence of ion–electron coupling in organic semiconductors.[149] While conventional semiconductors such as Si, CdSe, or GaP can be doped through substitution, polymers require doping through redox chemistry that necessitates charge-balancing ions. The localization of these ions on polymer backbones leads to electronic transport strongly dependent on both solvent and electrolyte identity. Poly(3,4-ethylenedioxythiophene)/poly(4-styrenesulfonate) has been reported to increase in conductivity from 0.8 μS cm^{-1} in the dry state

to 80 μS cm^{-1} with DMSO, with intermediate conductivities achieved with THF and other solvents of lower dielectric strengths.[148] The authors explicitly attributed the effect to dielectric screening of ion–electron interactions. Similarly, the conductivity of the copolymer poly(3,4-ethylenedioxythiophene)/poly(styrenesulfonate) (PEDOT:PSS) increases from 1 S cm^{-1} in the dry state to a maximum value of 1000 S cm^{-1} with DMF.[156] Exposure to various solvents with a range of dielectric strengths yielded PEDOT:PSS conductivities that were non-linear with dielectric strength, akin to the data reported here for the Zn system. Portale et al. attributed this enhancement to increased polaron delocalization, evident from the intensified bipolaron optical feature following solvent addition. Lastly, the seminal study on the metallically conductive polymer poly(benzimidazobenzophenanthroline) documented a 200-fold decrease in conductivity when doped with ions, attributed to the formation of coulombic trap states.[39] In contrast to the results report here, solvent addition further induced a 1000-fold diminishment of conductivity, which the authors ascribed to a solvent-induced switch from a band-type to hopping mechanism of charge transport. Evidence for this claim pointed to an increase in the conduction activation barrier from 0.07 eV when dry to 0.63 eV in the presence of MeCN. In the case of the Fe system on the other hand, addition of solvent maintains the activation barrier, suggesting the charge transport mechanism remains band-type.

While ion–electron interactions have been well-documented in polymer systems, this report is the first to quantify the coupling strength of ion and electrons with electrochemical impedance analysis. Scheme 3.3 summarizes the model employed here and the expected ICCT behavior in band-type versus hopping-type systems. For a band-type material, such as the Fe analogue, we expect an impedance response shown in dashed purple, arising from the presence of cations creating a frequency-dependent resistance to the itinerant charges. Hence, we term

these materials "ion-limited conductors". For hopping-type systems, such as the Zn analogue, we expect the impedance response shown in dotted red, which resembles the behavior of an "ideal (non-coupled) mixed conductor", but with lower impedance across all frequencies and distorted semi-circular features induced by ion–charge concerted motion. The phase of the $Q_{coupling}$ CPE offers a means to distinguish between concerted hopping-type mechanisms ($n \sim 0.5$) versus band-type conduction impeded by ion interactions ($n \ll 0.5$). While traditionally reserved for analyzing lower-frequency regions of Nyquist plots, i.e., the diffusion "tail", such Warburg-like circuit elements have been employed to describe similar distortions present in porous polyamide films impregnated by water and electrolyte.[157] This analysis, in combination with solvent-dependent activation barriers, provides some of the first evidence of redox-type hopping in microporous materials, although this mechanism is commonly invoked for MOFs, such as Zr(3-hydroxy-2-[7-(4-carboxy-2-hydroxyphenyl)-1,3,6,8-tetraoxo-3,6,7,8-tetrahydro-1H-benzo[lmn][3,8]phenanthrolin-2-yl]benzoate).[46] Just as PCET provides lower-energy redox pathways in biological systems,[42] the observation of concerted charge transport in $TMA_2ZnGe_4S_{10}$ suggests high energy intermediates may be avoided in inorganic systems through ICCT. Mixed conductors feature widely in electrochemical technologies such as fuel cells, batteries, supercapacitors, and electrocatalysts, where ions conduct to balance charges in porous electrodes.[120] However, achieving both high ionic and electronic conductivity remains an outstanding challenge. For example, while $LiFePO_4$ possesses large solid state Li^+ diffusion coefficients (10^{-9} cm^2 s^{-1}) the low electronic conductivity (10^{-9} S cm^{-2}) necessitates conductive additives.[158,159] In contrast, traditional metal oxide electrodes possess higher electronic conductivities (10^{-4}–10^{-6} S cm^{-2}), but are often hindered by poor ionic transport.[160] These results

are therefore critical to the design and analysis of microporous materials for energy storage applications.

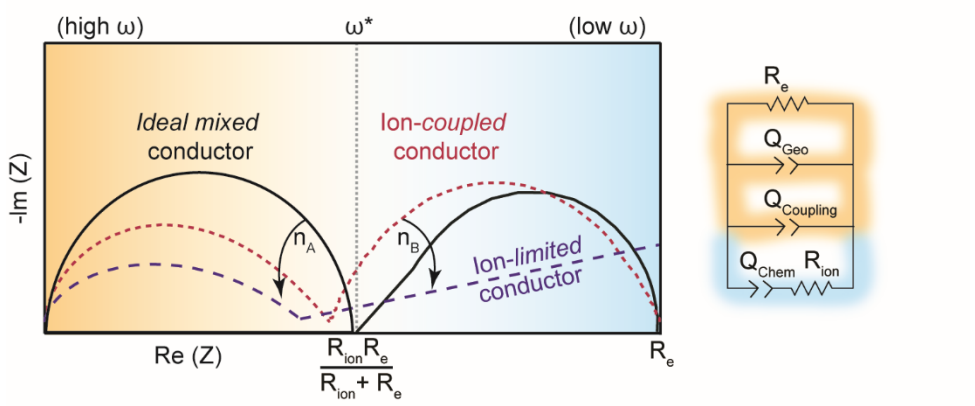

Scheme 3.3 Generalized impedance response for an ideal mixed conductor (black solid trace), an ion-coupled conductor (dotted red trace; $TMA_2ZnGe_4S_{10}$), and ion-limited conductor (dotted blue trace; $TMA_2FeGe_4S_{10}$).

Conclusions.

In conclusion, experimental comparison of $TMA_2FeGe_4S_{10}$ and $TMA_2ZnGe_4S_{10}$ reveals electrochemical signatures of ion-coupled transport and the mechanistic role of solvent in controlling band-type versus redox hopping conductivity in microporous materials. Non-linear responses in direct-current sweep voltammetry and chronoamperometry indicate diffusion-controlled hopping-type transport, whereas linearity supports the assignment of band-type conduction. Electrochemical impedance spectra point to concerted ion–electron hopping when constant phase elements fit to phase values of $n \sim 0.5$, whereas band-type electronic conduction appears impeded by ion interactions when $n \ll 0.5$. This analysis constitutes a novel method for quantifying ion-coupled conduction. Taken together, these signatures present a microscopic picture of how solvent controls ion-coupled transport in two distinct forms of conduction: whereas solvent improves electronic conductivity by screening ion–charge interactions in band-

type systems, it improves ambipolar diffusion in hopping-type systems by accelerating ion transport. Although developed with a model class of materials, these insights and methods unify observations of solvent- and electrolyte-dependent conduction already observed in wide-ranging classes of materials, while providing tools for designing electrochemical systems in general.

CHAPTER IV

IRON-BASED OXIDATIVE COUPLING ENABLES INTERLAYER CHARGE TRANSFER IN 2D VAN DER WAALS METAL-ORGANIC FRAMEWORKS

This section includes unpublished and coauthored material from the prospective manuscript McKenzie, J.; Pennington, L. P.; Kadota, K.; Ericson, T.; Cope, E.; Cozzolino, A. F.; Hendon, C. H.; Brozek, C. K. Interlayer Charge Transfer between 2D Van Der Waals Metal-Organic Frameworks.

In this chapter, the project idea was conceptualized by Jacob McKenzie, Kentaro Kadota, and Carl K. Brozek. The article was co-written by Jacob McKenzie, Doran Pennington, Carl K. Brozek, and Christopher H. Hendon. Experiments and analysis were performed by Jacob McKenzie, Kentaro Kadota, and Doran Pennington. Computations were performed by Elana Cope and Doran Pennington. Mössbauer spectra were collected and analyzed by Thomas Ericson under the supervision of Anthony F. Cozzolino.

Introduction.

Graphene, CrI_3, and other layered compounds derive their unique properties from weak interlayer van der Waals interactions that allow them to exist as atomically thin sheets. These 2D van der Waals (vdW) materials display distinct quantum mechanical behavior that finds use in a range of technologies including batteries,[161,162] catalysts,[163,164] superconductors,[165,166] topological insulators,[167] and photovoltaic devices.[168] However, strong interlayer interactions can also dominate the behavior of 2D vdW materials. For example, whereas monolayers of black phosphorous possess an optical band gap of 1.55 eV, the gap decreases to 1.05 eV for dimers and just 0.46 eV for bulk.[169] In addition, the already-high charge mobility of 286 $cm^2\ V^{-1}\ s^{-1}$ of black phosphorous when prepared as several stacked layers increases to 1000 $cm^2\ V^{-1}\ s^{-1}$ simply by

increasing the film thickness.[170] Similar layer-dependent phenomena manifest in tellurene (2D elemental Te) and certain metal chalcogenides including InSe, TiS_2, SnS, and the group-10 family (e.g., PtS_2 or $PtTe_2$).[171–175] On the other hand, various classes of layered materials, including the group-6 and group-7 transition metal dichalcogenides (e.g., WSe_2 and MoS_2) and ReS_2, display little if any dependence on layer thickness. This marked difference in interlayer interactions has been correlated with interlayer binding strengths, which range from a 'weak' 23 meV $Å^{-2}$ for graphene to a 'strong' 33 meV $Å^{-2}$ for black phosphorous.[176] Microscopically, "quasi-covalent bonding" between electron lone pairs in the so-called van der Waals gap between these layered compounds has been postulated as the origin of strong interlayer interactions. In fact, X-ray scattering measurements have detected electron density between TiS_2 sheets resembling S-S bonding interactions.[177] Beyond single-compound materials, interlayer interactions influence heterostructures as well. Practically, the often air unstable single-layer black phosphorous is stabilized though interfacing with hexaazatriphenylene derivatives, through exploitation of strong interlayer interactions.[178] Furthermore, band-edge offsets in heterojunctions such as $MoSe_2/WSe_2$ lead to interlayer excitons[179] with long recombination lifetimes and ultra-high charge carrier/thermal transport due to efficient polaron delocalization across layers.[169,180] Interlayer excitons find utility in advanced field-effect transistors,[181,182] photodetectors,[183,184] and quantum emitters.[185] Despite the importance of interlayer interactions in tuning 2D vdW behavior, little is known about their chemistry, in part due to the limited set of materials and synthetic methods for investigating them.

Here, we report a combined experimental-computational investigation into the tunable interlayer interactions of the 2D metal-organic framework (MOF) $Fe(SCN)_2(pyrazine)_2$. These 2D materials exfoliate under sonication to yield colloidally stable monolayer sheets that display an

intense and broad absorption band upon either chemical or electrochemical oxidation. Calculations indicate oxidation creates mixtures of Fe^{3+}/Fe^{2+} sheets that strongly interact with an anomalously large binding strength of ca. 83 meV/Å^2. Simulations also suggest that this absorption band arises from interlayer charge transfer between adjacent Fe^{3+}-SCN fragments with pyrazine across the vdW gap. Although this excitation resembles interlayer excitons, it occurs between materials that differ only in oxidation state rather than between heterodimers. Whereas interlayer excitons and binding strengths remain difficult to tune in conventional vdW materials,[186] the 2D vdW MOF is amenable to a range of chemical modification strategies. Experimentally, this interlayer charge transfer can be modulated with solvents of varying dielectric strength to screen the interlayer interaction, with electrolyte to separate the sheets, or by altering the chemical composition of the donor-acceptor components of the 2D MOF. Taken together, these results expand the types of interlayer interactions through synthetic tunability, while inching their orbital nature closer towards true covalent binding.

Results and Analysis.

In search of vdW materials with wide synthetic tunability, we targeted a subset of MOF structures due to their diverse compositions. Although most MOFs are electronic insulators, a growing family of atomically thin structures show the semiconducting or metallic behavior expected for vdW materials with strong interlayer interactions.[187–189] Indeed, recent reports indicate that charge mobility between sheets may exceed mobility within a 2D sheet.[190] However, studies of interlayer interactions between 2D MOFs remains largely limited to the "graphitic", honeycomb-type structures dominated primarily by π–π forces akin to graphene.[191] Inspired by the ability of the lone pairs in black phosphorous or TiS_2 to interact across the vdW

gap, we targeted the 2D layered MOF $Fe(SCN)_2(pyz)_2$ (Fe-SCN-pyz, Figures 4.1a and 4.1c), which features axial NCS^- groups.

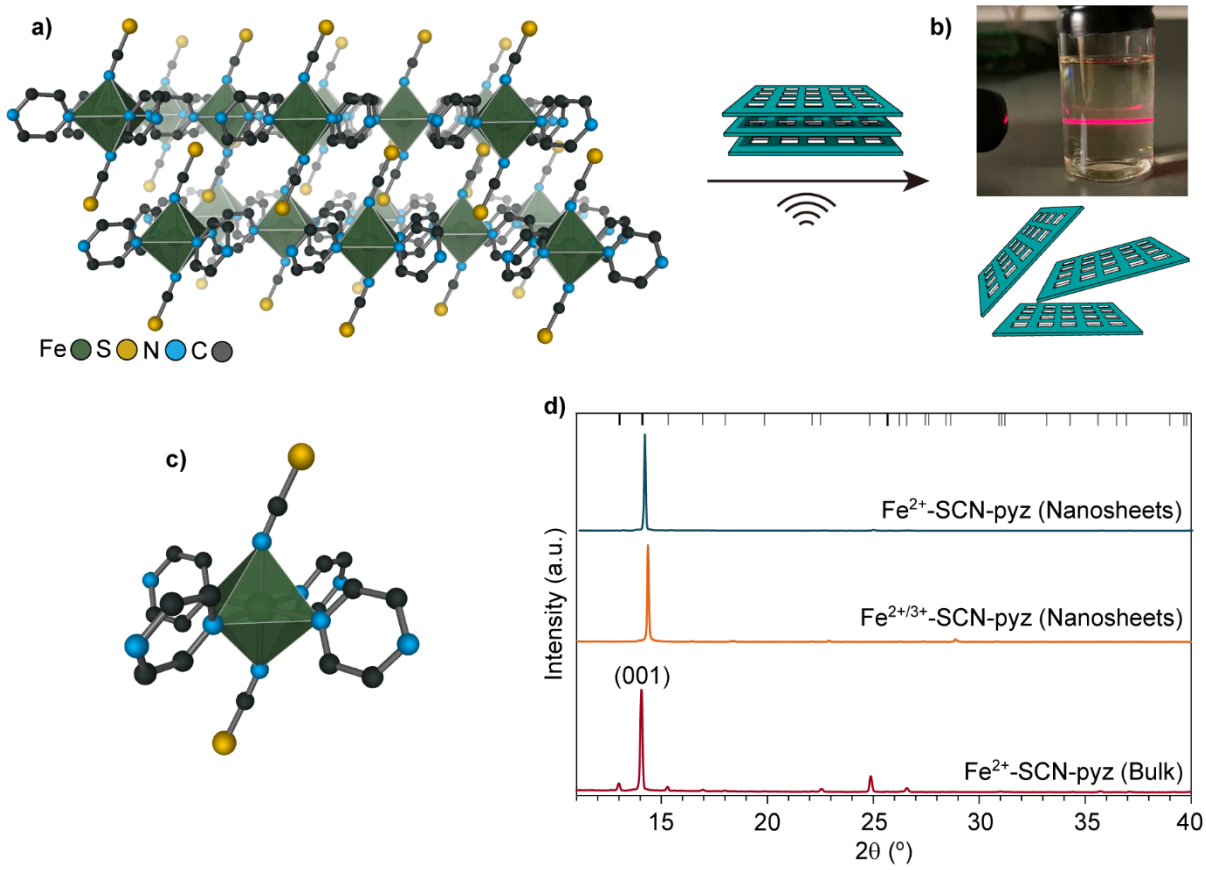

Figure 4.1 a) 3D crystalline structure for $Fe(SCN)_2(pyz)_2$. b) methanolic solution of exfoliated $Fe(SCN)_2(pyz)_2$ displaying the Tyndall effect. c) local octahedral coordination environment of iron centers. d) Powder x-ray diffraction patterns for the bulk and exfoliated 2D sheets pre and post atmospheric oxidation

We hypothesized that in a similar manner to lone pairs, the NCS^- groups would mediate vdW interactions and increase the accessible contact area between sheets. Similar pyrazine-bridged materials have exhibited semiconductor behavior.[192] The synthesis of the 2D layered $Fe(SCN)_2(pyz)_2$ (Fe-SCN-pyz) was accomplished following reported synthetic procedures.[193] The obtained microcrystalline powder was analyzed by powder x-ray diffraction (PXRD) and

the pattern matched expected reflections from the simulated structure (Figure 4.1d). The bright orange microcrystalline powder was exfoliated via ultrasonication in methanol to yield an optically clear yellow solution, which strongly displayed the Tyndall effect (Figure 4.1b). This nanosheet suspension was dried down to yield a light orange powder. The crystallinity of the material was maintained, with strong preferential orientation along the (001) crystallographic plane, indicating that periodicity existed primarily between sheets. These nanosheets were readily suspended within a variety of both polar and nonpolar solvents (Fig. C.4).

While the bright orange powder of the bulk structure in aerobic conditions is maintained indefinitely, the yellow methanolic solution of suspended nanosheets under aerobic conditions darkened and in the span of two weeks became a violet-colored solution. The violet-colored solution still strongly displayed the Tyndall effect, indicating sheets were still suspended after two weeks. This nanosheet suspension was dried down to yield a dark purple, nearly black powder. The crystallinity of this material was maintained with preferential orientation along the (001) crystallographic plane, with a slight shift of the (001) reflection indicating a relative contraction of interlayer spacing in the crystal lattice (Figure 4.1d). Figure 4.2a displays UV-Vis spectra of both the pristine nanosheets in anerobic conditions and after atmospheric exposure over two weeks suspended in MeCN. For both solutions, there are features at ~320 and ~260 nm assigned to $\pi - \pi^*$ and $n - \pi^*$ transitions in pyrazine respectively.[194] Also present is a feature at ~290 nm which is assigned to a $\pi - \pi^*$ transition in NCS^-.[195] However, while there is no absorption in the visible light under anerobic conditions, upon atmospheric exposure a broad absorption feature between 360-700 nm emerges.

In contrast to the bulk structure which was isovalent high spin Fe^{2+}, Mössbauer spectroscopy of nanosheets suspended in MeOH and exposed to atmospheric oxidation for two

months displayed two distinct doublets assigned to high spin Fe^{2+} and high spin Fe^{3+} (Fig. C.12). Interestingly, even with excessive atmospheric oxidation, the material is stabilized in a mixed valent state with 21% Fe^{2+} and 79% Fe^{3+}(Fig C.12). Further evidence of mixed valency was confirmed by DR UV-Vis-NIR of air oxidized nanosheets which displayed a broad band in the near IR, characteristic of an IVCT between Fe^{2+}-Fe^{3+} (Fig. C.6).

To further understand the interplay between Fe oxidation state and visible light absorption, spectroelectrochemistry was performed on a solution of nanosheets suspended in MeCN in anaerobic conditions. The electrochemical cell was a quartz cuvette with a platinum mesh working electrode, platinum wire counter electrode, silver wire pseudoreference electrode, and 0.1 M $TBAPF_6$ as the supporting electrolyte. Cyclic voltammetry measurements of the suspended nanosheets revealed a reversible redox feature centered at 400 mV vs. Ag that was assigned to the $Fe^{2+/3+}$ redox couple (Fig. C.9). To this solution, a constant 700 mV potential was applied while UV-Vis spectra were recorded in 2 minute intervals. Figure 4.2b displays the growing absorption feature at ~500 nm as an oxidizing potential is applied. The reversibility of this ~500 nm feature was explored by applying a subsequent 100 mV reducing potential after oxidizing, and the feature was bleached. Finally, 700 mV was applied once more and the ~500 nm feature returned (Fig. C.10).

These results suggest Fe^{2+} oxidation facilitates the emergence of the band in the visible light region. However, only the band around 440 nm can be directly attributed to Fe^{3+} and is assignable to a $SCN-Fe^{3+}$charge transfer. The band around 500 nm that also grows in with Fe^{2+} oxidation is instead assigned to a $NCS-pyz$ charge transfer, as assigned through supporting computations. For $Fe^{2+/3+}$-SCN-pyz, by simulating the oscillator strength of electronic transitions across the spectral window, individual bands which are responsible for optical absorption can be

investigated. The optical transition at ~510 nm displays charge density on NCS^- at the occupied level and charge density on pyrazine at the virtual level (Figure 4.3b). Critically, the virtual level is located on a different layer than the occupied level, demonstrating that the charge transfer occurs between layers. Furthermore, simulated absorption spectra for $Fe^{2+/3+}$-SCN-pyz monolayer and bulk shows the 510 nm transition is visible only in bulk, where charge transfer between layers is possible (Figure 4.3a).

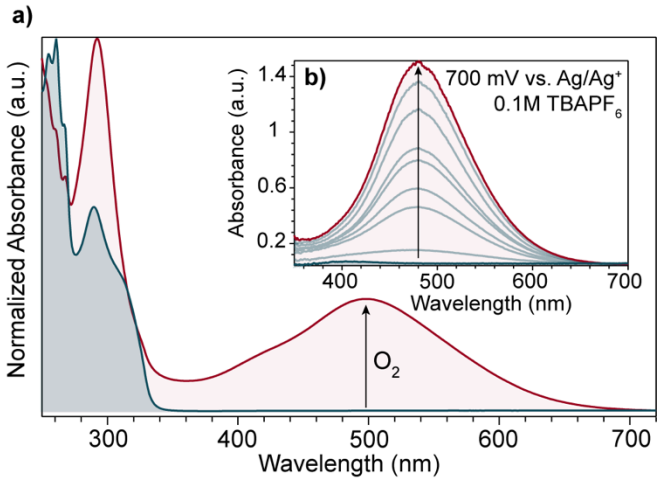

Figure 4.2 a) UV-Vis spectrum of exfoliated Fe-SCN-pyz nanosheets suspended in MeCN pre and post atmospheric oxidation. b) UV-Vis spectrum of exfoliated Fe-SCN-pyz nanosheets suspended in a 0.1M $TBAPF_6$ MeCN solution as 700mV vs Ag/Ag^+ is applied with a platinum mesh working electrode, platinum wire counter electrode, and silver wire pseudoreference.

The synergistic role of Fe^{2+} oxidation in promoting the interlayer charge transfer can be partially understood through simulations which support the experimentally observed contraction of the interlayer spacing upon oxidation [shift of (001) PXRD reflection]. Computations show that with Fe^{2+} oxidation the sheets in the layered structure become closer, with the distance between CNS^- and the closest N in pyrazine dramatically shortening from 4.09 Å to 3.47 Å. Furthermore, the interlayer coupling strength can be calculated by comparing the energy of the

$Fe^{2+/3+}$ layered structure to the energy of a $Fe^{2+/3+}$ monolayer. After normalizing the energy difference to the unit cell area in the covalent plane, a coupling strength of 83 meV/Å^2 is observed, which is higher than any previously-reported layered 2D material.[196]

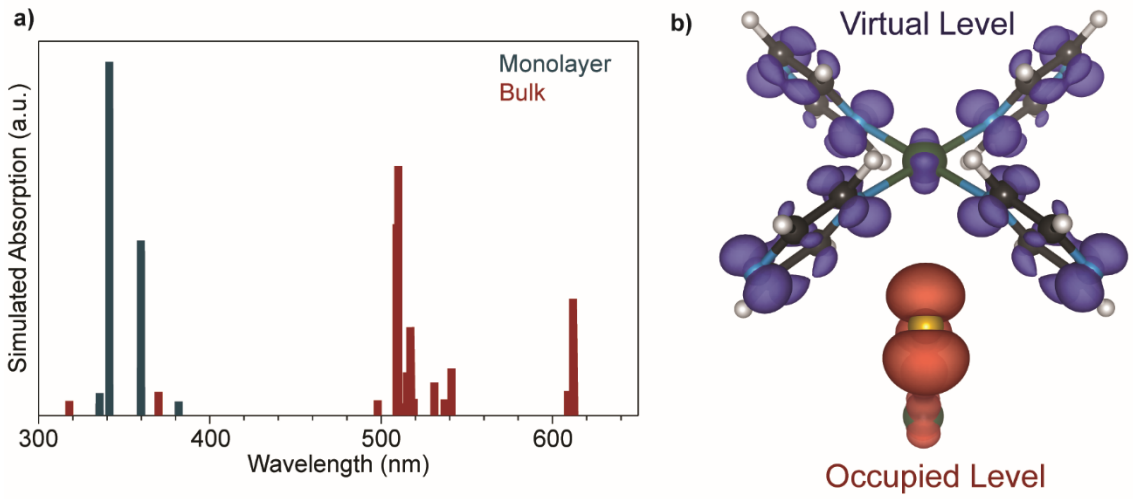

Figure 4.3 a) Simulated transitions and relative absorption strength for monolayer and bulk $Fe^{2+/3+}$-SCN-pyz. b) Occupied level orbitals and virtual level orbitals for the electronic transition at ~510 nm.

In addition to reduced interlayer distances, Fe^{2+} oxidation also distinctly alters the chemistry of the axial NCS^-. Fourier transform infrared spectroscopy for the pristine Fe^{2+}-SCN-pyz shows a characteristically strong absorption at 2050 cm^{-1} assigned to the C−N stretch in N−bound thiocyanate to Fe^{2+}. However, upon atmospheric exposure, the stretch broadens and splits into two bands of roughly equal proportions. The new band at 2140 cm^{-1} is assigned to N-bound thiocyanate to Fe^{3+}. The increase in the C−N bond energy for NCS^- bound to Fe^{3+} vs Fe^{2+} is explained by the reduction in π backbonding when Fe^{2+} oxidizes, leading to a strengthening of the C−N stretch in NCS^-. In addition, there is also a feature at 2020 cm^{-1} assigned to free NCS^-. Displaced NCS^- serves as a charge balancing anion and is generated from OH^- displacement upon atmospheric oxidation. This bound OH^- is observable in a moderately sharp IR stretch at

~3400 cm^{-1} (Fig C.15a). In summary, Fe^{2+} oxidation promotes the emergence of interlayer charge transfer both through a modulation of the Fe−NCS bond strength and a contraction in interlayer distance.

We next explored the solvent dependence of the interlayer charge transfer. Given the dielectric sensitivity of NCS^- seen in the UV-Vis response of the isostructural Co-SCN-pyz, we expected the interlayer charge transfer to have distinct solvatochromic effects (Figure 4.4a).[197]

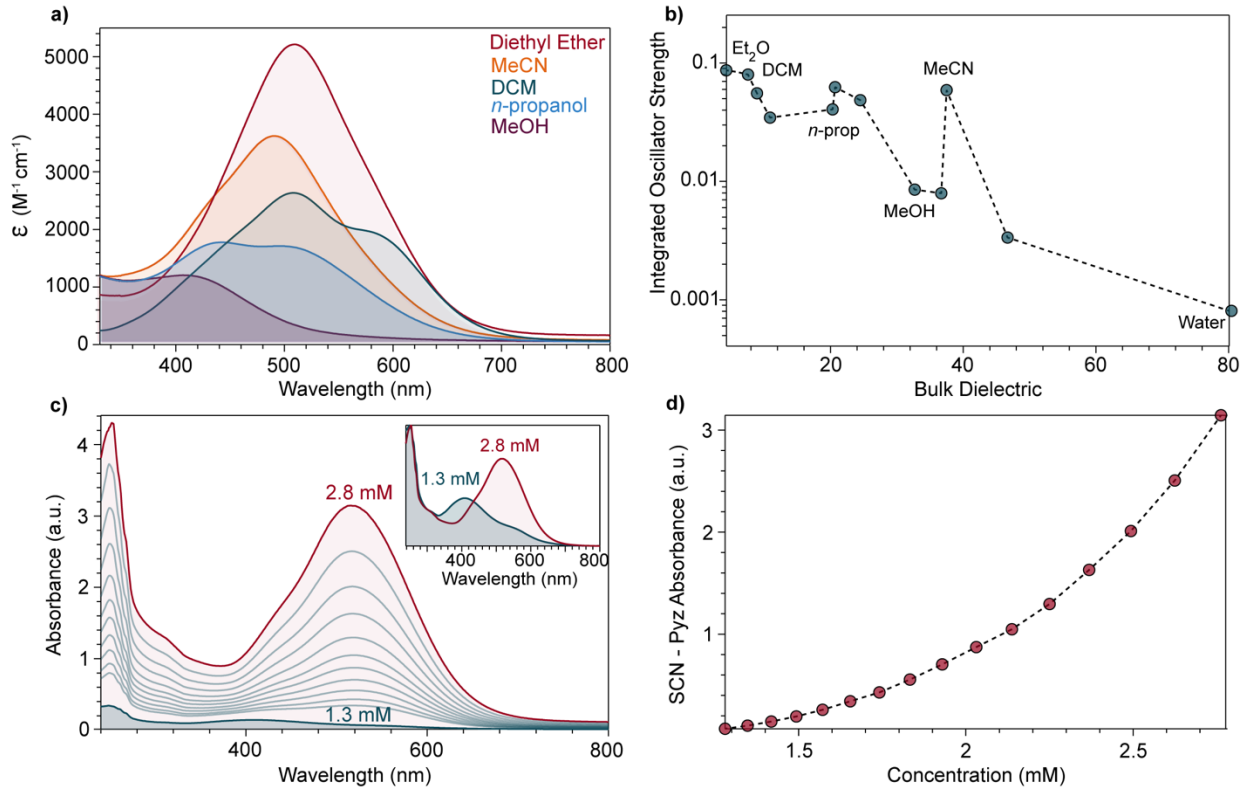

Figure 4.4 a) UV-Vis spectrum of atmospherically oxidized Fe-SCN-pyz nanosheets suspended in diethyl ether, MeCN, DCM, n-propanol, and MeOH at 184μM. b) Oscillator strength sum across the visible light bands vs solvent dielectric. c) Concentration dependence of atmospherically oxidized Fe-SCN-pyz nanosheets suspended in MeOH. d) Absorption at ~500nm as a function of concentration.

Indeed, in low dielectric solvents the charge transfer is intense and red shifted (such as Et_2O, THF, and DCM). The weaker solvent−SCN interactions strengthen interlayer interactions,

facilitating interlayer charge transfer through increased aggregation and/or increased electron density on NCS^-. In contrast, high dielectric solvents blue shift and weaken interlayer charge transfer, with the band nearly unobservable in protic solvents like MeOH. Strong solvent−SCN interactions reduce interlayer charge transfer through weakening interlayer interaction and/or reducing electron density on NCS^-.

Considering the previous results, we postulated that conditions that enable aggregation should modulate interlayer charge transfer. With this in mind, we theorized that there should be concentration dependent effects with a positive deviation from Beer-Lambert's law at sufficiently high concentrations.[198] Indeed, suspensions in MeOH at 184 μM in Figure 4.4a. only display a weak band around 400 nm attributed to the $SCN - Fe^{3+}$ charge transfer. When the sheets are suspended at the far higher concentration of 2800 μM, interlayer charge transfer is readily observed. (Figure 4.4c). The concentration dependence for the interlayer charge transfer absorption indeed has a positive deviation from Beer-Lambert's law at higher concentrations, supporting aggregation-assisted charge transfer (Figure 4.4d).

The interlayer charge transfer was further modulated through intercalation chemistry, with the expectation that a sufficiently large noncoordinating anion would disrupt interlayer coupling and charge transfer. Figure 4.5a shows the UV-Vis spectrum of air oxidized sheets suspended in MeCN as $TBABF_4$ is added to the solution. Indeed, the interlayer charge transfer blue shifts and decreases in intensity with increasing electrolyte addition, while monolayer features around ~300nm attributed to isolated NCS^- and pyrazine bands increase in intensity.

Furthermore, as expected, the size of the intercalating anion plays a crucial role in modulating interlayer coupling. When the larger anion PF_6^- is added to a nanosheet suspension from $TBAPF_6$, a comparatively minor decrease in the interlayer charge transfer band is observed

(Figure C.14b). This is understood by the bulkier PF_6^- proving less effective at intercalating between the sheets to disrupt interlayer electronic communication.

Conversely, when the smaller anion NO_3^- in $TBANO_3$ is added to nanosheet suspensions both the interlayer charge transfer and $SCN - Fe^{3+}$ bands are bleached by comparatively small equivalents (Figure C.14a). Fourier transform infrared spectroscopy reveals that while there are no significant changes to the IR stretches assigned to N−bound thiocyanate to either Fe^{3+} or Fe^{2+} with $TBABF_4$ or PF_6^- addition, with $TBANO_3$ addition, the IR stretch at 2140 cm^{-1} shows a large decrease (Figure C.15). This result indicates partial ligand replacement of NCS^- with NO_3^- preferentially on Fe^{3+} sites.

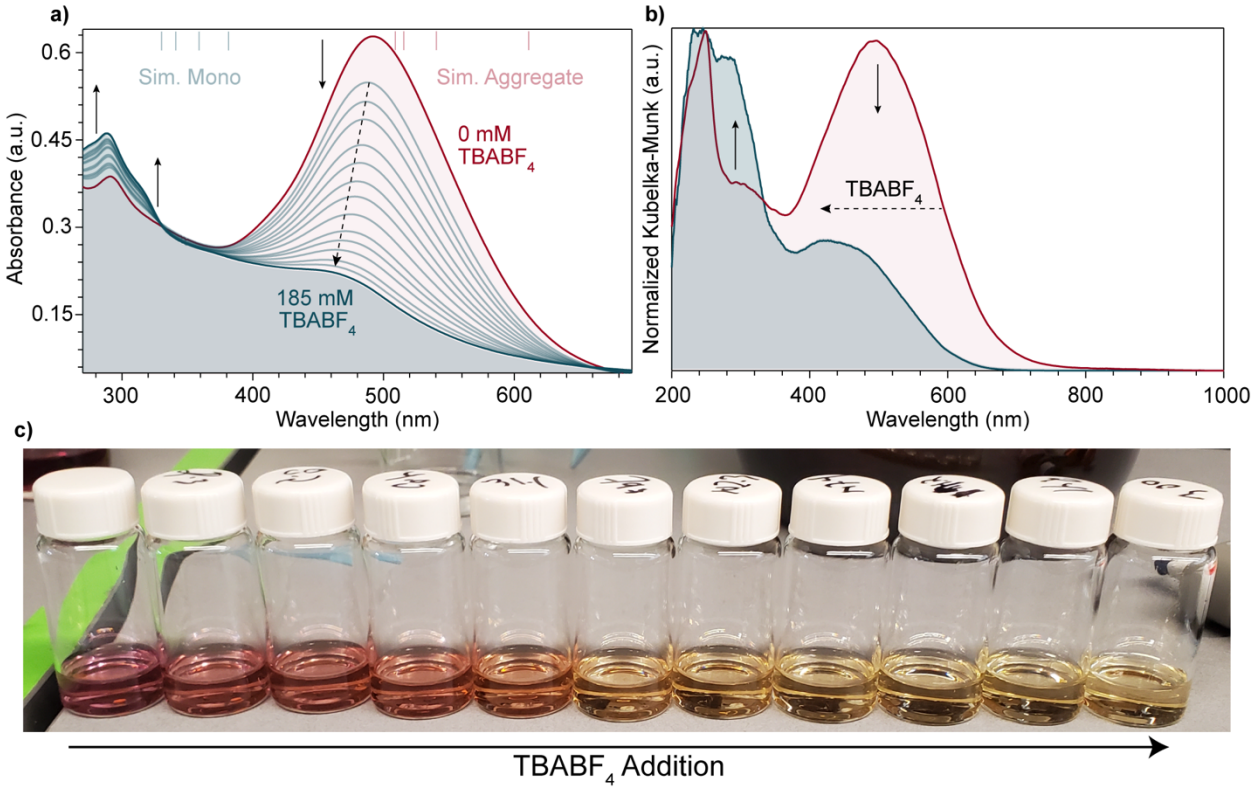

Figure 4.5 a) UV-Vis spectrum of atmospherically oxidized Fe-SCN-pyz nanosheets suspended in MeCN as $TBABF_4$ is titrated in (tick marks at top of graph denote the most intense simulated absorptions for mixed valent aggregates and monolayers). b) DR UV-Vis of atmospherically oxidized Fe-SCN-pyz before and after saturating the pellet with a 1M MeCN solution of $TBABF_4$. c) Photographic depiction of the solution color change as $TBABF_4$ is added.

The NCS^- displacement further stresses the importance of this ligand in mediating the charge transfer.

However, with all electrolytes added, the feature assigned to unbound NCS^- at 2020 cm^{-1} is unobservable, which indicates successful incorporation of BF_4^-, PF_6^-, or NO_3^- into lattice through displacement of the charge balancing NCS^- (Figure C.15). In the solid state, the same trends apply. The DR UV-Vis spectra seen in Figure 5.6b showcases that upon addition of $TBABF_4$ to oxidized nanosheet solutions, anion incorporation persists after recovery from solution. After electrolyte addition, there is a decrease in the band gap energy and a relative increase in higher energy absorptions, consistent with solution state UV-Vis results. In summary, these results suggest that the large electrolyte anions can intercalate between sheets and displace charge balancing NCS^-. The anion sizes are sufficiently large to force the sheets far enough apart that interlayer coupling is too weak to enable interlayer charge transfer.

Finally, given the synthetic landscape Fe-SCN-pyz affords with two potential linker substitutions, a variety of material analogs were synthesized to observe the significance of both NCS^- and pyz on facilitating interlayer charge transfer (Figure 4.6a). To tune the electronic nature of the donor orbitals the similar 2D net materials $Fe(Cl)_2(pyz)_2$ and $Fe(SeCN)_2(pyz)_2$ were synthesized. The successful synthesis of both was confirmed by PXRD (Figures C.1 and C.3). For Fe-Cl-pyz, upon atmospheric oxidation and suspension in THF no interlayer charge transfer is observed (Figure 4.6b). However, we do observe a strong band around 360 nm, which we instead assign to a $\mathrm{Cl} - Fe^{3+}$ charge transfer. For Fe-SeCN-pyz, there is a very weak absorption present around ~530 nm assigned to a $\mathrm{NCSe} - \mathrm{pyz}$ charge transfer, and a stronger absorption around 460 nm which we assign as a $\mathrm{SeCN} - Fe^{3+}$ charge transfer.

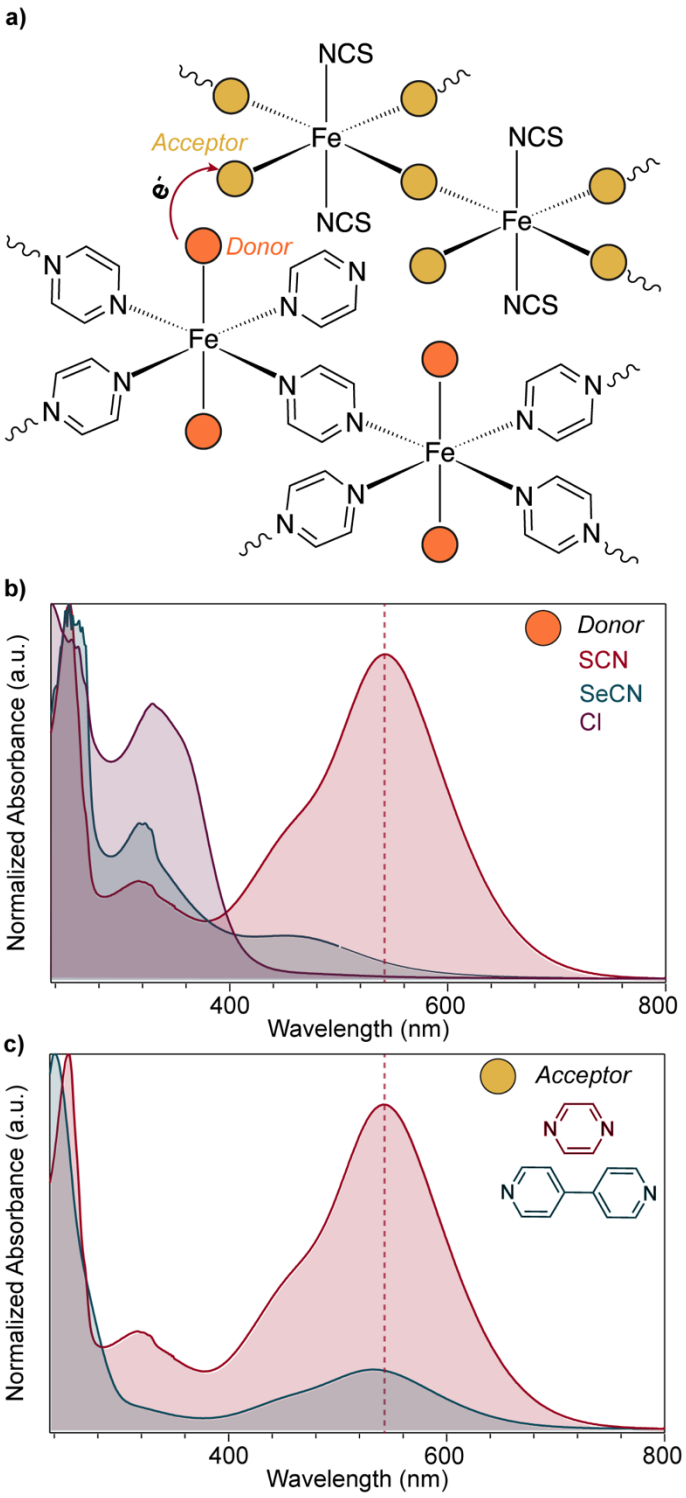

Figure 4.6 a) Depiction of the of the donor and acceptor atoms in the interlayer charge transfer. b) UV-Vis of atmospherically oxidized Fe-SCN-pyz and Fe-SCN-4,4'-Bipyridine suspended in THF. c) UV-Vis of atmospherically oxidized Fe-SCN-pyz, Fe-SeCN-pyz, and Fe-Cl-pyz suspended in THF.

In addition, the acceptor orbitals were tuned by synthesizing $Fe(SCN)_2$(4,4'-Bipyridine)$_2$. Upon desolvation at high heat and vacuum, the 2D net structure was confirmed by PXRD (Figure C.2). Unlike Fe-Cl-py and Fe-SeCN-pyz, upon atmospheric oxidation and suspension in THF a purple color was observed. Solution state UV-Vis seen in Figure 4.6c reveals that the interlayer $NCS-4,4'Bipyridine$ charge transfer is far weaker and slightly blue shifted relative to the $NCS-pyz$ charge transfer.

Discussion.

These results demonstrate one of the first reports on interlayer coupling in 2D MOFs. In summary, Fe^{2+}-SCN-pyz nanosheets in solution exhibit minimal interlayer coupling with a band gap of 3.9 eV, compared to 2.6 eV in bulk. However, with oxidation to $Fe^{2+/3+}$-SCN-pyz there is a strong interlayer stabilizing interaction, shifting the band gap from 3.9 eV to 2.4 eV in THF. This coupling along with proper donor and acceptor orbital alignment leads to an intersheet charge transfer. Fe oxidation promotes greater interlayer coupling by both reducing the interlayer distance as seen computationally and by PXRD, and by increasing electron density onto S in NCS^- as observed with FTIR. The charge transfer functions as an optical indicator for interlayer coupling, allowing for a systematic study into modulating interlayer interactions. Parameters such as the dielectric medium, intercalating species, and composition had profound effects on such interlayer interactions.

When considering solvent effects, preferential NCS−solvent interactions were exhibited in polar protic solvents leading to a substantial reduction in the interlayer charge transfer. Moreover, with nonpolar solvents interlayer interactions were strengthened with interlayer charge transfer extinction coefficients as high as ~5000 $M^{-1}cm^{-1}$. Through-space charge transfer in other MOF structures has only observed extinction coefficients between 20-110 $M^{-1}cm^{-1}$,[199,200] and in 2D vdw heterostructures as high as 1200 cm GW^{-1}. However, the dielectric medium only controlled interlayer coupling in the dilute limit as high concentrations of suspended nanosheets even in MeOH strongly displayed interlayer charge transfer. The interlayer coupling can be further tuned through the post-synthetic intercalation of different electrolyte species. Smaller noncoordinating anions such as BF_4^- were most effective at disrupting interlayer communication and bleaching interlayer charge transfer. Intercalation of molecular agents has been explored in

weakening interlayer interactions in MoS_2, albeit with far larger electrolyte anions that dramatically alter the crystalline structure and performance of the material.[201] Finally, the sensitivity of the interlayer charge transfer to material composition was explored by subjecting various analogs to similar conditions. The NCS^- is crucial in dictating the charge transfer as its axial position in the so-called vdw spacing mediates interlayer interactions. Substitutions for Cl and SeCN in Fe-SeCN(Cl)-pyz exhibited minimal if any interlayer charge transfer. Whereas, when 4,4'-Bipridine is substituted for pyrazine interlayer charge transfer is present, albeit less pronounced, related to changes in dynamics and electronic structure associated with 4,4'-Bipyridine.[202]

Although through space charge transfer has been observed in MOFs its often in rigid insoluble 3D structures where judicial ligand placement is required to promote $\pi - \pi$ interactions, which mediate charge transfer.[199,200,203,204] In contrast, this study explores charge transfer in MOFs mediated by lone pair interactions. While such behavior is largely unexplored in MOFs, lone pair-mediated interactions have been widely considered in 2D transition metal dichalcogenides and elemental phosphorous/tellurium, to describe anomalous interlayer interactions.[169,171,173,196,205–207]

In contrast to the traditional 2D vdw materials which are basically atomically flat, Fe-SCN-pyz has pendant NCS^- directed into the interlayer spacing, endowing the material with even greater interactive surface area. This combined with Fe induced oxidative coupling leads to a massive interlayer coupling strength of 81 meV/Å^2. This is the largest interlayer coupling strength ever reported with strongly interacting 2D vdw materials typically having values between 27 – 59 meV/Å^2.[196]

The massive interlayer coupling manifests in an intense optical absorption between interlayer orbitals. Interlayer coupling induced charge transfer while extensively studied in 2D materials has been limited primarily in-scope to 2D heterostructure devices and films, where the charge transfer is between two different monolayers with proper band alignments, that being the VBM and CBM lying in different material monolayers.[208–212] In addition, bilayers of one 2D van der waal material can exhibit charge transfer via twisiting a layer relative to the other, as explored commonly with graphene.[213] In contrast to these traditional 2D vdw materials, Fe^{2+}-SCN-pyz can be post-synthetically oxidized to a mixed valent $Fe^{2+/3+}$-SCN-pyz , promoting interlayer charge transfer between sheets via differing oxidation states as opposed to differing band edges. This fact allows for solution processability of the charge transfer material and unprecedented solution-state characterization of 2D vdw interlayer charge transfer. We found that proper orbital alignment and orbital energies is critical to realizing charge transfer with slight changes to orbital interactions through solvent dielectric, ligand substitution, and interlayer spacing completely bleaching interlayer charge transfer.

Conclusions.

In conclusion, through Fe redox modulation, this study showcases the emergence of a novel interlayer charge transfer band from $NCS-pyz$ meditated by a massive interlayer coupling strength. The coupling strength was explored for the first time in solution, where solvents that interacted favorably with the pendant NCS^- groups could effectively turn the interlayer charge transfer on and off. Furthermore, the interlayer coupling had strong anion sensitivity with small amounts of NO_3^- and BF_4^- weakening interlayer charge transfer through physical separation of sheets. Finally, substitution of NCS^- for $NCSe^-$ and Cl^- and 4,4'-bipyridine for pyrazine revealed the critical importance of axial NCS^- in mediating electronic

communication between layers. Taken together, this seminal study describes the key parameters that control interlayer coupling and through-space charge transfer, while cementing 2D vdw MOFs as ideal platforms for studying these emergent phenomena. These results provide new insights into future design of 2D vdw materials and optoelectronic devices where strong interlayer coupling and charge transfer is desired.

CHAPTER V

CONCLUDING REMARKS

This dissertation sheds light on fundamental questions of charge transport in high surface area and microporous conductors and provides several new material frameworks for studying emergent conduction phenomena. In particular, for the design and study of next-generation energy storage devices.

In Chapter II, we synthesized a forgotten but diverse class of materials known as Open-Framework Metal Chalcogenides (OFMCs). The highly covalent metal-sulfur bonds engender materials with dispersive bands and high charge mobility, with metal oxidation and sulfur vacancies introducing p-type charge carriers. $TMA_2FeGe_4S_{10}$ (Fe-S) stands as the most conductive OFMC ever reported, owing to its unique redox properties, which supports a readily accessible $Fe^{2+/3+}$ redox couple and stabilizes sulfur-based vacancy defects. Furthermore, we found that unlike typical framework-based conductors, the conduction mechanism in Fe-S is band-type. In Chapter III, we leveraged the ideality of the charge transport in Fe-S (band-type) Zn-S (redox hopping), and the nanoconfined TMA^+ cations within the micropores of the structure, to study interfacial interactions of mobile and immobile ions on charge transport. We found that solvent improves charge transport with DC conductivity scaling roughly with dielectric strength for both materials, but for mechanistically different reasons. In Zn-S, solvent facilitates redox hopping through improved ion diffusion, leading to a ~100,000 improvement in conductivity. In Fe-S, solvent improves charge mobility via dielectric screening of coulombic trap states between iterant charges and TMA^+. Furthermore, a novel electrochemical impedance model described distinctly local interactions between TMA^+ and charges. In particular, a CPE circuit element was employed that described the mean-field attraction between TMA^+ and

charges. From this model, Zn-S was described as an ion-coupled mixed conductor with ions and electrons moving in a concerted motion analogous to proton-coupled electron transport. Furthermore, Fe-S was described as an ion-limited conductor, with ions acting as charged trap states that decrease charge mobility. Finally, in Chapter IV, interfacial interactions were explored in 2D MOF Fe-SCN-pyz. We found massive interlayer interactions from axial NCS^- that endow the sheets with massive interactive surface area, and Fe oxidation which modulates the electronic structure of NCS^- and the communication between sheets. This massive interlayer interaction along with mixed charge states across layers, results in an interlayer charge in a solution-processable homostructure. This allowed for unprecedented control of the charge transfer and demonstrated that the interfacial chemistry between NCS^- and its environment dramatically affected charge transfer. In summary, high dielectric strength solvents completely nullified charge transfer whereas low dielectric solvents greatly enhanced it. Furthermore, electrolyte ions could be titrated into the solution, which nullified through-space charge transfer to varying extents depending on the anion identity.

Taken together, this dissertation describes the impacts of solvent and chemically inert ions on charge transport/transfer at the interfacial extremes of microporous conductors and 2D vdw materials decorated with axial ligands. To summarize, solvent and electrolyte intrusion into micropores dramatically affects charge transport in open framework metal chalcogenides, and solvent and electrolyte interactions with NCS^- in a 2D vdw MOF completely dictates interfacial charge transfer. In addition, Fe has an important role in the results of this dissertation. For example, the use of Fe in $TMA_2FeGe_4S_{10}$ realizes a novel microporous conductor, with unprecedented band-type conduction. In addition, the use of Fe in $Fe(SCN)_2(pyz)_2$ facilitates

mixed charge states in a 2D vdw material to allow unprecedented charge transfer across the vdw junction, in a solution-processable homostructure.

This dissertation answers fundamental questions of charge transport and charge transfer at the interfacial extreme of 2D materials/microporous conductors and ascribes further importance to Fe-based framework conductors. These materials, due to their high surface areas, have been identified as the ideal material class for next-generation energy storage technologies. In these technologies, solvent and electrolyte ions are critical to their function and directly dictate their performance, especially when considering nanoconfinement in microporous environments. Therefore, the results of this dissertation are critical in the design and operation of these advanced technologies, with advanced energy storage technologies imperative in complete decarbonization of society and stunting our alarming global temperature shifts.

APPENDIX A: SUPPLEMENTARY INFORMATION FOR CHAPTER 2

Experimental Methods.

Materials. All commercial chemicals were used as received unless stated otherwise. Germanium powder (99.99%, Sigma Aldrich), sublimed sulfur powder (99%, Strem), tetramethylammonium hydroxide pentahydrate (95%, Oakwood), selenium powder (99.7%, Acros Organics), iron(II) chloride tetrahydrate (98%, Alfa Aesar), iron(II) chloride (anhydrous, Strem), nickel(II) chloride hexahydrate (98%, Alfa Aesar), cobalt(II) acetate tetrahydrate (98%, Alfa Aesar), zinc(II) acetate dihydrate (98%, Sigma Aldrich), iron(III) chloride hexahydrate (97%, Strem), manganese(II) chloride tetrahydrate (ACS grade, Baker), zinc(II) nitrate hexahydrate (98%, Sigma Aldrich), barium sulfate (97.5%, Baker), N,N-dimethyl-p-phenylenediamine (97%, Sigma Aldrich), ferrocenium hexafluorophosphate ($FcPF_6$, 97%, Sigma Aldrich), naphthalene (99%, Sigma Aldrich), hydrochloric acid (reagent grade, Sigma Aldrich), hexanes (n-hexane, 45%, Oakwood Chemical), tetrahydrofuran (SPS grade, Oakwood Chemical), and ethanol (200 proof, Decon Labs). Solvothermal syntheses were conducted in autoclave PAAR bombs in Yamato Convection oven unless stated otherwise.

Characterization. Sample purity and crystallinity was verified by powder X-Ray diffraction (PXRD) with a Bruker D2 Phaser benchtop diffractometer. Diffuse reflectance UV-Vis was performed on a Perkin Elmer Lambda-1050 UV/Vis/NIR spectrophotometer with Harrick Scientific Praying Mantis Diffuse Reflection (DRP) accessory and PMT, InGaAs, and PbS 3- detector module. All samples were diluted with ground barium sulfate. Reflectance UV-Vis spectra were collected in the range of 200-2000 nm with 2-nm resolution unless stated otherwise.

Pressed pellet conductivity measurements. Pressed pellets were prepared by compressing ~30 mg of powders in a modified KBr pellet press die set with a hydraulic press at 2000psi for 30 minutes. The pellet press die set had tinned copper wires affixed to both sides with silver paint and epoxy. Electrical contact was made by pressing a pellet with the modified die set with the stainless-steel circular ends acting as the 2 electrodes. Direct-current (DC) conductivities were determined from the slopes of current-voltage (I-V) curves collected with a GAMRY Instruments Interface 5000E potentiostat, along with the electrode area (0.402 cm2) and pellet thickness, according to the equation below (where C is the slope of the I-V curve and m is the pellet thickness):

$$DC_{\sigma}: \frac{C * m}{0.402}$$

Samples were voltammetrically swept at 2 mV/s between −0.2 (−0.1) and 0.1 V while compressed at 1500 psi. Temperature-dependent measurements were conducted in a similar fashion with samples kept at fixed temperatures in a Yamato Convection oven.

Pressed Pellet EIS Measurements. Using the same setup for pressed pellet measurements and preparation, AC measurements were run with a DC voltage of 0 V with an AC amplitude of 150 mV from 2 MHz to 0.1 Hz.

^{57}Fe Mössbauer Spectroscopy. All samples were characterized by a SEE Co. ^{57}Fe Mössbauer spectrometer equipped with a Janis SVT-400 cryostat. The samples were prepared under a nitrogen atmosphere by placing up to 30 mg of fine powder in a 14.5 mm Teflon cup with a Teflon plunger pressed into the cup to hold the sample. Data were collected until the signal-to-noise was deemed sufficient for meaningful analysis. This was dependent on the amount of sample loaded and the intensity of the source but was typically longer than 1 week. Samples were maintained under a nitrogen atmosphere for the duration of the experiment.

Calibration of the instrument was performed using a standard iron sample provided by SEE Co. The data were analyzed using the Mössbauer spectral analysis software WMOSS4[214] written by Tom Kent and recently developed by Ion Prisecaru. The raw data were folded and calibrated using the iron standard supplied to us. The folded data were then fit to an appropriate model. We used two models to fit the data for this paper: the first is used for a pair of quadrupole doublets, and the second model is for a single quadrupole doublet. We used these models to refine the relevant parameters such as the shift of the quadrupole peak and the relative area of the peaks.

SQUID Magnetic Susceptibility Measurements. Direct current (DC) susceptibility measurements were performed with a Quantum Design MPMS-XL SQUID magnetometer. Samples were prepared under an inert atmosphere as finely ground microcrystalline powders sealed in polyethylene baggies. Dc susceptibility measurements were performed at fields of 1000, 5000, and 10000 Oe. Ac susceptibility measurements were performed at zero DC field with an AC field of 4 Oe. The data were corrected for the diamagnetic contributions of the sample holder and the sample itself through the use of Pascal's constants.[215] Magnetization curves (M vs. H) were recorded at 100 K from 0 to 3 T to check for the presence of unwanted ferromagnetic impurities.

XPS Measurements. X-ray photoelectron spectroscopy was performed on a ThermoScientific ESCALAB 250 X-ray photoelectron spectrometer. A survey scan was used to determine elements present before high-resolution scans were done on elements of interest. The binding energy scale was shifted to the hydrocarbon peak given by the tetramethyl ammonium cations residing within the frameworks.

$TMA_2FeGe4S_{10}$ Desulfurization. To 50 mg of $TMA_2FeGe_4S_{10}$ prepared *air-free* 2 ml of sparged DI water was added, and a paste was formed. The still wet paste was then heated at 160

°C under dynamic vacuum for ~12h. The resulting dark brown solid was then removed from heat and left under dynamic vacuum for another ~24h to remove any absorbed H_2S.

Methylene Blue Assay for H2S generation in $TMA_2FeGe_4S_{10}$. Following a procedure adapted from Bolton G. S. et. al.[216] 200 μL of a 300-mM solution of iron(III) chloride hexahydrate in 1.2 M HCl, 200 μL of a 200-mM solution of N,N-dimethyl-p-phenylenediamine in 7.2 M HCl, and 100 μL of a 1% (w/v) aq. solution of zinc(II) acetate dihydrate were added to a 4-ml vial and gently shaken to stir. In another vial, 50 mg of $TMA_2FeGe_4S_{10}$ prepared *air-free* was suspended in 5 ml of sparged DI water by ultrasonication. The sample was then aged in an 80 °C fixed temperature oven for 2h. Afterwards, the solution was allowed to reach room temperature before a 200 μL spike of the solution was added to the methylene blue cocktail solution and shaken gently. An instant deep blue color appeared that was allowed to develop for 1 hour before collecting a solution-phase UV-Vis spectrum of the reaction mixture.

Chemical Oxidation of $TMA_2MGe_4S_{10}$ (M = Mn, Co, and Ni). Under an inert nitrogen atmosphere, 26 mg (0.78 mmol) of $FcPF_6$ was dissolved in 4 mL of THF and left to stir for ~2 h. Fifteen milligrams of each framework was added to the respective vials and 1 mL of the $FcPF_6$ solution was added to each. The vials were left to stir overnight. The frameworks were then washed with THF (10 mL × 3) and then dried under dynamic vacuum at room temperature.

Chemical Oxidation of $TMA_2FeGe_4S_{10}$. The ferrocenium tetrafluoroborate stock solution was made by dissolving 0.3164 g of ferrocenium tetrafluoroborate in 10 mL of THF and left to stir overnight. $TMA_2FeGe_4S_{10}$ powder was suspended in 5 mL of THF and left to stir. To the stirring solution, 1 mL of the stock ferrocenium solution was added (1.5 equiv) to one vial and 275 μL (0.5 equiv) to another vial. The reactions were left to react for 36 h. To wash them,

the solids were centrifuged down under a positive N_2 pressure. The solids were then washed with THF (30 mL × 2) and hexanes (30 mL × 1).

Potential-Dependent Conductivity. A 0.1 M $TBAPF_6$ solution was prepared by dissolving 3.87 g of $TBAPF_6$ in 100 mL of acetonitrile under a positive nitrogen pressure. A three-electrode electrochemical cell was constructed (see Schematic A.1) by immersing a pressed pellet of $TMA_2FeGe_4S_{10}$ into a sparged electrolyte solution (0.1 M $TBAPF_6$ in acetonitrile). An insulated copper wire was appended to one side of the pellet by silver paint, with epoxy insulating the electrical contact to the pellet. An $Ag/AgNO_3$ pseudo-reference was utilized as well as a carbon counter electrode. A standard three-contact experiment was set up using a GAMRY Instruments Interface 5000E potentiostat. EIS measurements were collected with 25 mV AC perturbations at different DC voltages (−0.3–0.9 V) relative to the open-circuit potential. The bulk resistance of the pellet was determined by the low-frequency near-intersection on the *x*-axis of the Nyquist plot.

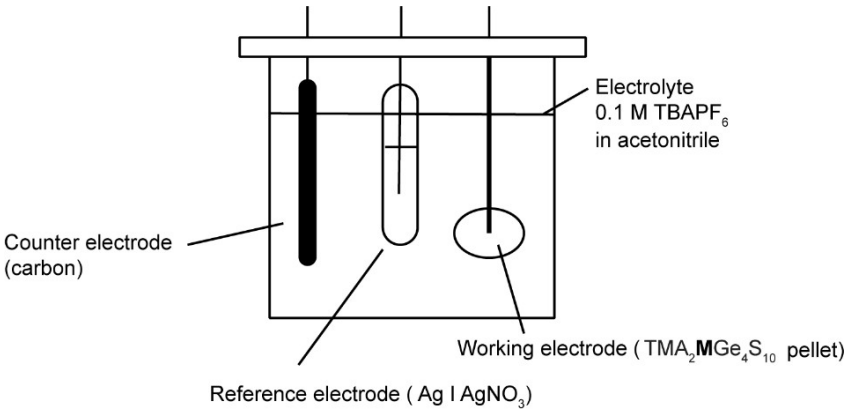

Scheme A.1 Depiction of electrochemical cell used for potential dependent conductivity measurements.

Synthetic Procedures

$TMA_4Ge_4S_{10}$. Following a procedure adapted from O. M. Yaghi et.al.,[68] germanium powder (1g, 13.76 mmol), sulfur powder (1.766 g, 6.88 mmol), and water (7.439 g, 412.8 mmol) were added to a Teflon Parr bomb. While slowly stirring this mixture with a glass rod, tetramethyl ammonium hydroxide pentahydrate (4.990 g, 27.53 mmol) was added and then the Parr bomb was sealed and placed in a fixed-temperature oven at 150 °C for 15h. The resulting yellow solution was vacuum filtered to remove unreacted germanium and then ~500 ml of acetone was added to induce precipitation of a white solid. The white powder was washed with acetone (20 ml × 3), hot toluene (20 ml × 3), and hexanes (20 ml × 3), then dried overnight under dynamic vacuum to afford an off- white powder. The resulting product was stored under positive N_2 atmosphere.

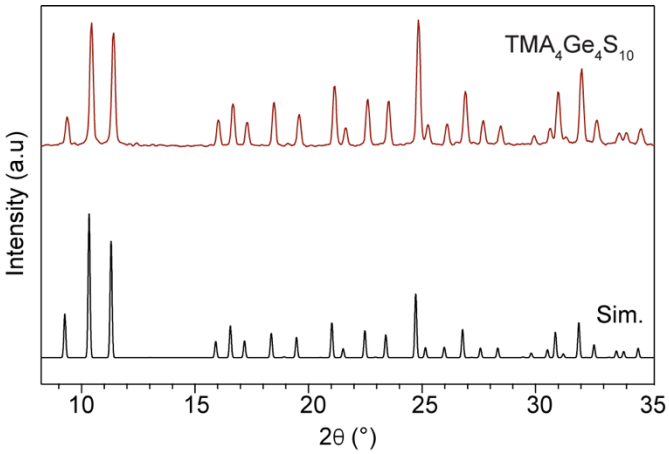

Figure A.1 Experimental (red trace) and simulated (black trace) powder X-ray diffraction patterns of $TMA_4Ge_4S_{10}$.

$TMA_4Ge_4Se_{10}$. Following a procedure adapted from Homayoun Ahari et. al.,[78] germanium powder (0.89 g, 12.2 mmol), selenium powder (2.43 g, 30.7 mmol), and water (4.4 g, 244 mmol) were added to a Teflon Parr bomb. While slowly stirring this mixture with a glass

rod, tetramethyl ammonium hydroxide pentahydrate (2.28 g, 12.5 mmol) was added. The Parr bomb was sealed and then placed in a fixed-temperature oven at 150 °C for 72h. The resulting yellow solution was vacuum-filtered to removed unreacted germanium before ~500 ml of acetone was added to the solution, causing instant orange precipitation. The orange powder was subsequently washed with acetone (20 ml ×3), hot toluene (20 ml ×3), and hexanes (20 ml ×3), then dried overnight under dynamic vacuum to afford a red-orange powder. The resulting product was stored under positive N_2 atmosphere.

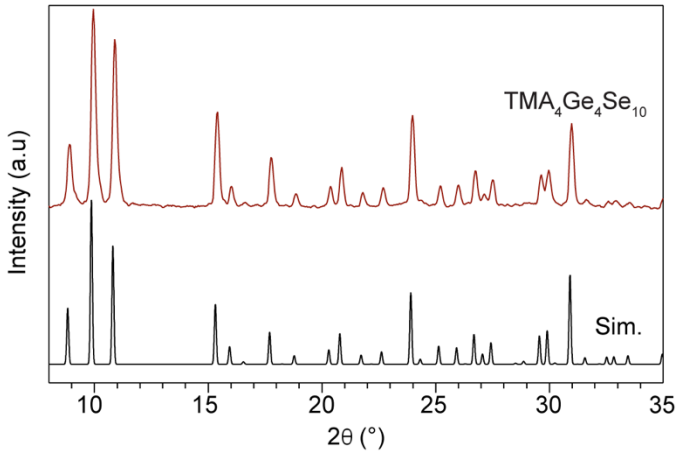

Figure A.2 Experimental (red trace) and simulated (black trace) powder X-ray diffraction patterns of $TMA_4Ge_4Se_{10}$.

All following procedures were adapted from the original synthesis of $TMA_2MnGe_4S_{10}$ by O. M. Yaghi et. al.[68]

$TMA_2MnGe_4S_{10}$. Manganese (II) chloride tetrahydrate (0.0776 g, 0.392 mmol) and $TMA_4Ge_4S_{10}$ (0.178 g, 0.196 mmol) were dissolved in 4 ml of ethanol and 8 ml of DI water, respectively. To the $TMA_4Ge_4S_{10}$ solution, the manganese solution was added dropwise over the course of ~2 minutes. The resulting mixture was allowed to react at room temperature for ~12h.

The white solid was washed with DI water (15 ml ×3) and then dried in a fixed temperature oven at 150 °C for ~12h. The resulting material was stored under ambient conditions.

$TMA_2FeGe_4S_{10}$ (*In-air synthesis*). Iron(II) chloride tetrahydrate (0.0779 g, 0.392 mmol) and $TMA_4Ge_4S_{10}$ (0.178 g, 0.196 mmol) were dissolved in 4 and 8 ml of DI water, respectively. The iron solution was added dropwise to the $TMA_4Ge_4S_{10}$ solution over the course of ~2 minutes. The resulting mixture was allowed to react at room temperature for ~12h. The bright orange solid was washed with DI water (15 ml ×3) and then dried in a fixed-temperature oven at 150 °C for ~12h. The resulting material was stored under ambient conditions.

Air-free synthesis. Anhydrous iron(II) chloride (0.0497 g, 0.392 mmol) and $TMA_4Ge_4S_{10}$ (0.178 g, 0.196 mmol) were dissolved in 4 ml and 8 ml of N_2-sparged DI water, respectively under positive nitrogen atmosphere. The iron solution was added dropwise to the $TMA_4Ge_4S_{10}$ solution over the course of ~2 minutes. The solution was allowed to react at room temperature for ~12h. The bright-orange solid was washed with sparged DI water (15 ml ×2), ethanol (15 ml ×2), and hexanes (15 ml ×2) sequentially. Then, the solid was dried with a stream of nitrogen and stored under positive N_2 atmosphere.

$TMA_2CoGe_4S_{10}$. Cobalt(II) acetate tetrahydrate (0.0976 g, 0.392 mmol) and $TMA_4Ge_4S_{10}$ (0.178 g, 0.196 mmol) were dissolved in 4 ml of ethanol and 8 ml of DI water, respectively. The cobalt solution was added dropwise to the $TMA_4Ge_4S_{10}$ solution over the course of ~2 minutes. The solution was left to react at room temperature for ~12h. The teal solid was washed with DI water (15 ml ×3) and then dried in a fixed temperature oven at 150 °C for ~12h. The resulting material was stored under ambient conditions.

$TMA_2NiGe_4S_{10}$. Nickel(II) chloride hexahydrate (0.0932 g, 0.392 mmol) and $TMA_4Ge_4S_{10}$ (0.178 g, 0.196 mmol) were dissolved in 4 ml of ethanol and 8 ml of DI water, respectively. The nickel solution was added dropwise to the $TMA_4Ge_4S_{10}$ solution over the course of ~2 minutes. The solution was left to react at room temperature for ~12h. The brown solid was washed with DI water (15 ml ×3) and then dried in a fixed temperature oven at 150 °C for ~12h. The resulting material was stored under ambient conditions.

$TMA_2ZnGe_4S_{10}$. Zinc(II) nitrate hexahydrate (0.1166 g, 0.392 mmol) and $TMA_4Ge_4S_{10}$ (0.178 g, 0.196 mmol) were dissolved in 4 and 8 ml of DI water, respectively. The zinc solution was added dropwise to the $TMA_4Ge_4S_{10}$ solution over the course of ~2 minutes. The resulting solution was left to react at room temperature for ~12h. The white solid was washed with DI water (15 ml ×3) and then dried in a fixed temperature oven at 150 °C for ~12h. The resulting material was stored under ambient conditions.

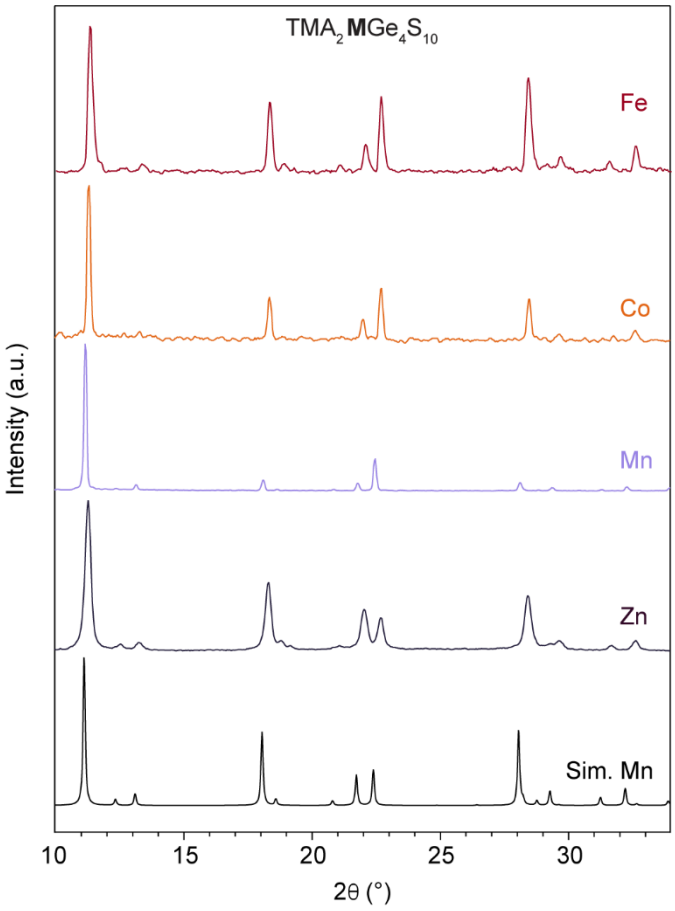

Figure A.3. Experimental powder X-ray diffraction patterns for $TMA_2MGe_4S_{10}$ (M: Mn, Fe, Co, and Zn) compared against simulated patterns of the Mn material.

All following procedures were adapted from the original synthesis of $TMA_2FeGe_4Se_{10}$ by Homayoun Ahari et. al.[78]

$TMA_2FeGe_4Se_{10}$ (*In-air synthesis*). Iron(II) chloride tetrahydrate (0.0779 g, 0.392 mmol) and $TMA_4Ge_4Se_{10}$ (0.270 g, 0.196 mmol) were dissolved in 4 and 8 ml of DI water, respectively. The iron solution was added dropwise to the $TMA_4Ge_4Se_{10}$ solution over the course of ~2 minutes. The solution was left to react at room temperature for ~12h. The resulting maroon solid was washed with DI water (15 ml ×3) and then dried in a fixed temperature oven at 150 °C for ~12h. The resulting material was stored under ambient conditions.

Air-free synthesis. Anhydrous iron(II) chloride (0.0497 g, 0.392 mmol) and $TMA_4Ge_4Se_{10}$ (0.270 g, 0.196 mmol) were dissolved in 4 ml and 8 ml of sparged DI water, respectively, under positive nitrogen atmosphere. The iron solution was added dropwise to the $TMA_4Ge_4Se_{10}$ solution over the course of ~2 minutes. The solution was left to react at room temperature for ~12h. The resulting maroon solid was washed with sparged DI water (15 ml ×2), ethanol (15 ml ×2), and hexanes (15 ml ×2) sequentially. Then, the solid was dried with a stream of nitrogen and stored under positive nitrogen atmosphere.

$TMA_2CoGe_4Se_{10}$. Cobalt(II) acetate tetrahydrate (0.0976 g, 0.392 mmol) and $TMA_4Ge_4Se_{10}$ (0.270 g, 0.196 mmol) were dissolved in 4 and 8 ml of sparged DI water respectively. To the $TMA_4Ge_4Se_{10}$ solution the cobalt solution was added dropwise over the course of ~2 minutes. The solution was left to react at room temperature for ~12h. The dark brown solid was washed with sparged DI water (15 ml ×2), ethanol (15 ml ×2), and hexanes (15 ml ×2) sequentially. Then, the solid was dried with a stream of nitrogen and stored under positive nitrogen atmosphere.

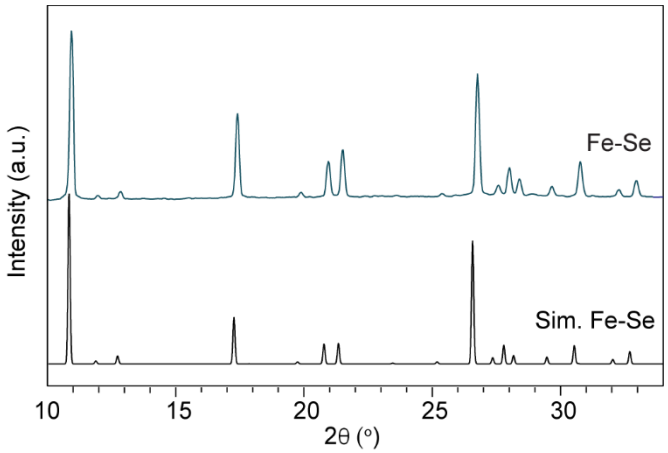

Figure A.4 Experimental and simulated powder X-ray diffraction patterns for $TMA_2FeGe_4Se_{10}$.

Le Bail Fits and Rietveld Refinements.

To confirm the purity of samples as well as index the new isostructural analogs ($TMA_2NiGe_4S_{10}$ and $TMA_2CoGe_4Se_{10}$), General Structure Analysis System (GSAS) was utilized for Le Bail fits and Rietveld Refinements. The known crystal structures of $TMA_2MnGe_4S_{10}$ and $TMA_2FeGe_4Se_{10}$[68,78] was used to index the other experimental powder patterns, and the refined unit cell parameters are summarized in table A.1. As a general note, the FWHM parameters U, V, W, X, and Y, sample displacement, and unit cell lattice parameters *a* and *c* were refined in each Le Bail fit. The fits were determined to be feasible structural solutions to the given powder patterns.[217]

Material	*a* (Angstroms)	*c* (Angstroms)	RWP (%)
Zn-S	9.401(4)	14.123(6)	14.71
Mn-S	9.515(2)	14.275(3)	24.21
Ni-S	9.483(1)	13.871(1)	26.21
Co-S	9.437(4)	14.025(5)	28.01
Fe-S	9.425(5)	14.200(7)	30.66
Fe-Se	9.708(1)	14.778(1)	13.27
Co-Se	9.693(2)	14.605(4)	19.85

Table A.1 Refined Lattice Parameters (*a,c*) for as synthesized materials.

SQUID Magnetic Susceptibility Data.

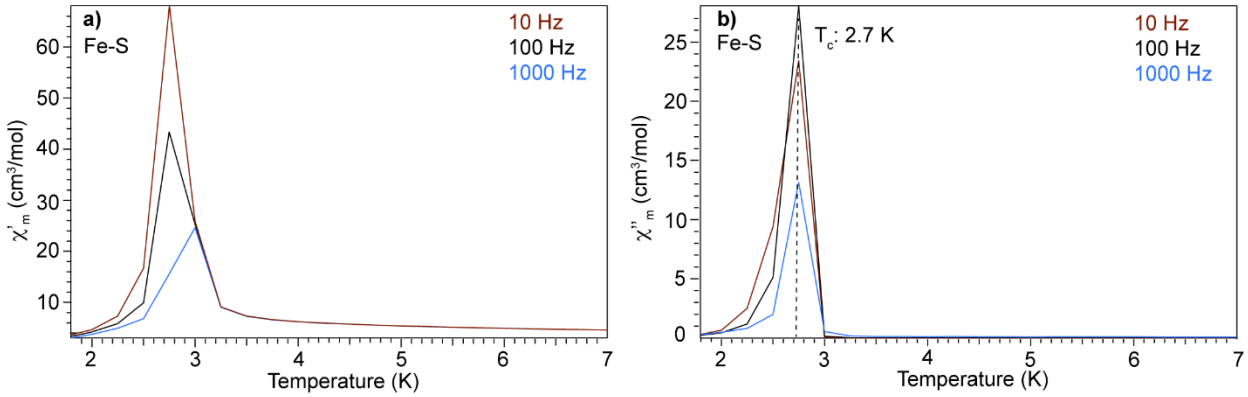

Figure A.5 AC magnetic susceptibility for $TMA_2FeGe_4S_{10}$ giving in-phase a) and out of phase b) components of X_M performed at frequencies of 10 (red trace), 100 (black trace), and 1000 (blue trace) Hz.

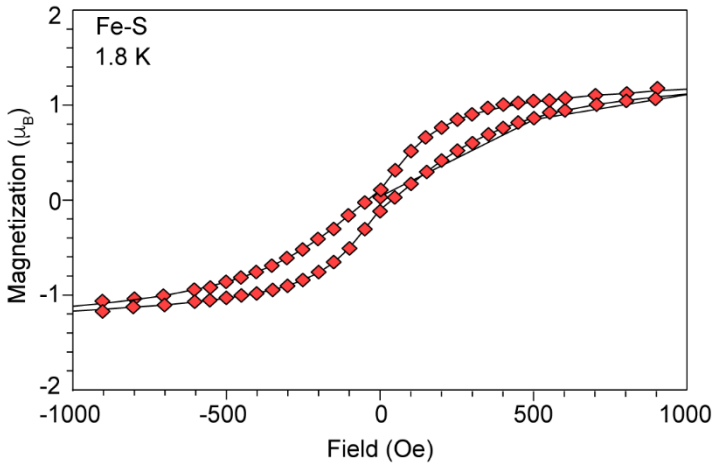

Figure A.6 Magnetization data for $TMA_2FeGe_4S_{10}$ at 1.8 K.

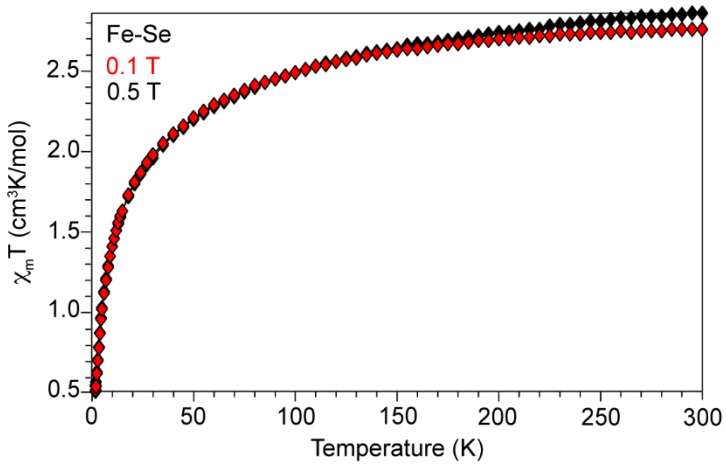

Figure A.7 DC magnetic susceptibility for $TMA_2FeGe_4Se_{10}$ at external magnetic field strengths of 0.1 (red trace) and 0.5(black trace) T.

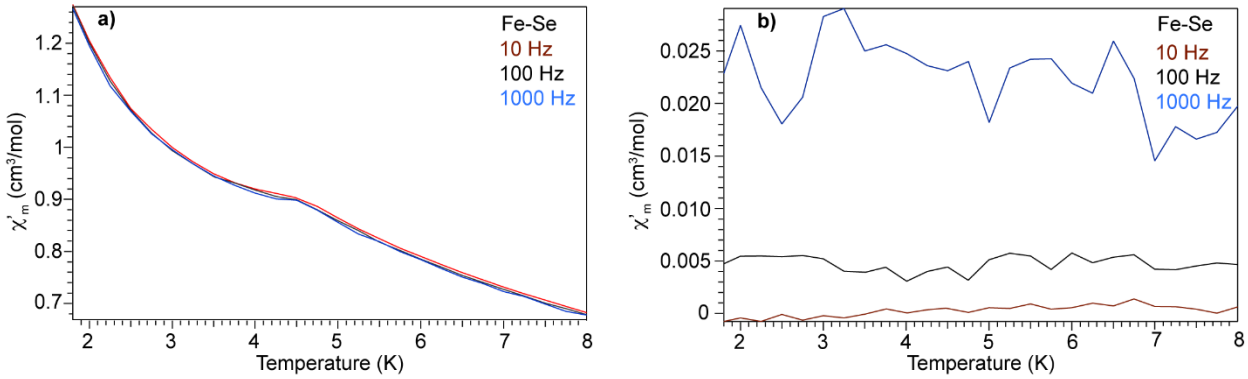

Figure A.8 AC magnetic susceptibility for $TMA_2FeGe_4Se_{10}$ giving in-phase a) and out of phase b) components of X_M collected at frequencies of 10 (red trace), 100 (black trace), and 1000 (blue trace) Hz.

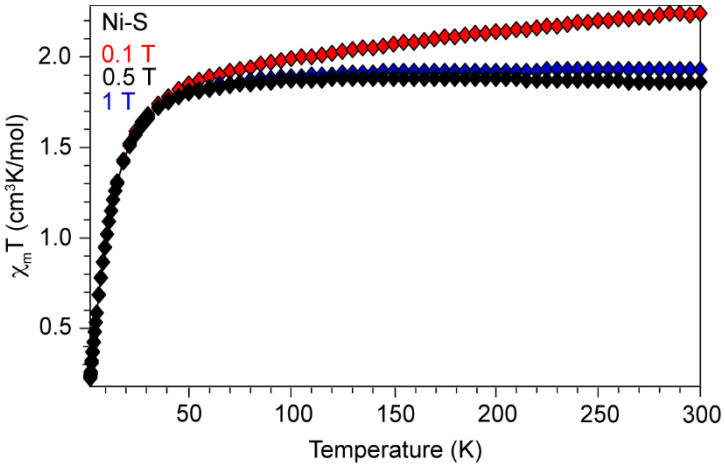

Figure A.9 DC magnetic susceptibility for $TMA_2NiGe_4S_{10}$ at external magnetic field strengths of 0.1 (red trace), 0.5 (black trace), and 1 (blue trace) T.

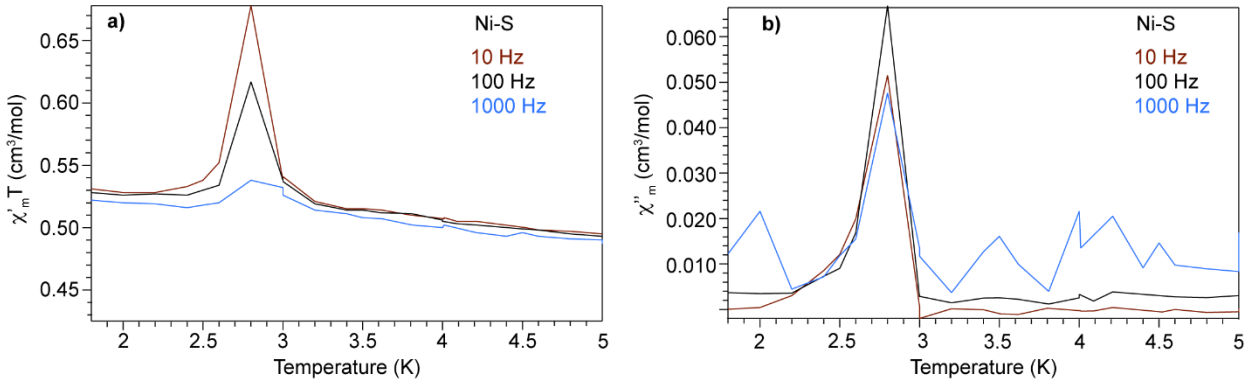

Figure A.10 AC magnetic susceptibility for $TMA_2NiGe_4S_{10}$ giving in-phase a) and out of phase b) components of X_M collected at frequencies of 10 (red trace), 100 (black trace), and 1000 (blue trace) Hz.

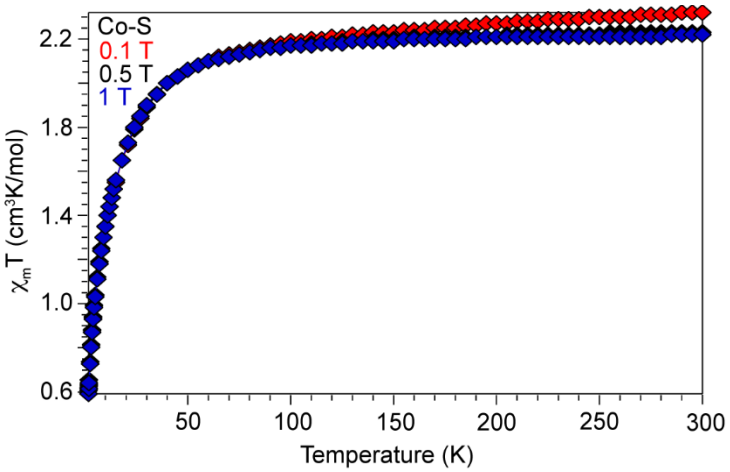

Figure A.11 DC magnetic susceptibility for $TMA_2CoGe_4S_{10}$ at external magnetic field strengths of 0.1 (red trace), 0.5 (black trace), and 1 (blue trace) T.

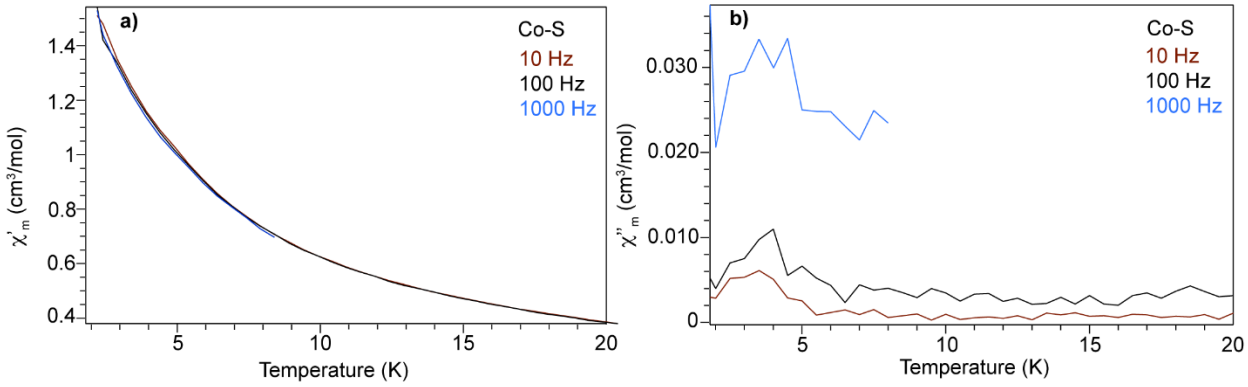

Figure A.12 AC magnetic susceptibility for $TMA_2CoGe_4S_{10}$ giving in-phase a) and out of phase b) components of X_M collected at frequencies of 10 (red trace), 100 (black trace), and 1000 (blue trace) Hz.

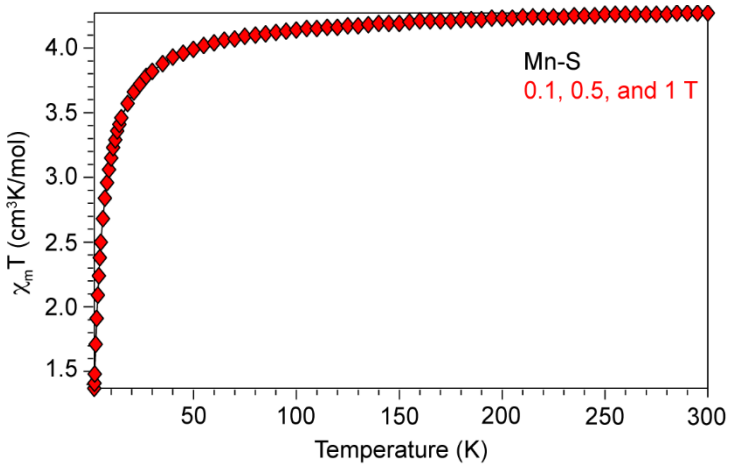

Figure A.13 DC magnetic susceptibility for $TMA_2MnGe_4S_{10}$ at external magnetic field strengths of 0.1, 0.5, and 1 (red traces) T.

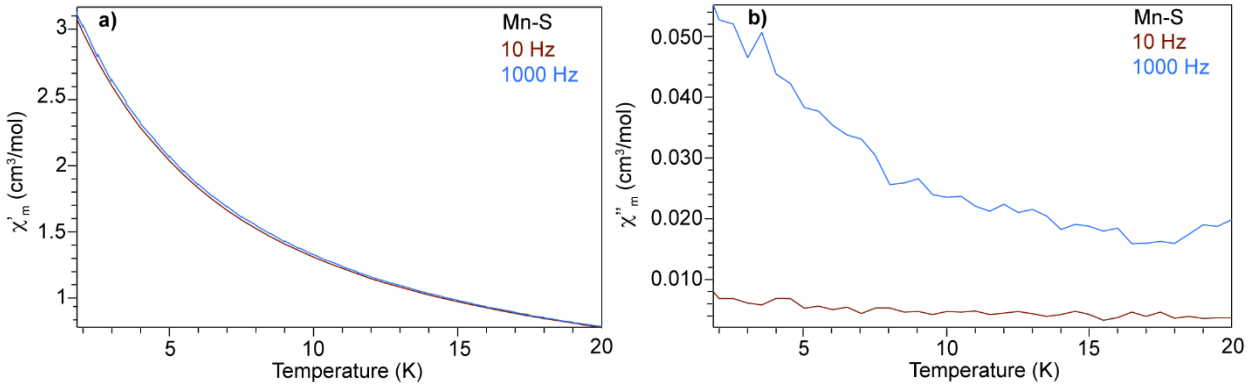

Figure A.14 AC magnetic susceptibility for $TMA_2MnGe_4S_{10}$ giving in-phase a) and out of phase b) components of X_M collected at frequencies of 10 (red trace) and 1000 (blue trace) Hz.

Ligand Field Analysis.

Transitions were assigned according to literature precedent[218] and ligand field parameters were determined using mathematical equations from A. B. P. Lever.[219] B' is defined as the reduction in the interelectronic repulsion parameter (B) when in the framework compared to the B value for the free metal ion, as calculated by the equation below (where B is the experimental interelectronic repulsion parameter and B_f is the interelectronic repulsion parameter of the free metal ion):

$$B' : \left(\frac{B - B_f}{B}\right) * 100$$

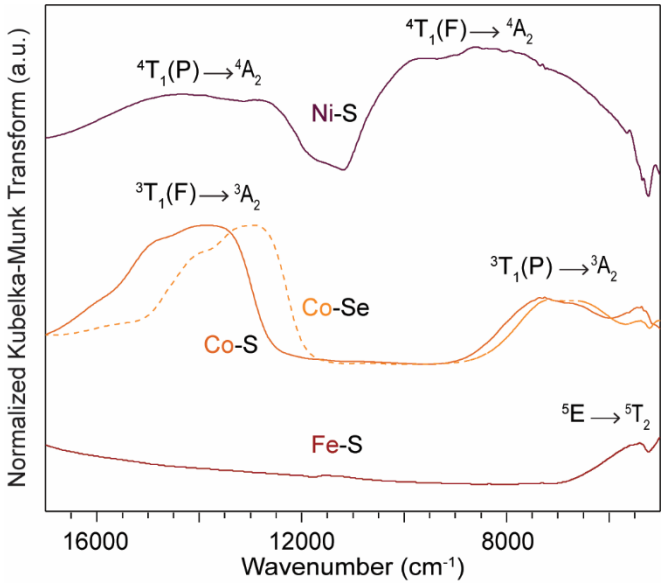

Figure A.15 Diffuse reflectance data plotted as the Kubelka-Munk function F(R) for $TMA_2NiGe_4S_{10}$ (purple trace), $TMA_2CoGe_4S_{10}$ (solid orange trace), $TMA_2CoGe_4Se_{10}$ (dotted orange trace), and $TMA_2FeGe_4S_{10}$ (red trace) in the region of ligand-field transitions.

Material	D_q (cm^{-1})	B (cm^{-1})	B' (%)
Ni-S	453	746	31
Co-S	409	603	46
Co-Se	392	549	51
Fe-S	524	N/A	N/A

Table A.2 Ligand field parameters as calculated from transitions observed in Figure A.15.

Gaussian Fits and Tauc Plots for Band Gap Determination.

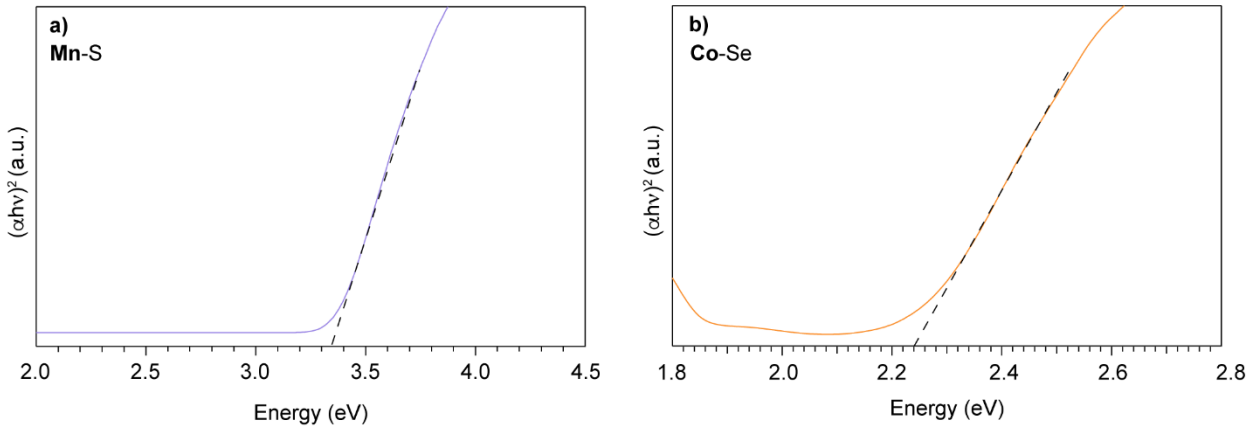

Figure A.16 Tauc plot transformation of diffuse reflectance data for $TMA_2MnGe_4S_{10}$ a) $TMA_2CoGe_4Se_{10}$ b) with dotted lines extrapolated to the x-axis interpreted as the band gap transition.

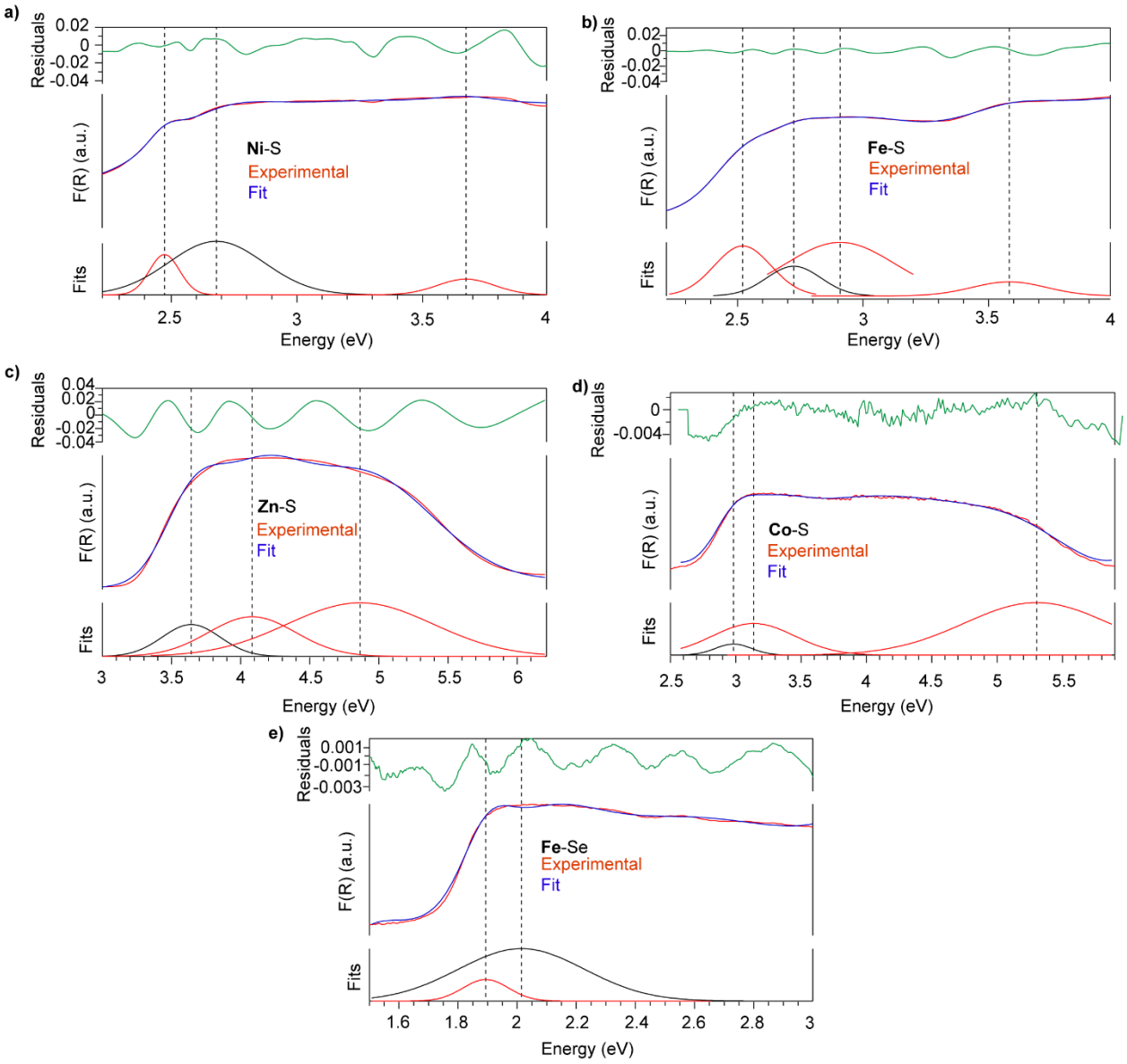

Figure A.17 Gaussian fits for $TMA_2NiGe_4S_{10}$ a) $TMA_2FeGe_4S_{10}$ b), $TMA_2ZnGe_4S_{10}$ c), $TMA_2CoGe_4S_{10}$ d) and $TMA_2FeGe_4Se_{10}$ e) with a LogPoly5 background. The green trace is residuals from the fitting function, the red and blue trace are the experimental and simulated Kubelka-Munk results respectively, and the bottom most red traces are the gaussians that give the best fit, with the black gaussian interpreted as the band gap transition.

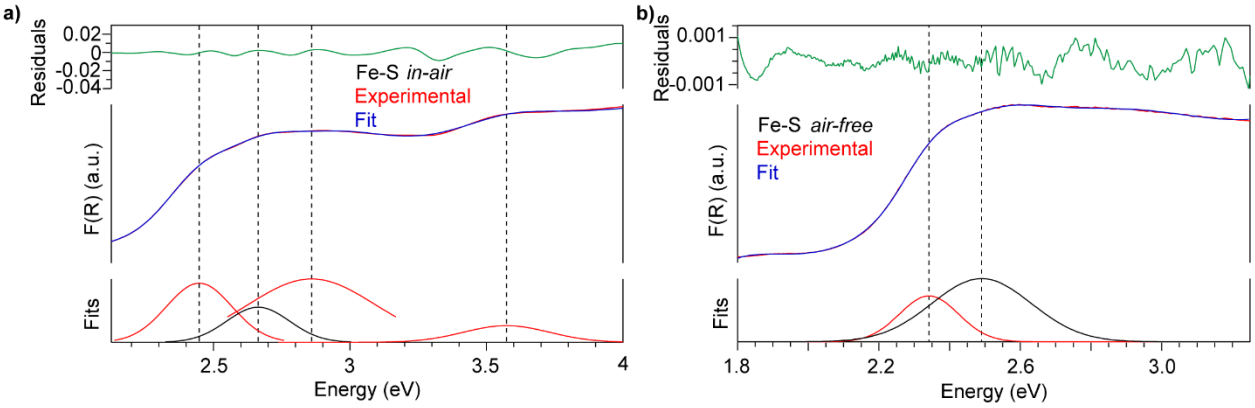

Figure A.18 Gaussian fits for $TMA_2FeGe_4S_{10}$ under *in-air* a) and *air-free* b) conditions with a LogPoly5 background. The green trace is residuals from the fitting function, the red and blue trace are the experimental and simulated Kubelka-Munk results respectively, and the bottom most red traces are the gaussians that give the best fit, with the black gaussian interpreted as the band gap transition.

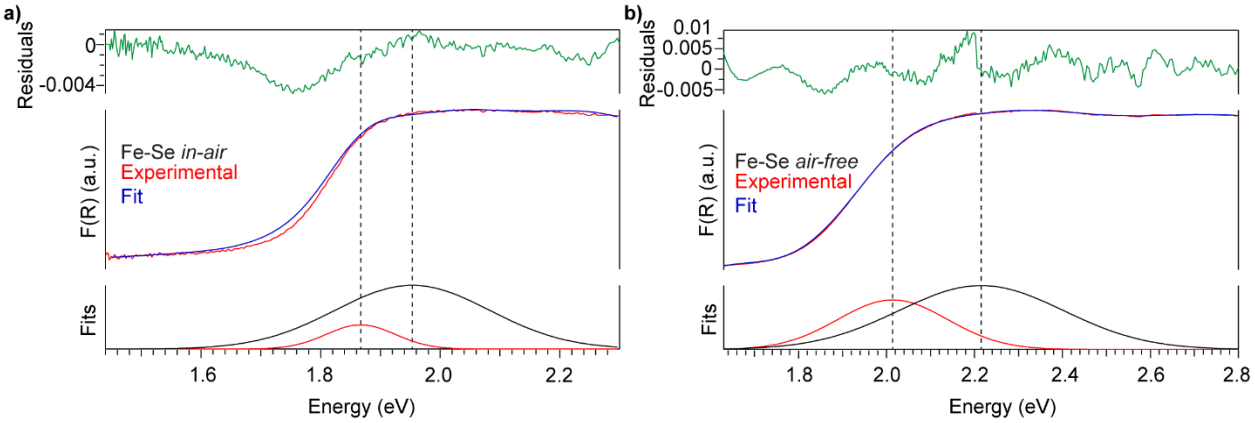

Figure A.19 Gaussian fits for $TMA_2FeGe_4Se_{10}$ under *in-air* a) and *air-free* b) conditions with a LogPoly5 background. The green trace is residuals from the fitting function, the red and blue trace are the experimental and simulated Kubelka-Munk results respectively, and the bottom most red traces are the gaussians that give the best fit, with the black gaussian interpreted as the band gap transition.

Computational Methods.

Structural optimization for all materials were performed with DFT as implemented in the Vienna ab initio Simulation Package (VASP, version 5.4.4).[220] All structures were equilibrated using the unrestricted GGA-PBEsol exchange–correlation functional[221] with the PAW plane wave method,[222] using the quasi-Newton relaxation routine (IBRION=1). Ionic relaxation was achieved when all forces were smaller than 0.005 eV $Å^{-1}$. The plane-wave cut off was set at 500 eV and the SCF convergence criterion was 10^{-6} eV, resulting in electronic convergence of 0.005 eV per atom. An automatic k-grid was used during the optimization with 3 × 3 × 2 sampling. Single point calculations were performed with a 3 × 3 × 2 k-grid to obtain initial wavefunctions before electronic properties calculations.

Electronic band structures along with partial density of states (pDOS) for each optimized structure were constructed with the HSEsol06,[223] (PBEsol+25% HF, with a screen length of 0.207) level of theory and with similar convergence criteria as above sampling along the high symmetry k-path as show in each band structure. The corresponding band gap for each optimized structure were then obtained from the valence band maximum and the conduction band minimum. Band decomposed charge density calculation at the Γ-point were performed to visualize the mixed-valence bands for the [$Fe^{III}Ge_4S_{10}$TMA] material.

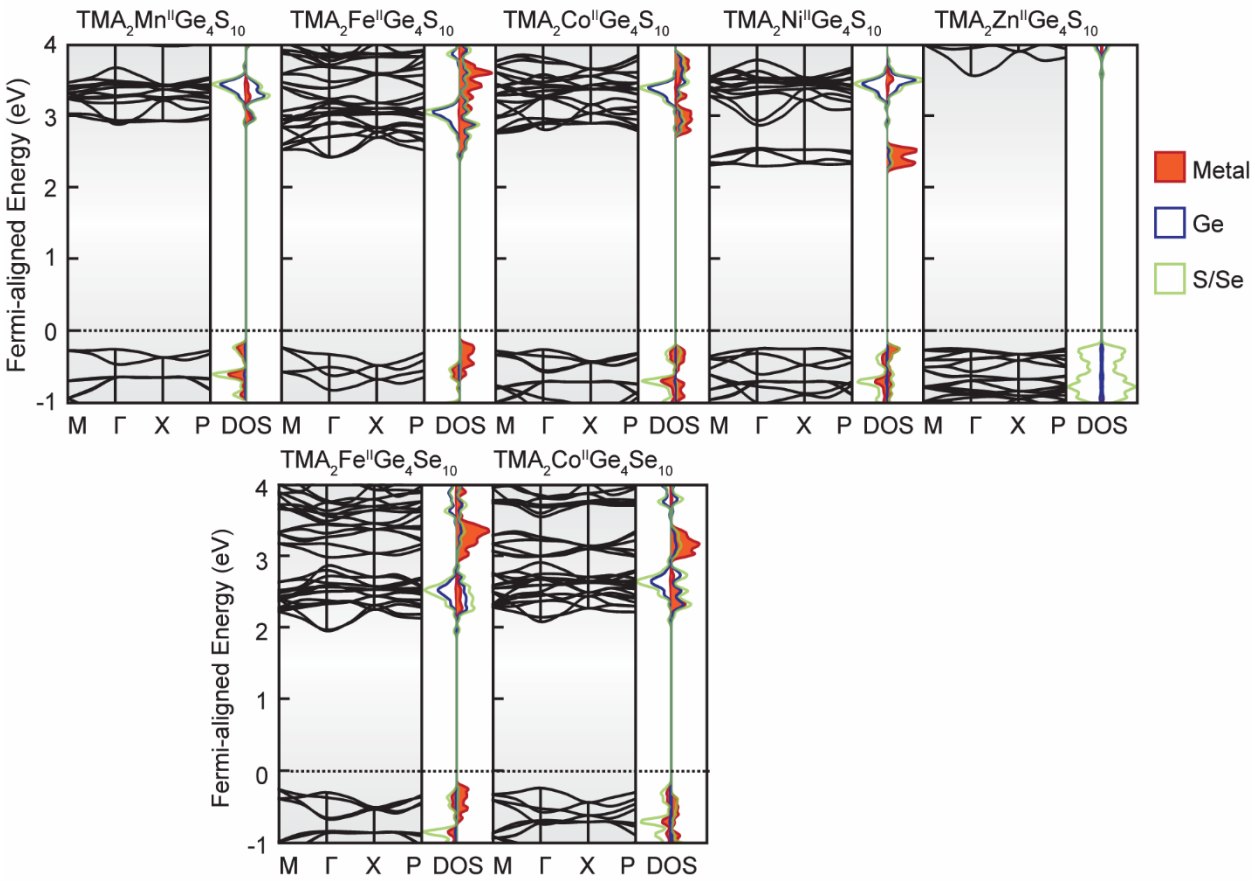

Figure A.20 Simulated band structures and pDOS states for as synthesized materials.

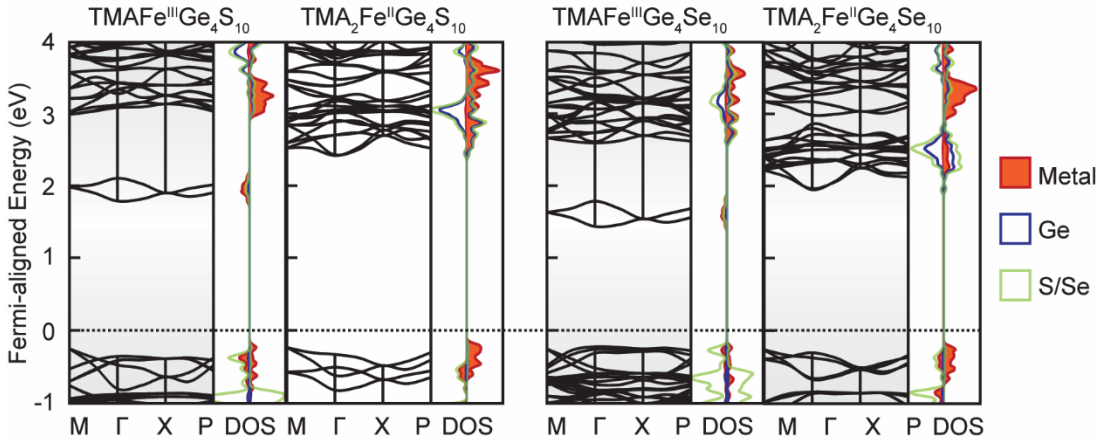

Figure A.21 Impact of Fe oxidation state on the simulated band structures and pDOS states for TMA_2FeGe_4S/Se_{10}.

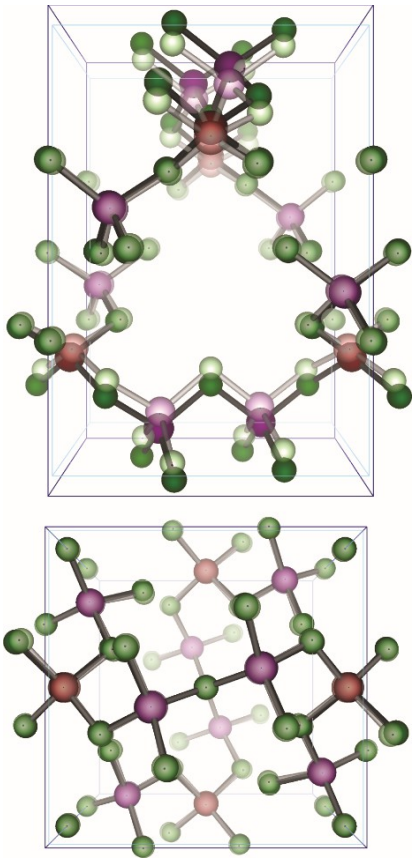

Figure A.22 Unit cell of $TMA_2FeGe_4S_{10}$ before (solid color) and after (faded) oxidation of Fe.

Materials	*Percent Occupancy of Element (%)*		
	Metal	*S/Se*	*Ge*
$Mn^{II}Ge_4S_{10}$	39	56	5
$Co^{II}Ge_4S_{10}$	49	47	4
$Fe^{II}Ge_4S_{10}$	84	9	7
$Ni^{II}Ge_4S_{10}$	45	51	4
$Zn^{II}Ge_4S_{10}$	4	92	4
$Co^{II}Ge_4Se_{10}$	31	64	5
$Fe^{II}Ge_4Se_{10}$	71	22	7
$Fe^{III}Ge_4S_{10}$	72	20	8
$Fe^{III}Ge_4Se_{10}$	39	55	6

Table A.3 Calculated relative percentage of each elements (M, Se/S, Ge) from pDOS at the VBM of MGe_4S/Se_{10} materials where M is Mn, Fe, Co, Ni, and Zn.

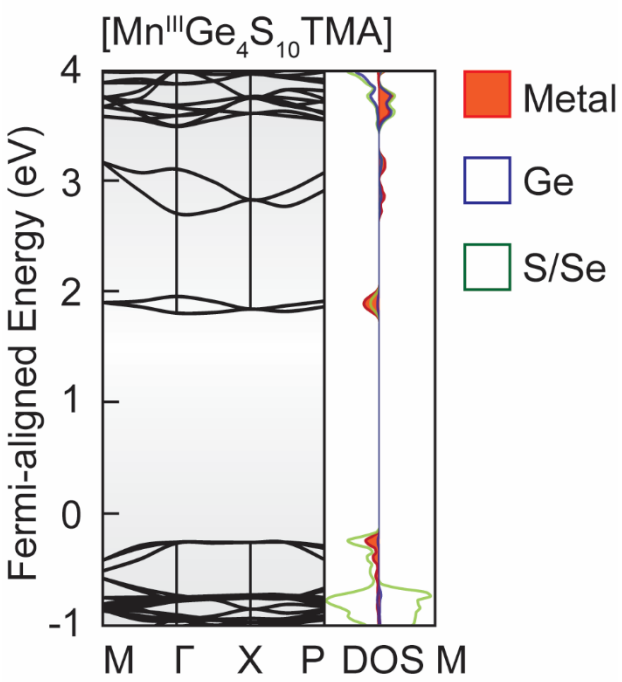

Figure A.23 Impact of Mn oxidation state on the simulated band structures and pDOS states for $TMA_2MnGe_4S_{10}$.

EIS Equivalent Circuit Fitting.

All EIS fits were performed using the open-source EIS Spectrum Analyzer software.[224] To fit, an equivalent circuit guess was built given the EIS response given and knowledge of the material and experimental constraints (e.g. use of ion blocking electrodes). The equivalent circuits were fit using the NM simp algorithm using the unweighted function. All capacitors used in fits were modeled as constant phase elements and all other circuit elements and there fitted values are summarized in the table below:

Material	Circuit Element	Fitted Value	Error (%)
Zn-S	Bulk Capacitance	19 nF	2.2
	n	0.73	0.31
	Interfacial Capacitance	1.1 μF	0.86
	n	0.46	0.92
	Bulk Resistance	674 kΩ	0.50
Fe-S	Bulk Capacitance	0.24 nF	0.28
	n	0.91	0.13
	Bulk Resistance	840 kΩ	1.1

Table A.4 Fitted values with percent error for circuit elements used in EIS fits for Zn-S and Fe-S pressed pellet AC measurements.

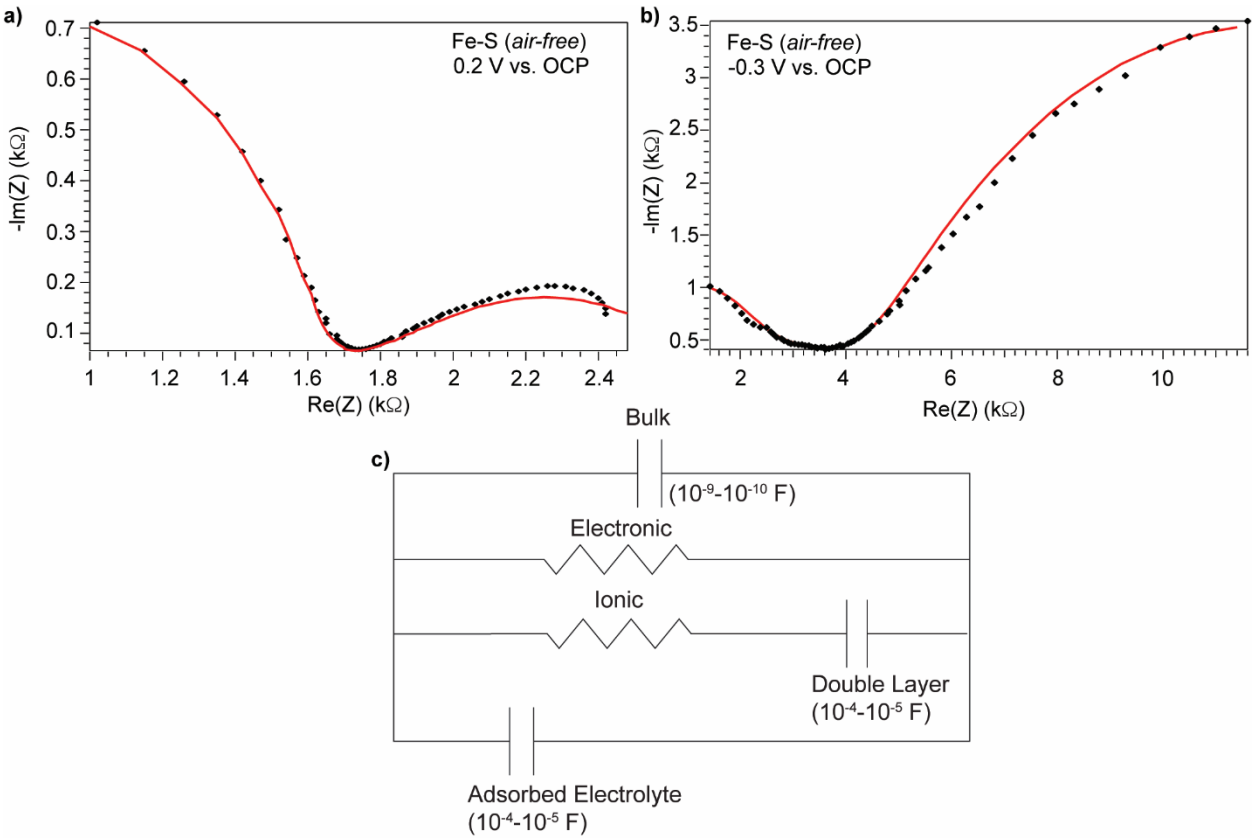

Figure A.24 EIS responses (black traces) at 0.2 V a) and -0.3 V b) vs. OCP from the 3 electrode pressed pellet measurements with a 0.1 M $TBAPF_6$ in MeCN, with a carbon counter electrode and a Ag/Ag(NO3) pseudo reference electrode. AC voltage of 25 mV was applied from 2Mhz to 0.1 Hz. The equivalent circuit used to produce the fits (red traces) is shown in panel c.

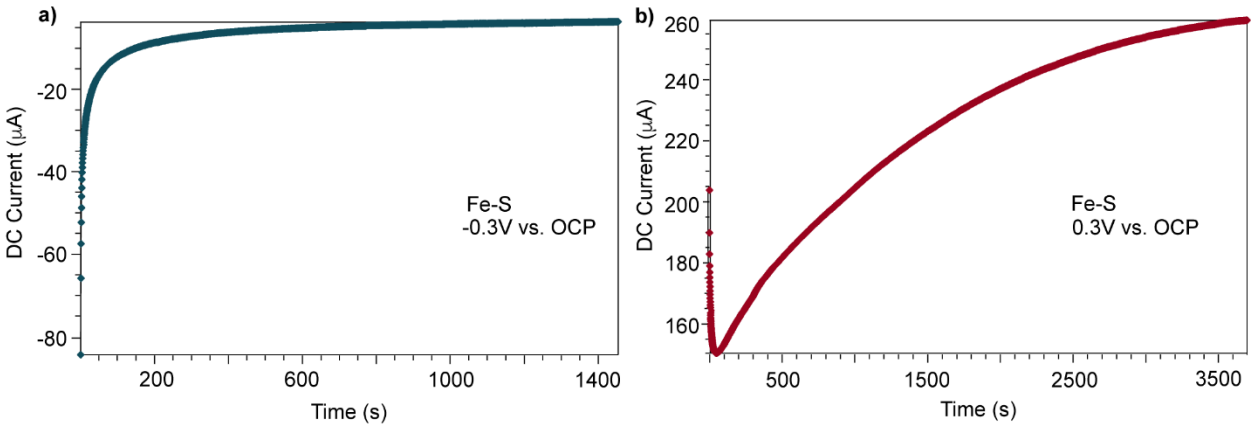

Figure A.25 Chronoamperometry traces for -0.3 V a) and 0.3 V b) vs. OCP from the experimental set-up detailed in Figure A.24.

Redox Chemistry of Frameworks.

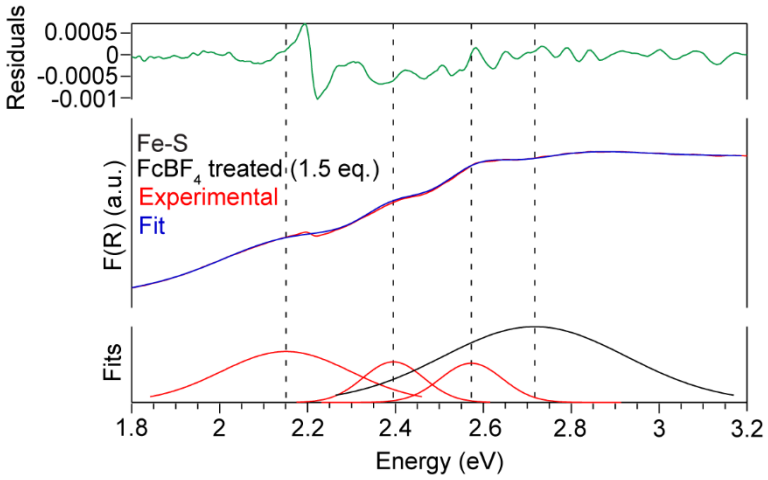

Figure A.26 Gaussian fits for $TMA_2FeGe_4S_{10}$ prepared by air-free conditions after $FcBF_4$ chemical treatment, with a LogPoly5 background. The green trace is residuals from the fitting function, the red and blue trace are the experimental and simulated Kubelka-Munk results respectively, and the bottom most red traces are the gaussians that give the best fit, with the black gaussian interpreted as the band gap transition.

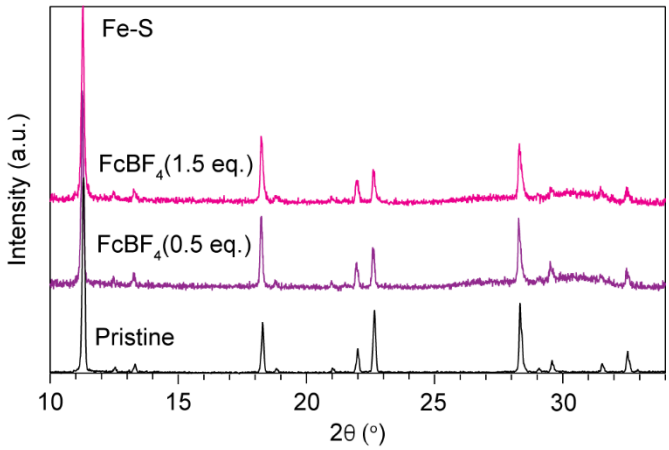

Figure A.27 Experimental powder X-ray diffraction patterns of $TMA_2FeGe_4S_{10}$ after $FcBF_4$ chemical treatment at 0.5 eq (purple trace) and 1.5 eq. (pink trace).

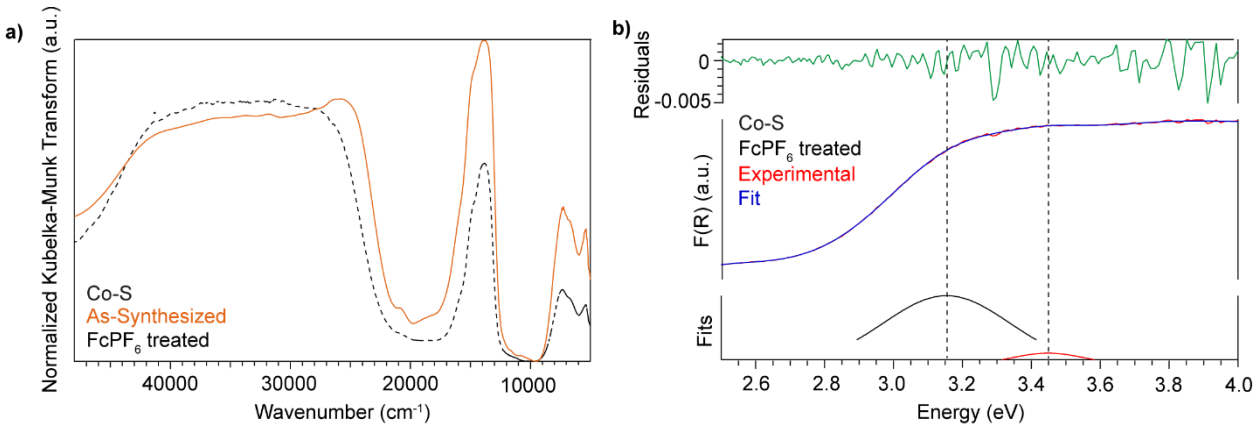

Figure A.28 a) Kubelka-Munk transform before (blue trace) and after (black trace) $FcPF_6$ chemical treatment for $TMA_2CoGe_4S_{10}$. b) Gaussian fit with a LogPoly5 background. The green trace is residuals from the fitting function, the red and blue trace are the experimental and simulated Kubelka-Munk results respectively, and the bottom most red traces are the gaussians that give the best fit, with the black gaussian interpreted as the band gap transition.

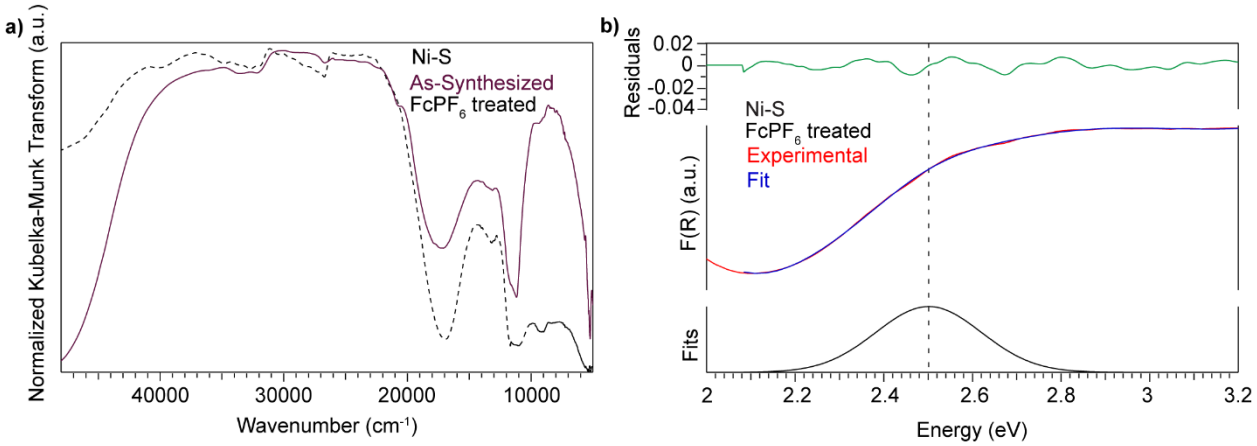

Figure A.29 a) Kubelka-Munk transform before (blue trace) and after (black trace) $FcPF_6$ chemical treatment for $TMA_2NiGe_4S_{10}$. b) Gaussian fit with a LogPoly5 background. The green trace is residuals from the fitting function, the red and blue trace are the experimental and simulated Kubelka-Munk results respectively, and the bottom most red traces are the gaussians that give the best fit, with the black gaussian interpreted as the band gap transition.

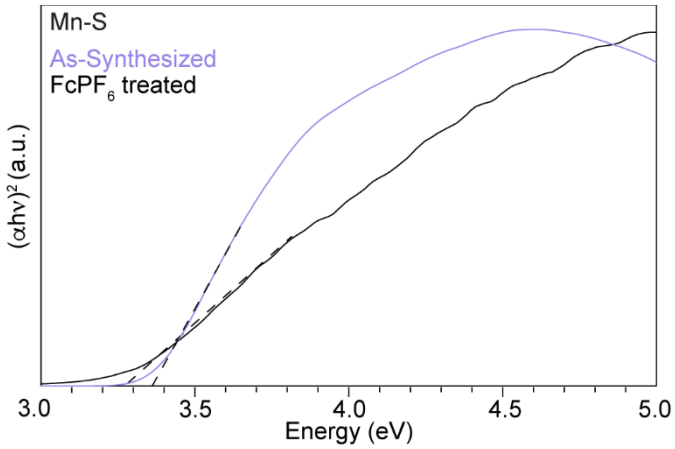

Figure A.30 Tauc plot transformation of diffuse reflectance data for $TMA_2MnGe_4S_{10}$ before (black trace) and after chemical treatment with $FcPF_6$ (purple trace) with dotted lines extrapolated to the *x*-axis interpreted as the band gap transition.

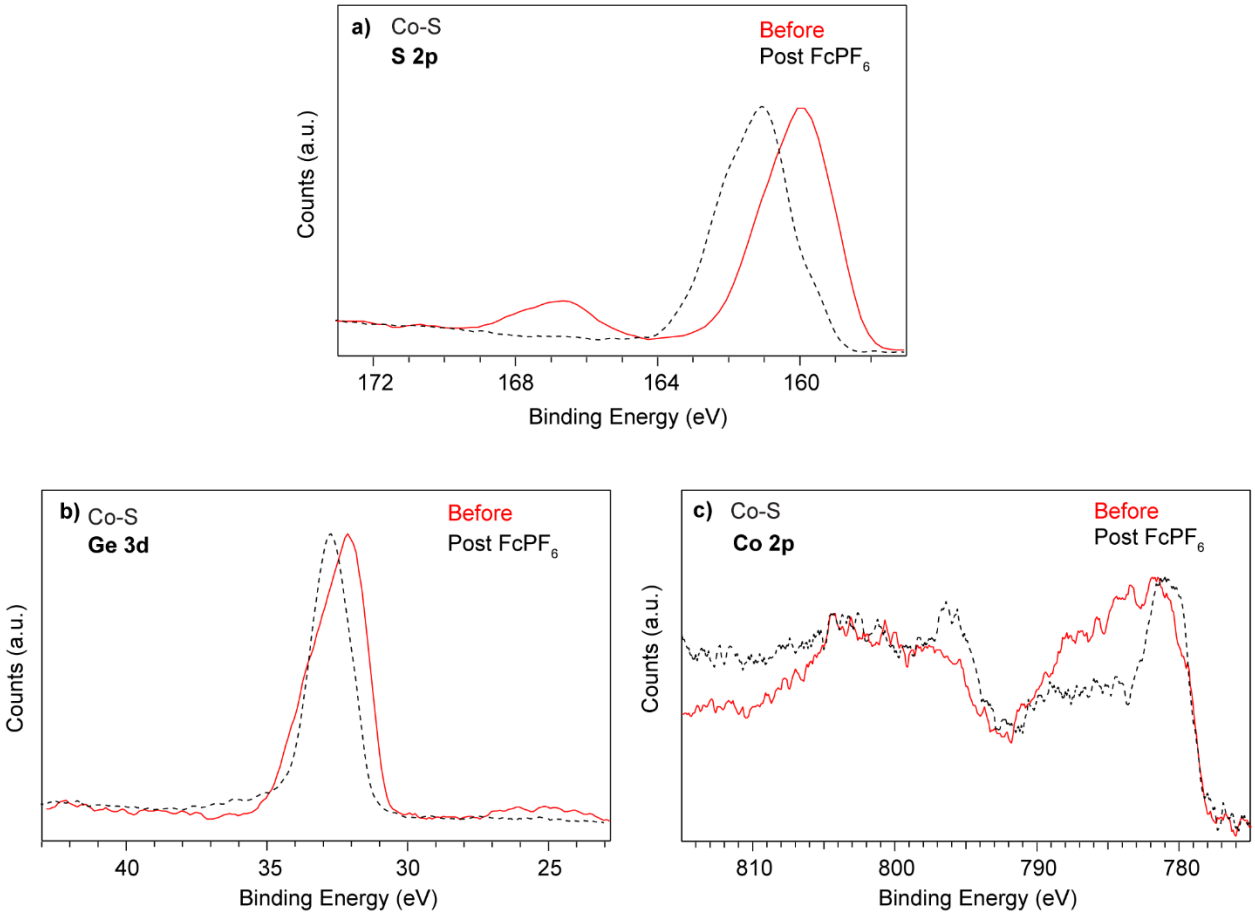

Figure A.31 High-resolution XPS spectra of $TMA_2CoGe_4S_{10}$ before (red trace) and after (black trace) treatment with $FcPF_6$, showing the S 2p a), Ge 3d b), and Co 2p c).

Element	Binding Energy (eV) Before	Binding Energy (eV) After
Ge 3d	31.35	32.95
Co 2p	781.7	780.8
S 2p	162.05	162.9

Table A.5 Binding energies of the S 2p, Ge 3d, and Co 2p features of $TMA_2CoGe_4S_{10}$ before and after treatment with $FcPF_6$.

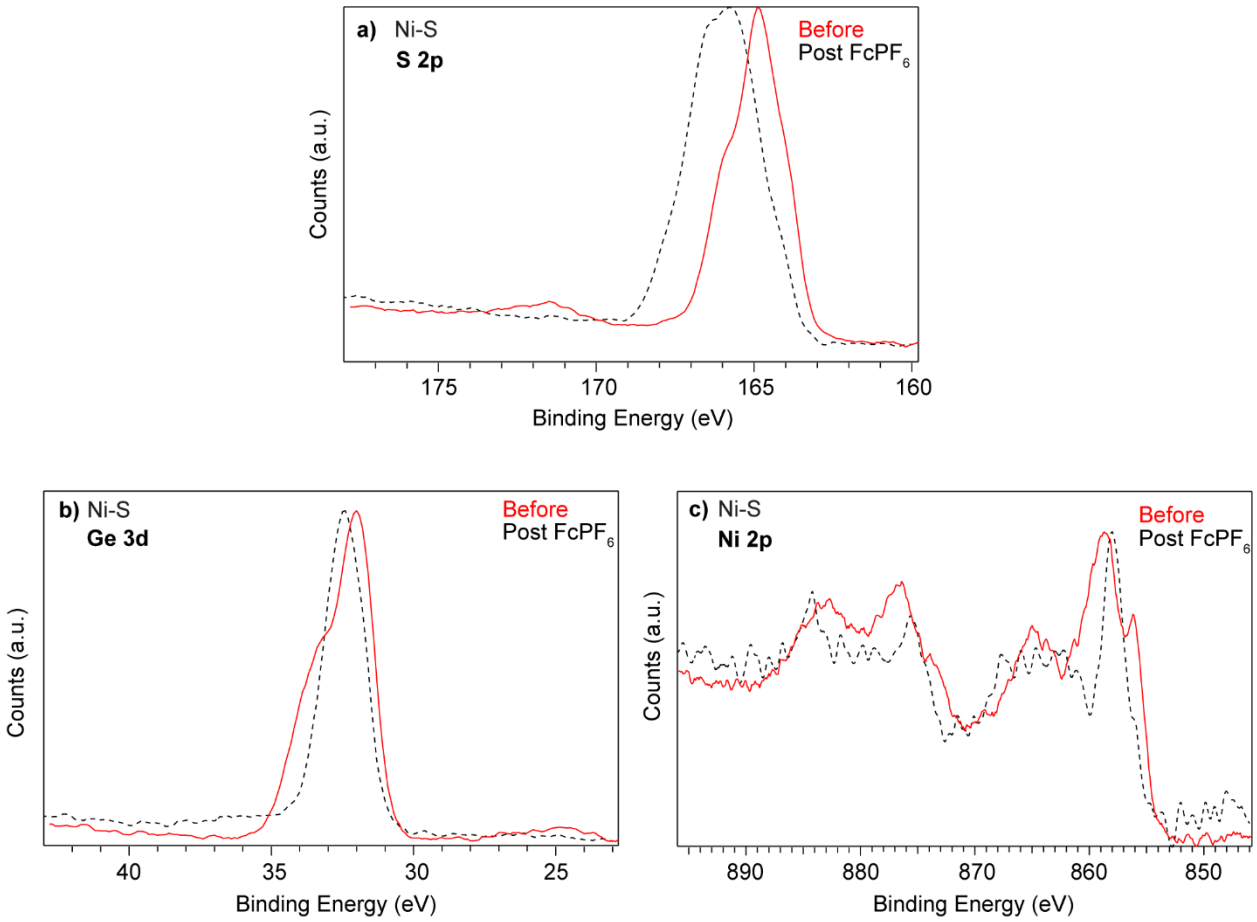

Figure A.32 High-resolution XPS spectra of $TMA_2NiGe_4S_{10}$ before (red trace) and after (black trace) treatment with $FcPF_6$, showing the S 2p a), Ge 3d b), and Ni 2p c).

Element	Binding Energy (eV) Before	Binding Energy (eV) After
Ge 3d	31.35	31.7
Ni 2p	856.8	856.35
S 2p	162.95	162.7

Table A.6 Binding energies of the S 2p, Ge 3d, and Ni 2p features of $TMA_2NiGe_4S_{10}$ before and after treatment with $FcPF_6$.

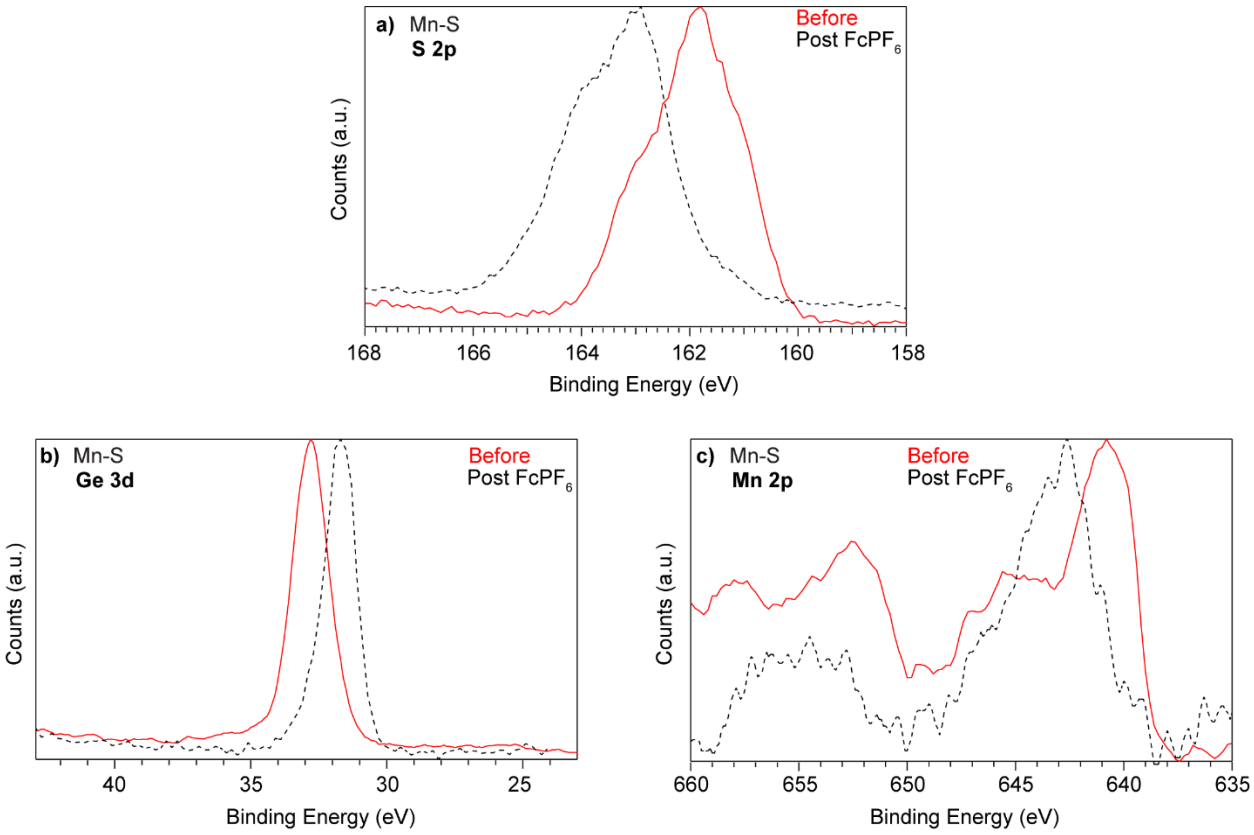

Figure A.33 High-resolution XPS spectra of $TMA_2MnGe_4S_{10}$ before (red trace) and after (black trace) treatment with $FcPF_6$, showing the S 2p a), Ge 3d b), and Mn 2p c).

Element	Binding Energy (eV) Before	Binding Energy (eV) After
Ge 3d	161.9	162.9
Mn 2p	640.8	642.8
S 2p	30.8	32

Table A.7 Binding energies of the S 2p, Ge 3d, and Mn 2p features of $TMA_2MnGe_4S_{10}$ before and after treatment with $FcPF_6$.

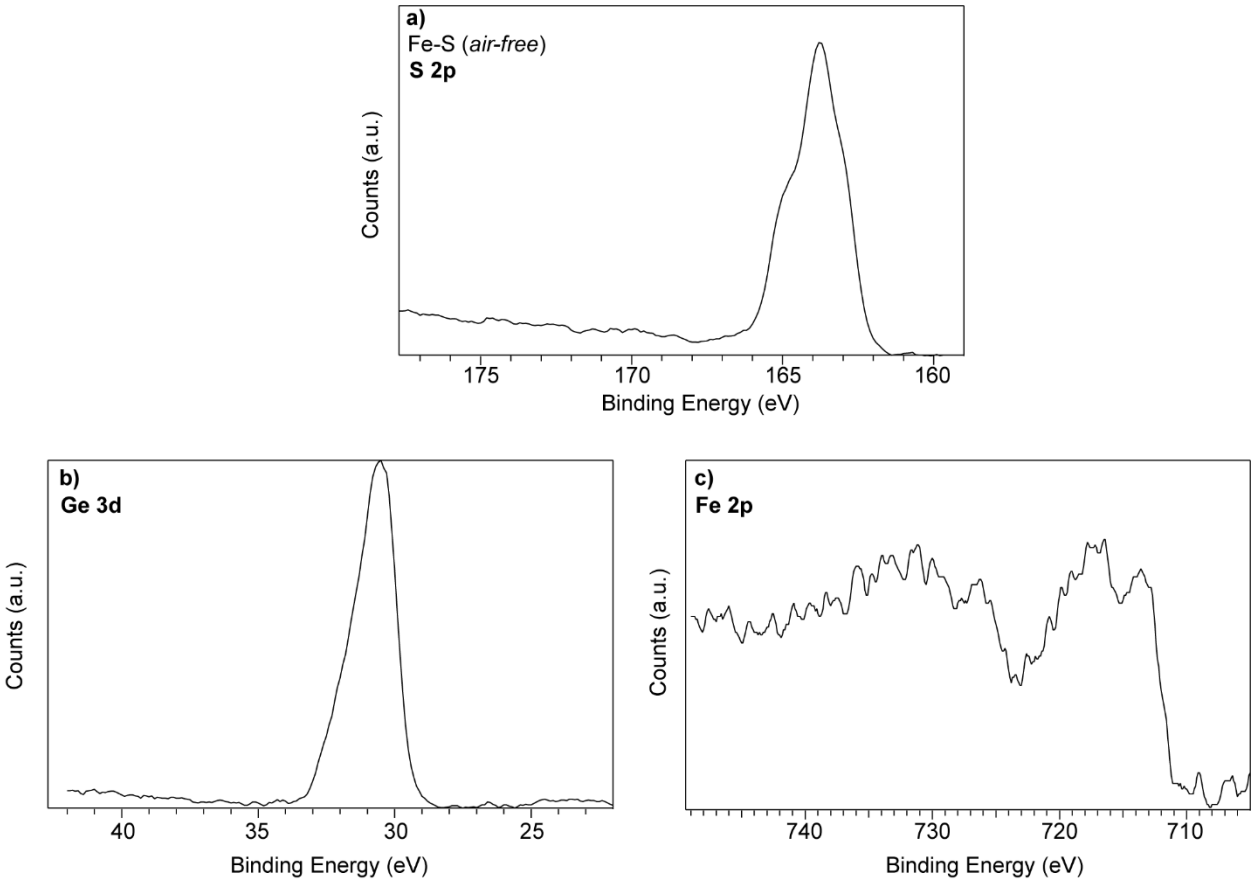

Figure A.34 High-resolution XPS spectra of $TMA_2FeGe_4S_{10}$ prepared *air-free* before (red trace) and after (black trace) treatment with $FcPF_6$, showing the S 2p a), Ge 3d b), and Fe 2p c).

Element	Binding Energy (eV)	Atomic Percent
Ge 3d	30.95	17.1
Fe 2p	712.1	2.1
S 2p	161.8	20.2

Table A.8 Binding energies of the S 2p, Ge 3d, and Fe 2p features of $TMA_2FeGe_4S_{10}$ prepared *air-free*.

Desulfurization of $TMA_2FeGe_4S_{10}$.

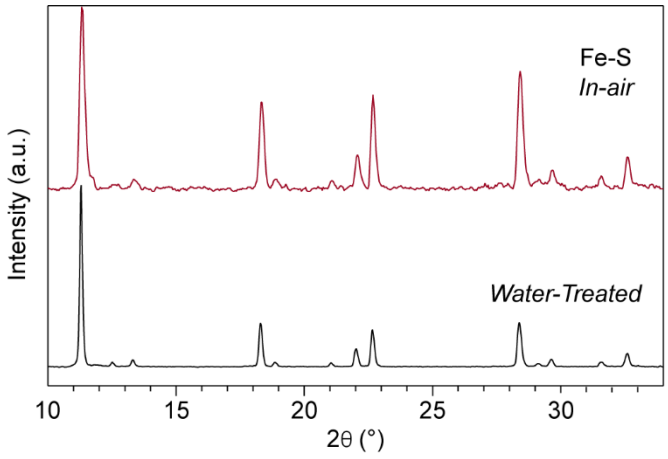

Figure A.35 Experimental powder X-ray diffraction patterns for $TMA_2FeGe_4S_{10}$ pre (red trace) and post desulfurization procedure.

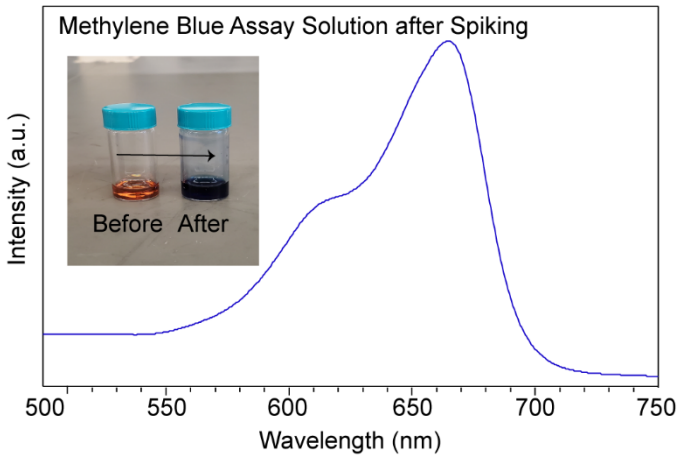

Figure A.36 UV-Vis spectrum of a dark blue solution that was allowed to develop for 1 hour after the orange methylene blue assay mixture was spiked with 200 µL of a solution containing $TMA_2FeGe_4S_{10}$ in 5 ml of water after aging in an 80 °C oven for 2 h.

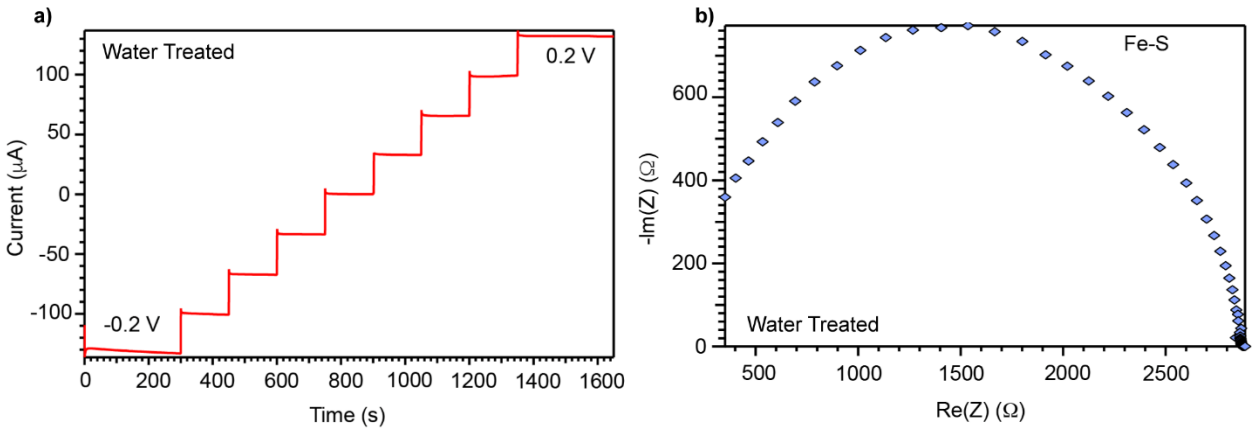

Figure A.37 Electrochemical characterization of water-treated Fe-S a) Pressed pellet chronoamperometry current transients from -0.2 to 0.2 V with 0.05 V step increments b) Pressed pellet EIS with a 50mV excitation from 2 Mhz to 0.1 Hz.

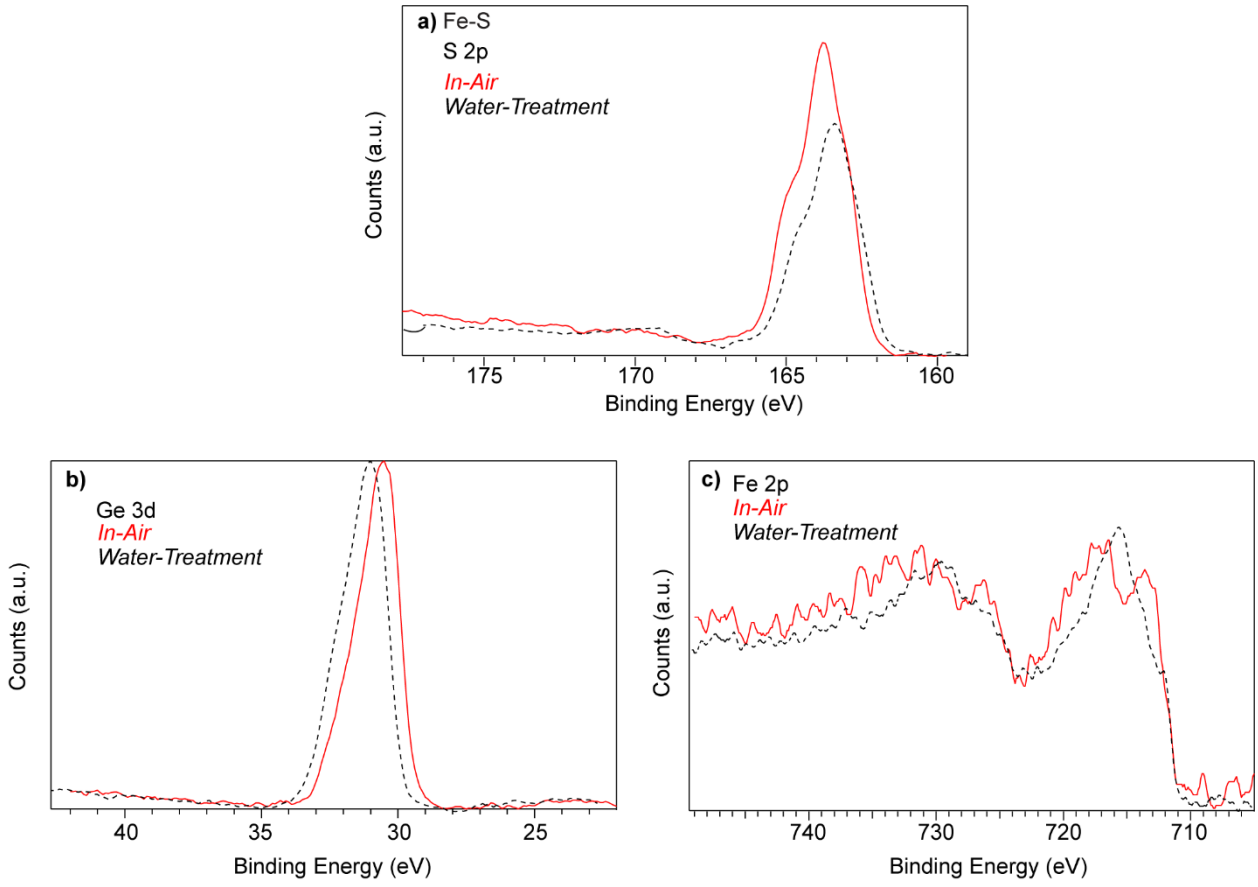

Figure A.38 High-resolution XPS spectra of $TMA_2FeGe_4S_{10}$ before (red trace) and after (black trace) water treatment, showing the S 2p a), Ge 3d b), and Fe 2p c).

Supplemental Electrochemical Data.

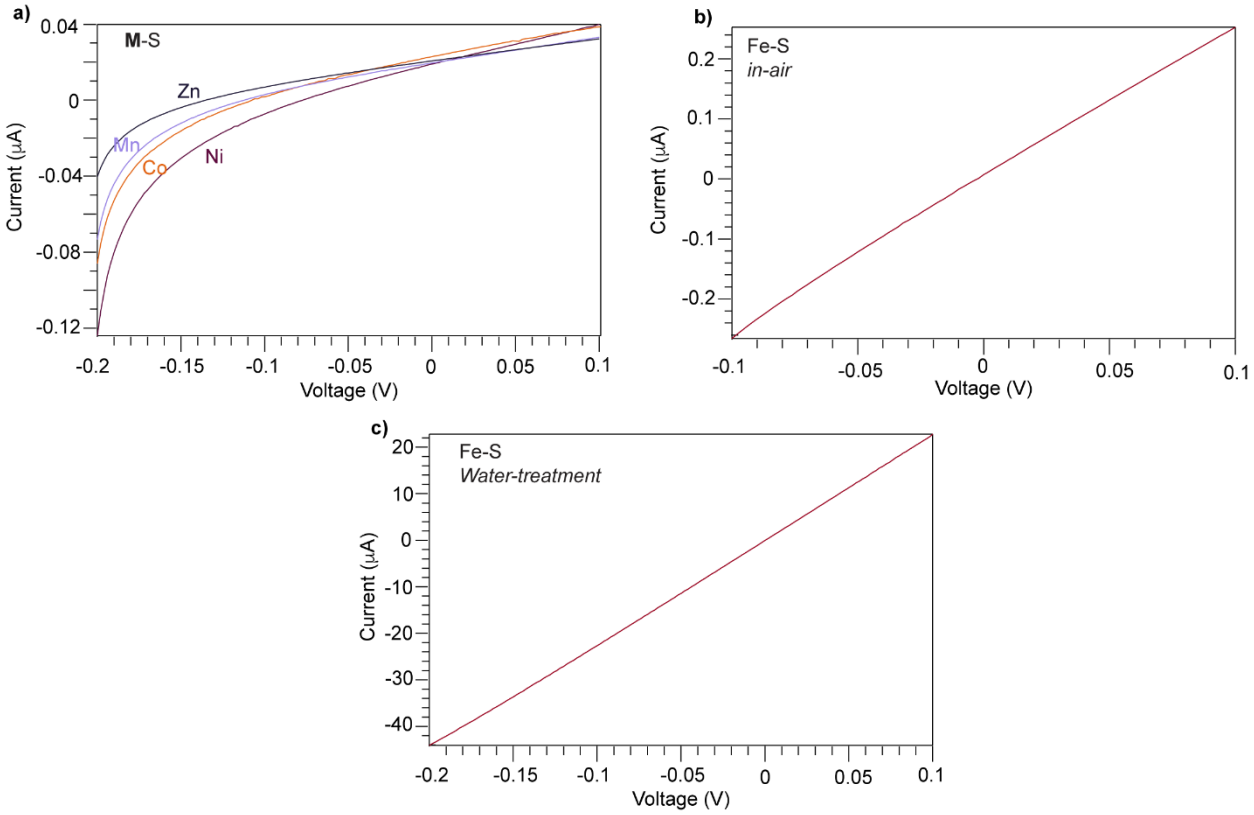

Figure A.39 Representative IV curves from 2 electrode pressed pellet measurements scanned at 2 mV/s for $TMA_2MGe_4S_{10}$ (M: Zn, Mn, Co, and Ni) a), $TMA_2FeGe_4S_{10}$ b), and $TMA_2FeGe_4S_{10}$ post water-treatment c).

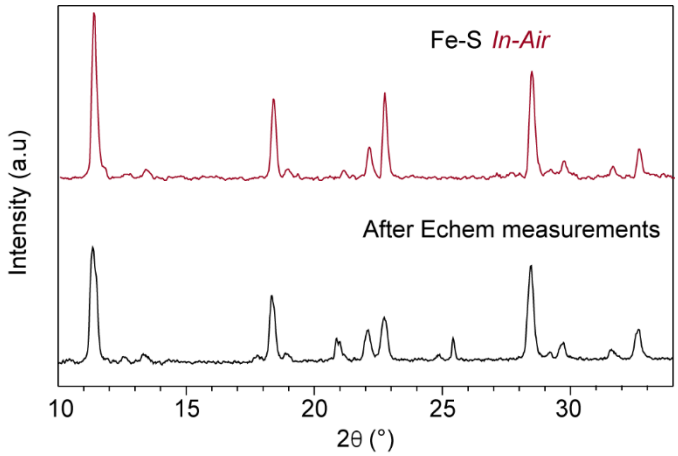

Figure A.40 Experimental powder X-ray diffraction patterns of $TMA_2FeGe_4S_{10}$ pristine (black trace) and after being pelletized at 2000 psi, used in electrochemical oxidation experiments, and left in air for ~10 months (red trace).

APPENDIX B: SUPPLEMENTARY INFORMATION FOR CHAPTER 3

Experimental Methods.

Materials. All commercial chemicals were used as received unless stated otherwise. Germanium powder (99.99%, Sigma Aldrich), sublimed sulfur powder (99%, Strem), tetramethylammonium hydroxide pentahydrate (95%, Oakwood Chemical), iron(II) chloride (anhydrous, Strem), zinc(II) nitrate hexahydrate (98%, Sigma Aldrich), hexanes (98.5%, Fisher Chemical), toluene (99.5%, Fisher Chemical), chloroform (99.9%, Fisher Chemical), tetrahydrofuran (99.9%, Oakwood Chemical), dichloromethane (99.5%, Fisher Chemical), tert-butanol (99%, J.T. Baker), 2-propanol (99%, Fisher Scientific), n-propanol (Macron Chemicals, 99%), acetone (99.5%, Fisher Chemical), ethanol ((200 proof, Decon Labs), methanol (99.8%, Fisher Chemical), formamide (Fisher Chemical, 99.5%), 1,2-dichlorobenzene (99%, Fisher Scientific) and nanopure water (Thermo Scientific, Barnstead Nanopure). Solvothermal syntheses were conducted in autoclave PAAR bombs in Yamato Convection oven unless stated otherwise.

Characterization. Sample purity and crystallinity was verified by powder X-ray diffraction (PXRD) with a Bruker D2 Phaser benchtop diffractometer.

Dry Pressed pellet conductivity measurements. Pressed pellets were prepared by compressing ~30 mg of powders in a modified KBr pellet press die set with a hydraulic press at 500 psi for 30 minutes. The pellet press die set was modified with tinned copper wires affixed to both sides with silver paint and epoxy. Electrical contacts were made by pressing a pellet with the modified die set comprised of stainless-steel circular ends serving as two electrode contacts. Direct-current (DC) conductivities were determined from the slopes of current-voltage (I-V)

curves collected with a GAMRY Instruments Interface 5000E potentiostat, along with the electrode area (0.402 cm^2) and pellet thickness, according to the equation below (where C is the slope of the most linear portion of the I-V curve and m is the pellet thickness):

$$\boldsymbol{DC_\sigma: \frac{C * m}{0.402}}$$

The associated error for conductivity measurements was found by compounding errors from both the pellet dimensions (m and the electrode area) and the linear regression analysis used to find C, using the following equation [where Δm is the error associated with the pellet thickness (0.002 cm, from the precision of the digital calipers utilized) Δa is the error associated with the electrode area (0.0045 cm^2) and ΔC is the error associated with the linear regression performed to obtain the slope:

$$\boldsymbol{\Delta DC_\sigma = DC_\sigma(\frac{\Delta m}{m} + \frac{\Delta a}{0.402} + \frac{\Delta C}{C})}$$

Unless specified otherwise, samples were swept voltammetrically at 2 mV/s between –0.2/(-0.1) and 0.1 V vs OCP compressed by a C-clamp. Temperature-dependent measurements were conducted in a similar fashion with samples kept at fixed temperatures in a Yamato Convection oven.

Dry pressed pellet EIS measurements. Using a setup identical to the pressed pellet conductivity measurements, AC measurements were run with a DC voltage of 0 V vs. OCP with an AC amplitude of 50 mV and 300 mV for $TMA_2FeGe_4S_{10}$ and $TMA_2ZnGe_4S_{10}$ respectively, from 2 MHz to 0.1 Hz.

Solvent dependent pressed pellet EIS measurements ($TMA_2FeGe_4S_{10}$). Using a setup identical to the pressed pellet conductivity measurements, AC measurements were run with a DC voltage of 0 V vs. OCP from 2 MHz to 0.1 (0.01) Hz after the addition of 10 µL of a solvent. An

AC voltage of 50 mV was employed for CH_2Cl_2, IPA, n-propanol, and EtOH; and 10 mV was the AC voltage for MeOH and deionized water. OCP was allowed to stabilize before beginning measurements.

Solvent dependent pressed pellet EIS measurements ($TMA_2ZnGe_4S_{10}$). Using a setup identical to the pressed pellet conductivity measurements, AC measurements were run with a DC voltage of 0 V vs. OCP from 2 MHz to 0.1 Hz after the addition of 10 μL of a solvent. An AC voltage of 50 mV was employed for CH_2Cl_2, IPA, n-propanol, EtOH, MeOH and deionized water. OCP was allowed to stabilize before beginning measurements.

Synthetic Procedures.

$TMA_4Ge_4S_{10}$. Following a procedure outlined in our previous report,1 germanium powder (1 g, 13.76 mmol), sulfur powder (1.77 g, 6.88 mmol), and water (7.44 g, 412.8 mmol) were added to a Teflon Parr bomb. While slowly stirring this mixture with a glass rod, tetramethyl ammonium hydroxide pentahydrate (4.99 g, 27.5 mmol) was added and then the Parr bomb was sealed and placed in a fixed-temperature oven at 150 °C for 15h. The resulting yellow solution was vacuum filtered to remove unreacted germanium and then ~500 ml of acetone was added to induce precipitation of a white solid. The white powder was washed with acetone (20 ml ×3), hot toluene (20 ml ×3), and hexanes (20 ml ×3), then dried overnight under dynamic vacuum to afford an off- white powder. The resulting product was stored under ambient conditions.

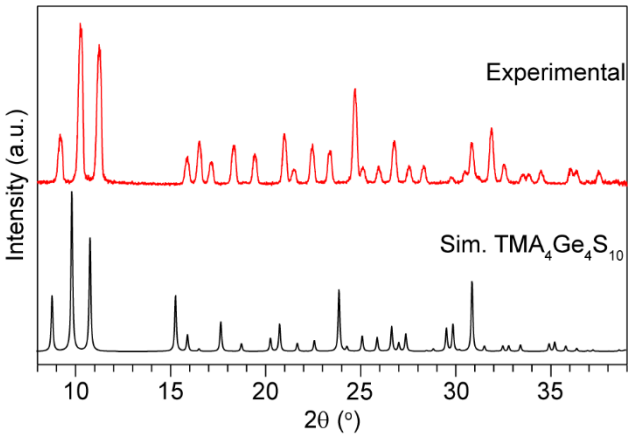

Figure B.1 Experimental (red trace) and simulated (black trace) powder X-ray diffraction patterns of $TMA_4Ge_4S_{10}$.

All procedures were followed as outlined in our previous report.[123]

$TMA_2FeGe_4S_{10}$. Anhydrous iron(II) chloride (0.050 g, 0.40 mmol) and $TMA_4Ge_4S_{10}$ (0.18 g, 0.20 mmol) were dissolved in 4 ml and 8 ml of N_2-sparged DI water, respectively under positive nitrogen atmosphere. The iron solution was added dropwise to the $TMA_4Ge_4S_{10}$ solution

over the course of ~2 minutes. The solution was allowed to react at room temperature for ~12h. The bright-orange solid was washed with sparged DI water (15 ml × 2), ethanol (15 ml × 2), and hexanes (15 ml × 2) sequentially. Then, the solid was dried with a stream of nitrogen and stored under positive N_2 atmosphere.

$TMA_2ZnGe_4S_{10}$. Zinc(II) nitrate hexahydrate (0.12 g, 0.40 mmol) and $TMA_4Ge_4S_{10}$ (0.18 g, 0.20 mmol) were dissolved in 4 and 8 ml of DI water, respectively. The zinc solution was added dropwise to the $TMA_4Ge_4S_{10}$ solution over the course of ~2 minutes. The resulting solution was left to react at room temperature for ~12h. The white solid was washed with DI water (15 ml × 3) and then dried in a fixed temperature oven at 150 °C for ~12 h. The resulting material was stored under ambient conditions.

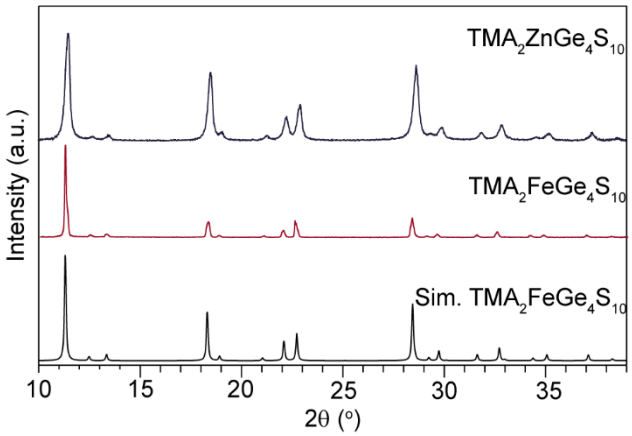

Figure B.2 Experimental powder X-ray diffraction patterns for $TMA_2MGe_4S_{10}$ (M: Fe and Zn) compared against a simulated pattern of $TMA_2FeGe_4S_{10}$.

DC Electrochemical Analyses.

Diffusion coefficients were obtained by plotting the current from chronoamperometry experiments vs. the sqrt(t) and utilizing the equation below (where n is number of electrons (1), F is Faraday's constant, D_0 is the diffusion coefficient, C_0 is the concentration of TMA^+, and A (0.402 cm^2) is the area of the electrode). The concentration of TMA^+ was calculated given the crystal structure for $TMA_2FeGe_4S_{10}$.[78]

$$i(t) = \frac{nFAD_0C_0}{\pi^{1/2}t^{1/2}}$$

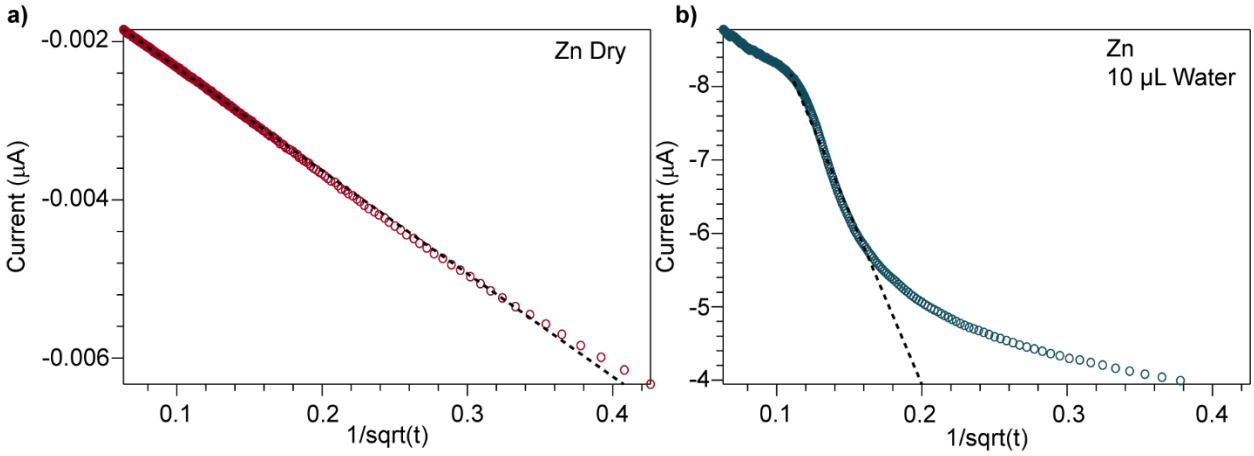

Figure B.3 Cottrell plots for the current transients obtained at -0.2V of a pressed pellet of $TMA_2ZnGe_4S_{10}$ before a) and after b) the addition of 10 µL of deionized water. The dotted trace fits are used to obtain diffusion coefficients.

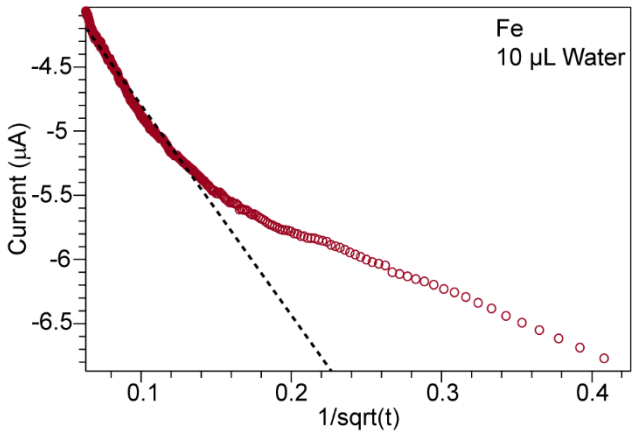

Figure B.4 Cottrell plots for the current transients obtained at -0.2V of a pressed pellet of $TMA_2FeGe_4S_{10}$ after the addition of 10 µL of deionized water. The dotted trace fits are used to obtain diffusion coefficients.

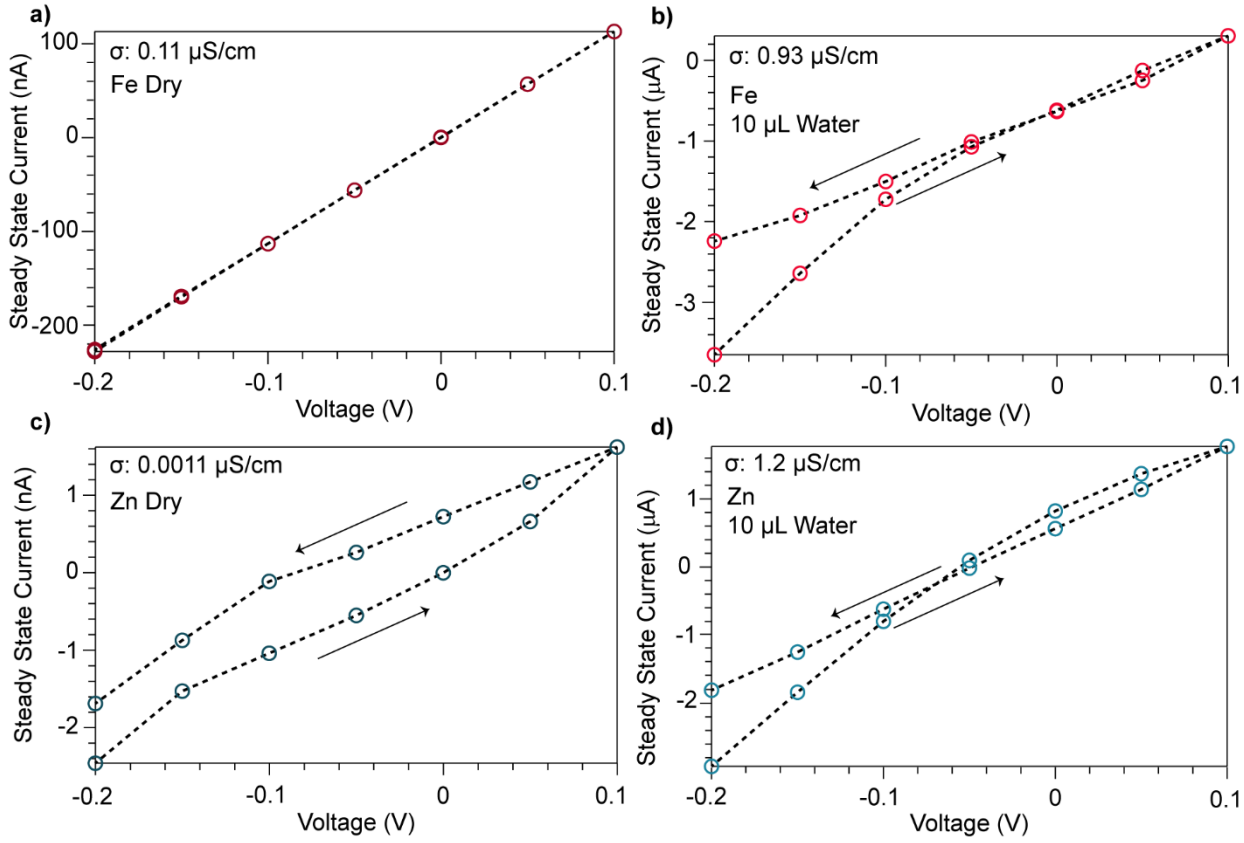

Figure B.5 Steady-state current values vs. applied potential derived from chronoamperometry experiments for pressed pellets of $TMA_2FeGe_4S_{10}$ before a) and after b) the addition of 10µL of deionized water and pressed pellets of $TMA_2ZnGe_4S_{10}$ before c) and after the addition of 10µL of deionized water d). Arrows denote the direction of potential scanned. Conductivity values are displayed and calculated from the slope of the return scan.

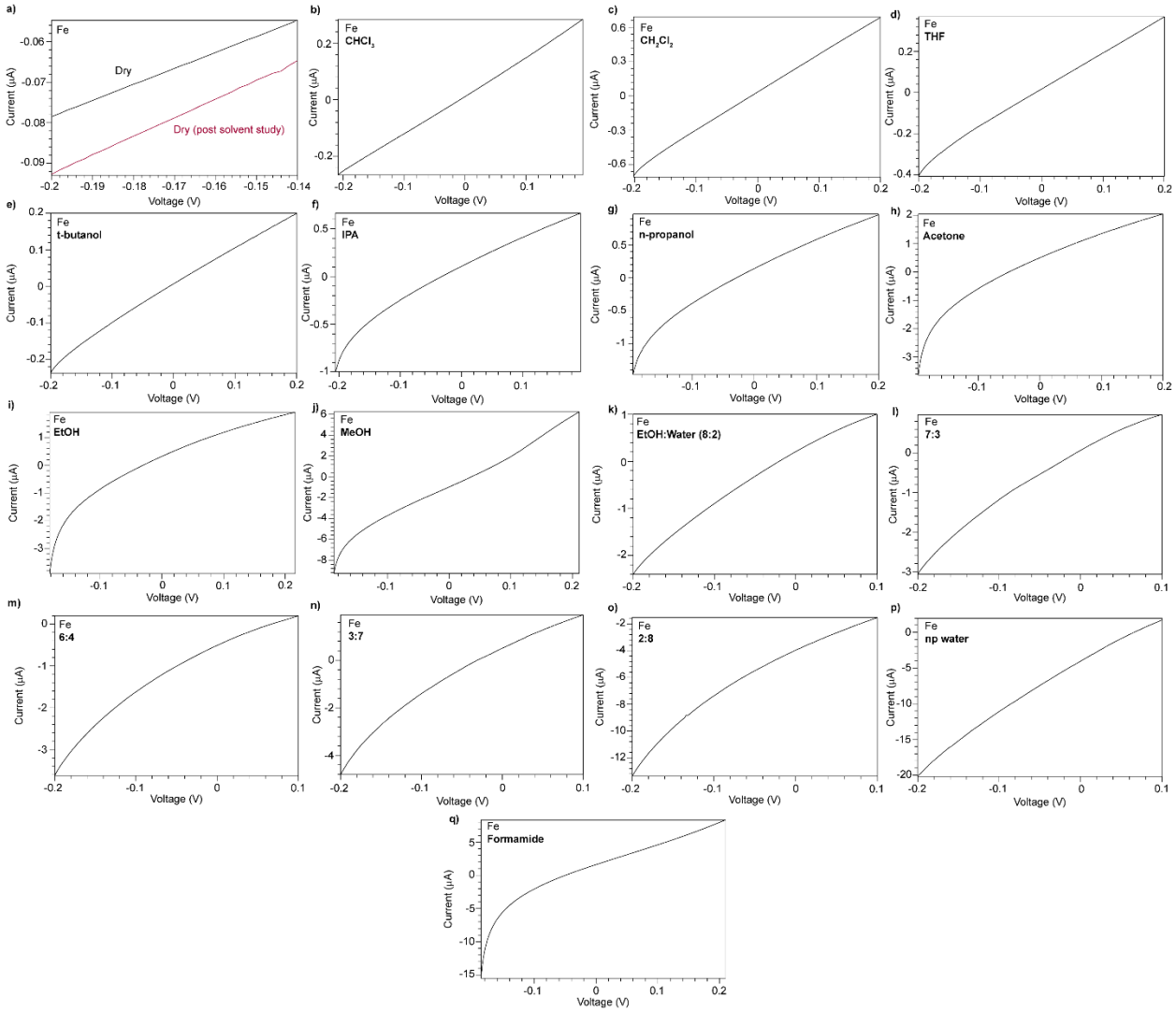

Figure B.6 I-V curves measured for pressed-pellets of $TMA_2FeGe_4S_{10}$ scanned at 2mV/s subjected to various conditions: Dry a), $CHCl_3$ b), CH_2Cl_2 c), THF d), t-butanol e), IPA f), n-propanol g), acetone h), EtOH i), MeOH j) EtOH:Water mixtures [8:2 k), 7:3 l), 6:4 m), 3:7 n), 2:8 o)], deionized water p), and formamide q).

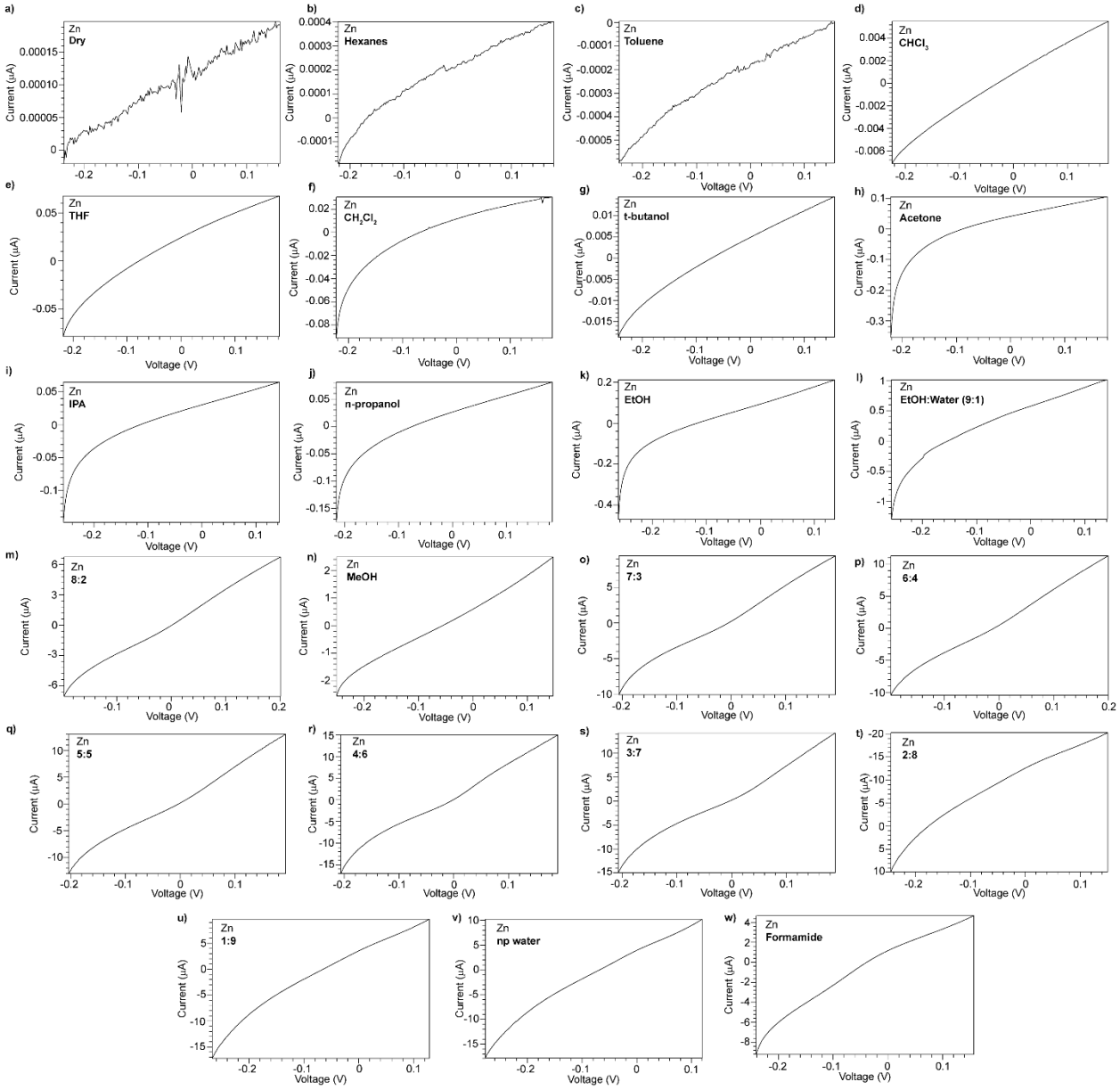

Figure B.7 I-V curves for pressed pellets of $TMA_2ZnGe_4S_{10}$ scanned at 2mV/s subjected to various conditions: Dry a), hexanes b), toluene c), $CHCl_3$ d), THF e), CH_2Cl_2 f), t-butanol g), acetone h), IPA i), n-propanol j), EtOH k), MeOH n) EtOH:Water mixtures [9:1 l). 8:2 m), 7:3 o), 6:4 p), 5:5 q), 4:6 (r), 3:7 s), 2:8 t), 1:9 u)], deionized water v), and formamide w).

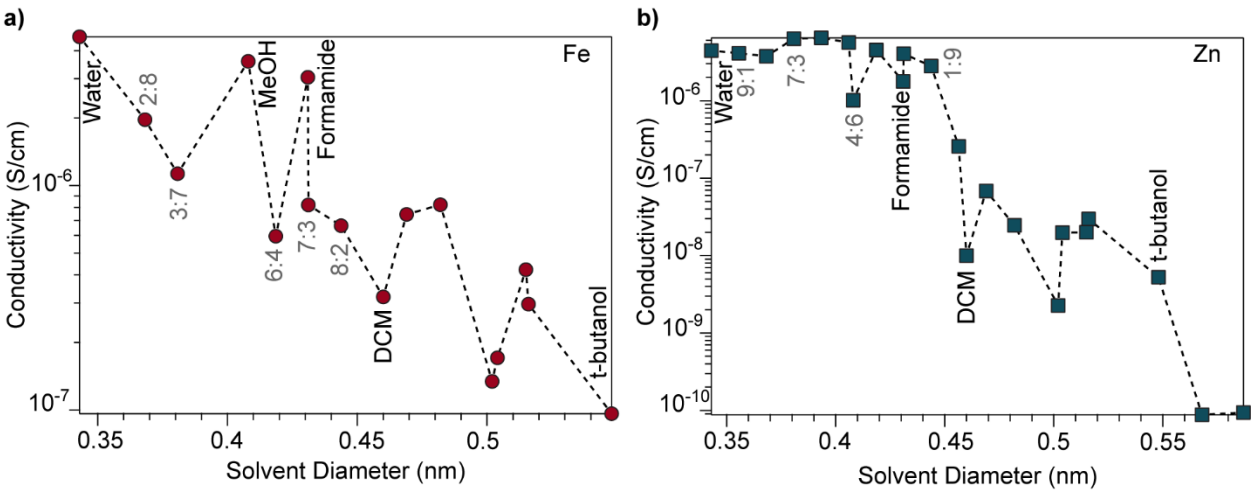

Figure B.8 Solvent-dependent DC conductivity values of $TMA_2FeGe_4S_{10}$ a) and $TMA_2ZnGe_4S_{10}$ b) pressed-pellets obtained from linear fits to I-V curves swept voltammetrically between –0.2 V and 0.2 V. The conductivity values are plotted vs. solvent size.

Electrochemical Impedance Analysis.

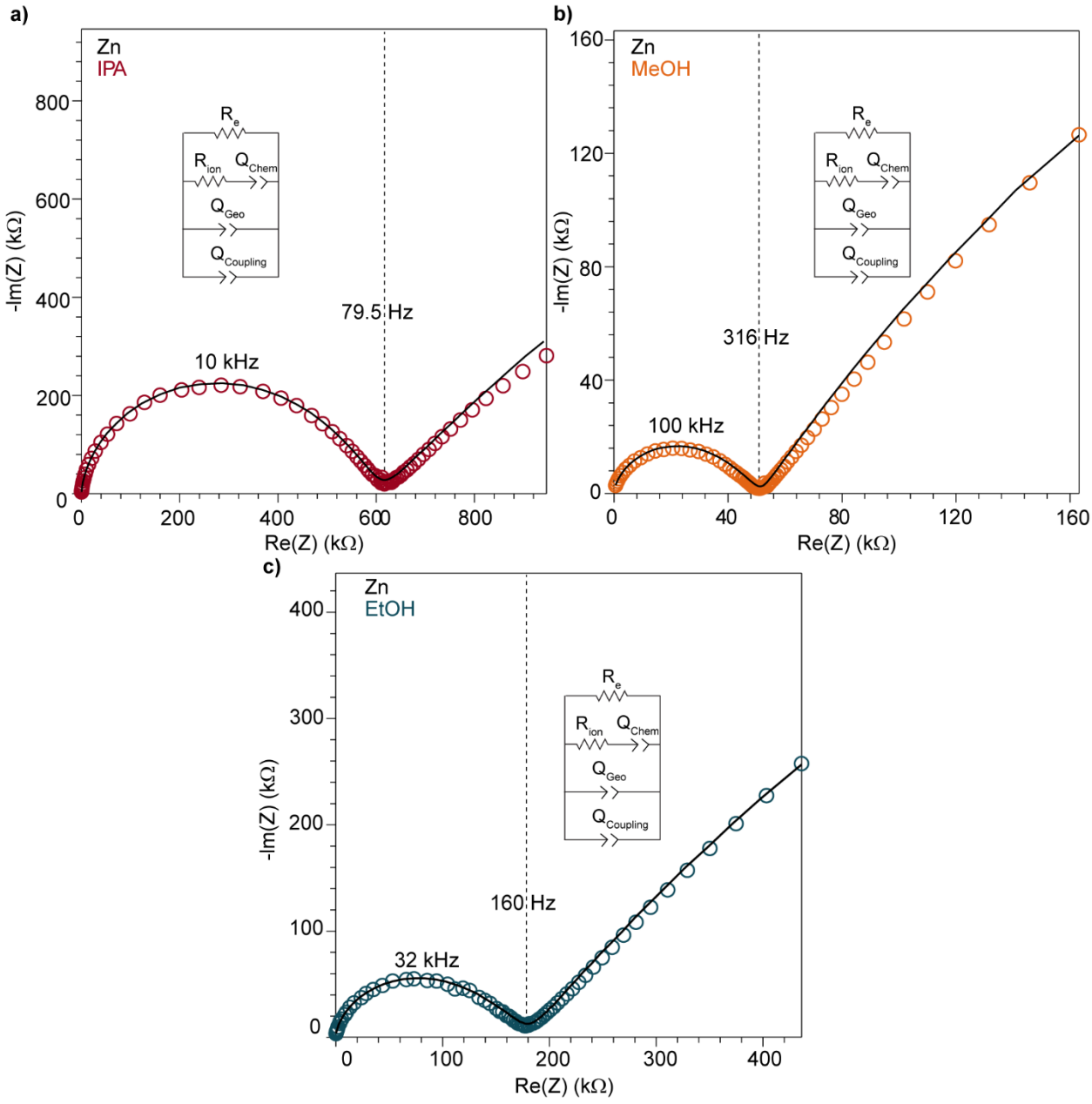

Figure B.9 Nyquist plots of $TMA_2ZnGe_4S_{10}$ pressed pellets after addition of IPA a), MeOH b), and EtOH c). Black traces represent fits to the equivalent circuit diagrams shown in the figure area.

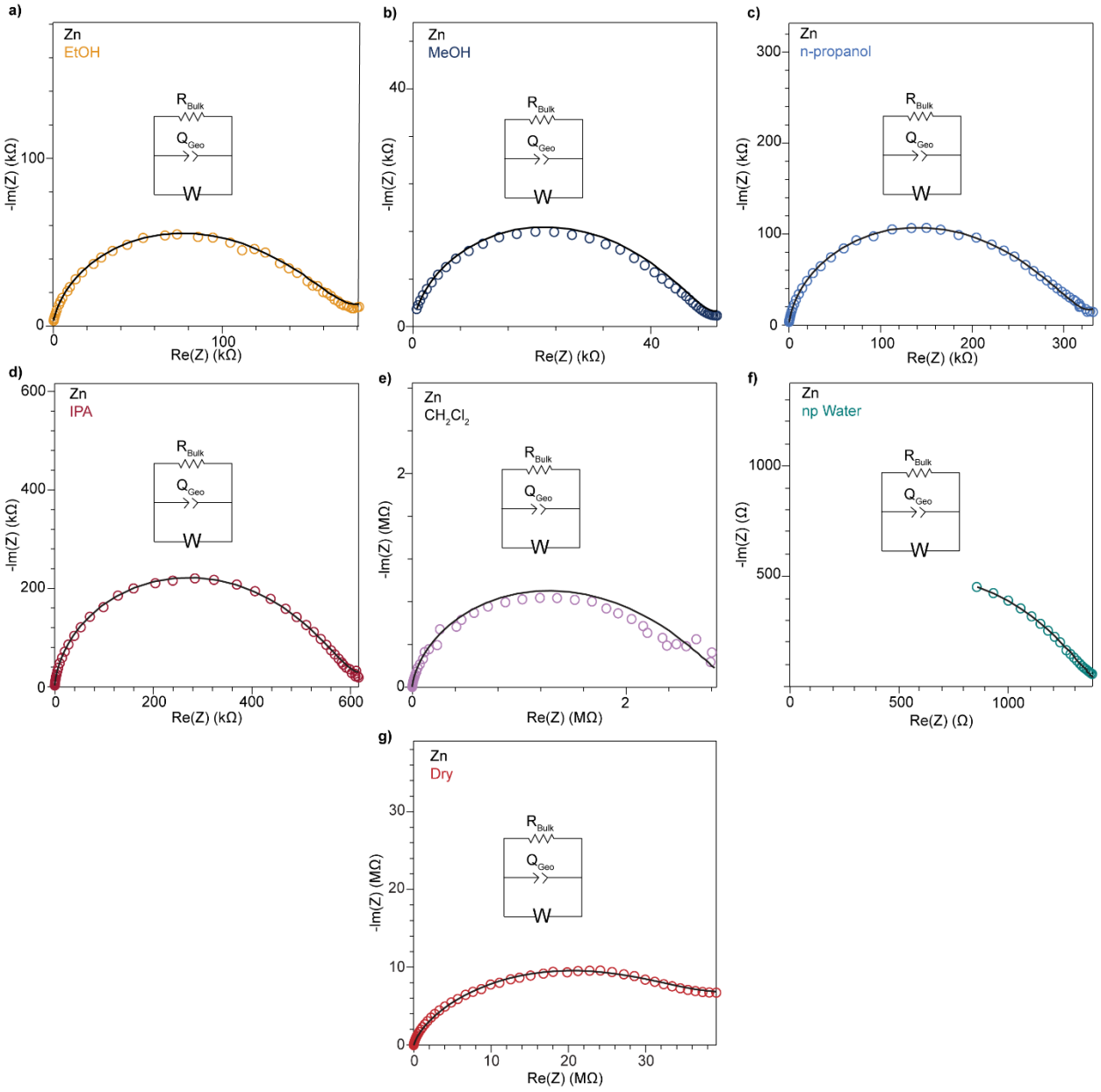

Figure B.10 Nyquist plots of $TMA_2ZnGe_4S_{10}$ pressed-pellets focused on the high frequency domain after addition of EtOH a), MeOH b), n-propanol c), IPA d), CH_2Cl_2 e), deionized water f), and dry g). Black traces represent fits to the displayed equivalent circuit diagrams and emphasize the effect of replacing a CPE for a Warburg element.

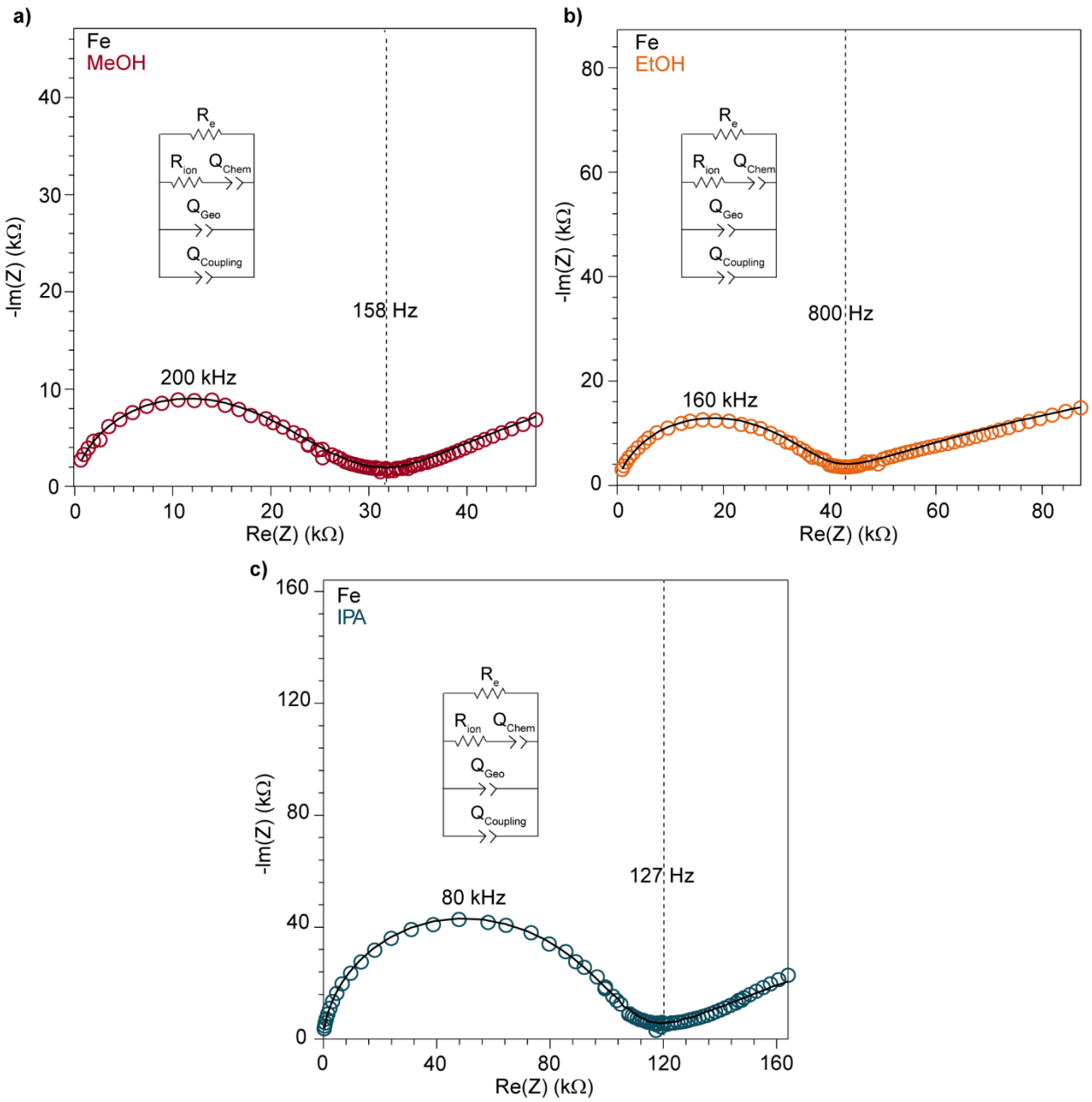

Figure B.11 Nyquist plots of $TMA_2FeGe_4S_{10}$ pressed pellets after addition of MeOH a), EtOH b), and IPA c). Black traces represent fits to the equivalent circuit diagrams shown in the figure area.

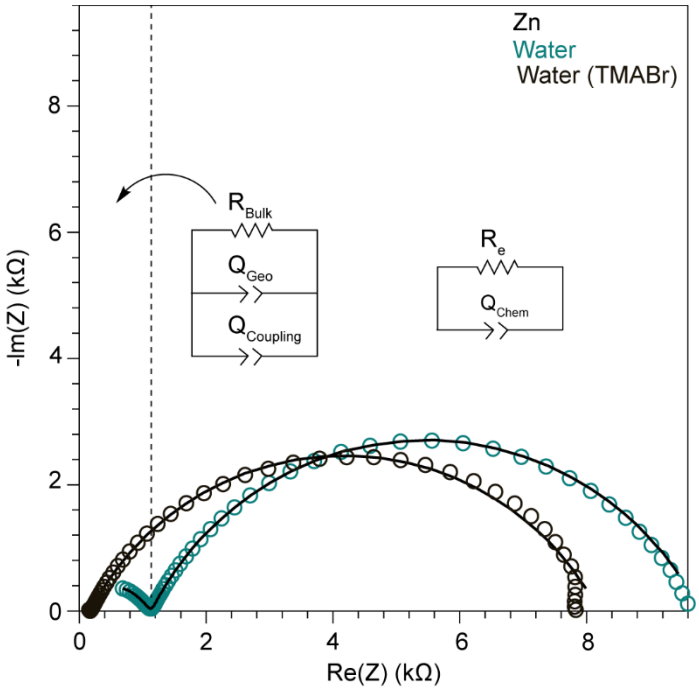

Figure B.12 Nyquist plots of $TMA_2ZnGe_4S_{10}$ pressed pellets after addition of deionized water a), and a 0.1M TMABr aqueous solution b). Black traces represent fits to the equivalent circuit diagram shown in the figure area.

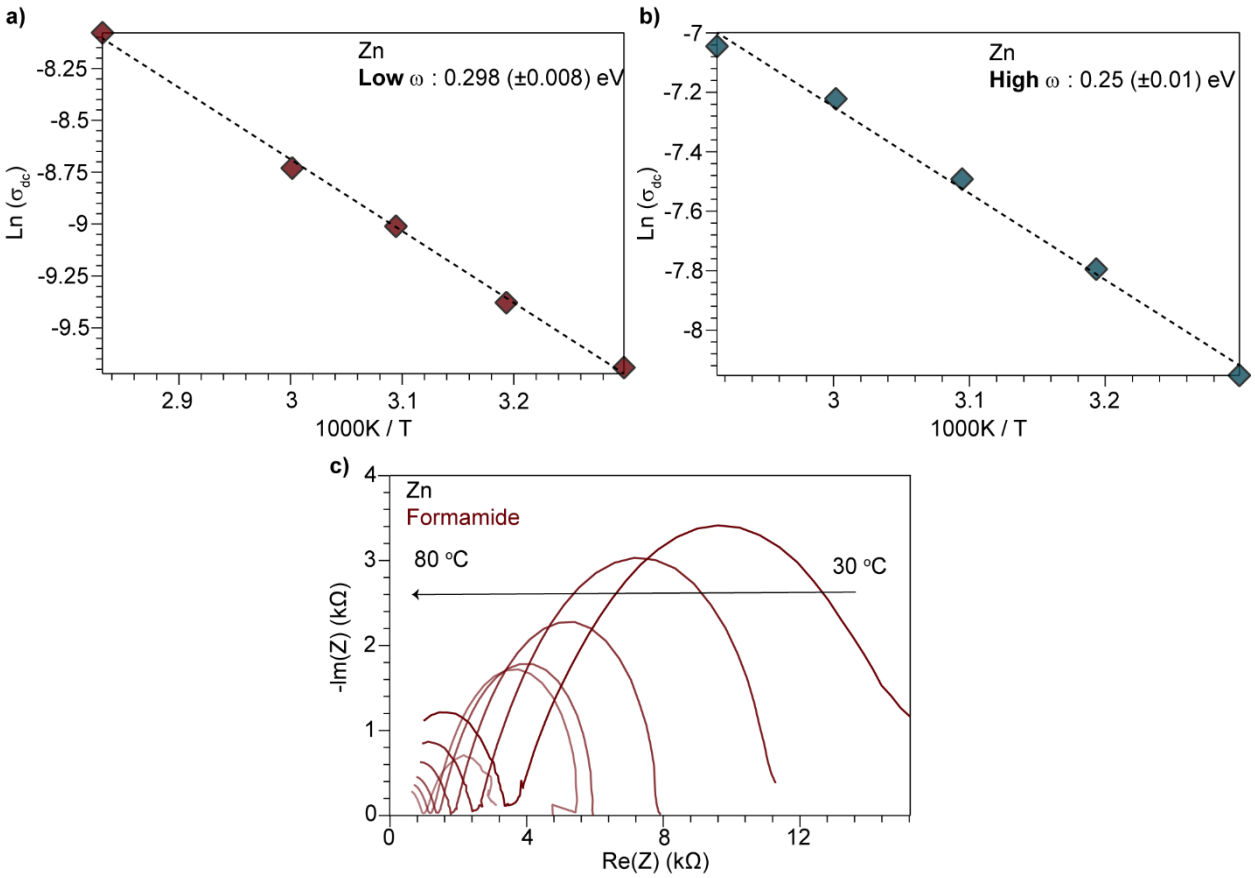

Figure B.13 Arrhenius plots for the low a) and high b) frequency *x*-intercept resistances from temperature-dependent EIS performed on pressed pellets of $TMA_2ZnGe_4S_{10}$ after formamide treatment c).

Solvent	Circuit Element	Fitted Value	Error (%)	Solvent	Circuit Element	Fitted Value	Error (%)
n-propanol	Bulk Q	0.039 nS.S^n	1.16				
	n						
	Chemical Q	19 µS.S^n	3.65				
	n	0.31	4.24				
	Ionic Resistance	87 kΩ	2.54	*Water*	Bulk Q	0.074 nS.S^n	7.99
	Electronic Resistance	395 kΩ	2.54		n	1	0.48
	Coupling Q	0.12 µS.S^n	3.5		Chemical Q	77 µS.S^n	2.31
	n	0.3	0.96		n	0.4	1.45
IPA	Bulk Q	0.025 nS.S^n	1.32		Ionic Resistance	1.3 kΩ	1.39
	n	0.99	0.089		Electronic Resistance	N/A	N/A
	Chemical Q	16 µS.S^n	4.74		Coupling Q	33 µS.S^n	4.3
	n	0.27	5.95		n	0.15	3.17
	Ionic Resistance	132 kΩ	0.84		Contact Resistance	200 Ω	0.4
	Electronic Resistance	0.092 MΩ	4.63	*DCM*	Bulk Q	0.042 nS.S^n	1.16
	Coupling Q	27 nS.S^n	5.2		n	0.96	0.08
	n	0.37	1.09		Chemical Q	N/A	N/A
MeOH	Bulk Q	0.063 nS.S^n	2.07		n	N/A	N/A
	n	0.95	0.14		Ionic Resistance	N/A	N/A
	Chemical Q	39 µS.S^n	5.74		Electronic Resistance	449 kΩ	0.86
	n	0.32	6.5		Coupling Q	8.2 nS.S^n	2.6
	Ionic Resistance	42 kΩ	1.16		n	0.29	0.86
	Electronic Resistance	145 kΩ	3.07				
	Coupling Q	0.35 µS.S^n	3.5	Dry	Bulk Q	0.036 nS.S^n	1.3
	n	0.3	0.9		n	0.97	0.09
EtOH	Bulk Q	0.032 nS.S^n	2.15		Chemical Q	N/A	N/A
	n	0.97	0.14		n	N/A	N/A
	Chemical Q	12 µS.S^n	2.23		Ionic Resistance	N/A	N/A
	n	0.25	2.22		Electronic Resistance	1.13 MΩ	0.93
	Ionic Resistance	44 kΩ	1.12		Coupling Q	7.8 nS.S^n	6.5
	Electronic Resistance	240 kΩ	2.7		n	0.37	1.7
	Coupling Q	11 nS.S^n	2.97				
	n	0.54	0.38				

Table B.1 Equivalent circuit fit parameters and their associated percent error for pressed pellet EIS performed on $TMA_2FeGe_4S_{10}$.

Solvent	Circuit Element	Fitted Value	Error (%)	Solvent	Circuit Element	Fitted Value	Error (%)
n-propanol	Bulk Q	0.022 nS.S^n	1.69	*DCM*	Bulk Q	0.030 nS.S^n	2.5
	n	1	0.12		n	0.98	0.18
	Chemical Q	3.2 µS.S^n	4.7		Chemical Q	N/A	N/A
	n	0.6	3.97		n	N/A	N/A
	Ionic Resistance	373 kΩ	1.12		Ionic Resistance	3.1 MΩ	3.3
	Electronic Resistance	3.22 MΩ	8.1		Electronic Resistance	N/A	N/A
	Coupling Q	8.4 nS.S^n	3.89		Coupling Q	4.3 nS.S^n	5.7
	n	0.48	0.66		n	0.45	1.5
IPA	Bulk Q	0.022 nS.S^n	1.23	*Water*	Bulk Q	0.051 nS.S^n	5.75
	n	1	0.09		n	1	0.35
	Chemical Q	2.4 µS.S^n	4.29		Chemical Q	20 µS.S^n	1.4
	n	0.52	4.2		n	0.71	0.46
	Ionic Resistance	686 kΩ	0.91		Ionic Resistance	1.1 kΩ	0.74
	Electronic Resistance	5.93 MΩ	6.7		Electronic Resistance	9.6 kΩ	0.97
	Coupling Q	2.2 nS.S^n	4.1		Coupling Q	0.46 µS.S^n	5.9
	n	0.55	0.6		n	0.41	0.93
MeOH	Bulk Q	0.031 nS.S^n	3.2		Contact Resistance	150 Ω	3.5
	n	0.98	0.21	*w/ TMABr*	Bulk Q	N/A	N/A
	Chemical Q	7 µS.S^n	3.53		n	N/A	N/A
	n	0.62	2.6		Chemical Q	31 µS.S^n	1
	Ionic Resistance	55 kΩ	1.39		n	0.7	0.3
	Electronic Resistance	1.03 MΩ	5.2		Ionic Resistance	180 Ω	1.02
	Coupling Q	22 nS.S^n	5.7		Electronic Resistance	8.2 kΩ	0.93
	n	0.48	0.84		Coupling Q	0.32 µS.S^n	10.8
EtOH	Bulk Q	0.021 nS.S^n	2.35		n	0.5	1.3
	n	1	0.16	*Dry*	Bulk Q	0.028 nS.S^n	5.5
	Chemical Q	3 µS.S^n	3.6		n	1	0.8
	n	0.56	2.96		Chemical Q	0.13 µS.S^n	2
	Ionic Resistance	193 kΩ	1.3		n	0.4	2.4
	Electronic Resistance	1.84 MΩ	3.75		Ionic Resistance	40 MΩ	0.37
	Coupling Q	11 nS.S^n	3.99		Electronic Resistance	N/A	N/A
	n	0.5	0.62		Coupling Q	2.8 nS.S^n	6.7
					n	0.48	0.44

Table B.2 Equivalent circuit fit parameters and their associated percent error for pressed pellet EIS performed on $TMA_2ZnGe_4S_{10}$.

Temperature Dependent DC Conductivity.

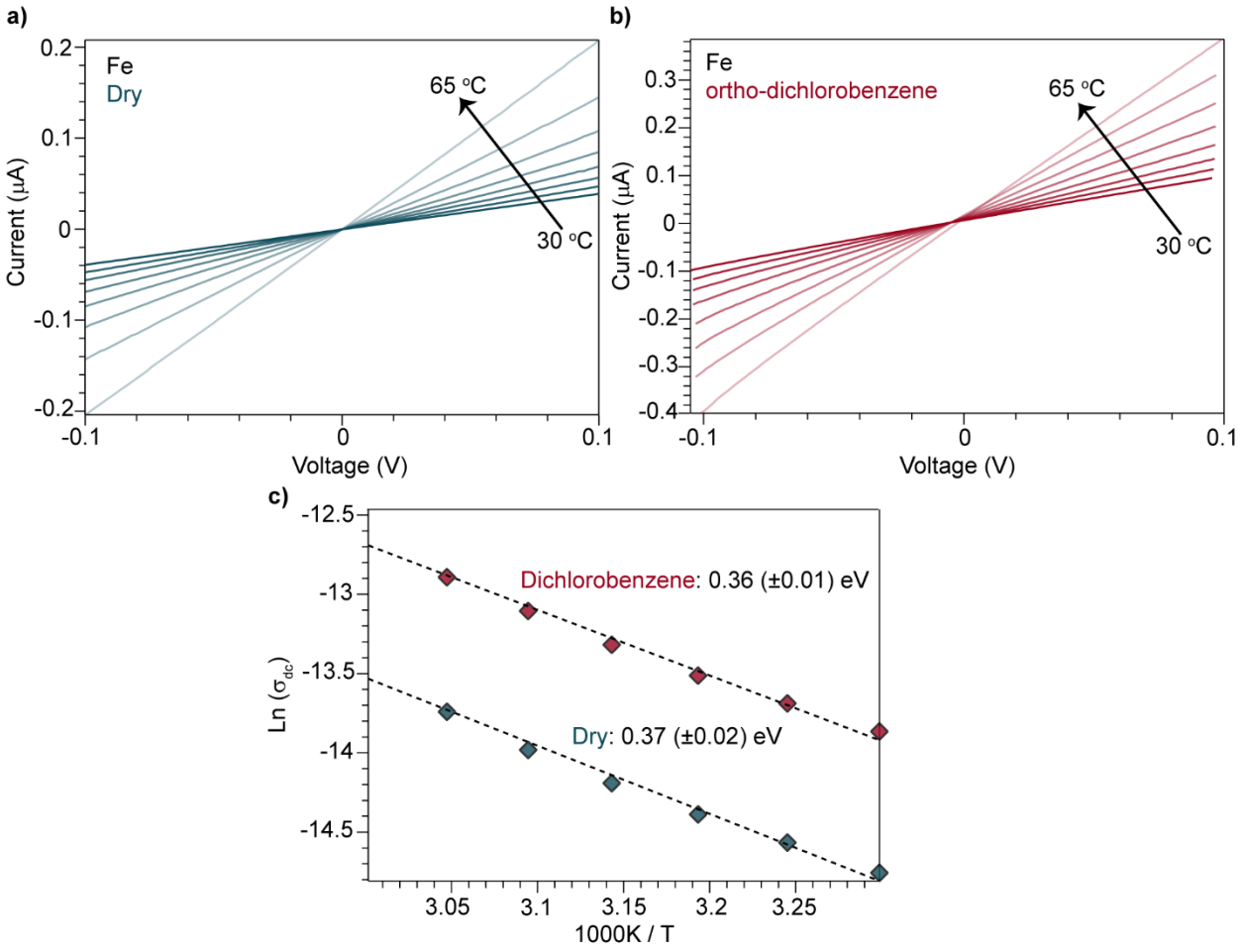

Figure B.14 I-V curves for pressed pellets of $TMA_2FeGe_4S_{10}$ scanned at 2mV/s from 30 - 65 °C before a) and after b) the addition of ortho-dichlorobenzene. Arrhenius fits (dotted traces) provide electronic conduction activation barriers for dry (blue) and ortho-dichlorobenzene (red).

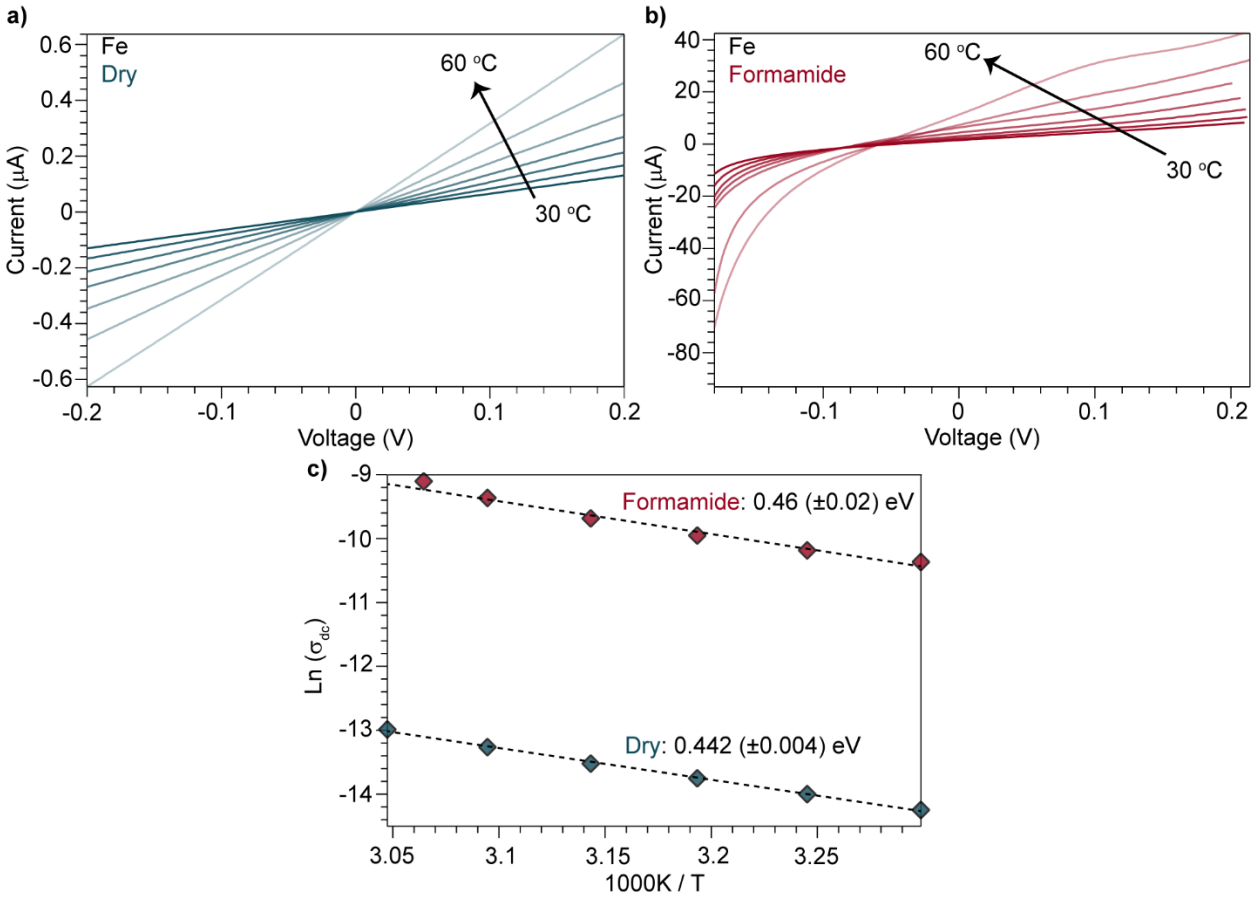

Figure B.15 I-V curves for pressed pellets of $TMA_2FeGe_4S_{10}$ scanned at 2mV/s from 30 - 60 °C before a) and after b) the addition of formamide. Arrhenius fits (dotted traces) provide electronic conduction activation barriers for dry (blue) and formamide (red).

APPENDIX C: SUPPLEMENTARY INFORMATION FOR CHAPTER 4

Experimental Methods.

Materials. All commercial chemicals were used as received unless stated otherwise. Iron(II) sulfate heptahydrate (ACS grade, Fisher Chemical), iron(II) chloride (anhydrous, Strem), potassium thiocyanate (ACS grade, Fisher Chemical), potassium selenocyanate (99%, Thermo Scientific Chemicals), pyrazine (99%, Sigma Aldrich), 4,4'-Bipyridine (98%, Fisher Chemical), tetrabutylammonium hexafluorophosphate (recrystallized ×3 from EtOH) (99%, Fisher Chemical), tetrabutylammonium tetrafluoroborate (recrystallized ×3 from MeOH/water mixtures) (99%, Fisher Chemical), tetrabutylammonium nitrate (98%, Fisher Scientific), ferrocenium tetrafluoroborate (technical grade, Sigma Aldrich), Diethyl ether (99%, Fisher Chemical), tetrahydrofuran (99.9%, Oakwood Chemical), N.N-Dimethylformamide (ACS grade, Fisher Chemical), dichloromethane (99.5%, Fisher Chemical), tert-butanol (99%, J.T. Baker), n-propanol (Macron Chemicals, 99%), acetone (99.5%, Fisher Chemical), ethanol ((200 proof, Decon Labs), methanol (99.8%, Fisher Chemical), Scientific) and nanopure water (Thermo Scientific, Barnstead Nanopure).

Characterization. Sample purity and crystallinity was verified by powder X-ray diffraction (PXRD) with a Bruker D2 Phaser benchtop diffractometer. Transmission electron microscope (TEM) images were collected with a FEI Tecnai by drop casting concentrated suspensions of nanosheet methanolic solutions onto carbon coated copper TEM grids, then drying in air. Solution state UV-Vis was collected on a Agilent Cary 5000 spectrophotometer and DR UV-Vis-NIR was collected on the same instrument with a Harrick Scientific Praying Mantis Diffuse Reflection (DRP) accessory. Reflectance samples were diluted and the

instrument was baselined with barium sulfate. Infrared Spectroscopy was collected with a Bruker Alpha II compact IR with an ATR attachment.

^{57}Fe Mössbauer Spectroscopy. All samples were characterized by a SEE Co. ^{57}Fe Mössbauer spectrometer equipped with a Janis SVT-400 cryostat. The samples were prepared under a nitrogen atmosphere by placing up to 30 mg of fine powder in a 14.5 mm Teflon cup with a Teflon plunger pressed into the cup to hold the sample. Data were collected until the signal-to-noise was deemed sufficient for meaningful analysis. This was dependent on the amount of sample loaded and the intensity of the source but was typically longer than 1 week. Samples were maintained under a nitrogen atmosphere for the duration of the experiment. Calibration of the instrument was performed using a standard iron sample provided by SEE Co. The data were analyzed using the Mössbauer spectral analysis software WMOSS4[214] written by Tom Kent and recently developed by Ion Prisecaru. The raw data were folded and calibrated using the iron standard supplied to us. The folded data were then fit to an appropriate model. We used two models to fit the data for this paper: the first is used for a pair of quadrupole doublets, and the second model is for a single quadrupole doublet. We used these models to refine the relevant parameters such as the shift of the quadrupole peak and the relative area of the peaks.

Chemical Oxidation of Fe-SCN-pyz with $FcBF_4$. Under inert N_2 atmosphere, the ferrocenium tetrafluoroborate stock solution was made by dissolving 0.070 g of ferrocenium tetrafluoroborate in 15 mL of THF and left to stir overnight. Under inert N_2 atmosphere, 0.0318 g of Fe-SCN-pyz powder was exfoliated in 20 ml of MeOH via ultrasonication. To 4 vials 4 ml of the Fe-SCN-pyz stock solution were added and 112, 280, 560, and 896 µL was added to each vial respectively (0.1 – 0.8 eq.). The solutions were left to stir for 48 hours. The resulting

solutions were dried down under dynamic vacuum and washed by ultrasonication with 10 ml of hexanes.

SpectroElectrochemistry of Suspensions of Fe-SCN-pyz. Under an inert N_2 atmosphere, in a typical experiment 25 mg of Fe-SCN-pyz was exfoliated in 25 ml of MeOH via ultrasonication. 1 ml of this solution was added to a vial and dried down under dynamic vacuum and resuspended in 8 ml of MeCN along with 310 mg of $TBAPF_6$ (recrystallized ×3 from EtOH). From this solution 4 ml was added into an quartz cuvette along with a platinum mesh working electrode, a platinum wire counter electrode, and a silver pseudoreference electrode. Under an N_2 atmosphere, in a ThorLabs cuvette holder with multimode step index fiber optic patch cables connected to a Agilent Cary 5000 spectrophotometer, UV-Vis spectra between 350-700nm were collected every 2 minutes as a potential is applied to the cuvette solution by a GAMRY Instruments Interface 5000E potentiostat.

Synthetic Procedures.

$Fe(SCN)_2(pyz)_2$. Following reported synthetic procedures,[193] 277.7 mg of $FeSO_4.7H_2O$, 160 mg of pyrazine, and 194 mg of KSCN are dissolved in 5 ml of DI water respectively. While stirring the $FeSO_4$ solution the KSCN solution is added drop-wise, followed by drop-wise addition of pyrazine. The solution was allowed to stir for 24h at RT. The resulting bright orange product was washed with water (15 ml ×2), EtOH (15 ml ×1), and diethyl ether (15 ml ×1). The product was dried overnight at RT under dynamic vacuum.

$Fe(SeCN)_2(pyz)_2$. 277.7 mg of $FeSO_4.7H_2O$, 160 mg of pyrazine, and 288 mg of KSCN are dissolved in 5 ml of DI water respectively. While stirring the $FeSO_4$ solution the KSeCN solution is added drop-wise, followed by drop-wise addition of pyrazine. The solution was allowed to stir for 24h at RT. The resulting bright orange product was washed with water (15 ml ×2), EtOH (15 ml ×1), and diethyl ether (15 ml ×1). The product was dried overnight at RT under dynamic vacuum.

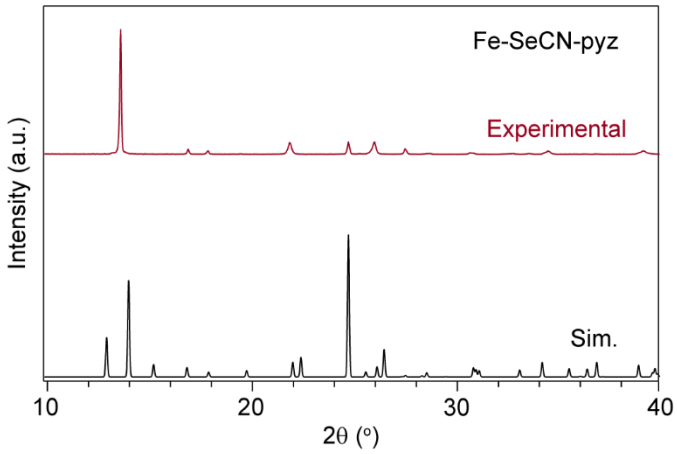

Figure C.1 Experimental (red trace) and simulated (black trace) powder X-ray diffraction patterns of $Fe(SeCN)_2(pyz)_2$.

$Fe(SCN)_2(4,4'\text{-Bipyridine})_2$. Following reported synthetic procedures,[225,226] 277.7 mg of $FeSO_4.7H_2O$, 306 mg of 4,4'-Bipyridine, and 194 mg of KSCN are dissolved in 5 ml of DI water respectively. While stirring the $FeSO_4$ solution the KSCN solution is added drop-wise, followed by drop-wise addition of 4,4'-Bipyridine. The solution was allowed to stir for 24h at RT. The resulting bright orange product was washed with water (15 ml ×2), EtOH (15 ml ×1), and diethyl ether (15 ml ×1). The product was dried overnight at 120 °C under dynamic vacuum.

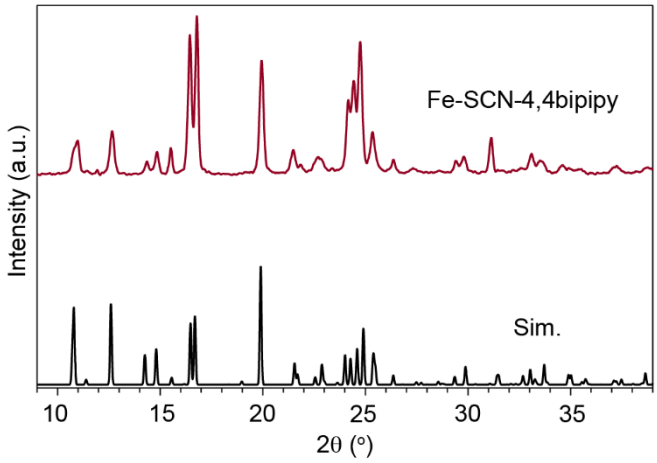

Figure C.2 Experimental (red trace) and simulated (black trace) powder X-ray diffraction patterns of desolvated $Fe(SCN)_2(4,4'\text{-Bipyridine})_2$.

$Fe(Cl)_2(pyz)_2$. Following reported synthetic procedures,[227] 100 mg of anhydrous chloride and 705 mg of pyrazine are dissolved in 4 and 1 ml of EtOH respectively. While stirring the $FeCl_2$ solution, the pyrazine solution is added drop-wise. The solution was allowed to stir for 24h at RT. The resulting bright red product was washed with EtOH (15 ml ×1), and diethyl ether (15 ml ×1). The product was dried overnight at RT under dynamic vacuum. A Rietveld refinement of the powder X-ray diffraction pattern obtained was performed on the product, using the known pattern from $Ni(Cl)_2(pyz)_2$.[228]

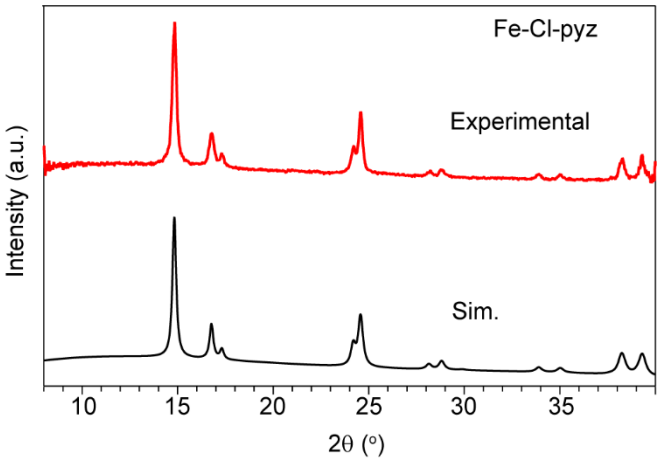

Figure C.3 Experimental (red trace) and simulated (black trace) powder X-ray diffraction patterns of $Fe(Cl)_2(pyz)_2$. The simulated pattern is the result of a Rietveld refinement from the known crystal structure of $Ni(Cl)_2(pyz)_2$.

Solution State and DR UV-Vis-NIR.

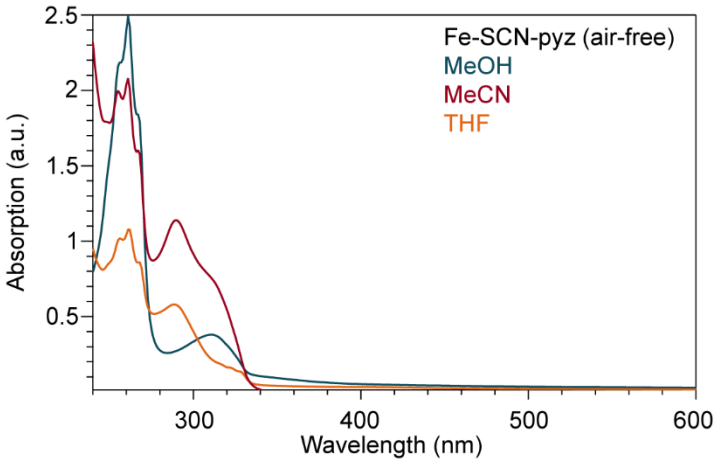

Figure C.4 UV-Vis spectrum of exfoliated Fe-SCN-pyz nanosheets suspended in MeOH, MeCN, and THF under inert N_2 atmosphere.

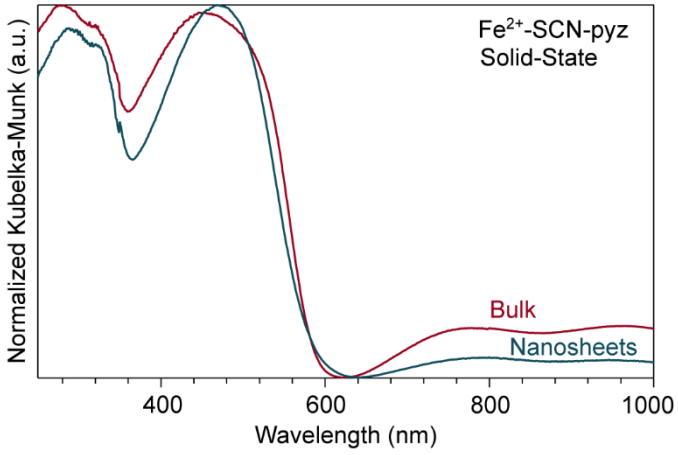

Figure C.5 DR UV-Vis spectrum of bulk and nanosheets of Fe-SCN-pyz under inert N_2 atmosphere.

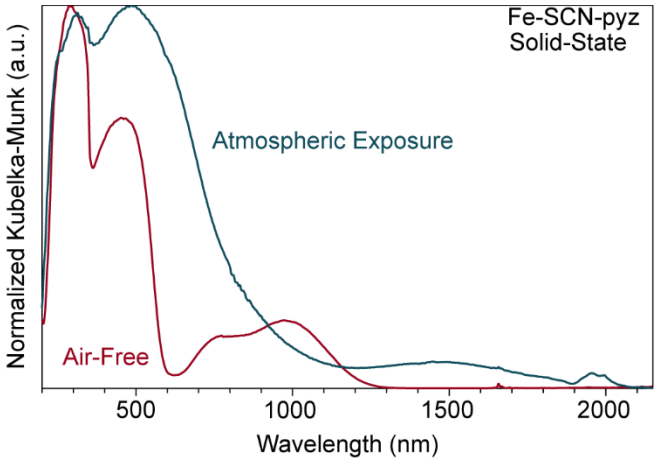

Figure C.6 DR UV-Vis spectrum of bulk Fe-SCN-pyz and nanosheets after 2 months of atmospheric exposure.

TEM Analysis.

Figure C.7 TEM images of bulk Fe-SCN-pyz prepared by drop-casting 10 mg/ml methanolic solutions onto TEM grids.

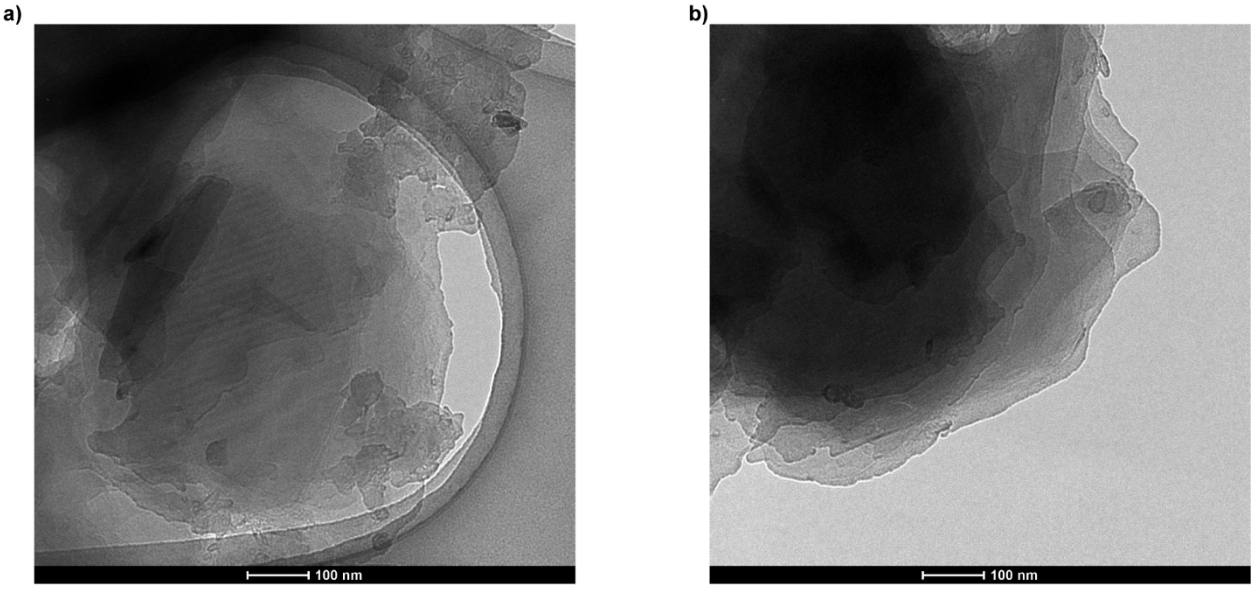

Figure C.8 a), b) TEM images of Fe-SCN-pyz nanosheets after 2 month of atmospheric exposure prepared by drop-casting 10 mg/ml methanolic solutions onto TEM grids. a) Moiré pattern of slip stacked nanosheets.

SpectroElectrochemistry.

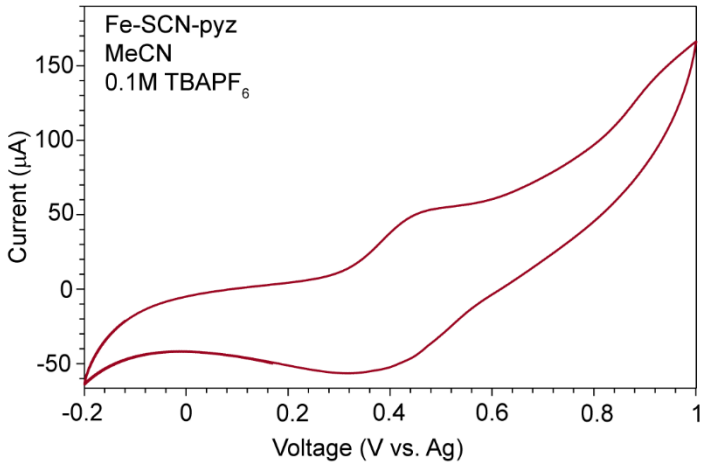

Figure C.9 Cyclic voltammetry of a solution of suspended Fe-SCN-pyz nanosheets in a 3 electrode cell with 0.1M $TBAPF_6$ as the supporting electrolyte, scanned at 10 mV/s.

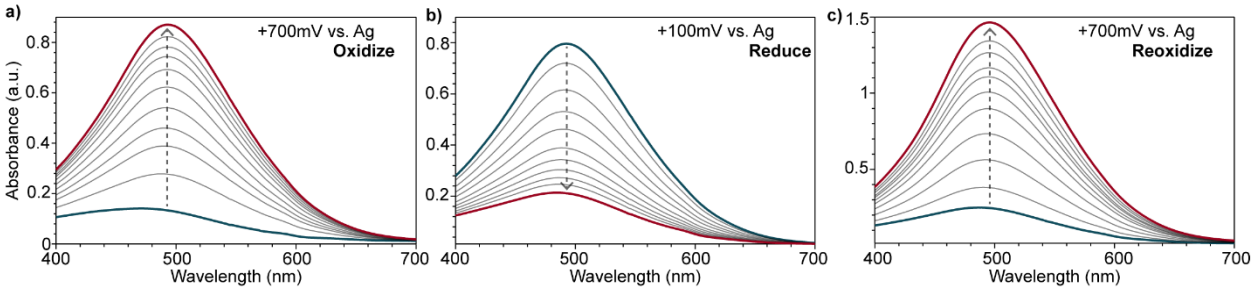

Figure C.10 UV-Vis spectrum of exfoliated Fe-SCN-pyz nanosheets suspended in a 0.1M $TBAPF_6$ MeCN solution as a) 700mV vs. Ag, b) 100 mV vs. Ag, and c) 700 mV vs. Ag is applied with a platinum mesh working electrode, platinum wire counter electrode, and silver wire pseudoreference.

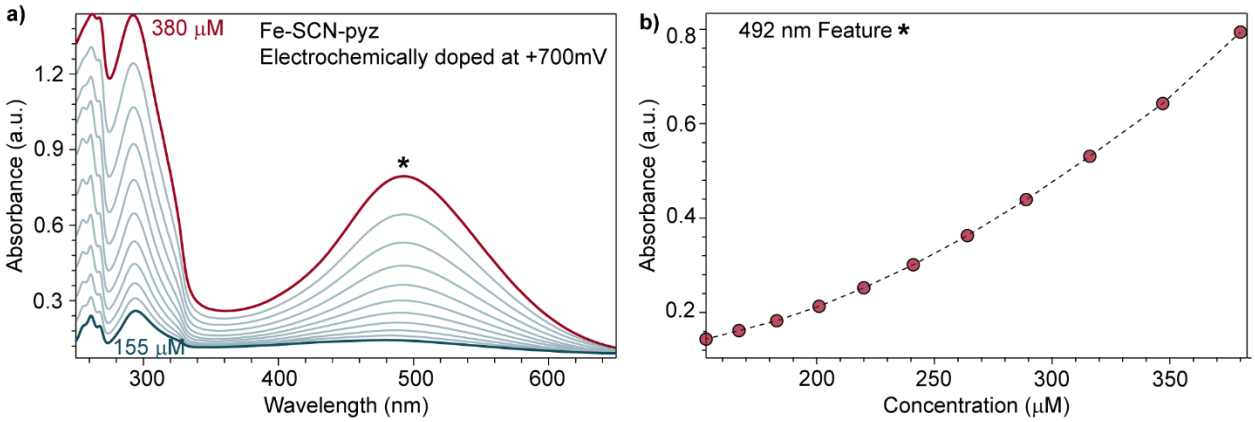

Figure C.11 a) Concentration dependence of electrochemically oxidized Fe-SCN-pyz nanosheets suspended in MeCN. b) Absorption at ~500nm as a function of concentration.

^{57}Fe Mössbauer Spectroscopy.

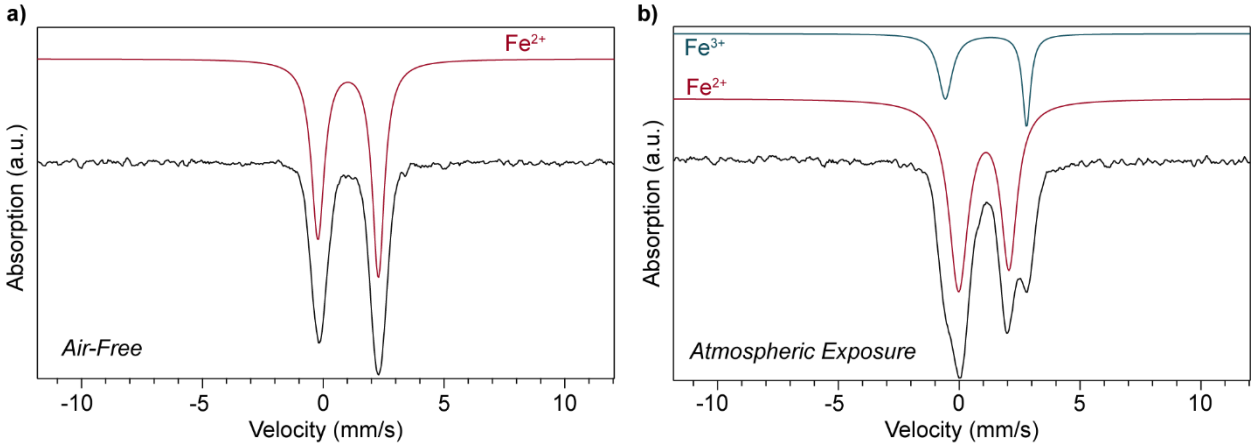

Figure C.12 Room-temperature Mössbauer spectrum of a) bulk Fe-SCN-pyz and b) Fe-SCN-pyz nanosheets after 2 months of air exposure.

Chemical Oxidation of Fe-SCN-pyz.

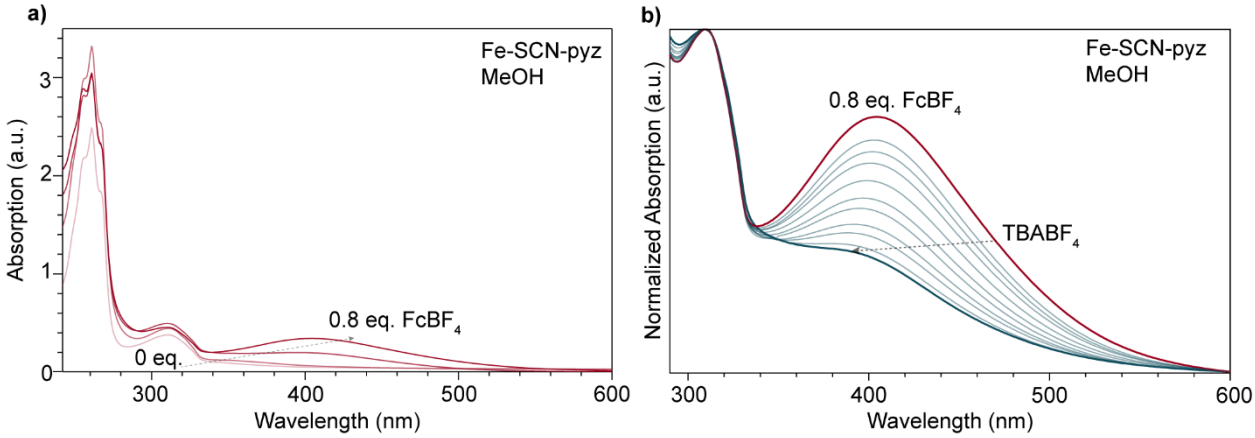

Figure C.13 a) UV-Vis spectrum of a Fe-SCN-pyz nanosheets subjected to ferrocenium oxidation (0 – 0.8 eq.) suspended in MeOH b) UV-Vis spectrum of 0.8 eq. ferrocenium oxidized sample as $TBABF_4$ is added to the solution.

Electrolyte Titration to Atmospherically Oxidized Fe-SCN-pyz Solutions.

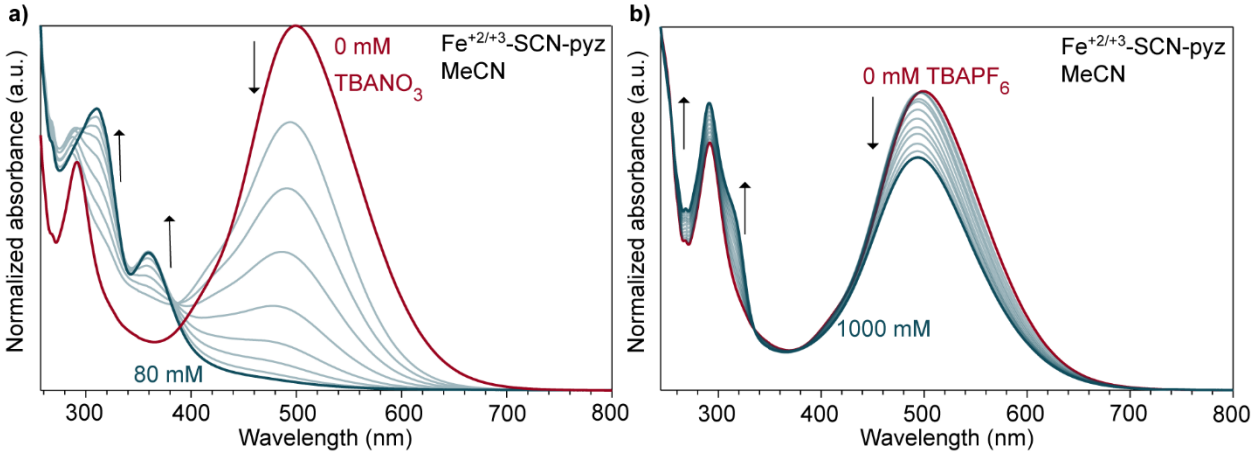

Figure C.14 a) UV-Vis spectrum of atmospherically oxidized Fe-SCN-pyz nanosheets suspended in MeCN as a) $TBANO_3$ b) $TBAPF_6$ is titrated in.

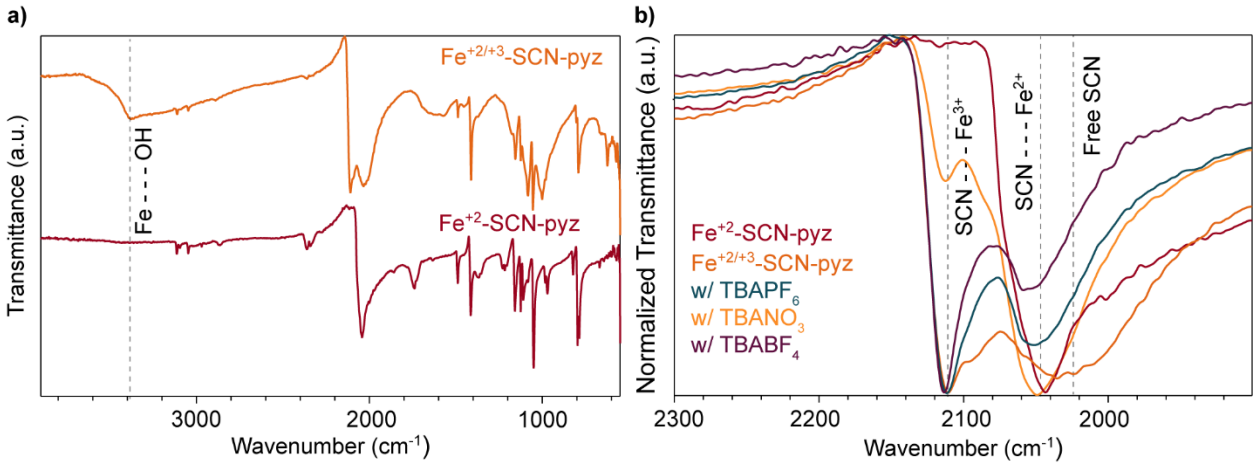

Figure C.15 a) FTIR full spectrum of atmospherically oxidized Fe-SCN-pyz nanosheets and bulk Fe-SCN-pyz b) FTIR spectrum highlighting C-N region for bulk Fe-SCN-pyz and oxidized Fe-SCN-pyz nanosheets pre and post addition of large excess of $TBANO_3$, $TBAPF_6$, and $TBABF_4$.

REFERENCES CITED

(1) Witze, A. Earth Boiled in 2023 — Will It Happen Again in 2024? *Nature* **2024**, *625* (7996), 637–639.

(2) Betts, R. A.; Belcher, S. E.; Hermanson, L.; Klein Tank, A.; Lowe, J. A.; Jones, C. D.; Morice, C. P.; Rayner, N. A.; Scaife, A. A.; Stott, P. A. Approaching 1.5 °C: How Will We Know We've Reached This Crucial Warming Mark? *Nature* **2023**, *624* (7990), 33–35.

(3) *Monthly atmospheric CO_2 concentration 2024*. Statista. https://www.statista.com/statistics/1091999/atmospheric-concentration-of-co2-historic/.

(4) Rocha, J.; Oliveira, S.; Viana, C. M.; Ribeiro, A. I. Chapter 8 - Climate Change and Its Impacts on Health, Environment and Economy. In *One Health*; Prata, J. C., Ribeiro, A. I., Rocha-Santos, T., Eds.; Academic Press, 2022; pp 253–279.

(5) Friedlingstein, P.; O'Sullivan, M.; Jones, M. W.; Andrew, R. M.; Bakker, D. C. E.; Hauck, J.; Landschützer, P.; Le Quéré, C.; Luijkx, I. T.; Peters, G. P.; Peters, W.; Pongratz, J.; Schwingshackl, C.; Sitch, S.; Canadell, J. G.; Ciais, P.; Jackson, R. B.; Alin, S. R.; Anthoni, P.; Barbero, L.; Bates, N. R.; Becker, M.; Bellouin, N.; Decharme, B.; Bopp, L.; Brasika, I. B. M.; Cadule, P.; Chamberlain, M. A.; Chandra, N.; Chau, T.-T.-T.; Chevallier, F.; Chini, L. P.; Cronin, M.; Dou, X.; Enyo, K.; Evans, W.; Falk, S.; Feely, R. A.; Feng, L.; Ford, D. J.; Gasser, T.; Ghattas, J.; Gkritzalis, T.; Grassi, G.; Gregor, L.; Gruber, N.; Gürses, Ö.; Harris, I.; Hefner, M.; Heinke, J.; Houghton, R. A.; Hurtt, G. C.; Iida, Y.; Ilyina, T.; Jacobson, A. R.; Jain, A.; Jarníková, T.; Jersild, A.; Jiang, F.; Jin, Z.; Joos, F.; Kato, E.; Keeling, R. F.; Kennedy, D.; Klein Goldewijk, K.; Knauer, J.; Korsbakken, J. I.; Körtzinger, A.; Lan, X.; Lefèvre, N.; Li, H.; Liu, J.; Liu, Z.; Ma, L.; Marland, G.; Mayot, N.; McGuire, P. C.; McKinley, G. A.; Meyer, G.; Morgan, E. J.; Munro, D. R.; Nakaoka, S.-I.; Niwa, Y.; O'Brien, K. M.; Olsen, A.; Omar, A. M.; Ono, T.; Paulsen, M.; Pierrot, D.; Pocock, K.; Poulter, B.; Powis, C. M.; Rehder, G.; Resplandy, L.; Robertson, E.; Rödenbeck, C.; Rosan, T. M.; Schwinger, J.; Séférian, R.; Smallman, T. L.; Smith, S. M.; Sospedra-Alfonso, R.; Sun, Q.; Sutton, A. J.; Sweeney, C.; Takao, S.; Tans, P. P.; Tian, H.; Tilbrook, B.; Tsujino, H.; Tubiello, F.; van der Werf, G. R.; van Ooijen, E.; Wanninkhof, R.; Watanabe, M.; Wimart-Rousseau, C.; Yang, D.; Yang, X.; Yuan, W.; Yue, X.; Zaehle, S.; Zeng, J.; Zheng, B. Global Carbon Budget 2023. *Earth Syst. Sci. Data* **2023**, *15* (12), 5301–5369.

(6) *Renewable Power Generation Costs in 2022*. https://www.irena.org/Publications/2023/Aug/Renewable-Power-Generation-Costs-in-2022.

(7) Arbabzadeh, M.; Sioshansi, R.; Johnson, J. X.; Keoleian, G. A. The Role of Energy Storage in Deep Decarbonization of Electricity Production. *Nat. Commun.* **2019**, *10* (1), 3413.

(8) Nikolaos, P. C.; Marios, F.; Dimitris, K. A Review of Pumped Hydro Storage Systems. *Energies* **2023**, *16* (11), 4516.

(9) Yao, F.; Livneh, B.; Rajagopalan, B.; Wang, J.; Crétaux, J.-F.; Wada, Y.; Berge-Nguyen, M. Satellites Reveal Widespread Decline in Global Lake Water Storage. *Science* **2023**, *380* (6646), 743–749.

(10) Wasti, A.; Ray, P.; Wi, S.; Folch, C.; Ubierna, M.; Karki, P. Climate Change and the Hydropower Sector: A Global Review. *WIREs Clim. Change* **2022**, *13* (2), e757.

(11) Mann, M. P.; van Bracht, M. N. Li-Ion Battery versus Pumped Storage for Bulk Energy Storage - A Comparison of Raw Material, Investment Costs and CO_2-Footprints.

(12) Augustyn, V.; Come, J.; Lowe, M. A.; Kim, J. W.; Taberna, P.-L.; Tolbert, S. H.; Abruña, H. D.; Simon, P.; Dunn, B. High-Rate Electrochemical Energy Storage through Li^+ Intercalation Pseudocapacitance. *Nat. Mater.* **2013**, *12* (6), 518–522.

(13) Choi, C.; Ashby, D. S.; Butts, D. M.; DeBlock, R. H.; Wei, Q.; Lau, J.; Dunn, B. Achieving High Energy Density and High Power Density with Pseudocapacitive Materials. *Nat. Rev. Mater.* **2020**, *5* (1), 5–19.

(14) Suwarno, S.; Nale, A.; Suwarta, P.; Wijayanti, I. D.; Ismail, M. Designing Nanoconfined $LiBH_4$ for Solid-State Electrolytes. *Front. Chem.* **2022**, *10*.

(15) Meng, X.; Guan, Z.; Zhao, J.; Cai, Z.; Li, S.; Bian, L.; Song, Y.; Guo, D.; Liu, X. Lithium-Pre-Intercalated T-Nb_2O_5/Graphene Composite Promoting Pseudocapacitive Performance for Ultralong Lifespan Capacitors. *Chem. Eng. J.* **2022**, *438*, 135492.

(16) Baumann, A. E.; Burns, D. A.; Liu, B.; Thoi, V. S. Metal-Organic Framework Functionalization and Design Strategies for Advanced Electrochemical Energy Storage Devices. *Commun. Chem.* **2019**, *2* (1), 1–14.

(17) Farha, O. K.; Eryazici, I.; Jeong, N. C.; Hauser, B. G.; Wilmer, C. E.; Sarjeant, A. A.; Snurr, R. Q.; Nguyen, S. T.; Yazaydın, A. Ö.; Hupp, J. T. Metal–Organic Framework Materials with Ultrahigh Surface Areas: Is the Sky the Limit? *J. Am. Chem. Soc.* **2012**, *134* (36), 15016–15021.

(18) Nam, K. W.; Park, S. S.; dos Reis, R.; Dravid, V. P.; Kim, H.; Mirkin, C. A.; Stoddart, J. F. Conductive 2D Metal-Organic Framework for High-Performance Cathodes in Aqueous Rechargeable Zinc Batteries. *Nat. Commun.* **2019**, *10* (1), 4948.

(19) Sheberla, D.; Bachman, J. C.; Elias, J. S.; Sun, C.-J.; Shao-Horn, Y.; Dincă, M. Conductive MOF Electrodes for Stable Supercapacitors with High Areal Capacitance. *Nat. Mater.* **2017**, *16* (2), 220–224.

(20) Asif, H. M.; Shakoor, Z.; Ibraheem, S.; Salama, A. M.; Khan, M. A.; Nguyen, T. A.; Yasin, G. Chapter 12 - Polyoxometalate-Based Metal Organic Frameworks (POMOFs) for Lithium-Ion Batteries. In *Metal-Organic Framework-Based Nanomaterials for Energy Conversion and Storage*; Gupta, R. K., Nguyen, T. A., Yasin, G., Eds.; Micro and Nano Technologies; Elsevier, 2022; pp 245–268.

(21) Xie, L. S.; Skorupskii, G.; Dincă, M. Electrically Conductive Metal–Organic Frameworks. *Chem. Rev.* **2020**, *120* (16), 8536–8580.

(22) Wang, H.-N.; Zhang, M.; Zhang, A.-M.; Shen, F.-C.; Wang, X.-K.; Sun, S.-N.; Chen, Y.-J.; Lan, Y.-Q. Polyoxometalate-Based Metal-Organic Frameworks with Conductive Polypyrrole for Supercapacitors. *ACS Appl. Mater. Interfaces* **2018**, *10* (38), 32265–32270.

(23) Clough, A. J.; Orchanian, N. M.; Skelton, J. M.; Neer, A. J.; Howard, S. A.; Downes, C. A.; Piper, L. F. J.; Walsh, A.; Melot, B. C.; Marinescu, S. C. Room Temperature Metallic Conductivity in a Metal–Organic Framework Induced by Oxidation. *J. Am. Chem. Soc.* **2019**, *141* (41), 16323–16330.

(24) Skorupskii, G.; Le, K. N.; Cordova, D. L. M.; Yang, L.; Chen, T.; Hendon, C. H.; Arguilla, M. Q.; Dincă, M. Porous Lanthanide Metal–Organic Frameworks with Metallic Conductivity. *Proc. Natl. Acad. Sci.* **2022**, *119* (34), e2205127119.

(25) Trikalitis, P. N.; Rangan, K. K.; Bakas, T.; Kanatzidis, M. G. Varied Pore Organization in Mesostructured Semiconductors Based on the $[SnSe_4]^{4-}$ Anion. *Nature* **2001**, *410* (6829), 671–675.

(26) Palchoudhury, S.; Ramasamy, K.; Han, J.; Chen, P.; Gupta, A. Transition Metal Chalcogenides for Next-Generation Energy Storage. *Nanoscale Adv.* **2023**, *5* (10), 2724–2742.

(27) Manzeli, S.; Ovchinnikov, D.; Pasquier, D.; Yazyev, O. V.; Kis, A. 2D Transition Metal Dichalcogenides. *Nat. Rev. Mater.* **2017**, *2* (8), 1–15.

(28) Sun, L.; Hendon, C. H.; Park, S. S.; Tulchinsky, Y.; Wan, R.; Wang, F.; Walsh, A.; Dincă, M. Is Iron Unique in Promoting Electrical Conductivity in MOFs? *Chem. Sci.* **2017**, *8* (6), 4450–4457.

(29) Yensen, N.; Allen, P. B. Open Source All-Iron Battery for Renewable Energy Storage. *HardwareX* **2019**, *6*, e00072.

(30) Darago, L. E.; Aubrey, M. L.; Yu, C. J.; Gonzalez, M. I.; Long, J. R. Electronic Conductivity, Ferrimagnetic Ordering, and Reductive Insertion Mediated by Organic Mixed-Valence in a Ferric Semiquinoid Metal–Organic Framework. *J. Am. Chem. Soc.* **2015**, *137* (50), 15703–15711.

(31) DeGayner, J. A.; Jeon, I.-R.; Sun, L.; Dincă, M.; Harris, T. D. 2D Conductive Iron-Quinoid Magnets Ordering up to Tc = 105 K via Heterogenous Redox Chemistry. *J. Am. Chem. Soc.* **2017**, *139* (11), 4175–4184.

(32) Xie, L. S.; Sun, L.; Wan, R.; Park, S. S.; DeGayner, J. A.; Hendon, C. H.; Dincă, M. Tunable Mixed-Valence Doping toward Record Electrical Conductivity in a Three-Dimensional Metal–Organic Framework. *J. Am. Chem. Soc.* **2018**, *140* (24), 7411–7414.

(33) Park, J. G.; Aubrey, M. L.; Oktawiec, J.; Chakarawet, K.; Darago, L. E.; Grandjean, F.; Long, G. J.; Long, J. R. Charge Delocalization and Bulk Electronic Conductivity in the Mixed-Valence Metal–Organic Framework Fe(1,2,3-Triazolate)$_2$(BF4)$_x$. *J. Am. Chem. Soc.* **2018**, *140* (27), 8526–8534.

(34) Kadota, K.; Chen, T.; Gormley, E. L.; Hendon, C. H.; Dincă, M.; Brozek, C. K. Electrically Conductive $[Fe_4S_4]^-$Based Organometallic Polymers. *Chem. Sci.* **2023**, *14* (41), 11410–11416.

(35) Saha, R.; Gupta, K.; Gómez García, C. J. Strategies to Improve Electrical Conductivity in Metal–Organic Frameworks: A Comparative Study. *Cryst. Growth Des.* **2024**, *24* (5), 2235–2265.

(36) Nakade, S.; Kambe, S.; Kitamura, T.; Wada, Y.; Yanagida, S. Effects of Lithium Ion Density on Electron Transport in Nanoporous TiO_2 Electrodes. *J. Phys. Chem. B* **2001**, *105* (38), 9150–9152.

(37) Kopidakis, N.; Schiff, E. A.; Park, N.-G.; van de Lagemaat, J.; Frank, A. J. Ambipolar Diffusion of Photocarriers in Electrolyte-Filled, Nanoporous TiO_2. *J. Phys. Chem. B* **2000**, *104* (16), 3930–3936.

(38) Yu, J.; Sushko, M. L.; Kerisit, S.; Rosso, K. M.; Liu, J. Kinetic Monte Carlo Study of Ambipolar Lithium Ion and Electron–Polaron Diffusion into Nanostructured TiO_2. *J. Phys. Chem. Lett.* **2012**, *3* (15), 2076–2081.

(39) Wilbourn, K.; Murray, R. W. The d.c. Redox versus Electronic Conductivity of the Ladder Polymer Poly(Benzimidazobenzophenanthroline). *J. Phys. Chem.* **1988**, *92* (12), 3642–3648.

(40) Zhang, Z.; Avdeev, M.; Chen, H.; Yin, W.; Kan, W. H.; He, G. Lithiated Prussian Blue Analogues as Positive Electrode Active Materials for Stable Non-Aqueous Lithium-Ion Batteries. *Nat. Commun.* **2022**, *13* (1), 7790.

(41) Knight, A. W.; Kalugin, N. G.; Coker, E.; Ilgen, A. G. Water Properties under Nano-Scale Confinement. *Sci. Rep.* **2019**, *9* (1), 8246.

(42) Hammes-Schiffer, S. Proton-Coupled Electron Transfer: Moving Together and Charging Forward. *J. Am. Chem. Soc.* **2015**, *137* (28), 8860–8871.

(43) Reece, S. Y.; Nocera, D. G. Proton-Coupled Electron Transfer in Biology: Results from Synergistic Studies in Natural and Model Systems. *Annu. Rev. Biochem.* **2009**, *78* (Volume 78, 2009), 673–699.

(44) Weinberg, D. R.; Gagliardi, C. J.; Hull, J. F.; Murphy, C. F.; Kent, C. A.; Westlake, B. C.; Paul, A.; Ess, D. H.; McCafferty, D. G.; Meyer, T. J. Proton-Coupled Electron Transfer. *Chem. Rev.* **2012**, *112* (7), 4016–4093.

(45) Cai, M.; Loague, Q.; Morris, A. J. Design Rules for Efficient Charge Transfer in Metal–Organic Framework Films: The Pore Size Effect. *J. Phys. Chem. Lett.* **2020**, *11* (3), 702–709.

(46) Castner, A. T.; Su, H.; Svensson Grape, E.; Inge, A. K.; Johnson, B. A.; Ahlquist, M. S. G.; Ott, S. Microscopic Insights into Cation-Coupled Electron Hopping Transport in a Metal–Organic Framework. *J. Am. Chem. Soc.* **2022**, *144* (13), 5910–5920.

(47) Liu, L.; Corma, A. Confining Isolated Atoms and Clusters in Crystalline Porous Materials for Catalysis. *Nat. Rev. Mater.* **2021**, *6* (3), 244–263.

(48) Li, Y.; Yu, J. Emerging Applications of Zeolites in Catalysis, Separation and Host–Guest Assembly. *Nat. Rev. Mater.* **2021**, 1–19.

(49) Liu, Y.; Wu, X.; Li, Z.; Zhang, J.; Liu, S.-X.; Liu, S.; Gu, L.; Zheng, L. R.; Li, J.; Wang, D.; Li, Y. Fabricating Polyoxometalates-Stabilized Single-Atom Site Catalysts in Confined Space with Enhanced Activity for Alkynes Diboration. *Nat. Commun.* **2021**, *12* (1), 4205.

(50) Zywitzki, D.; Jing, H.; Tüysüz, H.; Chan, C. K. High Surface Area, Amorphous Titania with Reactive Ti^{3+} through a Photo-Assisted Synthesis Method for Photocatalytic H_2 Generation. *J. Mater. Chem. A* **2017**, *5* (22), 10957–10967.

(51) Yang, D.; Gates, B. C. Catalysis by Metal Organic Frameworks: Perspective and Suggestions for Future Research. *ACS Catal.* **2019**, *9* (3), 1779–1798.

(52) Cheng, Q.; Okamoto, Y.; Tamura, N.; Tsuji, M.; Maruyama, S.; Matsuo, Y. Graphene-Like-Graphite as Fast-Chargeable and High-Capacity Anode Materials for Lithium Ion Batteries. *Sci. Rep.* **2017**, *7* (1), 14782.

(53) Bi, S.; Banda, H.; Chen, M.; Niu, L.; Chen, M.; Wu, T.; Wang, J.; Wang, R.; Feng, J.; Chen, T.; Dincă, M.; Kornyshev, A. A.; Feng, G. Molecular Understanding of Charge Storage and Charging Dynamics in Supercapacitors with MOF Electrodes and Ionic Liquid Electrolytes. *Nat. Mater.* **2020**, *19* (5), 552–558.

(54) Sun, C.; Rajasekhara, S.; Goodenough, J. B.; Zhou, F. Monodisperse Porous $LiFePO_4$ Microspheres for a High Power Li-Ion Battery Cathode. *J. Am. Chem. Soc.* **2011**, *133* (7), 2132–2135.

(55) Lee, E. J.; Lee, L.; Abbas, M. A.; Bang, J. H. The Influence of Surface Area, Porous Structure, and Surface State on the Supercapacitor Performance of Titanium Oxynitride: Implications for a Nanostructuring Strategy. *Phys. Chem. Chem. Phys.* **2017**, *19* (31), 21140–21151.

(56) Liu, Z.; Yuan, X.; Zhang, S.; Wang, J.; Huang, Q.; Yu, N.; Zhu, Y.; Fu, L.; Wang, F.; Chen, Y.; Wu, Y. Three-Dimensional Ordered Porous Electrode Materials for Electrochemical Energy Storage. *NPG Asia Mater.* **2019**, *11* (1), 1–21.

(57) Tao, X.; Gao, Y.; Wang, S.; Wang, X.; Liu, Y.; Zhao, Y.; Fan, F.; Dupuis, M.; Li, R.; Li, C. Interfacial Charge Modulation: An Efficient Strategy for Boosting Spatial Charge Separation on Semiconductor Photocatalysts. *Adv. Energy Mater.* **2019**, *9* (13), 1803951.

(58) Renault, C.; Nicole, L.; Sanchez, C.; Costentin, C.; Balland, V.; Limoges, B. Unraveling the Charge Transfer/Electron Transport in Mesoporous Semiconductive TiO_2 Films by Voltabsorptometry. *Phys. Chem. Chem. Phys.* **2015**, *17* (16), 10592–10607.

(59) Fabregat-Santiago, F.; Mora-Seró, I.; Garcia-Belmonte, G.; Bisquert, J. Cyclic Voltammetry Studies of Nanoporous Semiconductors. Capacitive and Reactive Properties of Nanocrystalline TiO_2 Electrodes in Aqueous Electrolyte. *J. Phys. Chem. B* **2003**, *107* (3), 758–768.

(60) Foo, C.; Li, Y.; Lebedev, K.; Chen, T.; Day, S.; Tang, C.; Tsang, S. C. E. Characterisation of Oxygen Defects and Nitrogen Impurities in TiO_2 Photocatalysts Using Variable-Temperature X-Ray Powder Diffraction. *Nat. Commun.* **2021**, *12* (1), 661.

(61) Sun, X.; Zhang, X.; Xie, Y. Surface Defects in Two-Dimensional Photocatalysts for Efficient Organic Synthesis. *Matter* **2020**, *2* (4), 842–861.

(62) Wu, S.; Tan, X.; Lei, J.; Chen, H.; Wang, L.; Zhang, J. Ga-Doped and Pt-Loaded Porous TiO_2–SiO_2 for Photocatalytic Nonoxidative Coupling of Methane. *J. Am. Chem. Soc.* **2019**, *141* (16), 6592–6600.

(63) Xiao, W.; Yang, S.; Zhang, P.; Li, P.; Wu, P.; Li, M.; Chen, N.; Jie, K.; Huang, C.; Zhang, N.; Dai, S. Facile Synthesis of Highly Porous Metal Oxides by Mechanochemical Nanocasting. *Chem. Mater.* **2018**, *30* (9), 2924–2929.

(64) Moosavi, S. M.; Nandy, A.; Jablonka, K. M.; Ongari, D.; Janet, J. P.; Boyd, P. G.; Lee, Y.; Smit, B.; Kulik, H. J. Understanding the Diversity of the Metal-Organic Framework Ecosystem. *Nat. Commun.* **2020**, *11* (1), 4068.

(65) Sheberla, D.; Sun, L.; Blood-Forsythe, M. A.; Er, S.; Wade, C. R.; Brozek, C. K.; Aspuru-Guzik, A.; Dincă, M. High Electrical Conductivity in Ni_3(2,3,6,7,10,11-Hexaiminotriphenylene)$_2$, a Semiconducting Metal–Organic Graphene Analogue. *J. Am. Chem. Soc.* **2014**, *136* (25), 8859–8862.

(66) Dong, R.; Han, P.; Arora, H.; Ballabio, M.; Karakus, M.; Zhang, Z.; Shekhar, C.; Adler, P.; Petkov, P. S.; Erbe, A.; Mannsfeld, S. C. B.; Felser, C.; Heine, T.; Bonn, M.; Feng, X.; Cánovas, E. High-Mobility Band-like Charge Transport in a Semiconducting Two-Dimensional Metal–Organic Framework. *Nat. Mater.* **2018**, *17* (11), 1027–1032.

(67) Gándara, F.; Uribe-Romo, F. J.; Britt, D. K.; Furukawa, H.; Lei, L.; Cheng, R.; Duan, X.; O'Keeffe, M.; Yaghi, O. M. Porous, Conductive Metal-Triazolates and Their Structural Elucidation by the Charge-Flipping Method. *Chem. – Eur. J.* **2012**, *18* (34), 10595–10601.

(68) Yaghi, O. M.; Sun, Z.; Richardson, D. A.; Groy, T. L. Directed Transformation of Molecules to Solids: Synthesis of a Microporous Sulfide from Molecular Germanium Sulfide Cages. *J. Am. Chem. Soc.* **1994**, *116* (2), 807–808.

(69) Rangan, K. K.; Billinge, S. J. L.; Petkov, V.; Heising, J.; Kanatzidis, M. G. Aqueous Mediated Synthesis of Mesostructured Manganese Germanium Sulfide with Hexagonal Order. *Chem. Mater.* **1999**, *11* (10), 2629–2632.

(70) Bag, S.; Kanatzidis, M. G. Chalcogels: Porous Metal−Chalcogenide Networks from Main-Group Metal Ions. Effect of Surface Polarizability on Selectivity in Gas Separation. *J. Am. Chem. Soc.* **2010**, *132* (42), 14951–14959.

(71) Bag, S.; Kanatzidis, M. G. Importance of Solution Equilibria in the Directed Assembly of Metal Chalcogenide Mesostructures. *J. Am. Chem. Soc.* **2008**, *130* (26), 8366–8376.

(72) Haddadpour, S.; Melullis, M.; Staesche, H.; Mariappan, C. R.; Roling, B.; Clérac, R.; Dehnen, S. Inorganic Frameworks from Selenidotetrelate Anions $[T_2Se_6]^{4-}$ (T = Ge, Sn): Synthesis, Structures, and Ionic Conductivity of $[K_2(H_2O)_3][MnGe_4Se_{10}]$ and $(NMe_4)_2[MSn_4Se_{10}]$ (M = Mn, Fe). *Inorg. Chem.* **2009**, *48* (4), 1689–1698.

(73) Rangan, K. K.; Trikalitis, P. N.; Kanatzidis, M. G. Light-Emitting Meso-Structured Sulfides with Hexagonal Symmetry: Supramolecular Assembly of $[Ge_4S_{10}]^{4-}$ Clusters with Trivalent Metal Ions and Cetylpyridinium Surfactant. *J. Am. Chem. Soc.* **2000**, *122* (41), 10230–10231.

(74) MacLachlan, M. J.; Coombs, N.; Bedard, R. L.; White, S.; Thompson, L. K.; Ozin, G. A. Mesostructured Metal Germanium Sulfides. *J. Am. Chem. Soc.* **1999**, *121* (51), 12005–12017.

(75) Zhang, J.; Bu, X.; Feng, P.; Wu, T. Metal Chalcogenide Supertetrahedral Clusters: Synthetic Control over Assembly, Dispersibility, and Their Functional Applications. *Acc. Chem. Res.* **2020**, *53* (10), 2261–2272.

(76) MacLachlan, M. J.; Coombs, N.; Ozin, G. A. Non-Aqueous Supramolecular Assembly of Mesostructured Metal Germanium Sulphides from $(Ge_4S_{10})^{4-}$ Clusters. *Nature* **1999**, *397* (6721), 681–684.

(77) Tsamourtzi, K.; Song, J.-H.; Bakas, T.; Freeman, A. J.; Trikalitis, P. N.; Kanatzidis, M. G. Straightforward Route to the Adamantane Clusters $[Sn_4Q_{10}]^{4-}$ (Q = S, Se, Te) and Use in the Assembly of Open-Framework Chalcogenides $(Me_4N)_2M[Sn_4Se_{10}]$ ($M = Mn^{II}$, Fe^{II}, Co^{II}, Zn^{II}) Including the First Telluride Member $(Me_4N)_2Mn[Ge_4Te_{10}]$. *Inorg. Chem.* **2008**, *47* (24), 11920–11929.

(78) Bowes, C. L.; Lough, A. J.; Malek, A.; Ozin, G. A.; Petrov, S.; Young, D. Thermally Stable Self-Assembling Open-Frameworks: Isostructural Cs^+ and $(CH_3)_4N^+$ Iron Germanium Sulfides. *Chem. Ber.* **1996**, *129* (3), 283–287.

(79) Duchardt, M.; Haddadpour, S.; Kaib, T.; Bron, P.; Roling, B.; Dehnen, S. Different Chemical Environments of $[Ge_4Se_{10}]^{4-}$ in the Li^+ Compounds $[Li_4(H_2O)_{16}][Ge_4Se_{10}]\cdot 4.33H_2O$, $[\{Li_4(Thf)_{12}\}Ge_4Se_{10}]$, and $[Li_2(H_2O)_8][MnGe_4Se_{10}]$, and Ionic Conductivity of Underlying "$Li_4Ge_4Se_{10}$." *Inorg. Chem.* **2021**, *60* (7), 5224–5231.

(80) Ahari, H.; Garcia, A.; Kirkby, S.; Ozin, G. A.; Young, D.; Lough, A. J. Self-Assembling Iron and Manganese Metal–Germanium–Selenide Frameworks: $[NMe_4]_2MGe_4Se_{10}$, Where M = Fe or Mn. *J. Chem. Soc. Dalton Trans.* **1998**, No. 12, 2023–2028.

(81) Mas-Ballesté, R.; Gómez-Navarro, C.; Gómez-Herrero, J.; Zamora, F. 2D Materials: To Graphene and Beyond. *Nanoscale* **2011**, *3* (1), 20–30.

(82) Li, Y.; Jiang, X.; Fu, Z.; Huang, Q.; Wang, G.-E.; Deng, W.-H.; Wang, C.; Li, Z.; Yin, W.; Chen, B.; Xu, G. Coordination Assembly of 2D Ordered Organic Metal Chalcogenides with Widely Tunable Electronic Band Gaps. *Nat. Commun.* **2020**, *11* (1), 261.

(83) Gütlich, P.; Bill, E.; Trautwein, A. X. Hyperfine Interactions. In *Mössbauer Spectroscopy and Transition Metal Chemistry: Fundamentals and Applications*; Gütlich, P., Bill, E., Trautwein, A. X., Eds.; Springer: Berlin, Heidelberg, 2011; pp 73–135.

(84) Levesanos, N.; Liyanage, W. P. R.; Ferentinos, E.; Raptopoulos, G.; Paraskevopoulou, P.; Sanakis, Y.; Choudhury, A.; Stavropoulos, P.; Nath, M.; Kyritsis, P. Investigating the Structural, Spectroscopic, and Electrochemical Properties of $[Fe(EPiPr_2)_2N_2]$ (E = S, Se) and the Formation of Iron Selenides by Chemical Vapor Deposition. *Eur. J. Inorg. Chem.* **2016**, *2016* (34), 5332–5339.

(85) Weakliem, H. A. Optical Spectra of Ni^{2+}, Co^{2+}, and Cu^{2+} in Tetrahedral Sites in Crystals. *J. Chem. Phys.* **1962**, *36* (8), 2117–2140.

(86) Dalal, M. *A Textbook of Inorganic Chemistry – Volume 1*; Dalal Institute, 2017.

(87) Jamnik, J.; Maier, J. Treatment of the Impedance of Mixed Conductors Equivalent Circuit Model and Explicit Approximate Solutions. *J. Electrochem. Soc.* **1999**, *146* (11), 4183.

(88) Poling, S. A.; Nelson, C. R.; Sutherland, J. T.; Martin, S. W. Synthesis and Characterization of the Thiogermanic Acids $H_4Ge_4S_{10}$ and $H_2Ge_4S_9$. *J. Phys. Chem. B* **2003**, *107* (23), 5413–5418.

(89) D. Hartle, M.; D. Pluth, M. A Practical Guide to Working with H_2S at the Interface of Chemistry and Biology. *Chem. Soc. Rev.* **2016**, *45* (22), 6108–6117.

(90) Shuai, Z.; Li, W.; Ren, J.; Jiang, Y.; Geng, H. Applying Marcus Theory to Describe the Carrier Transports in Organic Semiconductors: Limitations and Beyond. *J. Chem. Phys.* **2020**, *153* (8), 080902.

(91) Lin, S.; Usov, P. M.; Morris, A. J. The Role of Redox Hopping in Metal–Organic Framework Electrocatalysis. *Chem. Commun.* **2018**, *54* (51), 6965–6974.

(92) Feldman, B. J.; Burgmayer, P.; Murray, R. W. The Potential Dependence of Electrical Conductivity and Chemical Charge Storage of Poly(Pyrrole) Films on Electrodes. *J. Am. Chem. Soc.* **1985**, *107* (4), 872–878.

(93) Sun, L.; Miyakai, T.; Seki, S.; Dincă, M. Mn2(2,5-Disulfhydrylbenzene-1,4-Dicarboxylate): A Microporous Metal–Organic Framework with Infinite (−Mn–S−)$_\infty$ Chains and High Intrinsic Charge Mobility. *J. Am. Chem. Soc.* **2013**, *135* (22), 8185–8188.

(94) Sun, L.; Hendon, C. H.; Minier, M. A.; Walsh, A.; Dincă, M. Million-Fold Electrical Conductivity Enhancement in Fe_2(DEBDC) versus Mn_2(DEBDC) (E = S, O). *J. Am. Chem. Soc.* **2015**, *137* (19), 6164–6167.

(95) Huang, X.; Zhang, S.; Liu, L.; Yu, L.; Chen, G.; Xu, W.; Zhu, D. Superconductivity in a Copper(II)-Based Coordination Polymer with Perfect Kagome Structure. *Angew. Chem. Int. Ed.* **2018**, *57* (1), 146–150.

(96) Clough, A. J.; Skelton, J. M.; Downes, C. A.; de la Rosa, A. A.; Yoo, J. W.; Walsh, A.; Melot, B. C.; Marinescu, S. C. Metallic Conductivity in a Two-Dimensional Cobalt Dithiolene Metal–Organic Framework. *J. Am. Chem. Soc.* **2017**, *139* (31), 10863–10867.

(97) Chen, L.; San, K. A.; Turo, M. J.; Gembicky, M.; Fereidouni, S.; Kalaj, M.; Schimpf, A. M. Tunable Metal Oxide Frameworks via Coordination Assembly of Preyssler-Type Molecular Clusters. *J. Am. Chem. Soc.* **2019**, *141* (51), 20261–20268.

(98) Wang, J.; Zhao, L.; Gong, K. First-Principle Study of the Half-Metallic Ferromagnetic Compound $[(CH_3)_4N]_2FeGe_4S_{10}$. *J. Magn. Magn. Mater.* **2008**, *320* (10), 1696–1699.

(99) Qu, L.; Iguchi, H.; Takaishi, S.; Habib, F.; Leong, C. F.; D'Alessandro, D. M.; Yoshida, T.; Abe, H.; Nishibori, E.; Yamashita, M. Porous Molecular Conductor: Electrochemical Fabrication of Through-Space Conduction Pathways among Linear Coordination Polymers. *J. Am. Chem. Soc.* **2019**, *141* (17), 6802–6806.

(100) Merlet, C.; Rotenberg, B.; Madden, P. A.; Taberna, P.-L.; Simon, P.; Gogotsi, Y.; Salanne, M. On the Molecular Origin of Supercapacitance in Nanoporous Carbon Electrodes. *Nat. Mater.* **2012**, *11* (4), 306–310.

(101) Qian, Q.; Asinger, P. A.; Lee, M. J.; Han, G.; Mizrahi Rodriguez, K.; Lin, S.; Benedetti, F. M.; Wu, A. X.; Chi, W. S.; Smith, Z. P. MOF-Based Membranes for Gas Separations. *Chem. Rev.* **2020**, acs.chemrev.0c00119.

(102) Li, H.; Li, L.; Lin, R.-B.; Zhou, W.; Zhang, Z.; Xiang, S.; Chen, B. Porous Metal-Organic Frameworks for Gas Storage and Separation: Status and Challenges. *EnergyChem* **2019**, *1* (1), 100006.

(103) Silva-Gaspar, B.; Martinez-Franco, R.; Pirngruber, G.; Fécant, A.; Diaz, U.; Corma, A. Open-Framework Chalcogenide Materials - from Isolated Clusters to Highly Ordered Structures - and Their Photocalytic Applications. *Coord. Chem. Rev.* **2022**, *453*, 214243.

(104) Greiner, S.; Schwarz, B.; Ringenberg, M.; Dürr, M.; Ivanovic-Burmazovic, I.; Fichtner, M.; Anjass, M.; Streb, C. Redox-Inactive Ions Control the Redox-Activity of Molecular Vanadium Oxides. *Chem. Sci.* **2020**, *11* (17), 4450–4455.

(105) Kumar, A.; Lionetti, D.; Day, V. W.; Blakemore, J. D. Redox-Inactive Metal Cations Modulate the Reduction Potential of the Uranyl Ion in Macrocyclic Complexes. *J. Am. Chem. Soc.* **2020**, *142* (6), 3032–3041.

(106) Saito, K.; Nakagawa, M.; Mandal, M.; Ishikita, H. Role of Redox-Inactive Metals in Controlling the Redox Potential of Heterometallic Manganese–Oxido Clusters. *Photosynth. Res.* **2021**, *148* (3), 153–159.

(107) Feng, R.; Zhang, X.; Murugesan, V.; Hollas, A.; Chen, Y.; Shao, Y.; Walter, E.; Wellala, N. P. N.; Yan, L.; Rosso, K. M.; Wang, W. Reversible Ketone Hydrogenation and Dehydrogenation for Aqueous Organic Redox Flow Batteries. *Science* **2021**, *372* (6544), 836–840.

(108) Valdez, C. N.; Schimpf, A. M.; Gamelin, D. R.; Mayer, J. M. Proton-Controlled Reduction of ZnO Nanocrystals: Effects of Molecular Reductants, Cations, and Thermodynamic Limitations. *J. Am. Chem. Soc.* **2016**, jacs.5b12182-jacs.5b12182.

(109) Schimpf, A. M.; Gunthardt, C. E.; Rinehart, J. D.; Mayer, J. M.; Gamelin, D. R. Controlling Carrier Densities in Photochemically Reduced Colloidal ZnO Nanocrystals: Size Dependence and Role of the Hole Quencher. *J. Am. Chem. Soc.* **2013**, *135* (44), 16569–16577.

(110) Braten, M. N.; Gamelin, D. R.; Mayer, J. M. Reaction Dynamics of Proton-Coupled Electron Transfer from Reduced ZnO Nanocrystals. *ACS Nano* **2015**, *9* (10), 10258–10267.

(111) Liu, H.; Brozek, C. K.; Sun, S.; Lingerfelt, D. B.; Gamelin, D. R.; Li, X. A Hybrid Quantum-Classical Model of Electrostatics in Multiply Charged Quantum Dots. *J. Phys. Chem. C* **2017**, *121* (46), 26086–26095.

(112) Hartstein, K. H.; Brozek, C. K.; Hinterding, S. O. M.; Gamelin, D. R. Copper-Coupled Electron Transfer in Colloidal Plasmonic Copper-Sulfide Nanocrystals Probed by in Situ Spectroelectrochemistry. *J. Am. Chem. Soc.* **2018**, *140* (9), 3434–3442.

(113) Brozek, C. K.; Hartstein, K. H.; Gamelin, D. R. Potentiometric Titrations for Measuring the Capacitance of Colloidal Photodoped ZnO Nanocrystals. *J. Am. Chem. Soc.* **2016**, *138* (33), 10605–10610.

(114) Carroll, G. M.; Brozek, C. K.; Hartstein, K. H.; Tsui, E. Y.; Gamelin, D. R. Potentiometric Measurements of Semiconductor Nanocrystal Redox Potentials. *J. Am. Chem. Soc.* **2016**, *138* (13), 4310–4313.

(115) Fukuzumi, S.; Ohkubo, K. Metal Ion-Coupled and Decoupled Electron Transfer. *Coord. Chem. Rev.* **2010**, *254* (3–4), 372–385.

(116) Morimoto, Y.; Kotani, H.; Park, J.; Lee, Y. M.; Nam, W.; Fukuzumi, S. Metal Ion-Coupled Electron Transfer of a Nonheme Oxoiron(IV) Complex: Remarkable Enhancement of Electron-Transfer Rates by Sc3+. *J. Am. Chem. Soc.* **2011**, *133* (3), 403–405.

(117) Tsui, E. Y.; Agapie, T. Reduction Potentials of Heterometallic Manganese-Oxido Cubane Complexes Modulated by Redox-Inactive Metals. *Proc. Natl. Acad. Sci.* **2013**, *110* (25), 10084–10088.

(118) Yun, J.; Natu, V.; Echols, I.; Thakur, R. M.; Cao, H.; Tan, Z.; Radovic, M.; Green, M. J.; Barsoum, M. W.; Lutkenhaus, J. L. Anion Identity and Time Scale Affect the Cation Insertion Energy Storage Mechanism in $Ti_3C_2T_x$ MXene Multilayers. *ACS Energy Lett.* **2022**, *7* (5), 1828–1834.

(119) Mashtalir, O.; Lukatskaya, M. R.; Kolesnikov, A. I.; Raymundo-Piñero, E.; Naguib, M.; Barsoum, M. W.; Gogotsi, Y. The Effect of Hydrazine Intercalation on the Structure and Capacitance of 2D Titanium Carbide (MXene). *Nanoscale* **2016**, *8* (17), 9128–9133.

(120) Thackeray, M. M.; Thomas, J. O.; Whittingham, M. S. Science and Applications of Mixed Conductors for Lithium Batteries. *MRS Bull.* **2000**, *25* (3), 39–46.

(121) Zhang, J.; Feng, P.; Bu, X.; Wu, T. Atomically Precise Metal Chalcogenide Supertetrahedral Clusters: Frameworks to Molecules, and Structure to Function. *Natl. Sci. Rev.* **2022**, *9* (1), nwab076.

(122) Yang, H.; Zhang, J.; Luo, M.; Wang, W.; Lin, H.; Li, Y.; Li, D.; Feng, P.; Wu, T. The Largest Supertetrahedral Oxychalcogenide Nanocluster and Its Unique Assembly. *J. Am. Chem. Soc.* **2018**, *140* (36), 11189–11192.

(123) McKenzie, J.; Le, K. N.; Bardgett, D. J.; Collins, K. A.; Ericson, T.; Wojnar, M. K.; Chouinard, J.; Golledge, S.; Cozzolino, A. F.; Johnson, D. C.; Hendon, C. H.; Brozek, C. K. Conductivity in Open-Framework Chalcogenides Tuned via Band Engineering and Redox Chemistry. *Chem. Mater.* **2022**, *34* (4), 1905–1920.

(124) Weber, S. A. L.; Hermes, I. M.; Turren-Cruz, S.-H.; Gort, C.; Bergmann, V. W.; Gilson, L.; Hagfeldt, A.; Graetzel, M.; Tress, W.; Berger, R. How the Formation of Interfacial Charge Causes Hysteresis in Perovskite Solar Cells. *Energy Environ. Sci.* **2018**, *11* (9), 2404–2413.

(125) Singh, R.; Parashar, M. Origin of Hysteresis in Perovskite Solar Cells. In *Soft-Matter Thin Film Solar Cells*; AIP Publishing Books; AIP Publishing LLC, 2020; pp 1-1-1–42.

(126) Yang, T.-Y.; Gregori, G.; Pellet, N.; Grätzel, M.; Maier, J. The Significance of Ion Conduction in a Hybrid Organic–Inorganic Lead-Iodide-Based Perovskite Photosensitizer. *Angew. Chem. Int. Ed.* **2015**, *54* (27), 7905–7910.

(127) Rep, D. B. A.; Morpurgo, A. F.; Sloof, W. G.; Klapwijk, T. M. Mobile Ionic Impurities in Organic Semiconductors. *J. Appl. Phys.* **2003**, *93* (4), 2082–2090.

(128) Surridge, N. A.; Sosnoff, C. S.; Schmehl, R.; Facci, J. S.; Murray, R. W. Electron and Counterion Diffusion Constants in Mixed-Valent Polymeric Osmium Bipyridine Films. *J. Phys. Chem.* **1994**, *98* (3), 917–923.

(129) Ahrenholtz, S. R.; Epley, C. C.; Morris, A. J. Solvothermal Preparation of an Electrocatalytic Metalloporphyrin MOF Thin Film and Its Redox Hopping Charge-Transfer Mechanism. *J. Am. Chem. Soc.* **2014**, *136* (6), 2464–2472.

(130) Goswami, S.; Hod, I.; Duan, J. D.; Kung, C.-W.; Rimoldi, M.; Malliakas, C. D.; Palmer, R. H.; Farha, O. K.; Hupp, J. T. Anisotropic Redox Conductivity within a Metal–Organic Framework Material. *J. Am. Chem. Soc.* **2019**, *141* (44), 17696–17702.

(131) Johnson, E. M.; Ilic, S.; Morris, A. J. Design Strategies for Enhanced Conductivity in Metal–Organic Frameworks. *ACS Cent. Sci.* **2021**, *7* (3), 445–453.

(132) Celis-Salazar, P. J.; Cai, M.; Cucinell, C. A.; Ahrenholtz, S. R.; Epley, C. C.; Usov, P. M.; Morris, A. J. Independent Quantification of Electron and Ion Diffusion in Metallocene-Doped Metal–Organic Frameworks Thin Films. *J. Am. Chem. Soc.* **2019**, *141* (30), 11947–11953.

(133) Akerlof, G. DIELECTRIC CONSTANTS OF SOME ORGANIC SOLVENT-WATER MIXTURES AT VARIOUS TEMPERATURES. *J. Am. Chem. Soc.* **1932**, *54* (11), 4125–4139.

(134) Marcus, Y. *The Properties of Solvents*; Wiley series in solution chemistry; Wiley: Chichester ; New York, 1998.

(135) Imbrogno, J.; Maruyama, K.; Rivers, F.; Baltzegar, J. R.; Zhang, Z.; Meyer, P. W.; Ganesan, V.; Aoshima, S.; Lynd, N. A. Relationship between Ionic Conductivity, Glass Transition Temperature, and Dielectric Constant in Poly(Vinyl Ether) Lithium Electrolytes. *ACS Macro Lett.* **2021**, *10* (8), 1002–1007.

(136) Harikesh, P. C.; Surendran, A.; Ghosh, B.; John, R. A.; Moorthy, A.; Yantara, N.; Salim, T.; Thirumal, K.; Leong, W. L.; Mhaisalkar, S.; Mathews, N. Cubic NaSbS2 as an Ionic–Electronic Coupled Semiconductor for Switchable Photovoltaic and Neuromorphic Device Applications. *Adv. Mater.* **2020**, *32* (7), 1906976.

(137) Jamnik, J. Impedance Spectroscopy of Mixed Conductors with Semi-Blocking Boundaries. *Solid State Ion.* **2003**, *157* (1), 19–28.

(138) Lai, W.; Haile, S. M. Impedance Spectroscopy as a Tool for Chemical and Electrochemical Analysis of Mixed Conductors: A Case Study of Ceria. *J. Am. Ceram. Soc.* **2005**, *88* (11), 2979–2997.

(139) Holm, S.; Holm, T.; Martinsen, Ø. G. Simple Circuit Equivalents for the Constant Phase Element. *PLOS ONE* **2021**, *16* (3), e0248786.

(140) Lasia, A. The Origin of the Constant Phase Element. *J. Phys. Chem. Lett.* **2022**, *13* (2), 580–589.

(141) Alexander, C. L.; Tribollet, B.; Orazem, M. E. Contribution of Surface Distributions to Constant-Phase-Element (CPE) Behavior: 1. Influence of Roughness. *Electrochimica Acta* **2015**, *173*, 416–424.

(142) Alexander, C. L.; Tribollet, B.; Orazem, M. E. Contribution of Surface Distributions to Constant-Phase-Element (CPE) Behavior: 2. Capacitance. *Electrochimica Acta* **2016**, *188*, 566–573.

(143) Hirschorn, B.; Orazem, M. E.; Tribollet, B.; Vivier, V.; Frateur, I.; Musiani, M. Constant-Phase-Element Behavior Caused by Resistivity Distributions in Films: II. Applications. *J. Electrochem. Soc.* **2010**, *157* (12), C458.

(144) Jamnik, J.; Maier, J. Generalised Equivalent Circuits for Mass and Charge Transport: Chemical Capacitance and Its Implications. *Phys. Chem. Chem. Phys.* **2001**, *3* (9), 1668–1678.

(145) Amand, S.; Musiani, M.; Orazem, M. E.; Pébère, N.; Tribollet, B.; Vivier, V. Constant-Phase-Element Behavior Caused by Inhomogeneous Water Uptake in Anti-Corrosion Coatings. *Electrochimica Acta* **2013**, *87*, 693–700.

(146) Lee, J.-S.; Jamnik, J.; Maier, J. Generalized Equivalent Circuits for Mixed Conductors: Silver Sulfide as a Model System. *Monatshefte Für Chem. - Chem. Mon.* **2009**, *140* (9), 1113–1119.

(147) de Levie, R. On Porous Electrodes in Electrolyte Solutions: I. Capacitance Effects. *Electrochimica Acta* **1963**, *8* (10), 751–780.

(148) Kim, J. Y.; Jung, J. H.; Lee, D. E.; Joo, J. Enhancement of Electrical Conductivity of Poly(3,4-Ethylenedioxythiophene)/Poly(4-Styrenesulfonate) by a Change of Solvents. *Synth. Met.* **2002**, *126* (2), 311–316.

(149) Paulsen, B. D.; Tybrandt, K.; Stavrinidou, E.; Rivnay, J. Organic Mixed Ionic–Electronic Conductors. *Nat. Mater.* **2020**, *19* (1), 13–26.

(150) Zhdanov, V. P.; Kasemo, B. The Influence of the Electrolyte on the Electron Diffusion in Mesoporous Nanocrystalline TiO_2. *J. Phys. Condens. Matter* **2004**, *16* (15), 2625–2629.

(151) Celis-Salazar, P. J.; Epley, C. C.; Ahrenholtz, S. R.; Maza, W. A.; Usov, P. M.; Morris, A. J. Proton-Coupled Electron Transport in Anthraquinone-Based Zirconium Metal–Organic Frameworks. *Inorg. Chem.* **2017**, *56* (22), 13741–13747.

(152) Campbell, M. G.; Liu, S. F.; Swager, T. M.; Dincă, M. Chemiresistive Sensor Arrays from Conductive 2D Metal–Organic Frameworks. *J. Am. Chem. Soc.* **2015**, *137* (43), 13780–13783.

(153) Meng, Z.; Stolz, R. M.; Mirica, K. A. Two-Dimensional Chemiresistive Covalent Organic Framework with High Intrinsic Conductivity. *J. Am. Chem. Soc.* **2019**, *141* (30), 11929–11937.

(154) Huang, J.; He, Y.; Yao, M.-S.; He, J.; Xu, G.; Zeller, M.; Xu, Z. A Semiconducting Gyroidal Metal-Sulfur Framework for Chemiresistive Sensing. *J. Mater. Chem. A* **2017**, *5* (31), 16139–16143.

(155) Forster, R. J.; Iqbal, J.; Hjelm, J.; Keyes, T. E. Solvent Effects on Charge Transport through Solid Deposits of [Os(4,4′-Diphenyl-2,2′-Dipyridyl)$_2$Cl$_2$]. *Analyst* **2004**, *129* (12), 1186–1192.

(156) Dong, J.; Portale, G. Role of the Processing Solvent on the Electrical Conductivity of PEDOT:PSS. *Adv. Mater. Interfaces* **2020**, *7* (18), 2000641.

(157) Skale, S.; Doleček, V.; Slemnik, M. Substitution of the Constant Phase Element by Warburg Impedance for Protective Coatings. *Corros. Sci.* **2007**, *49* (3), 1045–1055.

(158) Balakrishnan, N. T. M.; Paul, A.; Krishnan, M. A.; Das, A.; Raphaez, L. R.; Ahn, J.-H.; Jabeen Fatima, M. J.; Prasanth, R. Lithium Iron Phosphate ($LiFePO_4$) as High-Performance Cathode Material for Lithium Ion Batteries. In *Metal, Metal-Oxides and Metal Sulfides for Batteries, Fuel Cells, Solar Cells, Photocatalysis and Health Sensors*; Rajendran, S., Karimi-Maleh, H., Qin, J., Lichtfouse, E., Eds.; Environmental Chemistry for a Sustainable World; Springer International Publishing: Cham, 2021; pp 35–73.

(159) Striebel, K.; Shim, J.; Srinivasan, V.; Newman, J. Comparison of $LiFePO_4$ from Different Sources. *J. Electrochem. Soc.* **2005**, *152* (4), A664.

(160) Park, M.; Zhang, X.; Chung, M.; Less, G. B.; Sastry, A. M. A Review of Conduction Phenomena in Li-Ion Batteries. *J. Power Sources* **2010**, *195* (24), 7904–7929.

(161) Wang, S.; Zhao, S.; Guo, X.; Wang, G. 2D Material-Based Heterostructures for Rechargeable Batteries. *Adv. Energy Mater.* **2022**, *12* (4), 2100864.

(162) Rojaee, R.; Shahbazian-Yassar, R. Two-Dimensional Materials to Address the Lithium Battery Challenges. *ACS Nano* **2020**, *14* (3), 2628–2658.

(163) Wang, Y.; Mao, J.; Meng, X.; Yu, L.; Deng, D.; Bao, X. Catalysis with Two-Dimensional Materials Confining Single Atoms: Concept, Design, and Applications. *Chem. Rev.* **2019**, *119* (3), 1806–1854.

(164) Deng, D.; Novoselov, K. S.; Fu, Q.; Zheng, N.; Tian, Z.; Bao, X. Catalysis with Two-Dimensional Materials and Their Heterostructures. *Nat. Nanotechnol.* **2016**, *11* (3), 218–230.

(165) Devarakonda, A.; Inoue, H.; Fang, S.; Ozsoy-Keskinbora, C.; Suzuki, T.; Kriener, M.; Fu, L.; Kaxiras, E.; Bell, D. C.; Checkelsky, J. G. Clean 2D Superconductivity in a Bulk van Der Waals Superlattice. *Science* **2020**, *370* (6513), 231–236.

(166) Niu, R.; Li, J.; Zhen, W.; Xu, F.; Weng, S.; Yue, Z.; Meng, X.; Xia, J.; Hao, N.; Zhang, C. Enhanced Superconductivity and Critical Current Density Due to the Interaction of $InSe_2$ Bonded Layer in $(InSe_2)0.12NbSe_2$. *J. Am. Chem. Soc.* **2024**, *146* (2), 1244–1249.

(167) Que, Y.; Chan, Y.-H.; Jia, J.; Das, A.; Tong, Z.; Chang, Y.-T.; Cui, Z.; Kumar, A.; Singh, G.; Mukherjee, S.; Lin, H.; Weber, B. A Gate-Tunable Ambipolar Quantum Phase Transition in a Topological Excitonic Insulator. *Adv. Mater.* **2024**, *36* (7), 2309356.

(168) Sauer, M. O.; Taghizadeh, A.; Petralanda, U.; Ovesen, M.; Thygesen, K. S.; Olsen, T.; Cornean, H.; Pedersen, T. G. Shift Current Photovoltaic Efficiency of 2D Materials. *Npj Comput. Mater.* **2023**, *9* (1), 1–9.

(169) Qiao, J.; Kong, X.; Hu, Z.-X.; Yang, F.; Ji, W. High-Mobility Transport Anisotropy and Linear Dichroism in Few-Layer Black Phosphorus. *Nat. Commun.* **2014**, *5* (1), 4475.

(170) Liu, H.; Neal, A. T.; Zhu, Z.; Luo, Z.; Xu, X.; Tománek, D.; Ye, P. D. Phosphorene: An Unexplored 2D Semiconductor with a High Hole Mobility. *ACS Nano* **2014**, *8* (4), 4033–4041.

(171) Qiao, J.; Pan, Y.; Yang, F.; Wang, C.; Chai, Y.; Ji, W. Few-Layer Tellurium: One-Dimensional-like Layered Elementary Semiconductor with Striking Physical Properties. *Sci. Bull.* **2018**, *63* (3), 159–168.

(172) Sutter, P.; Komsa, H. P.; Lu, H.; Gruverman, A.; Sutter, E. Few-Layer Tin Sulfide (SnS): Controlled Synthesis, Thickness Dependent Vibrational Properties, and Ferroelectricity. *Nano Today* **2021**, *37*, 101082.

(173) Zhao, Y.; Qiao, J.; Yu, P.; Hu, Z.; Lin, Z.; Lau, S. P.; Liu, Z.; Ji, W.; Chai, Y. Extraordinarily Strong Interlayer Interaction in 2D Layered PtS_2. *Adv. Mater.* **2016**, *28* (12), 2399–2407.

(174) Sun, Y.; Luo, S.; Zhao, X.-G.; Biswas, K.; Li, S.-L.; Zhang, L. InSe: A Two-Dimensional Material with Strong Interlayer Coupling. *Nanoscale* **2018**, *10* (17), 7991–7998.

(175) Ricci, M.; Ambrosetti, A.; Silvestrelli, P. L. Improving the Description of Interlayer Bonding in TiS_2 by Density Functional Theory. *J. Phys. Chem. C* **2020**, *124* (50), 27592–27603.

(176) Dai, Z.; Lu, N.; Liechti, K. M.; Huang, R. Mechanics at the Interfaces of 2D Materials: Challenges and Opportunities. *Curr. Opin. Solid State Mater. Sci.* **2020**, *24* (4), 100837.

(177) Kasai, H.; Tolborg, K.; Sist, M.; Zhang, J.; Hathwar, V. R.; Filsø, M. Ø.; Cenedese, S.; Sugimoto, K.; Overgaard, J.; Nishibori, E.; Iversen, B. B. X-Ray Electron Density Investigation of Chemical Bonding in van Der Waals Materials. *Nat. Mater.* **2018**, *17* (3), 249–252.

(178) Shi, H.; Fu, S.; Liu, Y.; Neumann, C.; Wang, M.; Dong, H.; Kot, P.; Bonn, M.; Wang, H. I.; Turchanin, A.; Schmidt, O. G.; Shaygan Nia, A.; Yang, S.; Feng, X. Molecularly Engineered Black Phosphorus Heterostructures with Improved Ambient Stability and Enhanced Charge Carrier Mobility. *Adv. Mater.* **2021**, *33* (48), 2105694.

(179) Miao, S.; Wang, T.; Huang, X.; Chen, D.; Lian, Z.; Wang, C.; Blei, M.; Taniguchi, T.; Watanabe, K.; Tongay, S.; Wang, Z.; Xiao, D.; Cui, Y.-T.; Shi, S.-F. Strong Interaction between Interlayer Excitons and Correlated Electrons in WSe_2/WS_2 Moiré Superlattice. *Nat. Commun.* **2021**, *12* (1), 3608.

(180) Duan, F.; Shen, C.; Zhang, H.; Qin, G. Hydrodynamically Enhanced Thermal Transport Due to Strong Interlayer Interactions: A Case Study of Strained Bilayer Graphene. *Phys. Rev. B* **2022**, *105* (12), 125406.

(181) Liu, Y.; Duan, X.; Shin, H.-J.; Park, S.; Huang, Y.; Duan, X. Promises and Prospects of Two-Dimensional Transistors. *Nature* **2021**, *591* (7848), 43–53.

(182) Long, G.; Maryenko, D.; Shen, J.; Xu, S.; Hou, J.; Wu, Z.; Wong, W. K.; Han, T.; Lin, J.; Cai, Y.; Lortz, R.; Wang, N. Achieving Ultrahigh Carrier Mobility in Two-Dimensional Hole Gas of Black Phosphorus. *Nano Lett.* **2016**, *16* (12), 7768–7773.

(183) Viti, L.; Politano, A.; Zhang, K.; Vitiello, M. S. Thermoelectric Terahertz Photodetectors Based on Selenium-Doped Black Phosphorus Flakes. *Nanoscale* **2019**, *11* (4), 1995–2002.

(184) Huang, M.; Wang, M.; Chen, C.; Ma, Z.; Li, X.; Han, J.; Wu, Y. Broadband Black-Phosphorus Photodetectors with High Responsivity. *Adv. Mater.* **2016**, *28* (18), 3481–3485.

(185) Yu, H.; Liu, G.-B.; Tang, J.; Xu, X.; Yao, W. Moiré Excitons: From Programmable Quantum Emitter Arrays to Spin-Orbit–Coupled Artificial Lattices. *Sci. Adv.* **2017**, *3* (11), e1701696.

(186) Bian, Z.; Miao, J.; Zhao, Y.; Chai, Y. Strong Interlayer Interaction for Engineering Two-Dimensional Materials. *Acc. Mater. Res.* **2022**, *3* (12), 1220–1231.

(187) Lu, Y.; Zhang, Y.; Yang, C.-Y.; Revuelta, S.; Qi, H.; Huang, C.; Jin, W.; Li, Z.; Vega-Mayoral, V.; Liu, Y.; Huang, X.; Pohl, D.; Položij, M.; Zhou, S.; Cánovas, E.; Heine, T.; Fabiano, S.; Feng, X.; Dong, R. Precise Tuning of Interlayer Electronic Coupling in Layered Conductive Metal-Organic Frameworks. *Nat. Commun.* **2022**, *13* (1), 7240.

(188) Apostol, P.; Gali, S. M.; Su, A.; Tie, D.; Zhang, Y.; Pal, S.; Lin, X.; Bakuru, V. R.; Rambabu, D.; Beljonne, D.; Dincă, M.; Vlad, A. Controlling Charge Transport in 2D Conductive MOFs─The Role of Nitrogen-Rich Ligands and Chemical Functionality. *J. Am. Chem. Soc.* **2023**, *145* (45), 24669–24677.

(189) Jakub, Z.; Shahsavar, A.; Planer, J.; Hrůza, D.; Herich, O.; Procházka, P.; Čechal, J. How the Support Defines Properties of 2D Metal–Organic Frameworks: Fe-TCNQ on Graphene versus Au(111). *J. Am. Chem. Soc.* **2024**, *146* (5), 3471–3482.

(190) Zhang, X.; Tian, X.; Wu, N.; Zhao, S.; Qin, Y.; Pan, F.; Yue, S.; Ma, X.; Qiao, J.; Xu, W.; Liu, W.; Liu, J.; Zhao, M.; Ostrikov, K. (Ken); Zeng, Z. Metal-Organic Frameworks with Fine-Tuned Interlayer Spacing for Microwave Absorption. *Sci. Adv.* **2024**, *10* (11), eadl6498.

(191) Day, R. W.; Bediako, D. K.; Rezaee, M.; Parent, L. R.; Skorupskii, G.; Arguilla, M. Q.; Hendon, C. H.; Stassen, I.; Gianneschi, N. C.; Kim, P.; Dincă, M. Single Crystals of Electrically Conductive Two-Dimensional Metal–Organic Frameworks: Structural and Electrical Transport Properties. *ACS Cent. Sci.* **2019**, *5* (12), 1959–1964.

(192) Pedersen, K. S.; Perlepe, P.; Aubrey, M. L.; Woodruff, D. N.; Reyes-Lillo, S. E.; Reinholdt, A.; Voigt, L.; Li, Z.; Borup, K.; Rouzières, M.; Samohvalov, D.; Wilhelm, F.; Rogalev, A.; Neaton, J. B.; Long, J. R.; Clérac, R. Formation of the Layered Conductive Magnet $CrCl_2(Pyrazine)_2$ through Redox-Active Coordination Chemistry. *Nat. Chem.* **2018**, *10* (10), 1056–1061.

(193) Wriedt, M.; Jeß, I.; Näther, C. Synthesis, Crystal Structure, and Thermal and Magnetic Properties of New Transition Metal–Pyrazine Coordination Polymers. *Eur. J. Inorg. Chem.* **2009**, *2009* (10), 1406–1413.

(194) Samir, B.; Kalalian, C.; Roth, E.; Salghi, R.; Chakir, A. Gas-Phase UV Absorption Spectra of Pyrazine, Pyrimidine and Pyridazine. *Chem. Phys. Lett.* **2020**, *751*, 137469.

(195) Burks, R.; Öhrström, L.; Amombo Noa, F. M. Clarifying the Complex Chemistry of Cobalt(II) Thiocyanate-Based Tests for Cocaine Using Single-Crystal X-Ray Diffraction and Spectroscopic Techniques. *J. Forensic Sci.* **2024**, *69* (1), 291–300.

(196) Huang, Y.; Pan, Y.-H.; Yang, R.; Bao, L.-H.; Meng, L.; Luo, H.-L.; Cai, Y.-Q.; Liu, G.-D.; Zhao, W.-J.; Zhou, Z.; Wu, L.-M.; Zhu, Z.-L.; Huang, M.; Liu, L.-W.; Liu, L.; Cheng, P.; Wu, K.-H.; Tian, S.-B.; Gu, C.-Z.; Shi, Y.-G.; Guo, Y.-F.; Cheng, Z. G.; Hu, J.-P.; Zhao, L.; Yang, G.-H.; Sutter, E.; Sutter, P.; Wang, Y.-L.; Ji, W.; Zhou, X.-J.; Gao, H.-J. Universal Mechanical Exfoliation of Large-Area 2D Crystals. *Nat. Commun.* **2020**, *11* (1), 2453.

(197) Luo, Y.-H.; Chen, C.; He, C.; Zhu, Y.-Y.; Hong, D.-L.; He, X.-T.; An, P.-J.; Wu, H.-S.; Sun, B.-W. Single-Layered Two-Dimensional Metal–Organic Framework Nanosheets as an in Situ Visual Test Paper for Solvents. *ACS Appl. Mater. Interfaces* **2018**, *10* (34), 28860–28867.

(198) Liu, Y.; Liu, H.; Yan, H.; Liu, Y.; Zhang, J.; Shan, W.; Lai, P.; Li, H.; Ren, L.; Li, Z.; Nie, L. Aggregation-Induced Absorption Enhancement for Deep Near-Infrared II Photoacoustic Imaging of Brain Gliomas In Vivo. *Adv. Sci.* **2019**, *6* (8), 1801615.

(199) Hua, C.; Doheny, P. W.; Ding, B.; Chan, B.; Yu, M.; Kepert, C. J.; D'Alessandro, D. M. Through-Space Intervalence Charge Transfer as a Mechanism for Charge Delocalization in Metal–Organic Frameworks. *J. Am. Chem. Soc.* **2018**, *140* (21), 6622–6630.

(200) Ding, B.; Hua, C.; Kepert, C. J.; D'Alessandro, D. M. Influence of Structure–Activity Relationships on through-Space Intervalence Charge Transfer in Metal–Organic Frameworks with Cofacial Redox-Active Units *Chem. Sci.* **2018**, *10* (5), 1392–1400.

(201) Wang, C.; He, Q.; Halim, U.; Liu, Y.; Zhu, E.; Lin, Z.; Xiao, H.; Duan, X.; Feng, Z.; Cheng, R.; Weiss, N. O.; Ye, G.; Huang, Y.-C.; Wu, H.; Cheng, H.-C.; Shakir, I.; Liao, L.; Chen, X.; Goddard III, W. A.; Huang, Y.; Duan, X. Monolayer Atomic Crystal Molecular Superlattices. *Nature* **2018**, *555* (7695), 231–236.

(202) Kallweit, C.; Haberhauer, G.; Woitschetzki, S. 4,4'-Bipyridine as a Unidirectional Switching Unit for a Molecular Pushing Motor. *Chem. Weinh. Bergstr. Ger.* **2014**, *20* (21), 6358–6365.

(203) Winkler, C.; Zojer, E. Strategies for Controlling Through-Space Charge Transport in Metal-Organic Frameworks via Structural Modifications. *Nanomaterials* **2020**, *10* (12), 2372.

(204) Nath, A.; Kumar, V.; Shukla, A.; Ghosh, H. N.; Mandal, S. Influence of Molecular Separation on Through-Space Intervalence Transient Charge Transfer in Metal–Organic Frameworks with Cofacially Arranged Redox Pairs. *Angew. Chem. Int. Ed.* **2023**, *62* (31), e202308034.

(205) Shulenburger, L.; Baczewski, A. D.; Zhu, Z.; Guan, J.; Tománek, D. The Nature of the Interlayer Interaction in Bulk and Few-Layer Phosphorus. *Nano Lett.* **2015**, *15* (12), 8170–8175.

(206) Yang, J.; Xu, R.; Pei, J.; Myint, Y. W.; Wang, F.; Wang, Z.; Zhang, S.; Yu, Z.; Lu, Y. Optical Tuning of Exciton and Trion Emissions in Monolayer Phosphorene. *Light Sci. Appl.* **2015**, *4* (7), e312–e312.

(207) Rodin, A. S.; Carvalho, A.; Castro Neto, A. H. Strain-Induced Gap Modification in Black Phosphorus. *Phys. Rev. Lett.* **2014**, 112 (17), 176801.

(208) Rosati, R.; Paradisanos, I.; Huang, L.; Gan, Z.; George, A.; Watanabe, K.; Taniguchi, T.; Lombez, L.; Renucci, P.; Turchanin, A.; Urbaszek, B.; Malic, E. Interface Engineering of Charge-Transfer Excitons in 2D Lateral Heterostructures. *Nat. Commun.* **2023**, *14* (1), 2438.

(209) Kallatt, S.; Das, S.; Chatterjee, S.; Majumdar, K. Interlayer Charge Transport Controlled by Exciton–Trion Coherent Coupling. *Npj 2D Mater. Appl.* **2019**, *3* (1), 1–8.

(210) Zhu, X.; Monahan, N. R.; Gong, Z.; Zhu, H.; Williams, K. W.; Nelson, C. A. Charge Transfer Excitons at van Der Waals Interfaces. *J. Am. Chem. Soc.* **2015**, *137* (26), 8313–8320.

(211) Liu, Y.; Elbanna, A.; Gao, W.; Pan, J.; Shen, Z.; Teng, J. Interlayer Excitons in Transition Metal Dichalcogenide Semiconductors for 2D Optoelectronics. *Adv. Mater.* **2022**, *34* (25), 2107138.

(212) Policht, V. R.; Mittenzwey, H.; Dogadov, O.; Katzer, M.; Villa, A.; Li, Q.; Kaiser, B.; Ross, A. M.; Scotognella, F.; Zhu, X.; Knorr, A.; Selig, M.; Cerullo, G.; Dal Conte, S. Time-Domain Observation of Interlayer Exciton Formation and Thermalization in a $MoSe_2/WSe_2$ Heterostructure. *Nat. Commun.* **2023**, *14* (1), 7273.

(213) Kim, H.; Choi, Y.; Lewandowski, C.; Thomson, A.; Zhang, Y.; Polski, R.; Watanabe, K.; Taniguchi, T.; Alicea, J.; Nadj-Perge, S. Evidence for Unconventional Superconductivity in Twisted Trilayer Graphene. *Nature* **2022**, *606* (7914), 494–500.

(214) Prisecaru, I. WMOSS4 Mössbauer Spectral Analysis Software. http://www.wmoss.org/.

(215) Bain, G. A.; Berry, J. F. Diamagnetic Corrections and Pascal's Constants. *J. Chem. Educ.* **2008**, *85* (4), 532.

(216) Bolton, S. G.; Pluth, M. D. Modified Cyclodextrins Solubilize Elemental Sulfur in Water and Enable Biological Sulfane Sulfur Delivery. *Chem. Sci.* **2020**, *11* (43), 11777–11784.

(217) Toby, B. H. R Factors in Rietveld Analysis: How Good Is Good Enough? *Powder Diffr.* **2006**, *21* (1), 67–70.

(218) B.N., F.; Hitchman, M. The Electronic Spectra of Complexes. In *Ligand Field Theory and Its Applications*; Wiley, 1999; pp 211–213.

(219) Lever, A. B. P. *Electronic spectra of some transition metal complexes: Derivation of D_q and B*. ACS Publications.

(220) Kresse, G.; Furthmüller, J. Efficiency of Ab-Initio Total Energy Calculations for Metals and Semiconductors Using a Plane-Wave Basis Set. *Comput. Mater. Sci.* **1996**, *6* (1), 15–50.

(221) Perdew, J. P.; Burke, K.; Ernzerhof, M. Generalized Gradient Approximation Made Simple [Phys. Rev. Lett. 77, 3865 (1996)]. *Phys. Rev. Lett.* **1997**, *78* (7), 1396–1396.

(222) Blöchl, P. E. Projector Augmented-Wave Method. *Phys. Rev. B* **1994**, *50* (24), 17953–17979.

(223) Krukau, A. V.; Vydrov, O. A.; Izmaylov, A. F.; Scuseria, G. E. Influence of the Exchange Screening Parameter on the Performance of Screened Hybrid Functionals. *J. Chem. Phys.* **2006**, *125* (22), 224106.

(224) Bondarenko A. S., Ragoisha G. A. EIS Spectrum Analyser, 2005. http://www.abc.chemistry.bsu.by/vi/analyser/.

(225) Adams, C. J.; Real, J. A.; Waddington, R. E. The Two-Dimensional Iron(II)–Thiocyanate–4,4′-Bipyridine Coordination Network. *CrystEngComm* **2010**, *12* (11), 3547–3553.

(226) Wriedt, M.; Sellmer, S.; Näther, C. Coordination Polymer Changing Its Magnetic Properties and Colour by Thermal Decomposition: Synthesis, Structure and Properties of New Thiocyanato Iron(II) Coordination Polymers Based on 4,4′-Bipyridine as Ligand. *Dalton Trans.* **2009**, No. 38, 7975–7984.

(227) Haynes, J. S.; Sams, J. R.; Thompson, R. C. Magnetic and Spectroscopic Study of Pyrazine-Bridged Iron(II) Halide Complexes. *Inorg. Chem.* **1986**, *25* (21), 3740–3744.

(228) Liu, J.; Goddard, P. A.; Singleton, J.; Brambleby, J.; Foronda, F.; Möller, J. S.; Kohama, Y.; Ghannadzadeh, S.; Ardavan, A.; Blundell, S. J.; Lancaster, T.; Xiao, F.; Williams, R. C.; Pratt, F. L.; Baker, P. J.; Wierschem, K.; Lapidus, S. H.; Stone, K. H.; Stephens, P. W.; Bendix, J.; Woods, T. J.; Carreiro, K. E.; Tran, H. E.; Villa, C. J.; Manson, J. L. Antiferromagnetism in a Family of S = 1 Square Lattice Coordination Polymers $NiX_2(Pyz)_2$ (X = Cl, Br, I, NCS; Pyz = Pyrazine). *Inorg. Chem.* **2016**, *55* (7), 3515–3529.